

Core-Shell Particles  
Experiments and Self-Consistent Field Modeling

**Thesis committee**

**Thesis supervisors**

Prof. dr. M.A. Cohen Stuart  
Professor of Physical Chemistry and Colloid Science  
Wageningen University

Prof. dr. ir. F.A.M. Leermakers  
Personal Chair at the Laboratory of  
Physical Chemistry and Colloid Science  
Wageningen University

**Thesis co-supervisor**

Dr. ir. J.M. Kleijn  
Assistent Professor at the Laboratory of  
Physical Chemistry and Colloid Science  
Wageningen University

**Other members**

Prof. dr. C.J.M. van Rijn	Organic Chemistry, Wageningen University
Prof. dr. W.J. Briels	Computational Biophysics, University of Twente
Prof. dr. O.V. Borisov	Institut Pluridisciplinaire de Recherche sur l'Environnement et les Matériaux, Pau, France
Dr. ir. F.G.H. van Wijk	Nuplex Resins, Bergen op Zoom

This research was conducted under the auspices of Graduate School VLAG.

Core-Shell Particles  
Experiments and Self-Consistent Field Modeling

P.A. Iakovlev

**Thesis**

submitted in fulfilment of the requirements  
for the degree of doctor  
at Wageningen University  
by the authority of the Rector Magnificus  
Prof. dr. M. J. Kropff  
in the presence of the

Thesis Committee appointed by the Academic Board  
to be defended in public  
on Friday May 13, 2011  
at 11:00 a.m. in the Aula.

130313

ISBN: 978-90-8585-868-3

# Propositions

1. The key for grasping the complex behavior of waterborne coatings is to understand the force-distance dependence of its core-shell resin particles (this thesis).
2. The remarkable match of SCF predictions and colloid probe AFM experiments enhances the credibility of both approaches (this thesis).
3. Research should only be coined "drug delivery" when clinical trials are performed (Alexander V. Kabanov lecture series in Moscow, 2003).
4. Science has to be driven by curiosity more than by funding.
5. Foreign students doing a PhD in the Netherlands would perform better if they knew how a PhD in the Netherlands differs from that in their home country.
6. Paint formulating not only benefits from detailed physical insights in the processes involved, but also from inspiration and improvisation.
7. Locking the laboratory during night hours inhibits creative processes: enlightening ideas seem best in the dark.
8. It is a waste to use a rich mixture of chemicals such as oil or gas as a fuel. One can make polymers out of it instead.

Propositions belonging to the thesis:  
Core-Shell Particles  
Experiments and Self-Consistent Field Modeling  
P.A. Iakovlev  
Wageningen, May 13, 2011

For my mother

This project is supported with a grant of the Dutch Programme EET (Economy, Ecology, Technology) a joint initiative of the Ministries of Economic Affairs, Education, Culture and Sciences and of Housing, Spatial Planning and the Environment.

Seven Strophes

х х х

М. Б.

I was but what you'd brush  
with your palm, what your leaning  
brow would hunch to in evening's  
raven-black hush.

I was but what your gaze  
in that dark could distinguish:  
a dim shape to begin with,  
later - features, a face.

It was you, on my right,  
on my left, with your heated  
sighs, who molded my helix  
whispering at my side.

It was you by that black  
window's trembling tulle pattern  
who laid in my raw cavern  
a voice calling you back.

I was practically blind.  
You, appearing, then hiding,  
gave me my sight and heightened  
it. Thus some leave behind

a trace. Thus they make worlds.  
Thus, having done so, at random  
wastefully they abandon  
their work to its whirls.

Thus, prey to speeds  
of light, heat, cold, or darkness,  
a sphere in space without markers  
spins and spins.

J. Brodsky, 1981

Я был только тем, чего  
ты касалась ладонью,  
над чем в глухую, воронью  
ночь склоняла чело.

Я был лишь тем, что ты  
там, снизу, различала:  
смутный облик сначала,  
много позже - черты.

Это ты, горяча,  
ошую, одесную  
раковину ушную  
мне творила, шепча.

Это ты, теребя  
штору, в сырую полость  
рта вложила мне голос,  
окликавший тебя.

Я был попросту слеп.  
Ты, возникая, прячась,  
даровала мне зрячесть.  
Так оставляют след.

Так творятся миры.  
Так, сотворив их, часто  
оставляют возвращаться,  
расточая дары.

Так, бросаем то в жар,  
то в холод, то в свет, то в темень,  
в мирозданьи потерян,  
кружится шар.

И.Бродский, 1981



# Contents

<b>1</b>	<b>Introduction</b>	<b>5</b>
1.1	General introduction . . . . .	5
1.2	Water-borne coatings . . . . .	7
1.3	The project and parties involved . . . . .	10
1.4	Core-shell particles . . . . .	11
1.5	Outline of this thesis . . . . .	13
<b>2</b>	<b>Characterization</b>	<b>19</b>
2.1	Abstract . . . . .	19
2.2	Introduction . . . . .	20
2.3	Materials and Methods . . . . .	22
2.3.1	Core-Shell Particles . . . . .	22
	Monomer composition . . . . .	22
	Particle synthesis . . . . .	24
2.3.2	Methods . . . . .	25
	Static Light Scattering: Zimm plots . . . . .	25
	Dynamic Light Scattering titrations . . . . .	26
	Potentiometric titrations . . . . .	26
	AFM in tapping mode . . . . .	27
	Theoretical fitting of DLS-titration data . . . . .	27
2.4	Results . . . . .	28
	SLS - Zimm plot . . . . .	28
	Potentiometric titrations . . . . .	29
	AFM imaging . . . . .	30
	Dynamic Light Scattering . . . . .	32
2.5	Discussion . . . . .	33
2.6	Conclusions . . . . .	37
<b>3</b>	<b>Hydrophobic Polyelectrolyte Brushes and Stars</b>	<b>39</b>
3.1	Abstract . . . . .	39
3.2	Introduction . . . . .	40

3.3	Self consistent field theory . . . . .	46
3.3.1	Lattices . . . . .	47
3.3.2	The SCF machinery . . . . .	51
3.3.3	From volume fractions to potentials . . . . .	52
3.3.4	From potentials to volume fractions . . . . .	54
3.3.5	Annealed charges . . . . .	58
3.3.6	Numerical recipe . . . . .	58
3.3.7	Thermodynamics and other measurables . . . . .	59
3.4	Isolated hydrophobic PE brush on a flat substrate in an aqueous solution . . . . .	61
3.4.1	Parameters . . . . .	61
3.4.2	Results and Discussion . . . . .	64
3.5	Thermodynamic stability of the flat PE brush . . . . .	81
3.5.1	Description and parameters . . . . .	81
3.5.2	Results and discussion . . . . .	82
3.6	Interactions between two flat HPE brushes . . . . .	85
3.7	Interactions between flat bilateral brushes . . . . .	92
3.8	Interacting laterally inhomogeneous brushes . . . . .	98
3.9	Isolated HPE stars . . . . .	104
3.9.1	Interacting PE Stars in cell-model . . . . .	113
3.9.2	Interacting PE stars in two-gradient model . . . . .	117
3.10	Discussion and conclusions . . . . .	124
<b>4</b>	<b>AFM force</b>	<b>127</b>
4.1	abstract . . . . .	127
4.2	Introduction . . . . .	128
4.3	Materials and Methods . . . . .	130
	Core-Shell Particles . . . . .	130
	Adsorption . . . . .	130
	Force Measurements . . . . .	132
	Measurements in 30% butyl glycol solutions . . . . .	134
	Theoretical fitting of the data . . . . .	134
4.4	Results . . . . .	137
	Bare surfaces . . . . .	137
	Force measurements upon approach of CSP layers in aqueous solutions . . . . .	137
	Forces upon retraction of CSP layers in continuous measurements; Aqueous solutions . . . . .	143
	CP-AFM force measurements with surface delay time. . . . .	144
	Measurements on CSP in 30% butyl glycol in water solutions . . . . .	151

---

4.5	Conclusions . . . . .	156
<b>5</b>	<b>Bending brushes</b>	<b>159</b>
5.1	abstract . . . . .	159
5.2	Introduction . . . . .	160
5.3	Numerical SCF method . . . . .	163
5.4	Analytical theory . . . . .	166
5.4.1	Theory for curved brushes . . . . .	166
5.4.2	The curvature free energy of a bilateral brush. . . . .	170
5.5	Numerical Results and Discussion . . . . .	174
5.5.1	Curved quenched polymer brush . . . . .	176
5.5.2	Bending of a bilateral polymer layer . . . . .	179
5.5.3	Bending moduli of a bilateral polymer brush . . . . .	183
5.6	Conclusions . . . . .	185
	<b>Summary and General Discussion</b>	<b>187</b>
	<b>Samenvatting</b>	<b>195</b>
	<b>References</b>	<b>197</b>
	<b>Acknowledgements</b>	<b>207</b>
	<b>Curriculum Vitae</b>	<b>209</b>
	<b>List of publications</b>	<b>211</b>

# Chapter 1

## Introduction

### 1.1 General introduction

A large portion of man-made objects around us is covered by a coating of some sort. Coatings are applied for many reasons. Very often this is done to protect objects from external harm, such as erosion, oxidation, dissolution, etcetera. In this case the coating is used to extend the lifetime of a product. The surfaces of objects may also be modified for aesthetic reasons. Even though the objects that needs protection typically differ in properties, application and appearance, coatings or paints often have quite similar compositions. Classical solvent-based paints are composite liquids before drying. Most of the paint compositions contain three main components: (i) a pigment, which gives color to the final coating layer, (ii) a binder, which holds the pigment particles together in the resulting film, and (iii) a solvent, which makes the pigment and binder disperse before application. Upon drying of a paint, the solvent typically evaporates. Then the pigments and binder come in intimate contact, eventually forming an opaque solid film. There are, of course, exceptions to this recipe, such as powder coatings, which contain no solvent and are melted upon application to form a continuous film, or coatings in which the binder initially has the role of a solvent and upon application turns into a binder by way of a chemical reaction. In these cases no solvents come free.

When objects need to be protected in outdoor applications, one of the main targets for a coating is to protect a product against water. Most paints used to acquire a long-lasting performance are still based on some apolar organic solvent. Such solvent is ideal to mix with the pigment and binder, both of which are for obvious reasons also apolar. As a result, the paint solution is stable and all components are nicely dispersed or even dissolved

in the solvent. Upon drying the resulting film is robust and water-repellent.

Indeed, solvent-based paints often give excellent results. The films are nice and smooth, they resist water and are long-lasting. What is unsatisfactory about these products is their general toxicity in a broad sense of the term. Due to the evaporation of large amounts of organic solvent, they are toxic when produced and applied. Organic solvents are often referred to as volatile organic compounds (VOC). VOCs harm both the people involved in the industrial processes, as well as the environment. Several decades ago this problem came to the attention of legislature all around the world and actions have been taken to limit the use of solvent-based paints. It is now widely accepted that the VOC emissions should be reduced significantly. In our view, such reduction is possible through innovation.

There are many options to limit the adverse effect of VOCs. The fastest and most straightforward ones are (i) to collect the VOCs at the application sites, (ii) to increase the content of the other components in the paint (and thus to decrease the solvent content) and (iii) to apply less harmful solvents. These actions may help on the short term, but are not expected to be the best ones in the long run. One of the more challenging, but also more promising actions, is to change the solvent in the coating formulation. More specifically one should radically change from using some organic dispersant to water as the solvent. This route is not easy nor straightforward. Changing the solvent from an apolar to a polar one means changing the pigment and binder as well. Moreover, using water as a solvent introduces much more structure: making dispersions or emulsions means presence of many interfaces. This implies a complete re-design of the paint formulation. By changing the formulation, one should keep in mind that the final coating needs to remain water-repellent. In recent years large investments and research efforts were directed to meet this challenge.

Apart from dispersion issues there may be many more aspects to take into account when paints are switched from solvent-borne to water-borne. One of these is that the equipment that is needed to produce and apply the coatings requires corresponding modifications. For instance, all the tubing should be exchanged to stainless steel. There are also logistical consequences, as water freezes at 0 °C at normal atmospheric pressure and this may give problems when paints are being transported in wintertime, e.g., in Siberia.

The toxicity issues, which drive the changes in technology, are not the only reason to switch to water-based paints. There are other positive outcomes of the replacement of solvent by water. As new performance-oriented coatings are being developed the switch to water-borne technology can also reduce energy consumption and costs, e.g., because water is much less expensive than corresponding VOCs it is replacing.

One may argue that the best solution is still 100% solids paints (which may be still liquid), however, this is extremely difficult to achieve, and dispersing and dissolving binders and pigments in water is considered easier as a short-term solution.

## 1.2 Water-borne coatings

It is necessary to mention here that so-called water-borne (WB) paints are already used in the automotive industry for coating of cars since the 1990s. For these paints the term water-borne is used even though in practice the formulations still contain large amounts of organic co-solvent. These organic co-solvents are undesired and tighter regulations may limit the co-solvent usage in the near future. Due to this there is a continued demand for innovations.

If we compare water as a solvent with typical organic counterparts, it is noticed that organic solvents have few tunable parameters to become compatible with the other paint compounds, while there are many more for water. In organic solvent the main tuning parameter is the temperature, which changes the density and viscosity of the solvent. In addition to the temperature, for water one can vary the salinity and acidity with little effort. We will see that these options introduce a level of complexity to WB coatings, and opens up many opportunities for paint developments. On the other hand is of course the fact that there are many organic solvents and only one water, so, in case of VOCs, the proper solvent could be picked up to match the other components, while in water-based paints the binder and pigment should be tuned to match water.

Now, let's list the essential physical properties of a coating, with an emphasis on automotive coatings. The most important characteristics, omitting the price and energy issues for the time-being, are:

- Long shelf life. A paint formulation must be a stable dispersion. This means that the particles that are in the dispersion should not precipitate nor aggregate for long periods of time before the paint is applied, nor should the WB paint be contaminated with fungi or microbes.
- Easy application and excellent appearance. This requires that the paint should have a low viscosity when pumped through the tubing and the spray-gun nozzle and a high viscosity when it sits on the surface that is being coated. These two conditions imply that the dispersion must be pseudoplastic or shear-thinning. Normally, a difference of several

orders of magnitude in viscosities between the low and high shear rates is desired.

- Homogeneous film formation. Upon drying and further weathering, the film should be plastic to avoid cracking. The dispersed particles should coalesce well to form a continuous phase.
- Good performance. The coating should not only be water-insoluble, but also resistant to organic solvents. The film should withstand UV-exposure and must be strong enough so that it does not suffer much damage from impacts of small stones.
- Durable. All the desired properties of coating listed above should be robust and long-lasting.

In fact, all these demands put together are too much for any single coating to achieve, be it solvent-borne or water-borne. Therefore, many objects requiring high quality coatings are covered by a multi-layer coating, where each individual layer specializes in one or more of the demands mentioned above.

Some of these requirements are not yet fully implemented in WB coatings without the use of organic co-solvents. For instance, the homogeneous film formation is still impossible without the use of co-solvents. Other requirements may seem incompatible from a first glance. For example, the stability of the dispersion means that the interactions between particles in water are repulsive. Under these conditions water likes to be between the particles. The final film should be water-repellent. This means that the resulting film should deny water to penetrate. Hence upon drying the film should switch from being hydrophilic to hydrophobic. This requirement calls for a "smart design" of the WB paints. To date there is still room for improvement and various approaches are in the stage of development.

The stricter rules set by regulations, together with higher performance demands from manufacturers, provide a constant need for improvement in coating formulations. There are several possible ways to approach this need.

In the paint industry, many improvements are now achieved by way of combinatorial chemistry and subsequent testing. In this approach a large set of slightly different formulations are produced. The products and formulations that performs best are selected via some high-throughput screening test.<sup>1,2</sup> One should realize that this is not a completely blind procedure. Of course one must have insight in the basic properties of the chemistry that is needed and know the rules how to design dispersions. In general the combinatorial route is helpful in fine-tuning a particular formulation.

It is instructive to formulate, in somewhat more detail, the physical chemical properties of water-borne paint formulations. To ensure the insolubility of the final coating layer, it should contain considerable amounts of hydrophobic material. Initially, that is, in the dispersion, this hydrophobic material should be made compatible with water. How to achieve this? Usually the hydrophobic material is dispersed into small colloidal particles, and these particles are stabilized somehow in water to avoid precipitation. There are of course, several ways to stabilize colloidal dispersions and there is a whole branch in physical chemistry dealing with this. Probably the easiest way to do this is by adding surfactants. Surfactant molecules will adsorb onto the hydrophobic colloids rendering their surface hydrophilic and making it compatible with water. This is not the ideal solution because the surfactants will stay in the film when the coating forms. A consequence of this is that the water-resistance is compromised. Moreover surfactants readily can form foams which are unwanted in paints. Another possibility is to add some water-soluble co-polymers to the dispersion. These may adsorb onto the colloidal particles with their hydrophobic part, keeping the hydrophilic one dissolved. By using polymers one can implement some tricks to overcome the requirement that the coating turns hydrophobic.

One of the tricks, which is probably most frequently used to solve the issue, is to introduce ionic species to the formulation. Water is polar, so it readily dissolves ions and electrostatic interactions play an important role in water. Relatively few charges on the surface of a colloid can make it repel other ones. Hence, charges can help the particles to be dispersed in water. Next, if it appears possible to suppress the charges when a coating has formed, and if small additions of water to the coating do not regenerate the charges, the target is in sight. It turns out that placing the charges directly on the surface of solid colloidal particles is not the best choice. A much more clever way is to use some additional charge-carriers, namely polyelectrolytes, and attach these to the surface of the colloids. The true charm of polyelectrolytes is that the same polymers can help to turn the repulsion between colloids to attraction upon drying: if the ionic groups are separated by a few hydrophobic segments in the polymer chains, that is when hydrophobic polyelectrolytes (HPE) are used, the interplay between electrostatic and hydrophobic forces can provide a switch in interaction from repulsion to attraction depending on the distance between the particles (and thus upon drying). On top of this, it turns out that these polyelectrolytes not only provide electrostatic repulsion to keep the particles in solution, but they also can introduce other essential properties to a paint solution, such as the extreme shear thinning.

The use of hydrophobic polyelectrolytes is a good example of a "smart



design" of WB coating systems. In true applications it is accompanied with various other smart tricks, such as cross-linking, which we do not describe here as these typically belong to the secret kitchen of the paint and resin producers. As a result present-day WB coatings can be applied to various objects, including automobiles.<sup>3</sup> On the other hand, many ideas about the internal structure and interactions that play role in coatings at different stages from synthesis to application and usage are not or only marginally supported by theoretical and/or experimental evidence. In other words, though being successfully produced and applied, the physics of WB coatings is, in general, not really well understood, and there is a lack of theoretical underpinning. This severely limits further developments of water-borne coating systems.

Colloidal stabilization by means of polymer adsorption or grafting is a classical topic in the field of colloid science. The topic is not only relevant for paints, but for a multitude of other areas such as food industry, pharmaceuticals, healthcare, etcetera. Focusing on polyelectrolytes, the first systems that were studied systematically were quenched anionic polymers. More recently, polyacids have gained more attention.<sup>4-6</sup> It must be mentioned that in most investigations there was a clear emphasis on colloidal stability issues while other important properties, such as the corresponding rheological behavior, are much less studied. Moreover, typical for academic research, ideal, well-defined, systems are preferred over complex ones. The obvious reason for this is that well-defined systems allow for a better understanding of particular properties. However, the latter type of systems are not typical for industrial formulations. This gap between industrial and academic research is not particularly helpful to quickly progress developments towards better WB coating systems. In this project we attempt to bridge the gap between industrial and academic research and work on a system provided by the industry in an academic setting.

### 1.3 The project and parties involved

The drawbacks of the poor knowledge about the intrinsic physico-chemical properties of coating dispersions in industry, and sometimes rather idealistic academic approach are well realized, and there is an effort to remove them. The Dutch government was willing to invest in academic research in this area and thus an "Economy-Ecology-Technology" (E.E.T.) project named Water-borne Automotive Coatings (Dutch name "E.E.T.K01155 Water borne automotive lakhsarsen") emerged in 2002. This project involves collaboration of a number of universities and industry. The participants are Akzo Nobel Chemicals

B.V., Nuplex Resins B.V., TU Delft (Laboratory of Joining and Mechanical Behavior of Materials), TU Delft (Laboratory of Polymer Materials and Engineering), Twente University (Computational Dispersion Rheology group), and Wageningen University (Laboratory for Physical Chemistry and Colloid Science). Nuplex Resins, Akzo Nobel Chemicals together with Delft university were mostly involved in issues concerning the design and mechanical properties of coatings. This included studies into developing standardized methods for stone damage tests and theory on how the coating reacts on impacts and how the damage could be reduced.

Other groups, i.e. Nuplex Resins, the Molecular Modeling group of prof. Briels at Twente University and our group at Wageningen were mostly investigating properties of the polymeric binder which forms the basecoat on automobiles. The main goals of this collaboration were to (i) find out how the molecular properties of binder resin determine its rheology, i.e. shear-thinning, (ii) to understand what the main role is of the co-solvent in the dispersion during shelf-life and upon application, and more generally (iii) to develop a good understanding on how the design and chemical composition of the particles provides for the properties of dispersion. Nuplex Resins provided a sample basecoat dispersion and chemical data about the synthesis step, as well as their expertise and views on how the dispersion is designed on molecular level and on how it works in a paint. Our mission was to check their knowledge and views from a physico-chemical perspective, point out the most relevant features of the particle design, and study inter-particle interactions which play a key role in the performance. In parallel, the basic information was used by the Twente Group to predict the dynamical properties of concentrated dispersion, such as the rheological behavior of the paint from a pure physical perspective, applying molecular dynamics tools.

## 1.4 Core-shell particles

The main objects of interest, studied in this thesis, are colloid particles that make up the binder component of a paint (see figure 1.1). As is outlined in this figure the system contains particles that are of the core-shell type and behave strongly pseudo-plastic. The chemistry is in line with the requirements discussed above. The core is made of hydrophobic material while the shell (corona) is a hydrophobic polyelectrolyte. We study the structure of these core-shell particles and their interactions in solution. We further try to point to the most relevant properties of the particle design. More generally, the physics of the dispersion is studied on a single-particle level. Additionally, the particular role of the co-solvent is investigated, aiming

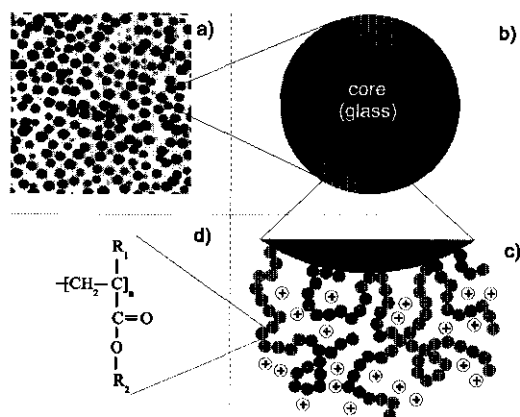


**Figure 1.1:** An illustration of core-shell particles (CSP) structure at different levels of magnification. a) AFM image of an adsorbed CSP layer (see chapter 2 for details); b) a very simplified overall structure of a single particle; c) a simplified representation of the shells, which contain ionic species and counterions; d) chemical structure of acrylic monomers, composing the particles. Here  $R_1$  is either a hydrogen (H), in case of acrylic monomers or a methyl group ( $\text{CH}_3$ ) in case of methacrylics and  $R_2$  could be hydrogen once again, making (meth)acrylic acid;  $\text{CH}_3$ , making (meth)acrylate;  $\text{CH}_2 - \text{CH}_2 - \text{OH}$ , making hydroxyethyl (meth)acrylate or  $(\text{CH}_2)_3 - \text{CH}_3$ , making butyl (meth)acrylate (for particular composition see chapter 2).

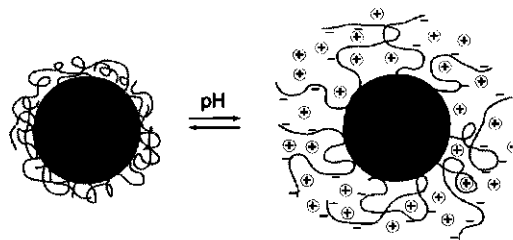


**Figure 1.2:** Illustration of changes in the shell structure with change in acidity of the solution: at low pH methacrylic groups are deionized, and shells are collapsed due to hydrophobic forces. With rise in pH the shells charge and swell due to osmotic pressure of the counterions that are trapped in the shells to compensate for the charges (see chapter 2 for details).

at the reduction or elimination of co-solvents in water-borne paints. Our research is performed in close collaboration with the group of prof. Briels at Twente University, who model the pseudo-plastic behavior of concentrated dispersions. Their modeling work requires input such as the particle pair interaction potential, which falls in the scope of our study.

The laboratory at Wageningen University is equipped with necessary tools to do the job. There are instruments for the molecular characterization of particles, such as potentiometric titration set-ups, light scattering equipment and atomic force microscopes. Additionally, the lab has a well-developed numerical method for modelling of polymeric systems. This method is used to underpin experimental findings and support the experimental program.

## 1.5 Outline of this thesis

This thesis is composed of four technical chapters complemented with a summary and a general discussion. We will briefly introduce these chapters focusing on the main targets and the methods used. We refer to the summary for an outline of the most important results.

In chapter 2 the target was to characterize the model paint dispersion that was provided to us by our industrial partner Nuplex Resins BV. We focused on the physical chemical properties of the binder (resin) particles and looked into the synthesis steps to get an idea of what properties these particles have. We show results for the molecular weight, size and charge of the particles. It turns out that the particles are surprisingly monodisperse (as found by atomic force microscopy (AFM)). We also give information on how the particles behave upon changing conditions, i.e., salinity and acidity

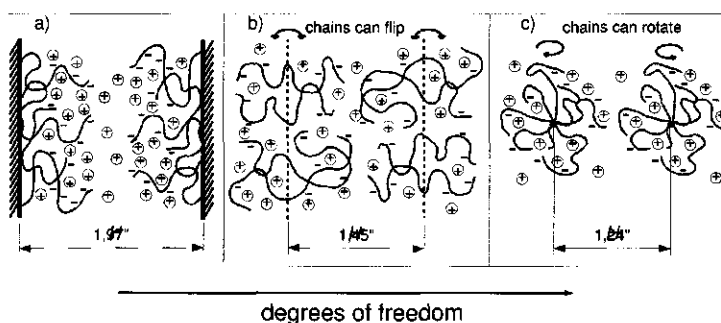


**Figure 1.3:** An illustration of different models studied theoretically. a) Polymer brushes, composed of hydrophobic polyelectrolytes and interactions between them; b) bilateral brushes, where chains are grafted to some layer on the lattice, and are allowed to travel through this layer when the layers are in confinement; c) polyelectrolyte stars. The degrees of freedom for polymer chains increase from the brushes to the stars - in interacting brushes the chains do not have space to escape from the contact with another brush, while in stars inhomogeneous conformations are possible (see chapter 2).

of water. As illustrated in figure 1.2 it was found that the shell layer can dramatically change its dimension with increasing pH. Such responsive nature is typical for weak polyelectrolyte brushes and therefore we argued that the corona structure has a brush-like nature.

With detailed knowledge of the structure of the particles and their response to changing conditions, we have put much effort into modelling of these complex particles. Results of this can be found in chapter 3. We focused on the equilibrium inter-particle interaction potentials and their dependence on the solvent properties and, most importantly, the ionic strength and pH. Any theoretical description requires, of course, many simplifications. We tried to keep the most relevant properties that are key for the way the particles interact in our model. Simplification may also have its advantages. The need to simplify forces one to think about the most important elements of a system and this helps to obtain more insight in a problem.

In slightly more detail we discuss in chapter 3 the Scheutjens-Fleer self-consistent field (SF-SCF) theory for hydrophobic polyelectrolyte (HPE) brushes in various geometries. This approach which implements mean-field approximations was initially developed in our group for calculation of homopolymer adsorption from solution onto macroscopic surfaces. The approach implemented in SF-SCF is anchored on theoretical considerations developed for macromolecules in the second half of the 20th century by Flory,<sup>7</sup> Volkenstein,<sup>8</sup> Ptitsyn and

Birshtein.<sup>9</sup> Additionally, the analogy between paths followed by Brownian particles and conformations of long polymer chains, noticed in works of Edwards<sup>10,11</sup> and De Gennes,<sup>12</sup> is used in the method by means of the Edwards diffusion equation. The diffusing particle (chain conformation) is affected by a mean-field potential, which itself is dependent on the paths taken by particle or polymer chain. A numerical procedure is used to optimize the field, so that the free energy of the system is minimal. This proved to be successful in predicting many aspects of polymers in inhomogeneous systems (that is, at interfaces). The method was extended to account for several additional features. For example, the electrostatics are accounted for by simultaneously solve the Poisson equation, leading to information on the electrostatic potential for a given space charge density. Initially, calculations considered systems with just one gradient direction (implementing the mean field approximation in the remaining two dimensions). Later, centrally-symmetrical (cylindrical, spherical) systems were considered as well. Subsequently also two-gradient coordinate systems were considered and, more recently, full three-gradient problems are being addressed. In the theory chapter we make use of these geometries which are schematically shown in figure 1.3. Calculations normally yield results that represent full equilibrium of all components in the system, which corresponds to a minimal free energy in the system. However, when the system suffers a first order phase transition, it is possible that close to the points of transition from one state to the other, meta-stable states can also be probed. The method produces for a given model many experimentally accessible predictions. Here we mention that one of the predictions is that the pair potentials between two opposing brush layers can be predicted. These can be compared, e.g. to the atomic force microscopy (AFM) measurements. However, one has to keep in mind that in experiments one typically probes the system in the dynamic state and for polymers the full equilibrium is not always reached.

Armed with detailed knowledge on the characterization and with detailed predictions of the equilibrium interactions between the particles, we proceeded to find experimental evidence of the theoretical predictions. We decided to measure the interaction force between particles using the colloid probe AFM approach. The results of this work can be found in chapter 4. The resin particles turned out to be rather small, that is, they are on the order of 100 nm. So, it was decided to measure interactions not on two particles, but rather on an ensemble of particles. The colloidal probe technique is ideal for this. As shown in fig. 1.4 a layer of adsorbed particles is present both on the flat substrate and on the 6  $\mu\text{m}$  colloidal probe. The forces that occur upon bringing these layers in close contact are measured. This requires certain assumptions and additional measurements, but in the end it yields a rather



**Figure 1.4:** A schematic representation of the colloidal probe AFM set-up: the colloidal probe is glued to the cantilever tip; both the probe and the opposing surface are hydrophobized with silazane, and then the particles are adsorbed both on probe and surface. Interaction forces are then measured between these two layers, placed in aqueous solution (see chapter 4).

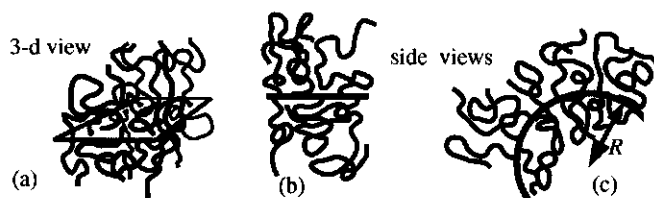


**Figure 1.5:** An illustration of the bilayer bending problem, studied in chapter 5. Polymer chains are grafted to both sides of some membrane, changing the radius of curvature we can derive the bending moduli. If we allow the chains to flip from one side of the membrane to the other, and study the bending in cylindrical coordinate system, in effect, it becomes similar to the bottle-brush bending problem.

clear picture. Particle interactions have been studied both in water and in a water - co-solvent mixture. We studied the interaction dependence on solvent properties in the range where particle structure changes most (information from chapter 2). The role of butyl glycol as co-solvent was monitored by following the changes in particle structure and the effect on the interaction between the particles.

In chapter 5 results are shown of a theoretical side project, which, on first sight, seems unrelated to the coating problem. The central issue of this chapter is to generate information on the physics of the bending rigidity of a polymer brush. One of the reasons why the numerical SF-SCF theory was used for this problem is that various (more approximate) theoretical approaches resulted in different conflicting predictions. Upon closer inspection this problem appears more directly related to the physics of particles covered

by polymer brushes. That is why the results of this study are included in this thesis. It turns out that the concept of the bilateral brush plays not only a dominant role in the bending problem, but also has a clear function in the study of the interaction between two hydrophobic polyelectrolyte brushes. The fundamental issue here is that upon bending of a bottle brush, or upon confinement of a HPE brush, the chains can escape from a compressed region to a less compressed one (see fig. 1.5). The bilateral brush is used in both approaches.

This thesis shows that the combination of characterization, theory and experiments is a powerful approach to understand complex systems. Even though many questions remain to be solved, we now have a deeper insight in how in water-borne paints the core-shell particles are used to simultaneously solve several seemingly conflicting requirements. These insights will be important to further develop WB-coatings.



## Chapter 2

# Characterization of a dispersion of acrylic core-shell particles

### 2.1 Abstract

In this chapter we present the physical-chemical characterization of an aqueous dispersion of acrylic core-shell particles (CSP). The system is a model for dispersions used in waterborne automotive coatings. The particles were synthesized at elevated temperatures via a two-step emulsion droplet polymerization and have mostly methacrylic polymer cores and acrylic polymeric shells. At room temperature, the cores are in a glassy state. The corona chains contain a fraction of methacrylic acid groups and may be classified as hydrophobic polyelectrolytes. The hydration of the shell strongly depends on the pH. The shell polymers are not chemically coupled to the core chains. Nevertheless, they remain associated with the core upto high pH values. Apparently, the shells are trapped with some of their (hydrophobic) moieties in the (glassy) core. We discuss results from potentiometric titrations, dynamic and static light scattering on dilute solutions of CSP, and tapping mode AFM imaging on physisorbed layers of particles. The data obtained from these measurements, together with the overall molecular composition of the particles and supplementary size-exclusion chromatography (SEC) data for the shell polymers, are used to forward a model for the CSP structure. This model sets constraints for the structural modeling with the mean-field Scheutjens-Fleer self-consistent-field (SF-SCF) theory. The parameters are tuned to give good quantitative agreement with experimental data, in particular with respect to the dramatic swelling of the shell polymer layer upon an increase of the pH.

## 2.2 Introduction

In paints, waterborne acrylic resin dispersions are progressively used as substitutes for solvent-based products. They find applications in decorative, industrial, and maintenance applications. Despite high demands for the performance in automotive coatings, recent improvements of waterborne coatings made them suitable for this type of applications as well.<sup>3</sup> The main approach that resulted in better formulations, involved high throughput combinatorial chemistry methods: many batches of similar resins are synthesized, and then these batches are screened for the best samples on the basis of a few relevant tests.<sup>1,2,13</sup>

Combinatorial chemistry is the method of choice when there are many relevant variables. For example combinatorial chemistry proved to be very fruitful in developments of catalysts. Indeed, for the design of a possible resin there is a large set of acrylic monomers. The number of feasible variants of arranging these into polymers is virtually unlimited as these will depend on mixing ratios, reaction conditions, rates of monomer feed, etcetera. There are, however, also important bottlenecks and drawbacks associated with this technique. The choice of the "best" formulation from a large set is based on some high-throughput test experiments. There may be numerous cases of false positive or false negative outcomes of such tests, which remains unnoticed especially when the physics of the dispersions, which somehow underpins these tests, is poorly understood. The other relevant issue for the industry is that high investments are needed to operate a high-throughput set-up. In this respect there is a potential to greatly reduce the costs, if certain part of the research protocols can be omitted. Again, molecular level knowledge of the dispersions and the ability to predict changes in properties of coatings upon certain changes in formulations, can reduce the costs of such set-ups to a great extent.<sup>13</sup> Our proposition is that the coatings performance may more efficiently be improved when deep insight in the behavior of the particles is available. In this chapter we report on the physical chemical characterization of a CSP system, which is a first step in the direction to obtain more realistic insights in these systems.

There is relatively little academic research on these complex and sometimes poorly defined systems. Indeed, the production samples are synthesized mainly via emulsion droplet polymerization, and this process is often described as random, or chaotic. This results in particles with chaotic polymer compositions, wherein the polymers themselves are typically (somehow) random copolymers. Additionally, the dispersions typically contain multiple remains of the reactions or some additives. Another issue lies in the scope of research activities, which typically focuses to some particular feature of a coating dispersion under

study. The relevance of the collected data for the overall performance of a paint is often rather speculative.<sup>14</sup> This situation may be improved when multiple aspects of the problem are considered. The characterisation of the CSP discussed in this chapter sets the stage for further investigations.

The core-shell particle (CSP) dispersion that we consider in this chapter was supplied to us by Nuplex Resins. The dispersion is a model system specially prepared for this study. It differs slightly from the real commercial product. The model system and the real product have key properties, such as the core-shell architecture, the glassy cores, the pH sensitivity of the shell chains and various physical properties, such as the extreme shear-thinning, in common. The model resin is simplified: some components essential for, e.g., the durability of the final paint are left out. In our study we focus on the properties of the shell polymers which are relevant for the colloidal stabilization and the inter-particle interactions and the mentioned shear-thinning behavior. We do not consider the mechanical properties of the drying films nor issues related to the final coating, but focus on the dispersions. Therefore, we trust that our results for this model resin are relevant for the corresponding properties of the real systems.

The particles are synthesized in two distinct steps: first the cores are polymerized at elevated temperatures and the reactions were terminated. Then the shell monomers are added and subsequently polymerized. The core monomers are methacrylates, so they undergo a glass transition when after the synthesis the system is cooled down to room temperature. They serve as impermeable, uncharged and hydrophobic polymer colloids to which the shells are adsorbed or, effectively, grafted (in a physical sense) during the synthesis step. The shells are acrylics except for a minority fraction of methacrylic acid monomers. The shells provide colloid-chemical stability of the cores and are believed to play a role in the pseudoplasticity of the dispersion. In our study the structural properties of the shell layer are placed central. We consider the cores as inert carrier particles.

In order to understand the properties of the particles that are most relevant for the applications we investigate the molecular structure and try to interpret these in terms of the conformations of polymers within single acrylic core-shell particles in dilute solutions or adsorbed onto a hydrophobic surface. We aim to correlate the molecular composition of the particles to their physical-chemical properties. Our insights are used to forward a molecular model for the shell chains that serves in subsequent self-consistent field investigations.

In strong contrast to few studies on industrial dispersions, there are many studies on better-defined experimental systems with similar overall characteristics. The concept of the stabilization of colloidal dispersions with

polyelectrolytes, is discussed in works of Pincus<sup>4</sup> and Wang.<sup>15</sup> The group of Ballauff *et al.* studied well-defined so-called spherical polyelectrolyte brushes, which are latex particles onto which polyelectrolyte chains are grafted.<sup>6,16-19</sup> Well-defined core-shell particles (micelles) made of block-copolymers in selective solvents are also well known. There are numerous experimental works on micelles with a polyelectrolyte corona.<sup>20-25</sup> The influences of the solvent quality, the pH and ionic strength, are well understood and explained or predicted in a number of theoretical works.<sup>26-30</sup> The particular case of polyelectrolyte layers in a poor solvent, which characterizes the shells of our particles, is studied in several theoretical works as well.<sup>31-35</sup> We will address these studies either for comparison purpose, or when we discuss possible differences between theory and experiment in relation to various scenarios of the structure of the shell layers of our core-shell particles.

This chapter is organized in the following manner: first we give information on relevant aspects of the synthesis, the chemical composition and possible arrangements of monomers in the polymers and their subsequent aggregation into particles. Then we briefly describe the experimental techniques used to characterize the particles. This is followed by the presentation of the key results and a critical discussion of the experimental data. We will summarize the properties of our core-shell particles, and forward a model of a particle which is based on collected data. The model is used in the theoretical analysis of some of the experimental findings.

## 2.3 Materials and Methods

### 2.3.1 Core-Shell Particles

#### Monomer composition

Here we list all the acrylic monomers that are used in particle synthesis and briefly describe relevant properties for each monomer. We pay some more attention to the shell monomers and point to relevant properties of homopolymers of each shell monomer. We finalize this section with a table that lists the monomers and proportions in which they are used during particle synthesis.

The monomers that compose the cores and shells of the particles are shown in figure 2.1. The methylmethacrylate (MMA) and *n*-butylmethacrylate (BuMA) core monomers are relatively hydrophobic and are widely used for the production of polymer glasses. Poly(MMA) has a glass transition temperature of  $T_g = 115^\circ\text{C}$ . For poly(BuMA) the glass transition temperature is  $T_g = 20^\circ\text{C}$ . BuMA monomers are mostly used as co-monomers to add

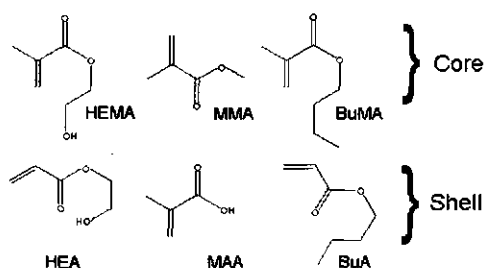


**Figure 2.1:** The chemical formulas for the core and shell monomers. The quality of water as a solvent for each monomer decreases from left to right.

plasticity to glasses. 2-Hydroxyethylmethacrylate (HEMA), and respective polymers, are water-soluble due to the presence of a polar hydroxyl group. It is added in a small quantity for further cross-linking of the cores in a final paint film. Cross-linked poly(HEMA) gels are hygroscopic and widely used in biomedical industries. The mixture of water-soluble and apolar monomers in copolymers become insoluble already at relatively small degrees of polymerization.

*n*-Butylacrylate (BuA) is one of the shell monomers. It is water-soluble up to 2 g/L. It forms polymers that have a low glass transition temperature  $T_g = -49$  °C. Hydroxyethylacrylate (HEA) is also a shell monomer. HEA polymers are water-soluble, similarly to poly(HEMA), and are even more hydrophilic. HEA monomers are added both to get better shell solubility in an aqueous solution and for the possibility to further cross-link the film once it is formed. This cross-linking will not be considered in any respect here.

Methacrylic acid (MAA) monomers are the most responsive ones in the shell. The stability and various other properties of dispersions of the CSP may be tuned by controlling the charge that originates from this monomer. Homopolymers of MAA are weak polyelectrolytes with a  $pK_{\text{eff}} = 7.3^{36}$  and respond to changes in pH and ionic strength. At a low pH, pMAA is still soluble in water. In these conditions it is in a relatively compact conformation and MAA shows some affinity for non-polar cosolvents.<sup>37, 38</sup> At high pH the chains are swollen due to the electrostatic repulsion between the monomers. The latter may be screened by salt.

The ratios in which the above mentioned monomers are added for particle synthesis are presented in table 2.1.

**Table 2.1:** Monomer composition of the core and the shell. (The molecular masses of the core and the shell are number-average masses of an average monomer)

Monomer	%wt in core/shell	$M_w$	%mon in core/shell	%wt total	%mon total
<i>Core</i>	87.5	133.2	-	-	-
BuMa	79.4	142.2	74.4	69.5	63.4
MMA	14.7	100.12	19.6	12.9	16.7
HEMA	5.9	100.12	6	5.2	5.2
<i>Shell</i>	12.5	110	-	-	-
BuA	56.5	128.17	48.4	7.1	7.2
HEA	25.4	116.12	24	3.2	3.5
MAA	18.1	72.06	27.6	2.3	4.1

### Particle synthesis

The monomers presented above are used to synthesize the core-shell particle dispersions. This is done in a two-step emulsion droplet polymerization reaction.<sup>39-41</sup> In the first step the cores of the particles are produced. In the second one the shells are formed. Importantly, in between these two steps, the synthesis of the core polymers is terminated. Hence, there is no chemical linkage between core and shell polymers. Instead, the shell polymers are physically adsorbed on the cores during the reaction conditions, i.e. low pH = 4 values and temperature of  $T = 85^\circ\text{C}$ . Upon cooling down of the dispersion, the cores undergo a glass transition ( $T_g = 33^\circ\text{C}$ ) and the shell polymers become effectively grafted to cores. This scenario is not straightforward, but it follows, as we will discuss, from our experimental results presented in this chapter and is discussed in subsequent chapters 3 and 4 as well.

Different types of monomers, synthesized into chains form co-polymers. All monomers of the core are methacrylates which are known to form more or less random polymers when mixed.<sup>42</sup> We thus believe that the cores are composed of random, rather homogeneous, copolymers. The situation for the shells may be different. Methacrylic acid radicals are known to react rapidly and more likely with similar monomers than with acrylic ones. Hence, the polymerization of MAA is earlier and the copolymers are expected to contain more MAA towards one of the ends.<sup>42,43</sup> The tapered nature of the shell chains may be important in the mechanism by which parts of the shell chains are trapped in, or (effectively) grafted to, the core.

After the synthesis the resulting dispersion contains a number of low molecular weight residues, namely the surfactants that stabilized the hydrophobic polymeric species during the synthesis, unreacted initiator molecules, salts

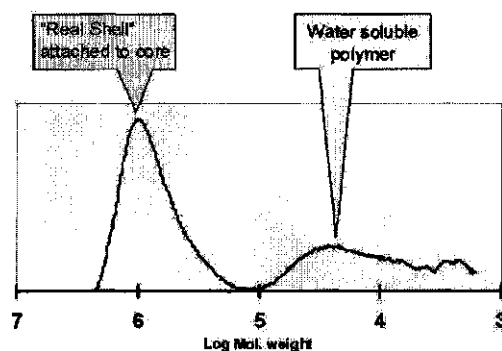


**Figure 2.2:** SEC data on shell polymers, synthesized in the absence of cores, obtained in hexafluoroisopropanol + 0.02M potassium fluoroacetate solution with gel-permeation chromatography. The data was provided to us by Nuplex Resins.

and small water-soluble copolymers which did not adsorb onto cores. To eliminate adverse effects from these residues, the dispersion was dialyzed for at least two weeks against demi-water, using 50000 Mw Spectra-Por membranes. The effectiveness of dialysis was checked with conductometry.

The size exclusion chromatogram (SEC) data for shell polymers, provided by the particle manufacturer, is presented in figure 2.2. Here the left peak corresponds to shell polymers, while the right one at low  $M_w$  point to the presence of short water-soluble polymers (these are most likely removed by dialysis). The mass-averaged molecular weight of the shell polymers, determined from this figure (left peak) is  $M_w = (1.22 \pm 0.02)10^6$  g/mol, and the number-averaged molecular weight is  $M_n = (1.07 \pm 0.02)10^6$  g/mol, so that the polydispersity index,  $PDI = 1.14 \pm 0.02$ . Taking the average molecular weight of one monomer as  $M_w = 110$ , we estimated the degree of polymerization of the shell polymers to be  $N \approx 9000$ .

## 2.3.2 Methods

### Static Light Scattering: Zimm plots

In order to get information on molecular weight of the particles, as well as their radius of gyration and second virial coefficient, light scattering measurements at different angles and concentrations have been performed. Such static light scattering (SLS) experiments were analyzed by the method of Zimm. The measurements were carried out using a light-scattering set-up equipped with a 400 mW argon ion laser with a wavelength of  $\lambda = 514.5$  nm. The

reference toluene solution and CSP solutions have been filtered several times to avoid any dust in the scattering cells. The temperature was controlled by a Haake C35 thermostat to  $T = 298 \pm 0.1$  K. A refractive index matching bath of filtered cis-decalin surrounded the quartz cylindrical scattering cell. The total static light scattering intensity ( $I$ ) was recorded as a function of scattering angle ( $15^\circ$ - $120^\circ$ ). A set of solutions with decreasing concentration was prepared from the dialyzed CSP dispersion. The pH was set to the value of pH = 7.8 and the ionic strength to 2 mM with phosphate buffer.

The refractive index increment of the particles was measured with a differential refractometer (Shodex RI-71, Separations) coupled to a pump. This set-up was first calibrated with a NaCl solution, then the refractive indexes of CSP solutions at different concentrations was measured.

### Dynamic Light Scattering titrations

Dynamic light scattering (DLS) measurements were performed with the same optical setup as used for the SLS ones. In this case the light scattering apparatus was used with a home-built scattering cell which allowed acid-base titrations between the measurements, using a Schott-Geräte automatic titration setup. In this way the hydrodynamic radius of the particles could be measured under varying pH conditions, while the integrity of the particles was monitored by observing the scattered light intensity. DLS measurements were performed at  $90^\circ$  scattering angle. The change in pH was implemented through the titration of 0.005 to 0.1 mL of acid (HCl) or base (NaOH) in consecutive steps and the pH was monitored during the titration. The ionic strength of the acid or base solution matched the ionic strength of the initial CSP solution, so that the ionic strength of solution remained constant during the titration. The intensity of the light scattering is corrected for the dilution. The acid titration to reach low values of the pH (below 5), typically result in a (reversible) precipitation of the sample. Hence, in the experiments we first increased the pH and then decreased it again to estimate the reversibility of the changes that are observed.

### Potentiometric titrations

Equilibrium potentiometric (PT) titrations were performed using a Schott-Geräte TR 250 titrator with a feed-back loop to adjust the speed of titration to the response of the system when the pH is changed. Measurements were performed using a pre-calibrated reference electrode, using dialyzed CSP dispersions of 2 g/L and corresponding blank solutions.



### AFM in tapping mode

Particles were adsorbed from a critical solution ( $I = 1$  M;  $\text{pH} = 6$ ;  $C_p = 2$  g/L, under these conditions particles precipitate within a day) onto silica surfaces that were hydrophobized with hexamethyldisilazane (for the description of adsorption procedure see chapter 4). Under these critical conditions the resulting adsorbed layer is a dense monolayer (random close packing) of CSP. AFM images were collected in tapping mode using a Nanoscope III AFM (Veeco) with standard tapping mode cantilevers (Veeco), either on freshly-dried CSP layers, or on freshly-prepared monolayers in acontact with solution using a fluid cell. The scans are taken consecutively for several hours to let the system fully equilibrate and to eliminate the drift of the AFM apparatus.

### Theoretical fitting of DLS-titration data

Below we will develop a molecular model of a CSP tailored to fit (especially) the DLS-titration data. In this model the shell chains are mimicked by an effective polymer brush composed of (homodisperse) hydrophobic polyelectrolytes grafted onto a curved hydrophobic substrate. This simplified model suites the self-consistent field approach in its classical form, that is making use of the machinery of Scheutjens and Fleer using a one-gradient spherical coordinate system. An extensive description of the theory and its application to hydrophobic polyelectrolyte brushes may be found in chapter 3 of this thesis, and is not repeated here.

In the model the cores of the particle are implemented as curved impenetrable hydrophobic surfaces to which the shell polymers are end-grafted. The radius for the cores is taken from AFM and DLS data for the cases when the shells are collapsed. A correction of the radius is made for the contribution of the shell chains (hence, the ratio of the fractions of core to shell monomers, as follows from the synthesis of CSP, is used). In order to keep the number of parameters as low as possible, the shell polymers are considered to be monodisperse and are taken as regular copolymers, consisting of just two types of segments: weak acid groups, separated by a few hydrophobic segments with  $\chi_w = 1$ . The fraction of acid groups is fixed to  $f = 0.25$ , which corresponds to the monomer composition of the shell. We have lowered the fraction of acid groups somewhat with respect to the monomer feed, to correct for the loss of some monomers to short water-soluble polymers during synthesis. The total number of ionizable groups per particle is kept constant at  $n_c = 2.5 \times 10^5$ , which corresponds to the number that is determined via a combination of SLS and PT data (see below). The polymer chain-length  $N$  was varied to find the best fit for the DLS data. Instead of a hydrodynamic

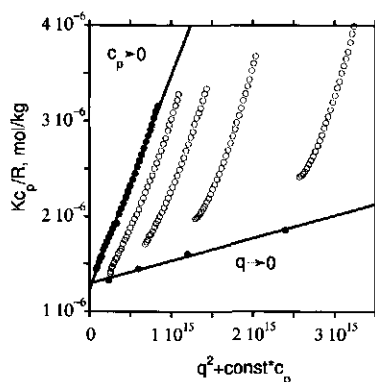


**Figure 2.3:** The Zimm plot for a CSP dispersion at  $\text{pH} = 7.8$  and  $I = 2 \text{ mM}$ . The concentrations of CSPs are 0.06; 0.024; 0.012; 0.006 g/L from right to left and the constant is  $10^{17} \text{ m}^3/\text{kg}$ .

radius as determined by DLS, we calculate the first moment of the free polymer ends distribution, and used this as a reasonable approximation for the hydrodynamic radius in the case of spherical particles:

$$R_m = R_c + \frac{\sum_r L(r) r \varphi(r, N)}{\sum_r L(r) \varphi(r, N)} \quad (2.1)$$

In this equation  $r$  is the lattice coordinate (in the case of the one-dimensional calculations) which represents the distance to the substrate (in units of the segment size). The value  $L(r) = 4/3\pi(\tau^3 - (r-1)^3)$  is the number of lattice sites at a specific coordinate and  $\varphi(r, N)$  is the end-point distribution. As we solely model the shells of the particles, taking the core as just an impenetrable surface, we inserted the value for the core size  $R_c$  in equation 2.1 to obtain the overall particle size  $R_m$ .

Apart from the distribution of the brush chains, we also obtain information on the local degree of dissociation of the acid groups. The overall degree of dissociation of the acid groups  $\alpha$  will be used to compare to the potentiometric titration data.

## 2.4 Results

### SLS - Zimm plot

For Zimm plots it is necessary to know the refractive index increment of the CSP solution. Using the approach mentioned above we obtained a value

of  $dn/dc = 0.15 \pm 0.005$  mL/g. This value was used for all ionic strength conditions and pH values used in our study. From the Zimm plot we find estimates for the mass, the size and the interaction radius of the CSPs.

In figure 2.3 we show the Zimm plot for pH = 7.8 and  $I = 2$  mM. Under these conditions the particles are negatively charged, the corona chains are swollen and the particles repel each other. As usual, two extrapolations, one to zero concentration and one to zero scattering angle, were performed. The combined limit of zero concentration and zero scattering angle points to a well defined intercept, which is interpreted as  $1/M_w$ . The slope of the fit to zero concentrations gives the value of the gyration radius. The slope of the fit to zero angle points to the second virial coefficient, which is positive as expected. The SLS results are the following:  $M_w = (7.9 \pm 0.1) \times 10^5$  kg/mol;  $B_2(\text{pH} = 7.8) = (1.1 \pm 0.1) \times 10^{-5}$  mol m<sup>3</sup>kg<sup>-2</sup> and  $R_g(\text{pH} = 7.8) = 74 \pm 3$  nm.

### Potentiometric titrations

In figure 2.4a we present a typical potentiometric titration curve for our CSP solution at  $I = 0.1$  mM. In this plot the degree of dissociation of the MAA groups  $\alpha$ , where it is taken that  $\alpha = 1$  at high pH, is given as a function of the pH. As expected an increase of the pH results in the dissociation of the methacrylic acid groups. The effective  $pK$  of the particles, that is the value of the pH at which half the groups is dissociated, is found to be  $pK_{\text{eff}} = 7.88 \pm 0.02$ . This value is close to the value of  $pK = 7.3$  for pure poly(MAA).<sup>36</sup> The slightly higher value may be due to the fact that in our case the polyacids are not dissolved in solution, but attached to the cores of the particles, which results in a greater interaction between the charged groups. The overall titration curve has a distinctive S-shape, which is relatively sharp (the changes take place in a limited pH interval). Such sharp S-shaped titration curve is reasonable for hydrophobic polyelectrolyte (HPE) chains. Clearly HPE's can switch rather suddenly from a neutral (deionized) form, where the chains are, due to hydrophobic forces, in a collapsed state, to a highly charged state where the shell layer is swollen and the chain conformations are stretched by the electrostatic forces. Intermediate states, where the shell layer is weakly charged and the chains are not strongly stretched, are relatively unfavorable and the particles undergo the collapse-to-swollen transition in a rather narrow window of pH values.

The  $\text{pH} \approx pK_{\text{eff}}$  will be the central pH value for our investigations. Around this value, the CSP system is most adaptive to changes and not surprisingly the interest from an application point of view is in this pH range. Alongside with changes in the degree of dissociation of the carboxylic acids

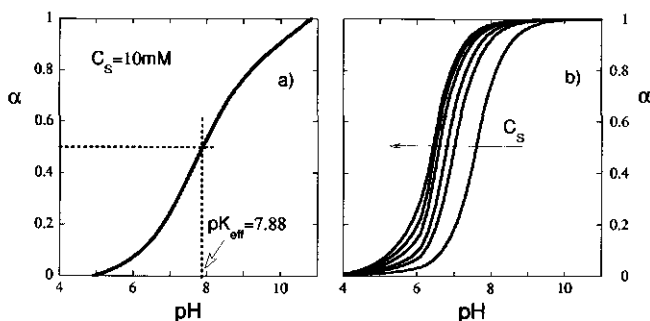


**Figure 2.4:** a) Potentiometric titration (PT) curve of the CSP system. The particle concentration  $c = 5$  g/L and the ionic strength is 10 mM. b) Theoretical curves for the degree of dissociation of shell chains as a function of the pH for the CSP model (details are given in the text) at different ionic strengths values  $I = 1, 5, 10, 25, 50$  and  $100$  mM (from left to right)

groups, we may anticipate changes in the size of the particles and variations in the strength of interactions between CSPs.

### AFM imaging

Next, we present several AFM images of the adsorbed layer of particles at the highest density of this layer. Again we refer to chapter 4 for the details of how the surfaces are hydrophobized and how the adsorption of the particles was optimized. Here we focus on the direct observations of the particles using the tapping mode approach. Observables are the average size of the CSPs and the polydispersity of the size.

In the top left view graph of figure 2.5 a typical CSP adsorption pattern is shown. The image is obtained on the dry layer of particles. The particles are still separated from each other and the surface coverage was determined to be  $\Gamma = 52 \pm 2\%$  (this coverage has been corrected for the broadening effect due to the pyramidal shape of the tip). The coverage is close to the random closed packing limit  $\Gamma_{jam} = 54.7\%$ , which is the maximal possible value for random and irreversible adsorption of spherical particles, also known as the jamming limit.<sup>44–46</sup> The other important feature, readily seen from this image, is that the particles are rather monodisperse. We recorded the sizes of a 100 of particles and determined their polydispersity to be  $P_d = 1.03$

The remainder of Fig. 2.5 is used to illustrate how the sizes of the particles are estimated. In short, we consider pairs of particles that are in intimate contact (cf. fig. 2.5 right top/left bottom where three individual pairs are

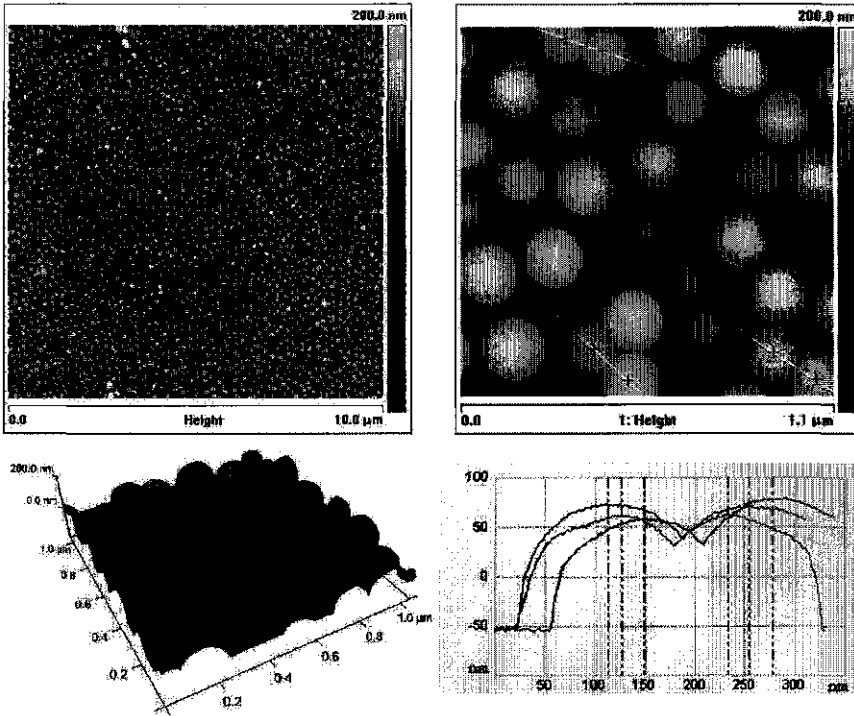


**Figure 2.5:** Top graphs: Contour plots for tapping mode images of a dry layer of adsorbed CSP on silica surface, pre-treated with hexamethyldisilazane, from 1 M NaCl solution of  $c = 1$  g/L at  $\text{pH} = 6$ . A contour plot with higher resolution is shown at the top right and the corresponding 3d image is shown at the bottom left. Height profiles were generated for cases that two particles are in very close contact. Three of these height profiles are shown in the graph at the right bottom.

indicated). In order to avoid any broadening effects due to the finite size of the cantilever tip, we use the distances between the peaks of such adjacent particles and interpret this distance and the average diameter of the touching particles. This is a standard procedure in case of spherical objects. The average value of particle radius as determined in this way is  $R = 65 \pm 5$  nm, which is a number averaged quantity.

Knowing the fractions of monomers that form cores and shells, and assuming that upon AFM imaging both the cores and shells are fully collapsed and have similar densities (dried sample), we can determine the core radius from simple geometrical considerations. The value we get is  $R_c = 62 \pm 5$  nm. This value is used below in the SCF calculations as the radius at which the impenetrable surface is placed onto which the shells polymers are grafted.

### Dynamic Light Scattering

The initial dialyzed sample was diluted 10,000 times for the DLS experiments. This resulted in typical concentrations of the order of 1 mg/L. In order to see the effect of the screening of the charges by salt, three sets of measurements have been performed in aqueous solutions of CSP: with no added salt, at 10 mM and at 100 mM NaCl. In each measurement the pH has been varied in the whole range of particle stability. In addition we also followed the aggregation of the particles at low pH values and the return to the dispersed state upon an increase of the pH.

We first discuss how the hydrodynamic size of the CSP increases with increasing pH. This result is shown in figure 2.6a. At a low pH the shell chains are collapsed onto the core and the particle size is found to be similar to that determined by AFM. In this regime the concentration of salt does not play a role. Upon an increase of the pH, the carboxylic groups dissociate and acquire a negative charge. The electrostatic interactions attract counterions and the shell layer will swell as a result of the osmotic pressure due to the internalized salt ions. An increase in the ionic strength of solution leads to the screening of the charges. This allows the particles to become charged already at a somewhat lower pH. The swelling of the shell layer is clearly reduced by the addition of salt. Indeed, in the fully charged state (high pH) the hydrodynamic size at low ionic strength, that is when the particles are in demi-water, is about twice as large as in 100 mM salt solution. The shell polymers are likely to fully stretch at low ionic strength and high pH values. We will return to this point below.

The colloidal stability at low pH is a decreasing function of the ionic strength. At 100 mM salt the particles start to precipitate already at pH = 6, whereas in demi-water they are still stable down to pH = 4.3. In both

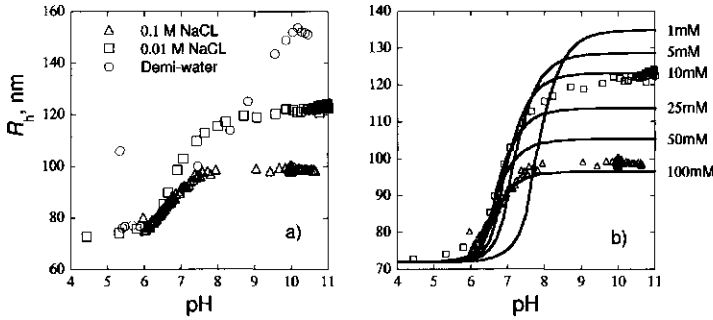


**Figure 2.6:** a) Hydrodynamic radii of the particles determined with DLS at different pH values for demi-water, 10 mM and 100 mM NaCl solutions. b) The theoretical fits of DLS data, calculated for a CSP with hard core and a shell, consisting of monodisperse,  $N = 370$ , regular hydrophobic ( $\chi_w = 1$ ) polyelectrolytes with a fraction of  $f = 0.25$  weak ( $pK = 5.5$ ) acid groups and grafting density adjusted so that the amount of charges per particle corresponds to the experimental value of  $n_c = 2.5 \times 10^5$ .

**Table 2.2:** Physical characteristics of the particles, obtained during characterization.

$M_w$ [g/mol]	$R_h$ [nm]	$R_g$ (pH = 7.8) [nm]	$\rho_p$ [g/mL]
$7.9 \pm 0.1 \times 10^8$	70 - 150	$74 \pm 3$	$0.77 \pm 0.02$
$n_c$ , per particle	$R_{core}$ (est) [nm]	$S_{eff}$ [nm <sup>2</sup> ] per shell chain	$N$
$2.5 \times 10^5$	$62 \pm 5$	$20 \pm 1$	370

cases the colloidal stability can be recovered when the pH is increased again.

The average intensity of the scattered light at  $90^\circ$  has been recorded and interpreted in terms of the integrity of the particles. These measurements revealed (not shown) that at low pH the intensity drops abruptly when particles precipitate (sediment), but at high pH the intensity is constant. This implies that the shell polymers are fixed to the cores and do not detach even when the electrostatic forces are large.

## 2.5 Discussion

In table 2.2 we have collected the basic results that were extracted from the light scattering and AFM measurements. In this section we will try to evaluate the consistency of the results, derive some secondary results from the experiments and discuss the results in relation to the model calculations.

Using the molecular weight (from the Zimm plot) and the radius of gyration, we can estimate the average density of the CSP by  $\rho = (7.7 \pm 0.5) \times 10^2 \text{ kg/m}^3$ , which realistically points to the fact that the corona of the CSP is swollen at pH = 7.8.

We have found various measures for the size of the particles. It is reasonable to investigate the consistency of these results. From the value of  $B_2$  one can estimate the excluded volume of the particles. This points to an interaction radius. We found a surprisingly high value of order of a micrometer. Physically this suggests that the CSPs interact with each other already at a very large distance. We have problems to understand how the interaction radius would be significantly larger than the hydrodynamic radius. At our defense, we should mention that the second virial coefficients is more often found to be high for polyelectrolyte systems (see<sup>47</sup> for example). A classical approach to interpret the  $B_2$  for ideal polyelectrolytes involves the concept of a Donnan layer and electroneutrality. This yields a "Donnan  $B_2$ " that is given by:

$$B_2 = \frac{Z_{\text{eff}}^2}{4C_s M_n^2} \quad (2.2)$$

where  $Z_{\text{eff}}$  is the effective charge on the polyelectrolyte molecule,  $C_s$  the salt concentration and  $M_n$  is number-average molecular weight.<sup>48</sup> Using this equation, implementing a value for the polydispersity of our particles from AFM images,  $M_w/M_n = 1.03$  to retrieve  $M_n$  from the experimental value of  $M_w$  and inserting the salt concentration in the system of  $2 \times 10^{-3} \text{ M}$ , we arrive at an effective charge value  $Z_{\text{eff}} \approx 5000$ . This value is about two orders of magnitude lower than the estimate found by potentiometric titrations for this pH. Again, such low value for the effective charge,  $Z_{\text{eff}}$ , is more often encountered in polyelectrolyte systems.<sup>49</sup> We thus conclude that we do not yet understand why the interaction radius for the particles is so large.

The size as found by AFM is only slightly smaller than the hydrodynamic radius as determined by DLS for the condition at low pH where the particles are almost uncharged and have a minimal size. Indeed this suggest that the CSP at a low pH are rather compact and the shell layer is only marginally hydrated. Whether at low pH values parts of the shell chains are in a melt, crystalline or glassy state is unknown. This issue is obviously related to one of the central questions of how the shell chains happen to be associated to the core.

The gyration radius as found by the SLS measurements corresponds to pH = 7.8. In this case the shells are already swollen due to the appearance of the charges in the shell layer. From this standpoint it is reasonable that the gyration radius as found by SLS is somewhat larger than the size found in AFM. Of course with light scattering a weight average radius is found,



but considering the small value for the polydispersity, we argue that the SLS size is larger than the AFM size mainly because of the swelling of the shell.

Knowing the molecular weight  $M_w$  of the particles from the Zimm plot, and the concentration of CSP in the potentiometric titration experiments, we may relate the amount of titrant needed to charge up the particles to the total number of MAA groups per particle. We find a value of  $n_c = (2.5 \pm 0.1) \times 10^5$  chargeable groups per particle. To check how realistic this number is, we can calculate how many MAA groups are expected to be incorporated into our particle from the input data of the synthesis. When we multiply the fraction of MAA added (which is 2.3wt%, cf table 2.1) with the  $M_w$  of each particle (from the Zimm plot) and divide this by the weight of one MAA monomer, we arrive at a value of  $n_c = (2.6 \pm 0.2) \times 10^5$ , which is in excellent agreement with the result from potentiometric titrations. This implies that most of the monomers introduced in the synthesis mixture are indeed incorporated into the shell polymers.

In figure 2.4b we present theoretical fits for the experimental titration curve. The parameter set for the model is discussed in the methods section. The brush is composed of chains with a length of  $N = 370$  segments. This value gave the best quantitative match between the model calculations and the experimental data. The curves in this plot correspond to different ionic strengths of the solution. In agreement with the experimental results, the titration curves have a rather sharp S-shape transition from the deionized to a charged state. Again, this is a feature that is distinctive for hydrophobic polyelectrolytes (HPE). Indeed, polyelectrolytes in a good solvent have a much wider titration curve, that is the increase in the charging starts already at lower pH.<sup>50,51</sup> As discussed above already the  $pK_{\text{eff}}$  shifts to higher values with lowering ionic strengths. Comparison of the theoretical results with the experimental ones, however, we notice that the experimental curve is significantly wider. One possible explanation for this is that in the experimental system the shells are composed of chains with different lengths. A polydisperse brush will have a broader transition region. We decided to keep the model as simple as possible and therefor have not implemented a polydisperse brush model.

Using the same model, we present the DLS-titration measurements with the predictions in fig. 2.6b for  $I = 10$  and 100 mM. Qualitatively, the model calculations follow the experimental trends, albeit that the model features a slightly stronger ionic strength dependence.

In the model calculations the degree of polymerization of the shell chains that fitted the experiments best was  $N = 370$ . This is in contrast contrasted to the SEC data (see fig.2.2) for the shell polymers that point to a degree of polymerization that is about 24 times larger. This huge difference clearly

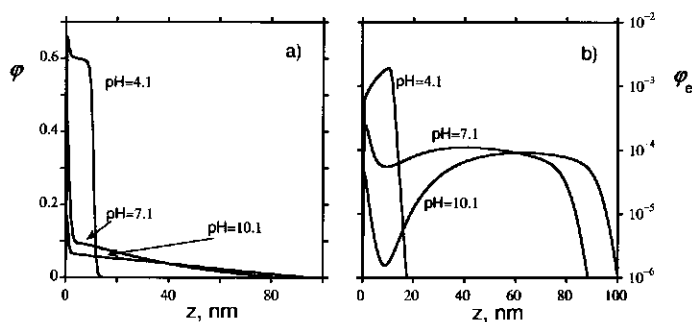


**Figure 2.7:** a) Polymer and b) polymer ends density profiles for the CSP shell model at three different pH values at  $I = 10$  mM

points to a complex structure of the shell layer. We envision that the shell polymers are present in the form of loops. Both ends of a given loop are connected to the core by a string of apolar segments, while the middle parts contain the chargeable units and can be stretched similarly as in a brush. From brush theory it is known that a brush composed of loops of length  $N$  can be described by a brush composed of end-grafted linear chains with length  $N/2$  with doubled grafting density. Hence, we envision that the shell polymers loop 10 to 20 times on average. The looped structure is consistent with an inhomogeneous distribution of apolar and charged monomers along the contour of the shell chains, mentioned above. At this stage we can not exclude that the number of loops may vary with the pH and ionic strength.

We believe that the shell layer, even though it is composed of very long chains, is reasonably accurately represented by a brush with relatively short chains. We haste to mention that in reality the length of the swellable parts must be polydisperse and it may well be that the chargeable groups are not fully homogeneously distributed. As more detailed information on the composition of the chains is lacking, we feel that the most simple model as introduced above is a good first-order approximation.

In order to get some feeling for the structure of the shell at different pH values, we end this chapter by presenting some typical predictions from the model of the shell shell layer in figure 2.7. In this figure we give both the polymer density profile (fig. 2.7a) as well as the end-point distribution (fig. 2.7b) as found in the radial coordinate system. We have selected three values for the pH, namely pH = 4.1 where the shell is collapsed, pH = 10.1 where the shell layer is fully swollen, and in the middle point of transition (pH = 7.1). The model predicts that the shell in the collapsed state reaches high densities of  $\phi = 0.6$ . The free ends are rather evenly distributed throughout this dense

layer with a slight increase toward the outer border. At intermediate pH (7.1), we have the so-called microphase segregated brush: some of the chains become charged whereas others remain neutral. These charged chains escape from the collapsed phase and this lowers the thickness of the collapsed phase. The charged chains form a strongly hydrated corona layer. The end-point distribution becomes bimodal, which is characteristic for the microphase segregated brush.<sup>52</sup> In the SCF model the transition appears to be abrupt. However, in reality the transition is smooth due to finite chain length effects. Interestingly, the bimodal distribution of chain ends point to the situation that the chains split into two populations. One being charged and swollen and the other one neutral and collapsed. Apparently mixed conformations for which part of a chain is collapsed and the remainder swollen must be rare. At high pH values the chains are strongly stretched at the expense of the collapsed phase. Comparison of the length of the chains ( $N = 370$ ) with the height of the brush proves that the chains are strongly stretched, almost to their complete contour length. This result is common for PE brushes composed of chains with a sufficiently high charge density along the contour. The poor solvent conditions for the apolar segments which tend to compact the shell layer are completely overruled by the strong electrostatic forces that extend the layer.

Although the micro-phase segregated scenario that presents itself for the hydrophobic polyelectrolyte brush at intermediate pH values is attractive, a note of caution is necessary. In the model it was assumed that the composition along the contour of the polymers is regular. For regular HPE's the partially collapsed chain is expected to be a rare event. This may not be true for blocky polymers with uneven distribution of apolar and charged blocks. In this case the distribution of apolar and charged segments may lead to inhomogeneous conformations that, as argued above, leads to loops. Nevertheless we believe that our model brush may give a realistic picture, as we can imagine that in typical stretches of  $N \approx 370$  segments the charge distribution along the shell chains might well be approximately homogeneous.

## 2.6 Conclusions

We have studied the molecular structure of acrylic core-shell particles (CSP) that have been synthesized by emulsion droplet polymerization. These particles proved to be well-defined, monodisperse and spherical, with 67 nm glassy cores and swellable shells which are adsorbed and effectively (physically) grafted to the cores.

The shells of the particles contain methacrylic acid groups and may

be classified as weak hydrophobic polyelectrolytes: at low ionic strength they are collapsed and (in the absence of surfactants) can not provide any colloidal stability of the dispersion. On the other hand, when the pH is increased, the MAA segments dissociate. Now the shells swell with water. Counterions that penetrate the shell for electrostatic reasons generate an osmotic pressure which triggers additional swelling of the layer. The collapse-swelling transition is found to be rather sharp as it occurs in the region  $6 < \text{pH} < 9$  and the swelling was found to decrease with increasing ionic strength.

Combining the data of potentiometric titrations with static light scattering, we were able to determine relevant parameters of the particles, such as the average molecular weight, the amount of acid groups per particle and the particle density.

The particles were also adsorbed onto a hydrophobized silica surface and then imaged by means of atomic force microscopy in tapping mode. The obtained images proved that the CSP are rather monodisperse and spherical. The particle sizes obtained from AFM are consistent with the data from DLS and SLS.

The swelling of the shells has been modeled using the mean-field SF-SCF method using a one-gradient spherical coordinate system. We modeled the shells as a monodisperse polymer layer, grafted on a spherical surface, which mimics the cores of the particles. The polymer chains in the shell are composed of hydrophobic segments and weak acid groups in ratio 3 to 1, which mimics the monomer composition in the experimental system. The chain length of the brush is selected to fit the DLS data and should correlate with the length of chargeable loops of the physisorbed polymers. The model gives a good agreement with experimental data. Both the pH and ionic strength dependence of the thickness of the shell are well reproduced.

## Chapter 3

# Hydrophobic Polyelectrolyte Brushes and Stars: a Numerical Self-Consistent Field Study <sup>a</sup>

### 3.1 Abstract

A polyelectrolyte brush, that is, an ensemble of polyelectrolyte chains end-grafted to a substrate, is ideally suited to modify particles and surfaces such that these become compatible with a solvent, i.e., water. The theoretical modeling of these systems is important to be able to tune these systems to optimal performance, especially when the bare (i.e., non-electrostatic) interactions of the polymer chains with water are marginal or poor. Here we use a lattice-based freely-jointed chain self-consistent field theory with the aim to understand colloidal stability issues. We thus consider pair interactions between both two similarly charged flat, laterally (in)homogeneous polyelectrolyte (PE) brushes and two PE stars, composed of chains with hydrophobic segments and ionizable or charged groups in an aqueous solvent. A wide variety of tunable parameters is investigated: the chain length, grafting density and composition, the ionic strength, the pH and the solvent quality. For a wide range of conditions phase segregation into two states is found: in this case part of the chains is stretched and is highly charged, other chains are collapsed and loose most of their charges. The interactions between such two-state brushes is analysed. The results of this study are relevant for experimental systems of colloids, stabilized by polyelectrolytes such as core-shell particles, but there are also strong links to biological brushes that apart

---

<sup>a</sup>To be submitted by: P.A. Iakovlev, J.M. Kleijn, F.A.M. Leermakers, M. A. Cohen Stuart, to: *Advances in Polymer Science*

from the charges along the chain, typically are composed of relatively apolar polypeptide or polysaccharide chains.

## 3.2 Introduction

A polymer brush is a term reserved for systems in which at some interface there is a large collection of polymers that are restricted by one of their ends to this interface such that the polymer layer is densely packed. The overlap of the polymers introduces lateral interactions and especially when the chains are in a good solvent, this causes the chains to be strongly stretched outward. The polymer brush has unique properties and occurs in a wide range of natural as well as man-made systems. Our interest is in the properties of brushes in aqueous solutions.

There are not so many types of polymer for which water is a good solvent. Polyelectrolytes (PE) that have a large number of charged groups along the backbone do as a rule dissolve in water. In such cases one is inclined to think that the bare interaction with water (that is the interaction with water in the absence of the charges) can be ignored and one should focus on the electrostatic effects only. We will show in this chapter that is a dangerous practice, that is, one will lose many interesting features and obtain a distorted picture especially for physical chemical conditions that are typical for applications (not so low ionic strength cases).

The effects of grafted polyelectrolyte (PE) chains onto the surface of colloidal particles have been addressed in a number of theoretical<sup>4,34,53-55</sup> and experimental<sup>6,56-64</sup> papers from which the main effects are clear and well understood. It is known<sup>4,62</sup> that in polar solvents such polyelectrolyte brushes typically will result in the steric stabilization of such a system. This implies that there is a repulsive interaction force between two PE decorated particles when these are brought together. This repulsion is, in most cases, attributed to the osmotic pressure of the counterions inside the polymer layer.<sup>4,64,65</sup> This effect of counterion localization inside the PE layers is observed in both MD-simulations<sup>18,66-68</sup> and experimental measurements of osmotic pressures and electrophoretic mobilities inside the layers.<sup>17,51</sup>

Depending on the ratio between the radius of a colloid to be stabilized and the thickness of the stabilizing polyelectrolyte layer, the system can be approximated either by a flat polymer brush, in the case of large colloids with a thin stabilizing layer, or by a polymer star in the opposite limit. Below we briefly describe the advances made in the studies of both cases and explain the main goals of our study.

According to theoretical predictions, the internal structure of a polyelectrolyte

brush with pH-dependent charges vary depending on external conditions.<sup>69</sup> For example, the height of a brush (effective thickness of the polymer layer) in a good solvent will go through a maximum as the ionic strength of the solution changes: at low ionic strength the brush is weakly charged and the density profile is similar to that of a non-charged brush; then, with an increase in the ionic strength the brush charges and swells, the reason for this swelling being the osmotic pressure of the counterions which compensate the polymer charge; a still further increase in the ionic strength of the solution leads to a strong screening of the charges and the height of the brush decreases again.

As already mentioned, polyelectrolytes often have apolar organic backbones which are insoluble in aqueous solvents.<sup>33, 70, 71</sup> Indeed for, e.g., paint applications, it may be crucial that the dried colloidal system forms a film that is later insoluble by polar solvents. These complementary conditions, namely the charges on the PE chain and the hydrophobic character of the backbone, gives special requirements to such systems. For example, the polymer layer should, for such systems, be near the edge between providing repulsion and attraction in the colloidal system. The dual character may be an inherent property of many systems that are stabilized by a PE-brush.

The more complicated case of a polyelectrolyte brush with a hydrophobic backbone has (of course) been studied before in a number of papers theoretically<sup>31, 33, 35, 72</sup> and experimentally.<sup>73-76</sup> First studies,<sup>33, 35</sup> based on a simple Alexander - de Gennes box model,<sup>77, 78</sup> show the possibility of a first-order phase transition of a brush from a swollen to a collapsed state upon a decrease in solvent quality. This transition is accompanied by a de-ionization of the polymer chains. As a consequence of the model used, the brush collapses or swells all at once, though in reality one may expect the appearance of several phases within the brush at the point of transition. This effect of so-called microphase segregation has been theoretically studied<sup>31, 52, 72</sup> and observed experimentally.<sup>76</sup> The overall picture is that a polyelectrolyte brush in a poor solvent can have several states: (i) a charged and swollen state, (ii) a microphase segregated state when part of the chains are charged and swollen and the other part is uncharged and collapsed, and (iii) a fully uncharged and collapsed state. Whether the brush is in one state or another will depend on the solvent quality, pH, ionic strength, its grafting density (number of chains per unit area), the fraction of chargeable groups, etc. One of the interesting points is that for the flat geometry the conformational characteristics of a hydrophobic polyelectrolyte brush are practically independent of the chain length.

Another interesting distinctive feature of hydrophobic PE brushes as compared to the hydrophilic ones is that the nature of the acids or bases composing the charges on the chain does not play a major role for its structure.<sup>31</sup>

Theoretical studies of polyelectrolyte brushes usually distinguish between two cases: one with a constant number of charges along the chain, the so-called quenched case (strong polybases or polyacids) and the other one with a number of charges which vary according to the surrounding media, i.e., proton and salt concentration.<sup>79</sup> The latter case, known as annealed polyelectrolytes, is the more general one and corresponds to real systems in a better way. It is believed that in the case of hydrophobic PE brushes the differences between quenched and annealed cases are minor (when the overall number of charges is similar in the two cases). Below we will pay attention to both PE types and arrive more or less to the same conclusion. However, we do find interesting differences that are worth discussing.

We next consider the interactions between two polyelectrolyte (PE) brushes. Such systems are schematically depicted in figure 3.1. In fig. 3.1a we show two PE brushes that are placed a distance  $H$  apart. Our interest will be in the case that the PE is in poor solvent condition. This means that we consider the case that in the absence of the charges, the PE chains would not be solvated by the solvent (this aspect is not depicted in fig 3.1). Upon approach, depending on conditions mentioned above, one can imagine several different scenarios. If the brushes are initially swollen, highly charged and far from the point of the transition into the microphase segregated state, one will find a repulsive interaction upon the approach of one brush to the other. Such a layer will provide an excellent steric stabilization of the system. On the other hand, when the two brushes are collapsed at the initial state (i.e., at large distances), bringing them together will result in attraction. This means that no steric stabilization is achieved.

The most interesting and complicated scenario is the one when the brush is initially in a state that is close to the phase transition. For instance, if the brushes are initially charged and swollen, the mutual compression will lead to an electrostatic repulsion due to counterion disjoining pressure at a longer range, but then the hydrophobic attraction takes a leading role at short separation distances. In other words, the transition may be triggered by compression. This effect has been described for quenched polyelectrolyte brushes in poor solvents by Misra et al.,<sup>34</sup> and should not be very much different for the annealed system due to similarities in the structure of brushes in the most interesting osmotic regime in both cases (compare, for example, polymer brush profiles from ref<sup>34</sup> and ref<sup>72</sup>).

Below, we will discuss the properties of PE brushes in the initial non-compressed state, essential as a reference to study of non-trivial interaction forces. Then we study the repulsion-attraction transition itself in more detail and consider more complicated systems in the end of our survey. These more complicated systems are introduced next.



One interesting case of a tethered polyelectrolyte system is that of polyelectrolyte stars. Again we refer to figure 3.1c for a schematic representation of this system. In this case the chains are attached to each other (in the figure indicated by a small black dot), rather than to a flat surface. This brings additional phenomena into consideration, i.e., a faster density decrease with distance from the center, a non-trivial scaling of the size on the number of arms or ionic strength of the solution and important differences in systems with various polymer chain lengths.<sup>28,29,65</sup> One reason why polyelectrolyte stars are studied is to help understand more complicated systems of self-assembling block copolymers, small colloids stabilized by polyelectrolytes or more complex branched systems. Pair interactions between polyelectrolyte stars have attracted intense interest in recent years<sup>30,80</sup> due to relevance of these studies to experimental observations, the complexity of the system and an additional degree of freedom of these systems as compared to the flat brushes case. Indeed, when the two stars approach each other, the chains can redistribute in such a way that the field of contact will contain an optimal (not necessarily lower) amount of polymer segments. This redistribution is indicated by black arrows in fig. 3.1.

There are not many theoretical approaches that can be used to analyse PE brush systems with molecular resolution. Computer simulations, such as molecular dynamics or Monte Carlo, give exact results for a given model, but have intrinsic problems covering the appropriate length scales. These simulation methods also have difficulty in taking the charge regulation in an annealed PE layer into account. Perhaps more relevant is that these simulation methods bypass the computation of the partition function and therefore have no easy access to the thermodynamic quantities that contain the information relevant to the pair interactions between brushes. The approach used in the present work is a numerical self-consistent field (SCF) theory, which predicts (on a mean field level) measurable structural properties and gives accurate thermodynamic information.

More specifically we use the implementation developed by Scheutjens and Fleer<sup>81</sup> and extended to polyelectrolyte systems by Israels et al.<sup>69</sup> The models used below can be characterized as being mesoscopic. The polymers are considered to be composed of segments that are represented by some united atom. For such a segment we account for the charge (either quenched or annealed) as well as the short range interactions (solvencies). In brushes these polymers are grafted (constrained) by one of their ends to some coordinate(s). Modeling simultaneously two brushes at a given distance apart, allows to study the colloidal stability issues. In order to make a gradual switch from the case of interactions between flat PE brushes to PE stars, we will consider a third type of system, which lies in between these two cases. We will study

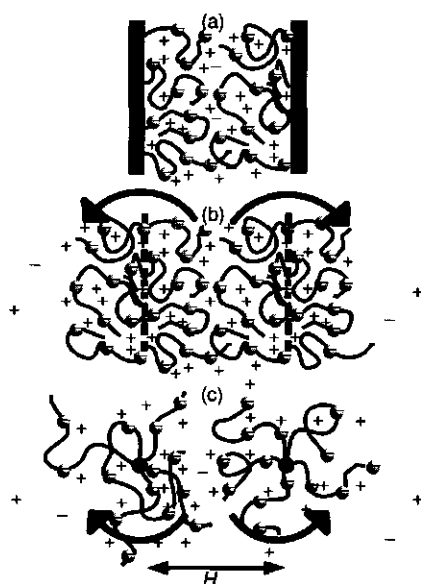


**Figure 3.1:** Schematic representation of three systems of interest studied in this chapter. In all three systems we consider two types of brushes composed of (hydrophobic) polyelectrolyte PE chains a distance  $H$  apart. In figure (a) we show PE brushes that have no possibility to relocate their chains because the chains are grafted onto a solid substrate. In figure (b) we present the so-called bilateral brush composed of chains end-grafted to some penetrable plane so that the chains can translocate (flip-flop) from one side to the other. In figure (c) we show two stars of PE chains. The arms can relocate radially. The arrows schematically illustrate the relocation degree of freedom. In this figure we have drawn negative charges on the chains and there are both positive and negative ionic species in the system. Each system is, in total, electroneutral, that is that there are an equal number of positive and negative charges in the system.

the interactions between two double-sided so-called bilateral PE brushes. The bilateral brush consist of chains grafted to some imaginary flat interface in such a way that the chains can pass from one side of this interface to the other (see figure 3.1b). We reason that the degree of freedom to translocate will effectively reduce the strength of interaction between two of these bilateral brushes as compared to the flat brushes grafted to the impenetrable surface. As we consider this system to be laterally homogeneous, it can be studied in a one-gradient self-consistent field formalism similar to that used for flat brushes (depicted in fig. 3.1a). Moreover, the additional possibility of flip-flop relaxation makes the bilateral brush close to that of the two-gradient analysis of two PE stars (stars can be studied in a two-gradient SCF formalism instead of the three-gradient case because we can make use of the axial symmetry of the system). The introduction of this relaxation mechanism brings in some interesting scenarios in the picture of two interacting PE brushes.

Another issue that we wish to address in this work is the influence of the polymer-surface interactions. Indeed, if in the real system we aim to understand the stabilization of some hydrophobic colloid with hydrophobic polyelectrolytes, there typically will be some attraction between the non-charged polymer chains and the surface of this colloid. In our default parameter setting this interaction will be included. In classical polymer brush theory, however, the interactions that the polymer chains have with the surface are typically ignored. The reason for this is that some residual adsorption of segments to the surface does not fundamentally change the scaling behavior of, e.g. the brush height with the chain length. Such interaction only complicates the problem somewhat. Below we will study the effects for the interaction between two polyelectrolyte brushes that originate from the presence/absence of the polymer-surface attraction. Especially for hydrophobic polyelectrolyte brushes the effects are significant.

At the end of this introduction we like to mention that this theoretical study has been triggered by an experimental system of core-shell particles with a hydrophobic core of aggregated polymers and a shell, composed of slightly more hydrophilic polymers that are adsorbed onto this core. These corona chains obtain their overall better solubility by the presence of a fraction of carboxylic acid groups. So when the corona is charged and swollen, the core-shell particles are colloidal stable. In the absence of these charges the corona will collapse onto the core with a corresponding loss of the colloidal stability. Though we try to make this theoretical study broad and applicable for a range of different systems, the choice of some parameters is guided by the properties of this experimental system.

We will first outline the self-consistent field model that is used to analyse

the structure and thermodynamics of our systems of interest in section 3.3. Isolated brushes that serve as a reference to rationalise the pair interactions are discussed in section 3.4. Referring once again to figure 3.1 we will consider the systems presented in this figure in order. The flat brushes will be discussed first in section 3.6, followed by bilateral brushes in section 3.7. We briefly will discuss the effect of lateral inhomogeneous brushes in section 3.8 and end with the computationally more challenging problem of interacting stars (see section 3.9.2).

### 3.3 Self consistent field theory

Our interest is in the behavior of polyelectrolytes (PE) grafted by one end onto either flat, or highly curved substrates, immersed in an aqueous solution containing a fixed concentration of 1:1 electrolyte at a given pH. In the most general case the charge in the PE chain depends on the pH in the solution, i.e., the chains have annealed charges. However, sometimes the degree of charging is approximately constant over a wide pH range, whereas they only start to vary at extreme values of the pH. When the system is considered in the constant charge regime, we refer to these systems as quenched polyelectrolytes.

The first issue we should address is the notion of the solvent quality.<sup>7,12</sup> The solvent quality for a polymer chain can be characterized by a second virial coefficient,  $v$ , which gives the free energy effect (both energy and entropy) for mixing of polymer segments with solvent on a segment level. For neutral polymers  $v = 1 - 2\chi_{AB}$ , where  $\chi_{AB} = (Z/2k_B T)(2U_{AB} - U_{AA} - U_{BB})$  is the well-known Flory-Huggins exchange interaction energy parameter. In this parameter  $Z$  is the number of contacts of a segment (equal to the coordination number in a lattice; see below) and  $k_B T$  is used to make it dimensionless. A positive value for this interaction parameter means that the (free) energy effects  $U$  for unlike contacts  $U_{AB}$  are higher than those for the like contacts  $U_{AA}$  and  $U_{BB}$ . The second virial coefficient, which is often referred to as the effective excluded-volume parameter, must be positive to dissolve long polymers and when it is negative a solution of such polymer chains will phase separate into a polymer rich and a solvent rich phase.

For polyelectrolyte chains one can split up the virial coefficient into a bare one and an electrostatic contribution, that is  $v = (1 - 2\chi) + v_e$ .<sup>82</sup> The effective electrostatic excluded-volume parameter increases with the amount of charges sitting on the polymer chains (and their valency) and decreases with the ionic strength,  $v_e = \nu^2 / \varphi_s^b$ , where  $\nu$  is the valency of the ionic species and  $\varphi_s^b$  is ionic strength of solution. For annealed systems the valency is

replaced by the fraction of charges  $\alpha$  that depends on the pH. From this it is easily seen that for sufficiently low ionic strength and high charge densities along the chain the overall virial coefficient will be much larger than unity even when  $\chi > 0.5$ . Indeed this is the case for many naturally occurring polymers: they would not dissolve in the absence of their charges. When the ionic strength is very low the value of  $v_e$  can easily dominate the second virial coefficient. Below, we will typically be interested in cases where both terms are important.

As a result the physics of polyelectrolytes in general and grafted polyelectrolyte brushes more specifically, brings together a large number of issues. Below we present a self-consistent field theory that is built on the Poisson equation for all the electrostatic issues and the Edwards equation<sup>10</sup> for the conformational degrees of freedom of the end-grafted polymers. The theory reduces to the Flory-Huggins theory for polymer solutions in the absence of volume fraction gradients in the system (and in the absence of the grafting constraint). The set of equations is solved numerically which prompts for a discretization scheme. Indeed, the choice of the coordinate system is a rather fundamental one and we therefore will start with this feature first.

### 3.3.1 Lattices

It is necessary to stress that models within the self-consistent field theory are constructed using severe approximations.<sup>83,84</sup> The use of a discrete set of coordinates onto which the self-consistent field machinery is implemented is probably one of the minor ones. Indeed, as long as one is interested in properties of the system that occur at length scales much larger than the discretization length, we do not expect any adverse effects. However, when one becomes interested in features on length scales that are small compared to the discretization length, one should better consider complementary approaches. The neglect of various types of correlations, which will be discussed below, involves undoubtedly more serious approximations.

Here we follow Scheutjens and Fleer<sup>81,85,86</sup> who suggested to use a relatively simple discretization scheme. It rests upon the idea that the polymer chains can be split up into segments. The segments are numbered  $s = 1, 2, \dots, N$  and for each segment  $s$  the segment type  $A$  is specified. To bypass all kind of intricate problems these authors suggest to consider segments as units with isotropic features with characteristic dimension  $b$ . We refer to figure 3.2 in which this length is indicated. Solvent molecules as well as ions are also assumed to have this characteristic length. Within the set of segment types we thus have, e.g., polymer segments, solvent, cations, anions, etc.

Next, the three dimensional space is taken to be built up by lattice sites,

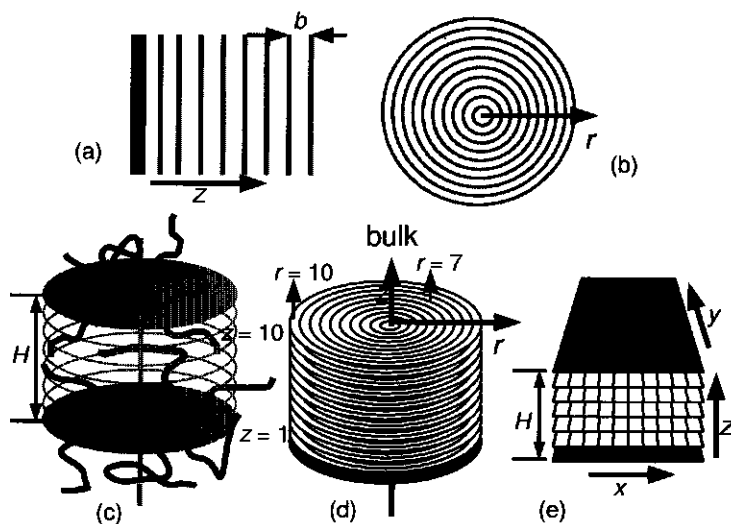


**Figure 3.2:** a) The one-gradient flat lattice. The  $z$ -axis runs perpendicular to the surface (indicated in black). The characteristic length  $b$  is indicated. Far from the surface there exist a homogeneous bulk solution. b) a cross section of a spherical lattice in the one-gradient approximation. Lattice layers with increasing  $r$  have an increasing number of sites. c,d) The cylindrical coordinate system, with  $(z, r)$  pointing to a layer  $z$  and a shell  $r$  within the layer. d) In black we indicate the surface. Layers  $z = 1$  and  $z = 10$  are indicated as well as two rings within layer 10, i.e.,  $r = 7, 10$ . c) An artistic graph with two stars grafted to the central axis of the cylindrical coordinate system at a separation distance  $H$ . The layers in which the stars are grafted are drawn gray for presentation purpose only. e) A two-gradient flat coordinate system. Here the mean-field approximation is applied along lines of lattice sites in the  $y$ -direction, and gradients are present in  $x$  direction (parallel to the surface) and in the  $z$ -direction (perpendicular to the surface). On both sides of the system a surface exists. The surfaces are separated by a distance  $H$ . Both (d,e) reduce to (a) when the mean field averaging is extended over the  $r$  and  $x$  direction, respectively. All linear lengths are made dimensionless by the lattice length  $b$ .

again with  $b$  as the fundamental length unit. The segments of the polymer chain, as well as the monomeric species in the system are restricted such that they can only take places on these discrete set of lattice sites. The elegance of the Scheutjens-Fleer discretisation scheme is thus that there is just one fundamental length.

Within the lattice we are going to identify layers of sites. Again in figure 3.2 we show a few examples of lattices where we indicated the lattice layers. In these figures the individual lattice sites within such a layer are not indicated for clarity of presentation. The choice of lattice layers strongly depends on the symmetry expected for the system of interest. If there is a flat surface, one typically will take the layers to be planar arrangements of lattice cells parallel to such surface (cf fig 3.2a,d). Below we will use a general coordinate  $\mathbf{r}$  to refer to a layer of lattice sites. In specific cases, however, we will implement the coordinate  $z$  to refer to flat layers (cf fig 3.2a), and the coordinate  $r$  when the sites within each layer are organised otherwise, e.g. when we consider a PE-star (cf fig 3.2b). For the interaction of a pair of stars we can not suffice with a lattice with only one gradient direction. Instead we need two (cf fig 3.2c,d,e). Now the mean-field approximation is applied within concentric rings of lattice sites. Within a given layer  $z = 1, 2, \dots$ , we have concentric rings  $r = 1, 2, \dots$  and thus  $\mathbf{r} = (z, r)$ , refers to a particular ring of lattice site  $r$  in layer  $z$ .<sup>87-89</sup>

Below we will also be interested in brushes that, for one reason or another, do not remain laterally homogeneous. Such situations can be investigated using two gradient lattices. Referring to fig 3.2e we choose these two gradient directions as  $x$ - and  $z$ -coordinates and one direction over which the mean field approximation is applied (the  $y$ -direction). In this case the inhomogeneities extend infinitely long into the  $y$ -direction (dikes; linear micelles). We may refer to this as the 'two-gradient flat' lattice as all layers of lattice sites are linear arrangements of lattice sites. Now we thus have  $\mathbf{r} = (z, x)$ .

One reason to use lattice models is that it is straightforward to count the fraction of sites occupied by a particular segment of type  $A$ , we will refer to this volume fraction by  $\varphi_A(\mathbf{r})$ . In other words, the lattice model brings quite naturally to account for the (excluded) volume of the molecular species. The lattice also makes the possible number of conformations of chain molecules countable. For example a dimer can, once its first segment is on the lattice, put its second monomer in only  $Z$  different lattice sites ( $Z$  is the lattice coordination number). It is important to realise that a fraction of these dimers have segments in the same layer, some of these have the second segment in a following layer and the remainder has the second segment in a previous layer.

Each set of coordinates is characterized by a few quantities. There is

the number of lattice sites  $L(\mathbf{r})$  that exists in each specified coordinate. As the volume of a lattice site is taken  $v = b^3$  (cubic volume element), the number of sites per coordinate follows from the volume  $V(\mathbf{r})$  available per  $\mathbf{r}$ . For a spherical coordinate system we have  $L(r) = V(r)/b^3 = \frac{4}{3}\pi(r^3 - (r-1)^3)$  (here  $r$  is expressed in units of  $b$ ). For a ring of lattice sites (present in the two-gradient cylindrical coordinate system),  $L(z, r) = 4\pi(r^2 - (r-1)^2) \forall z$ . For a one-gradient flat lattice it suffices to mention that the number of lattice sites per unit area is constant, i.e.,  $L(z) = 1$ , or in the two-gradient approximation we normalise the number of sites per unit length in the  $y$  direction, i.e.,  $L(z, x) = 1$ . Next, there are *a priori* step probabilities  $\lambda(\mathbf{r}, \mathbf{r}')$ . These quantities specify the probability to go from coordinate  $\mathbf{r}$  to coordinate  $\mathbf{r}'$  with a step of length  $b$ . From this it is clear that it will assume non-zero values for pairs of sites that are neighbors in the system and obey to the constraint

$$\sum_{\mathbf{r}'} \lambda(\mathbf{r}, \mathbf{r}') = 1 \quad (3.1)$$

where the summation obviously runs over all neighbors. We will encounter the use of the step probabilities, e.g., in the computation of the segment potentials as well as in the evaluation of the statistical weight of chain conformations. The *a priori* step probabilities obey to certain rules to make sure that they properly account for the imposed lattice geometry. More specifically the properties are chosen such that the theory obeys the inversion symmetry. This means that, e.g. when doing the chain statistics, it should be inconsequential whether the evaluation of the statistical weights is started at one end of the polymer chain or on the other end. As a result the step probabilities obey to an internal balance equation

$$L(\mathbf{r})\lambda(\mathbf{r}, \mathbf{r}') = L(\mathbf{r}')\lambda(\mathbf{r}', \mathbf{r}) \quad (3.2)$$

This internal balance is automatically obtained if the step probabilities are made proportional to the surface area shared by the two neighboring sites.

The target of the calculations is to find the optimum distribution of the molecules in this discrete set of coordinates  $\mathbf{r} = (z, r)$ . To quantify the optimisation there is a mean-field free energy. To evaluate this, we need to choose the chain model in which the conformational degrees of freedom that are allowed are explicitly defined - here we will implement a freely-jointed chain model-. In this free energy one also need to specify what interactions are felt by the molecules. We will consider short-range interactions similarly as in the Flory-Huggins theory in combination with electrostatic interactions. This free energy can be expressed as a functional over the volume fractions



and, characteristic for mean-field theories, also as a functional over segment potentials. On the lattice both quantities, the volume fractions  $\varphi(\mathbf{r})$  as well as the segment potentials  $u(\mathbf{r})$ , assume discrete values. From the extremisation of our free energy functional (more correctly, a saddle point is needed, as the free energy functional is minimized with respect to the segment densities and maximized with respect to the potentials) we learn how the volume fractions follow from the potentials and how the potentials follow from the volume fractions. This leads to the machinery which is outlined in more detail below.

### 3.3.2 The SCF machinery

As told, the SCF machinery naturally splits up into two subtasks, namely the one to compute the volume fractions and the one to compute the segment potentials. For each segment type in the system we will have this pair of (discrete) functions and as they depend on each other, the solution of the equations is called the self-consistent solution. At this stage it is appropriate to specify in some detail which molecules are in our systems. The discussion of the parameters that further specify the system is given in separate sections.

In most of our systems we discuss below there exist one or two surfaces. We will reserve the letter  $S$  to refer to the material that provides the surface. The volume fraction profile of the surface units is fixed throughout the calculations. It assumes the value unity  $\varphi_S(\mathbf{r}) = 1$  at regions in space where there is a surface and is zero otherwise. This implies that all other molecular parameters cannot enter the region where there is a surface, they can at best adsorb onto these surfaces and such a phenomenon is controlled by the interaction parameters.

All our systems will feature a polyelectrolyte brush. A polymer brush consists of chains that have their first segment restricted to a specified coordinate (either next to the surface or at a central position in the case of a star) and their last segment  $s = N$  is free to take any position (as long as it is not further than  $Nb$  from the grafting spot). The concept of a brush, however, is reserved for those systems that have a sufficiently high grafting density such that the chains feel each others presence strongly. Due to this lateral interactions the chains stretch in the normal direction. As a result of this stretching there are many characteristics of the polymer brush that scale proportional to the chain length.

Our polymer chains consist of segments  $P$  and  $C$ . The  $P$  segments are typically hydrophobic and uncharged, whereas the  $C$  segments either have a permanent charge (quenched) or obtain a variable charge (annealed) - below we will consider carboxylic group as a generic chargeable unit. These  $C$

segments are taken to be in a theta solvent. The C-segments are distributed homogeneously along the chains (the distribution is quenched). Next there will always be a pair of monomeric species present, one with a permanent positive charge and one with a negative charge. The concentration (volume fraction) of this 1:1 electrolyte is one of the main variables in the system. In addition we have a solvent, representing water. In the case of annealed charges, we will assume water to have three possible internal states: the neutral, the positively and the negatively charged internal state. The fraction of protons in the bulk defines the pH in the solution. This latter quantity is another natural variable in our system. The following paragraphs discuss the necessary ingredients to model such systems.

### 3.3.3 From volume fractions to potentials

The mean-field free energy functional features potentials and volume fractions. From the extremisation of this free energy  $F$  it follows that the mean field potentials can be written, for an arbitrary segment A, as

$$u_A(\mathbf{r}) = u'(\mathbf{r}) + \frac{\partial F^{\text{int}}}{\partial \varphi_A(\mathbf{r})} \quad (3.3)$$

where  $F^{\text{int}}$  is the interaction part of the free energy functional. Eqn 3.3 can uniquely be computed when all volume fractions are available. Physically, a segment potential collects the reversible work that is needed to bring a segment of type A from the bulk (reference point) to the coordinate  $\mathbf{r}$ . The first contribution,  $u'$  is known as the Lagrange field, as its value is coupled to the incompressibility constraint imposed on the volume fractions:

$$\sum_A \varphi_A(\mathbf{r}) = 1 \quad \forall \mathbf{r} \quad (3.4)$$

Physically, the Lagrange potential represents the work to give up a lattice site in the bulk and to create an empty site at the specified coordinate. As all segments are assumed (by construction) to be of the same size, we find that the Lagrange field is not a function of the segment type. The second term in the segment potential originates from differentiating the interaction part of the free energy. Basically we are interested in systems for which there are both short-range interactions - as in the Flory-Huggins theory, as well as electrostatic interactions - similar to the Gouy Chapman theory for charged interfaces.

The true number of binary contacts, such as polymer / solvent, polymer / polymer, solvent / solvent, are difficult to evaluate because, in principle,

the probability of such a contact is relatively high when such a contact is favorable (decreases the free energy) and is relatively low when the contacts are unfavorable (increases the free energy). Here the point of reference is the *a priori* probability of such contact, which coincides with the appropriate volume fractions. The mentioned correlation effects are ignored in the SCF theory. More specifically, the *a priori* contacts (given by the volume fractions) are the ones that are implemented in a first-order (Bragg-Williams) mean-field theory. Here we will account for the binary interactions for those segments that sit on neighboring lattice sites only. The result is

$$u_A^{\text{int}}(\mathbf{r}) = \sum_B \chi_{AB} (\langle \varphi_B(\mathbf{r}) \rangle - \varphi_B^b) \quad (3.5)$$

where the angular brackets are needed to account for the interactions between A and B segments that do not reside on the same coordinate. Here we meet the first use of the step probabilities

$$\langle \varphi_B(\mathbf{r}) \rangle = \sum_{\mathbf{r}'} \lambda(\mathbf{r}, \mathbf{r}') \varphi_B(\mathbf{r}') \approx \varphi_B(\mathbf{r}) + b^2 \lambda \nabla^2 \varphi_B(\mathbf{r}) \quad (3.6)$$

The quantity  $\langle \varphi_A(\mathbf{r}) \rangle$  is known as the site fraction of A at  $\mathbf{r}$ . On the r.h.s. of Eqn 3.6 we show that the site fraction has a continuum analogue. The Laplace operator is different for each lattice geometry. For a one-gradient flat lattice it reduces to a second derivative. The  $\lambda$  is the probability to step from one layer to the neighboring one in the bulk phase (limit of the flat lattice). In Eqn 3.5  $\varphi_B^b$  is the volume fraction of component B in the bulk. This quantity is introduced for convenience so that the potential is normalised to zero in the bulk.

In the Gouy-Chapman theory for charged segments we have an electrostatic contribution to the segment potential. Again, this term follows from proper differentiation of the free energy contribution due to the electrostatic forces. Below we will implement in some cases that the polymer segments can choose from different internal states (i.e., in a charged or in a neutral state). Anticipating this part of the discussion we introduce the subindex  $k$  which refers to one of these internal states. We will assume that the internal state does not influence the short-range interactions mentioned above, but this information is obviously relevant for the electrostatic contribution. We thus have for segment A in internal state  $k$  the electrostatic part of the segment potential

$$u_{Ak}^e(\mathbf{r}) = \frac{\nu_{Ak} e \psi(\mathbf{r})}{k_B T} \quad (3.7)$$

where  $\nu_{Ak}$  is the valency of segment type A in state  $k$ ,  $\psi(\mathbf{r})$  the electrostatic potential,  $e$  the elementary charge and  $k_B T$  the thermal energy. In this work we will assume that the dielectric permittivity of the medium is homogeneous and fixed to the bulk value  $\epsilon$ . In such an approximation it is not necessary to account for a polarisation term in the segment potential.

At this stage it is important to mention that the electrostatic potentials can be evaluated once the volume fractions are known. The first step is to find the charge density profile

$$q(\mathbf{r}) = e \sum_A \sum_k \varphi_{Ak} \nu_{Ak} \quad (3.8)$$

which is used in the well-known Poisson equation

$$\nabla^2 \psi(\mathbf{r}) = -\frac{q(\mathbf{r})}{\epsilon} \quad (3.9)$$

The Laplace operator should be implemented according to the coordinate system at hand. It turns out that the discrete version of the Poisson equation, for all geometries used, can be written using the site fractions

$$\frac{1}{b^2 \lambda} (\langle \psi(\mathbf{r}) \rangle - \psi(\mathbf{r})) = -\frac{q(\mathbf{r})}{\epsilon} \quad (3.10)$$

The presence of charged species brings in extra constraints on the composition of the system. We already mentioned the incompressibility constraint. In this case the system as a whole should also remain electroneutral. Fortunately this automatically is maintained if the boundary conditions are properly implemented. However, for a realistic system we must impose that also the bulk remains electroneutral, i.e.,  $\sum_A \sum_k \varphi_{Ak}^b \nu_{Ak} = 0$ . In practice this means that for one of the ionic species, the so-called neutraliser, the bulk volume fraction is an adjustable parameter and not fixed by the input.

At the end of this section it is appropriate to sum up the three contributions to the segment potential

$$u_{Ak}(\mathbf{r}) = u'(\mathbf{r}) + u_A^{\text{int}}(\mathbf{r}) + u_{Ak}^e(\mathbf{r}) \quad (3.11)$$

### 3.3.4 From potentials to volume fractions

The task to compute the volume fractions is the second issue. To do so we need to evaluate the statistical weight of all possible and allowed conformations of the molecules in the system. In principle all realistic conformations have the property of self-avoidance, meaning that a polymer chain cannot visit the same (lattice) site twice. Generating (on a lattice) all self-avoiding

chain conformations is only possible for chains with a length upto about 30 segments. For longer chains extra approximations become unavoidable. Within a freely-jointed chain model, which allows chain backfolding, it is possible to implement a very efficient propagator scheme.

The first step to prepare for the propagators is to define so-called free segment distribution functions  $G_i(\mathbf{r}, s)$  for segment  $s$  of molecule number  $i$  at coordinate  $\mathbf{r}$ . To this end the segment potentials of Eqn 3.11 are used in the Boltzmann equation:

$$G_{Ak}(\mathbf{r}) = \exp\left(-\frac{u_{Ak}(\mathbf{r})}{k_B T}\right) \quad (3.12)$$

Below we will show that the internal states of segments are linked through appropriate reaction equilibria. For given pH and bulk composition, we can evaluate the probability that in the bulk segment type A is in state  $k$ , i.e., all  $\alpha_{Ak}^b$  values are known. We can use these to obtain an overall free segment weighting factor for segment A at coordinate  $\mathbf{r}$ :

$$G_A(\mathbf{r}) = \sum_k \alpha_{Ak}^b G_{Ak}(\mathbf{r}) \quad (3.13)$$

These weighting factors depend on the segment type and our goal is to obtain corresponding quantities that depend on the segment ranking numbers. In principle this translation can easily be implemented by making use of so-called chain architecture operators  $\delta_{i,s}^A$  which are quantities that obtain the value unity when segment  $s$  of molecule  $i$  is of type A and zero otherwise. The information needed to set these chain architecture operators follows uniquely from the input. Now

$$G_i(\mathbf{r}, s) = \sum_A \delta_{i,s}^A G_A(\mathbf{r}) \quad (3.14)$$

For the monomeric species in the system we now can easily compute the volume fraction distribution

$$\varphi_i(\mathbf{r}) = C_i G_i(\mathbf{r}, 1) \quad (3.15)$$

The normalisation constant  $C_i = \varphi_i^b$  is found by realising that  $G_i = 1$  in the bulk.

For polymeric species the volume fraction follow, at least in principle from solving the Edwards diffusion equation<sup>10</sup>

$$\frac{\partial G_i}{\partial s} = b^2 \lambda \nabla^2 G_i - \frac{u}{k_B T} G_i \quad (3.16)$$

wherein the spatial and ranking number dependences are not indicated for simplicity reasons. This equation needs to be solved with the relevant starting condition. In our case we have to account for the fact that the first segment is fixed to a specified coordinate. Moreover it needs to be supplemented with the proper boundary conditions. We can make use of known properties of the Green's functions that solve this differential equation to efficiently evaluate the volume fractions from it. It can be shown that the Edwards equation simplifies to a propagator equation. As the efficient method to compute the volume fractions requires two complementary propagators we present both of them at the same time

$$G_i(\mathbf{r}, s | \mathbf{r}^*, 1) = G_i(\mathbf{r}, s) \langle G_i(\mathbf{r}, s - 1 | \mathbf{r}^*, 1) \rangle \quad (3.17)$$

$$G_i(\mathbf{r}, s | N) = G_i(\mathbf{r}, s) \langle G_i(\mathbf{r}, s + 1 | N) \rangle \quad (3.18)$$

The physical implications of these equations are perhaps best illustrated by briefly mentioning how these propagators are related to the Edwards equation. We may proceed starting by Eqn 3.18 and translate the site fraction (cf Eqn 3.6) to its continuous analogue

$$G_i(\mathbf{r}, s | N) = \exp \left( -\frac{u_i(\mathbf{r})}{k_B T} \right) (G_i(\mathbf{r}, s + 1 | N) + \lambda \nabla^2 G_i(\mathbf{r}, s + 1 | N)) \quad (3.19)$$

For an infinitesimal change in the contour length of the chain we can Taylor expand the Boltzmann term and replace it by  $1 - \frac{u_i(\mathbf{r}, s)}{k_B T}$ . The discrete difference  $G_i(\mathbf{r}, s | N) - G_i(\mathbf{r}, s - 1 | N)$  is in the continuous limit replaced by  $\frac{\partial G_i(\mathbf{r}, s | N)}{\partial s}$  and by ignoring the small contribution  $u \times \nabla^2 G$  we retrieve Eqn 3.16.

The two propagators have different initial conditions. The forward propagator of Eqn 3.17 is started by the first segment and as this segment is restricted to coordinate  $\mathbf{r}^*$  we implement  $G_i(\mathbf{r}, 1 | \mathbf{r}^*, 1) = G_i(\mathbf{r}, 1)$  for  $\mathbf{r} = \mathbf{r}^*$  and zero otherwise. The backward propagator is started at segment  $s = N$ . As there are no explicit constraints on this chain end we have  $G_i(\mathbf{r}, N | N) = G_i(\mathbf{r}, N)$  for all coordinates.

The volume fractions follow from the so-called composition law

$$\varphi_i(\mathbf{r}, s) = C_i \frac{G_i(\mathbf{r}, s | \mathbf{r}^*, 1) G_i(\mathbf{r}, s | N)}{G_i(\mathbf{r}, s)} \quad (3.20)$$

In this equation the normalisation  $C_i$  follows from the conservation of segments. It is given by  $C_i = \frac{\sigma}{G_i(N | \mathbf{r}^*, 1)}$  where  $\sigma$  is the grafting density, that is the number of grafted chains in the system per unit area. In the star-polyelectrolyte it

is the number of arms (chains) per star. The single-chain partition function  $G_i(N|\mathbf{r}^*, 1)$  collects the combined statistical weight of having these chains in the system and is computed by

$$G_i(N|\mathbf{r}^*, 1) = \sum_{\mathbf{r}} L(\mathbf{r}) G_i(\mathbf{r}, N|\mathbf{r}^*, 1) \quad (3.21)$$

In Eqn 3.20 we combine two sub-partition functions that have the overlapping segment  $s$  and the overlapping coordinate  $\mathbf{r}$  in common, but were initiated at the complementary chain ends. The division by  $G_i(\mathbf{r}, s)$  corrects for the fact that the Boltzmann weight for segment  $s$  is included in both complementary end-point distributions.

Collecting the volume fraction distribution per molecule involves the summation over all its segments

$$\varphi_i(\mathbf{r}) = \sum_s \varphi_i(\mathbf{r}, s) \quad (3.22)$$

The subsequent summation over all coordinates should lead to the grafting density, i.e.,

$$\sigma_i = \frac{1}{N_i} \sum_{\mathbf{r}} L(\mathbf{r}) \varphi_i(\mathbf{r}) \quad (3.23)$$

Very often this quantity is converted to the amount of molecule  $i$  (per unit area) in the system  $\theta_i$ . The conversion factor is simply the chain length, i.e.,  $\theta_i = \sigma_i N_i$ . For the monomeric species we may also compute the amount, i.e.,  $\theta_j = \sum_{\mathbf{r}} L(\mathbf{r}) \varphi_j(\mathbf{r})$ . For the segment potentials we need to collect the volume fraction profiles for a particular segment type. In general such a segment can be located on different molecules so that

$$\varphi_A(\mathbf{r}) = \sum_i \sum_s \varphi_i(\mathbf{r}, s) \delta_{i,s}^A \quad (3.24)$$

A complication presents itself in the case when segments have multiple internal states. From the propagators we can extract only the overall volume fractions per segment type. To split up the overall distributions into those that depend on the internal state of the segment we need to know the local probability of segment type  $A$  to be in state  $k$ , i.e.,  $\alpha_{Ak}(\mathbf{r})$ . This fraction is given by

$$\alpha_{Ak}(\mathbf{r}) = \alpha_{Ak}^b \frac{G_{Ak}(\mathbf{r})}{G_A(\mathbf{r})} \quad (3.25)$$

and thus

$$\varphi_{Ak}(\mathbf{r}) = \alpha_{Ak}(\mathbf{r})\varphi_A(\mathbf{r}) \quad (3.26)$$

### 3.3.5 Annealed charges

Above we mentioned that the internal states for a particular segment obey to some chemical reaction equilibrium. Here we go into the necessary details. Let us start with water and consider the equilibrium



with the equilibrium condition

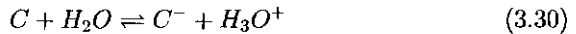
$$2\mu_{H_2O} = \mu_{H_3O^+} + \mu_{OH^-} \quad (3.28)$$

Ignoring activity corrections we write  $\mu = \mu^\# + k_B T \ln \varphi$  and

$$\exp \left( \frac{2\mu_{H_2O}^\# - \mu_{H_3O^+}^\# - \mu_{OH^-}^\#}{k_B T} \right) = K_W = \frac{(\varphi_{H_3O^+})(\varphi_{OH^-})}{\varphi_{H_2O}^2} \quad (3.29)$$

Which defines the dimensionless auto-dissociation constant  $K_W$ . We can number the internal states of water  $k = 1, 2, 3$  for the neutral, the proton and hydroxyl ion and the charge  $\nu_{Wk} = 0, 1, -1$  for  $k = 1, 2, 3$ , respectively.

Similarly we have the acid groups in the polymer chain with generic name  $C$ . This segment is either in the neutral state  $k = 1$  and  $\nu_{C1} = 0$  or in the negatively charged state  $k = 2$  with  $\nu_{C2} = -1$ . The reaction equilibrium



with a corresponding dimensionless constant  $K_A$ .

### 3.3.6 Numerical recipe

From the above it is clear that the volume fractions follow, using the propagator scheme, from the segment potentials. On the other hand the segment potentials follow uniquely from the volume fraction profiles. Only in rare cases it is possible to solve this set of equations analytically. Typically, however a numerical iteration scheme is needed to find the self-consistent field solution. For an acceptable self-consistent field solution it is true that the volume fraction both follow from and determine the segment potentials and inversely the potentials both follow from the volume fractions and determine the



segment potentials. An acceptable solution also obeys the incompressibility constraint meaning that the sum over the volume fractions equal unity.

The numerical algorithm which makes use of a Newton-like iteration converges in order  $10^2$  to  $10^3$  iterations to a precision of 7 significant digits.<sup>90</sup> However in the low ionic strength limit and/or in the case of low charge densities a significantly higher number of iterations is required. Systems with annealed charges typically are more difficult to solve.

### 3.3.7 Thermodynamics and other measurables

Once a fixed (self-consistent field) point is found, it is possible to evaluate the free energy  $F$  of the system. This free energy is the starting point for the analysis of various other thermodynamic quantities. Important for the present analysis is to evaluate the free energy of interaction. Typically our interest is in a system in which the number of grafted chains as well as the chemical potentials of all mobile components are fixed. In this case the characteristic function is a semi-open free energy  $F^{po}$ . For all components the system is open (transport is allowed) except for the grafted chains. This thermodynamic potential is computed from

$$F^{po} = F - \sum_j \mu_j n_j \quad (3.31)$$

where  $\mu_j$  is the chemical potential of component  $j$  and  $n_j$  is the number of molecules of type  $j$  in the system. We note that for the case of annealed chains we should also extract the chemical contributions of the protons that are stored in the uncharged units of the polymer, i.e., we need to subtract from the free energy the product  $\theta_{C1} \times \mu_{H_3O^+}$ , where  $\theta_{C1}$  is the number of segments of type C in state  $k = 1$  in the system (per unit area).

The free energy may be expressed in the volume fraction and segment potentials as:

$$\begin{aligned} \frac{F}{k_B T} = & \sum_i \frac{\theta_i}{N_i} \ln N_i C_i + \sum_{A,k} \theta_{Ak} \ln \alpha_{Ak}^b - \\ & \sum_{\mathbf{r}, A, k} L(\mathbf{r}) \varphi_{Ak}(\mathbf{r}) u_{Ak}(\mathbf{r}) + \frac{1}{2} \sum_{\mathbf{r}, A, B} L(\mathbf{r}) \varphi_A(\mathbf{r}) \chi_{AB} \langle \varphi_B(\mathbf{r}) \rangle + \frac{1}{2} \sum_{\mathbf{r}} L(\mathbf{r}) q(\mathbf{r}) \psi(\mathbf{r}) \end{aligned} \quad (3.32)$$

The chemical potentials follow from the corresponding homogeneous bulk phase. We first focus on the chemical potentials for the monomeric species (these are the only ones that are mobile in our system). For molecules that exist in just one state we have

$$\frac{\mu_i}{k_B T} = \ln \varphi_i^b + 1 - \sum_j \frac{\varphi_j^b}{N_j} + \frac{1}{2} \sum_{AB} (\varphi_A^b - \delta_{A,i}) \chi_{AB} (\varphi_B^b - \delta_{B,i}) \quad (3.33)$$

where  $\delta_{A,i}$  is unity when molecule  $i$  consists of segment type  $i$  and zero otherwise. For water we have three internal states with corresponding  $\alpha_{Wk}^b$  values. For the chemical potential of water in state  $k$  we have to add a term  $\alpha_{Wk}^b \ln \alpha_{Wk}^b$ .

The chemical potential of the polymer is found from  $\mu = \frac{\partial F}{\partial \sigma}$  for fixed area. Let molecule  $i$  be the grafted polymer, it turns out that the chemical potentials can be derived from the normalisation constant  $C_i$  that set the grafting density (cf the text below eqn 3.20). Then

$$\frac{\mu_i}{k_B T} = \ln N_i C_i + 1 - N_i \sum_j \frac{\varphi_j}{N_j} + \sum_{A,B} N_{i,A} \chi_{AB} \varphi_B^b - \frac{1}{2} N_i \sum_{A,B} \varphi_A^b \chi_{AB} \varphi_B^b + \sum_{A,k} N_{i,A} \alpha_{Ak} \ln \alpha_{Ak} \quad (3.34)$$

where  $N_{i,A}$  is the number of A segments in molecule  $i$ . The last term in eqn 3.34 is needed for systems that have annealed charges only and the accent at the summation sign reminds us about this.

For the free energy of interaction we take the characteristic function at large separations as the reference and thus

$$F^{\text{int}}(H) = F^{\text{po}}(H) - F^{\text{po}}(\infty) \quad (3.35)$$

It is possible to carry out various types of analysis to characterise the structure of the PE brushes. One of these, which may be mentioned here is the measurement of the brush height. A common procedure to estimate the height is to compute the first moment over the end-point distribution (the free end). Mathematically,

$$h_g = \frac{\sum_{\mathbf{r}} L(\mathbf{r})(|\mathbf{r} - \mathbf{r}^*|) \varphi_i(\mathbf{r}, N)}{\sum_{\mathbf{r}} L(\mathbf{r}) \varphi_i(\mathbf{r}, N)} \quad (3.36)$$

One of the next issues of interest for polyelectrolyte brushes with annealed charges is to compute the average degree of dissociation of the chargeable groups in the brush. We will use the variable  $\alpha$  for this

$$\alpha \equiv \frac{\sum_{\mathbf{r}} L(\mathbf{r}) \varphi_C(\mathbf{r}) \alpha_{C2}(\mathbf{r})}{\sum_{\mathbf{r}} L(\mathbf{r}) \varphi_C(\mathbf{r})} \quad (3.37)$$

where we recall that state  $k = 2$  of segment type C is the one that carries the charge. This must be contrasted to the (fractional) charge on the quenched brush segments, which is set manually in the range 0 to 1 (by way of the valency of the C-segment and we fix  $\alpha = \nu_C$ ). As  $\alpha$  is used in both quenched and annealed cases we will specify in each case whether the brush has annealed or quenched charges.

### 3.4 Isolated hydrophobic PE brush on a flat substrate in an aqueous solution

Flat homogeneous PE brushes in good solvents have been studied within a one-gradient Scheutjens-Fleer self-consistent field (SF-SCF) model extended to charged polymers more than a decade ago.<sup>69,81</sup> Here our focus is on the poor solvent conditions of a single laterally homogeneous flat polyelectrolyte brush composed of long polymer chains grafted to a solid surface. This system will be analysed in depth as it serves as a reference to the other systems used to study the colloidal interactions. In the following we will first discuss all parameters that are used in the modeling. After that the results will be presented and discussed.

#### 3.4.1 Parameters

The chains are composed of a number of hydrophobic segments, some of which bear a charged or chargeable group. This type of polymer brush has been considered previously (see, for example<sup>31</sup>), but a detailed study is still lacking. Therefore it is timely to perform an in depth study, specifically stressing the differences as well as similarities that arise from the quenched or annealed nature of the ionizable polymer groups. We consider this detailed study as a reference for the subsequent investigation of the interactions between brushes.

The hydrophobic PE brush is characterized by a large set of parameters. A number of parameters is also relevant for a non-charged brush, namely the chain length  $N$ , grafting density  $\sigma$  and segment interaction parameters  $\chi_{AB}$ . Specific for both strong and weak polyelectrolyte brush we have the amount of salt in bulk, and for weak polyelectrolyte brush - additionally the pH in the bulk, the degree of dissociation of the charged groups  $\alpha$  and the  $pK_A$  of the segments. Below we will vary each of these parameters, fixing the remaining

parameters and comparing the outcome for quenched and annealed brushes. As there are so many variables we first define a "normal" set of parameters (the defaults) which will be fixed unless stated otherwise. This set is chosen in such a way to mimic our experimental conditions. To allow for a good comparison between quenched and annealed brushes, we should make the two systems as identical as possible, with the only difference being the way the ionizable groups get their charge - through the input parameters (quenched) or according to surrounding conditions (annealed).

The brush chains consist of hydrophobic polymers with a large number of segments. Each monomer is considered to be of length  $b$  equal to the Bjerrum length  $l_B \approx 0.7$  nm in water. Indeed, this Bjerrum length is chosen as the unit of length and all linear dimensions will be normalised by this length. Such procedure is common for polyelectrolytes studies. The default value of the degree of polymerisation (chain length) is  $N = 200$ . This is long enough to reveal the polymeric features of the system, and does not give too long computation times. The chains are grafted to the surface with a grafting density  $\sigma^* < \sigma < 1$ . The lower limit,  $\sigma^* \sim 1/N$  represents the overlap grafting density, below this value uncharged chains are separate "mushrooms". Mushrooms do not interact and thus do not obey to the definition of a polymer brush. The upper limit is a fully packed polymer layer. The default value for the grafting density is  $\sigma = 0.2$ . One may argue that such a high grafting density is not easily obtained in experimental systems. As this may be true for polymer brushes in good solvents, it may be possible to reach high grafting densities when the brushes are in poor solvents. Moreover, as we will see, the variation of this parameter over a wide range does not affect the overall behavior of the system too much. The high grafting density allows us to worry less about the lateral structure of the brushes that might develop in collapsing brushes at lower grafting densities.

In the default case the grafting surface has hydrophobic properties. This is done to provide good wetting conditions of the surface by the polymer chains. The Flory-Huggins interaction parameter between the surface and the solvent is set to  $\chi_{sw} = 1$ , making the surface effectively wanting to "hide" behind the polymer. Additionally the attraction of hydrophobic polymer segments to the surface is introduced:  $\chi_{sp} = -1$ . This condition provides complete elimination of a depletion gap which is normally present in the proximity of a surface due to lack of conformational degrees of freedom. A slightly lower affinity for the charged/chargeable groups with the surface is implemented  $\chi_{sc} = -0.5$  which is consistent with the hydrophobic nature of the surface.

The chains can be one of the two types: quenched or annealed. In both cases they contain a fraction  $\Phi = 0.25$  of charged or chargeable groups and thus the default polymer has maximum of  $200/4 = 50$  charged groups

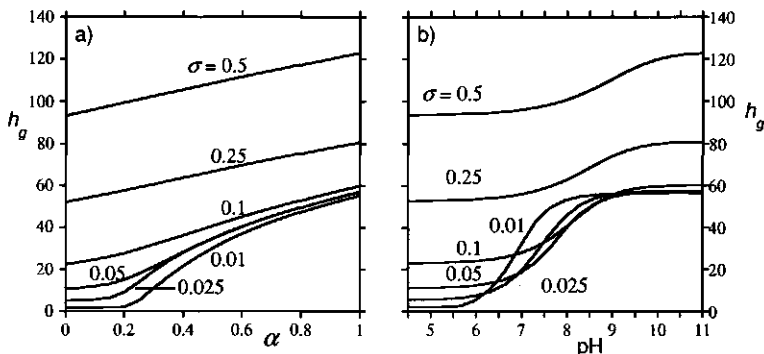


**Figure 3.3:** a) The height of the quenched brush,  $h_g$  as a function of the charge on the C segment  $\alpha = \nu_C$ . b) The height of the annealed brush as a function of the pH. The different values for the grafting densities are indicated. All other parameters have their default value.

regularly distributed along the chain. Hence the sequence of segments is  $(X)1((P)_3(C)_1)_{N/4}$ , where X is the grafting segment, P is the uncharged (apolar) segment, C a charged or chargeable segment placed in theta-conditions,  $\chi_{CW} = 0.5$ . In the annealed case, the average charge on C depends on the pH. In the quenched case we put a fractional charge  $\nu_C$  on the segment C (below we will also use the quantity  $\alpha$  to denote to this fractional charge of the C segments). The value of  $\nu_C$  in the quenched polymers is typically chosen so that the quenched and annealed chains can be directly compared. In the annealed case the ionic groups can be either protonated or deprotonated, thus the valency on each group can be either zero  $\nu_{C1} = 0$  or negative unity  $\nu_{C2} = -1$ . The frequency of occurrence of these states depends on the surrounding conditions, so that some segments are charged, while others are deionized. As explained above, the pH of the solvent and the local electrostatic potential affects the degree of dissociation of the ionizable groups. For the default case we have chosen for  $pK_A = 5.3$ , this roughly corresponds to a carboxylic acid. The remaining fraction  $1 - \Phi = 0.75$  of the polymer segments is hydrophobic, with a default polymer-solvent interaction parameter set to  $\chi_{PW} = 1$ .

For simplicity reasons all other FH interaction parameters (i.e., those that involve the ions) have the default value of zero.

The brush system is immersed in a bulk polar solvent which also contains salt in a molar concentration  $C_s$ . Note that the values for pK, pH and salt concentrations in this work mostly do not have round values, as one would

expect in a theoretical analysis; instead the dimensionless quantities used in the modeling have these round values. This issue originates from the lattice nature of the model: in the calculations we express all the concentrations in volume fractions rather than in moles per liter. The transition to moles per liter is then done by multiplying volume fractions by the amount of moles of "water" in a liter, that is roughly 5 in our case due to lattice site volume of  $(0.7\text{nm})^3$  instead of  $(0.31\text{nm})^3$ , which is the volume of a real water molecule (and would result in a conversion factor of 55). As all the (monomeric) molecular species in our system are considered of the same size, namely the size of the lattice site, the transition to moles per liter could not be absolutely accurate, so the values presented on the plots and in text have a comparative and a qualitative character rather than a strict quantitative one.

The default value for the salt concentration is  $C_s = 5 \times 10^{-4}$  M, or equivalently  $\varphi_s^b = 10^{-4}$ . This means that in the default system virtually no added salt is present.

The dielectric constant in the system is fixed to  $\epsilon = 80\epsilon_0$  where  $\epsilon_0$  is the dielectric permittivity of vacuum. The temperature is fixed to room temperature  $T = 298.15$  K.

### 3.4.2 Results and Discussion

In the case of PE brushes of chains homogeneously grafted onto a flat substrate, it is reasonable to average the volume fractions along layers parallel to the surface. This means that we have only one gradient direction. We will use the  $z$ -coordinate for this (see figure 3.2a). The lateral homogeneity should not always be taken for granted. In this section, however, we will impose the lateral homogeneity and further on we will pay attention to the possible lateral structure that may develop. Here we thus implement the one-gradient approximation and mention that in this approach all quantities will be normalised per unit area. In the following there is a clear focus on those properties of the PE brushes that are, at least in principle, measurable.

In figure 3.3 we present the variation of the brush height (as measured by the first moment over the end-point distribution (cf eqn 3.36) upon charging up the brush, both in the quenched (fig. 3.3a) as well as in the annealed (fig. 3.3b) case. It is clear that upon swelling the brush height increases in a non-trivial way. Indeed, upon the addition of the charge the so-called collapse - swelling transition occurs. In these figures we present results for several grafting densities. Though in both cases the increase in the effective charge leads to the swelling of the brush, the way this swelling occurs is rather different. In the annealed case the transition is S-shaped at any grafting density. The swelling occurs as a sharper transition and occurs at lower pH

values at low densities. We realise that with increasing grafting density we place charged groups closer to each other and at high grafting density the brush cannot make as dramatic changes in the distances between charges as in the low grafting density regime. Indeed, the situation is similar to that of a single polyelectrolyte: the more frequent the charges are along its backbone, the more gradual is, e.g. the titration curve.

We note that the height of the brushes at low grafting densities ( $\sigma < 0.1$ ) converge to almost the same value. This is a specific feature of a hydrophobic PE brush: chains in a brush with a very low grafting density are stretched by the interactions of the charges on the same chain. This is in contrast to a classical (neutral) brush case when the neighboring chains stretch each other due to the inter-chain excluded-volume interactions. As the stretching is due to intra-molecular effects, the addition of a new chain does not affect the rest. For high grafting densities however, the maximum stretching becomes a strong function of the grafting density because now inter-molecular interactions play an important role as well.

In the quenched case, fig. 3.3a, the height of the brush as a function of the degree of charging tends to be more linear, especially at higher grafting densities, than in the annealed brush. Indeed, when the system has an extra degree of freedom to adjust its charges along the contour, the transition is sharper. In other words if the charge density along the contour is fixed (quenched brush) the system is forced to respond more or less proportional to the charge density. Interestingly, if we plot for the annealed case the height as a function of the average charge (and not as a function of the pH), the two figures are very similar. This shows that it is of interest to know how the charge develops in an annealed PE as a function of the pH.

In figure 3.4 we give the so-called charge titration curves for the annealed PE brush for different values of the grafting density. In such graph we plot the average degree of dissociation  $\alpha$  as computed from eqn 3.37 as a function of the pH. Indeed such titration curves are of interest because upon the change of the pH the system undergoes the collapse - swelling transition. Even though rather dramatic changes take place in the brush (as illustrated by fig. 3.3 and other results discussed below), the titration curves are very smooth. Quite naturally the degree of dissociation is low for  $\text{pH} \ll \text{p}K_A$ , and has a limit of unity for high pH values. It is important to mention that with increasing grafting density the charging up of the brush occurs over a larger pH interval, i.e., the curves are more smooth. From this plot we can determine an effective dissociation constant  $\text{p}K_{\text{eff}}$ . We define this value as the pH at which half of the C segments are dissociated. The effective dissociation constant is presented as a function of grafting density in the inset of fig. 3.4. From this inset we see that the denser brushes dissociate at higher pH.

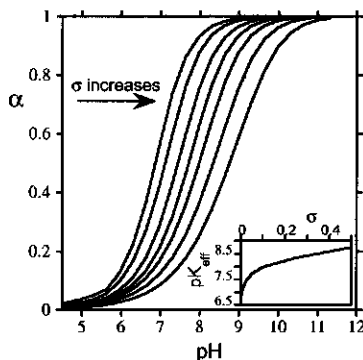


**Figure 3.4:** A set of pH titration curves, defined by the overall degree of dissociation of the chargeable  $C$  groups in the chain as a function of the pH, for an annealed hydrophobic PE brush for several different grafting densities ( $\sigma = 0.005, 0.01, 0.025, 0.05, 0.1, 0.25, 0.5$ ). In the inset the effective  $pK_{eff} = pH(\alpha = 0.5)$  is plotted as a function of the grafting density.

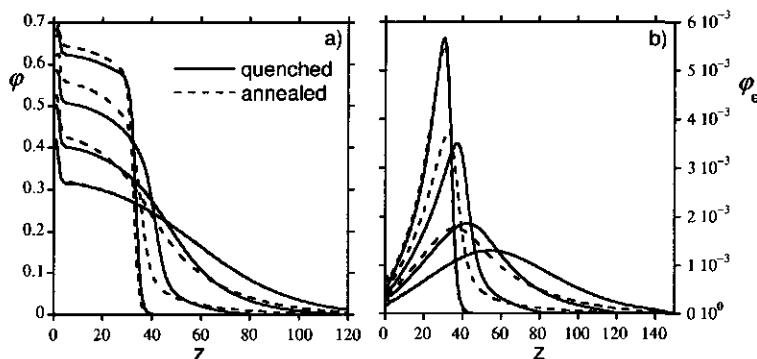


**Figure 3.5:** a) The overall volume fraction of the polymer chain  $\varphi(z) = \varphi_P(z) + \varphi_C(z)$  as a function of the distance from the surface. b) The volume fraction profile for the end-segment of the grafted polymer chains  $\varphi_e(z)$ . In both graphs we have results for a brush with quenched charges with  $\alpha = 0.05, 0.3, 0.6, 1.0$  (solid lines), combined with the corresponding brush with annealed charges  $pH = 4.3, 7.3, 8.3, 9.3$  (dashed lines). All other parameters have their default values.



At this stage it is of interest to inspect the structure of the brush in somewhat more detail. In figure 3.5a we present the overall volume fraction profile for the polymer segments for corresponding quenched and annealed brushes, and in figure 3.5b we show the corresponding distributions of the free ends. We have carefully selected systems such that the average degree of dissociation ( $\alpha$ ) in the annealed case is close to that fixed in the quenched cases.

Inspection of these figures reveals that only a strongly charged brush ( $\alpha = 1$  or  $pH = 9.3$ ) becomes stretched and swollen, whereas brushes with a lower charge density are in essence collapsed with only a minor part of the chains forming a long and effectively charged tail. In the collapsed region of the brush the hydrophobic interactions are dominant, whereas in the tail, that is the dilute outer part of the brush, the electrostatics plays the most important role. Note that as the quenched brush is homogeneously charged, the tail in this case is shorter, and the collapsed interior has a lower density than that of the annealed brush. The latter is due to the counterions which have to penetrate into the interior of the brush to neutralize the fixed charges. These small ions swell the quenched brush at given salt concentration as they generate a local high osmotic pressure. In contrast, in the annealed case the interior is not charged at all (see figure 3.8 below). As a result there are no ions needed to compensate the charges and thus there is no extra built-up of osmotic pressure. Consequently, the tendency to collapse is larger for the annealed brush.

The differences between the two cases (quenched versus annealed) become almost invisible in the extreme cases of low and high degrees of ionization. This is due to the similarities in the configuration of charge along the chains in these regimes.

The overall conclusion from the results presented thus far is that the differences in the quenched and annealed cases are not extremely large, though the addition of an extra degree of freedom to the system allows for a better response to changing conditions.

We now switch our attention to the effects of the molecular weight of the grafted polymers. The annealed and quenched cases are considered separately. We start in figure 3.6 with the overall volume fraction profile and the end-point distributions in the quenched brush for three values of the chain length and three values for the fraction of charges  $\alpha = \nu_C$ . All profiles extend further in the  $z$  direction upon the increase of the length of the chains. In the brush regime a linear dependence of the brush height with the degree of polymerisation is anticipated (see fig. 3.9 below) and thus the profiles in the normalised coordinate  $z/N$  should look similar. Inspection shows that the overall volume fractions as shown in fig. 3.6a indeed follow

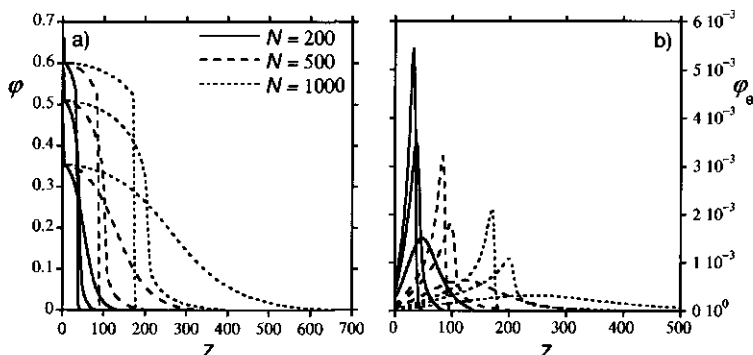


**Figure 3.6:** a) The overall volume fraction of the polymer chain  $\phi(z)$  in a brush with quenched charges as a function of the distance from the surface. b) The volume fraction profile for the end-segment of the grafted polymer chains  $\phi_e(z)$ . The degree of polymerisation  $N$  is indicated. For each chain length we varied the valency  $\alpha = 0.1, 0.3, 0.8$ . Curves with the higher charge densities have contributions at higher  $z$ -values. The grafting density is fixed to  $\sigma = 0.1$ . All other parameters have their default values.

this dependence. When we move our attention to the end-point distributions shown in fig. 3.6b we should realise that the number of end points in the system is given by the grafting density  $\sigma$ . This means that the integral of the end-point distributions is the same for all these graphs ( $\sigma = 0.1$ ). As longer chains extend over larger distances, it is natural that the end-point densities scale down proportional to  $N$ . In other words the distributions should overlap when plotted as  $N\phi_e(z/N)$ . Such effect is observed indeed.

In figure 3.7 we present the corresponding data for the annealed brush, where the pH in the solution is the control parameter. Comparison of fig 3.6 with fig. 3.7 reveals again that the annealed brush has a slightly higher density in the interior than the quenched one. One notable feature of the overall volume fraction profiles for the annealed case is the abrupt boundary between the collapsed part of the brush and the swollen tail. The interface becomes sharper at higher values of  $N$  and for intermediate values of the pH. This interface is like a second flat hydrophobic surface onto which the charged tails are sparsely grafted. The existence of this additional interface gives rise to the appearance of a bimodal distribution of the tails which will be presented and discussed in more detail below.

Figure 3.8 presents the unique feature of the annealed brush: its exterior is charged to a much higher degree than its interior. At a high pH however the interior is not completely uncharged. The reason is that the electrostatic

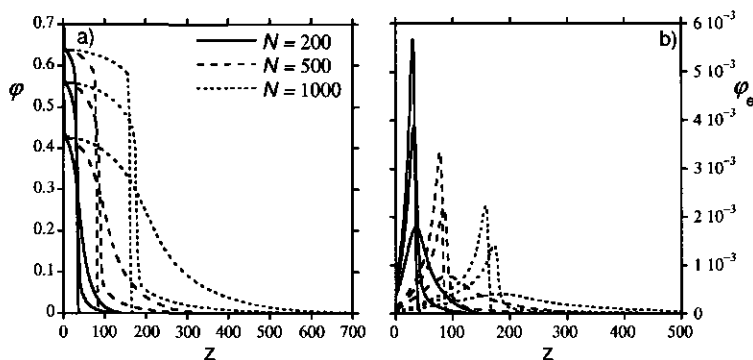


**Figure 3.7:** a) The overall volume fraction profile  $\phi(z)$  in a brush with annealed charges. b) The volume fraction profile for the end-segment of the grafted polymer chains  $\phi_e(z)$ . The degree of polymerisation  $N$  is indicated. For each chain length we varied the pH of the solution  $\text{pH} = 5.3, 7.3, 8.3$ . Curves with the higher pH have contributions at higher  $z$ -values. The grafting density is fixed to  $\sigma = 0.1$ . All other parameters have their default values.

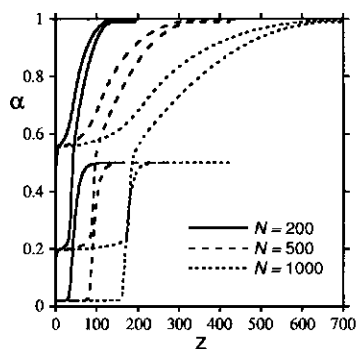


**Figure 3.8:** The degree of dissociation of the chargeable groups as a function of the distance to the surface. The degree of polymerisation  $N$  is indicated. For each chain length three pH values are considered. From bottom to top:  $\text{pH} = 5.3, 7.3, 8.3$ . The grafting density is fixed to  $\sigma = 0.1$ . All other parameters have their default values.

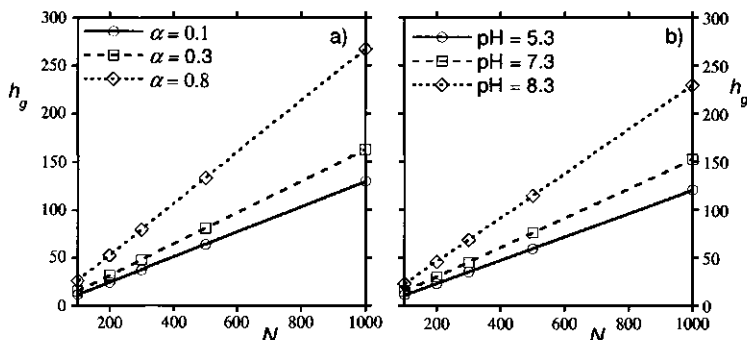


**Figure 3.9:** The brush height  $h_g$  measured as the first moment over the end-point distribution as a function of the degree of polymerisation  $N$ ; a) for the quenched brush for three values of the valency of the C units as indicated, b) for the annealed brush for three values of the pH as indicated. All other parameters have their default values.

potential, which is high in the collapsed region of the brush, will only suppress the charges with respect to that in the bulk. This means that the annealed brush can choose to compensate the brush charges by inviting small counterions to be in the brush or to take up a proton. For high pH it will use both options. As a result, at high pH, the quenched and annealed brushes behave in a very similar manner.

Above we already anticipated that various brush characteristics should scale with the degree of polymerisation. That this remains true for a partially collapsed PE brush is not trivial. In figure 3.9 we show that the anticipated linearity is indeed found for the brush height  $h_g$ , for both the quenched and annealed cases. The slope of  $h_g(N)$  is a strong function of the (average) charge density in the brush. The increase of the slope with increasing charge density shows that the chains either are collapsed (and the chain is in the dense part of the brush) or it is extended and has its segments in the tail. It is reasonable that both regions in the profile grow proportional to  $N$  (cf figs. 3.6,3.7) and thus the average height will also scale proportional with  $N$ . If there would be many mixed chain conformations, i.e., part of a given chain is in the collapsed part and another part of the chain is in the tail, there is no easy mechanism to recover a linear scaling with  $N$ .

The grafting density, that is the number of chains per unit area, is a parameter that is, at least in principle, under experimental control. That is why it is also of interest to present the response of the brush upon changes of the grafting density. We will again split the results in a graph that is

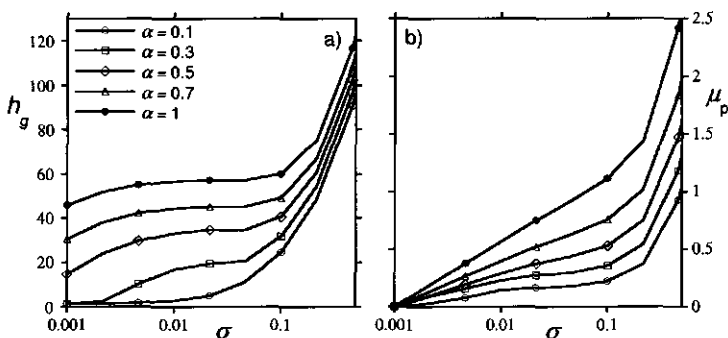


**Figure 3.10:** a) The brush height  $h_g$  measured as a function of the logarithm of the grafting density  $\sigma$ , b) The chemical potential of the grafted chains  $\mu_p$  as a function of the grafting density. The brush is composed of chains with quenched charges and the degree of charging of the C segments is indicated. All other parameters have their default values.

dedicated to the quenched brush (fig. 3.10) and a corresponding one to the annealed brush (fig. 3.11). In both figures the figure (a) presents the height of the brush and the view graph (b) gives the chemical potential of the grafted chains as a function of the grafting density.

Comparison of annealed and quenched brushes reveals a significant difference at low grafting densities: in the quenched case the height always increases with increasing grafting density, whereas for the annealed brush the height can diminish upon an increase in the grafting density. This occurs at values of pH close to the  $pK_{eff}$ . This phenomenon is a direct consequence of the possibility to vary the degree of dissociation in the annealed brush (see also fig. 3.13b below). At low grafting densities there is not enough material to form a compact layer, in which hydrophobic interactions will dominate. This puts a quenched brush into a very unfavorable intermediate condition: segments are sparsely charged, but the chains still have a large number of contacts with the surrounding water. The annealed brush simply charges completely. With increasing grafting density, the possibility for the annealed brush to form an uncharged collapsed layer presents itself; this decreases the overall height. A further increase in the grafting density leads to the elimination of the differences between the two types of brushes.

In figures 3.10b and 3.11b we present the chemical potential of the grafted polymer chains as function of grafting density. Quite arbitrarily the chemical potentials are normalized to zero for the grafting density  $\sigma = 0.001$  and are plotted in units of  $k_B T$  per segment, i.e.,  $\mu_p \equiv \frac{1}{k_B T} (\mu_i - \mu_i(\sigma_i = 0.001)) / N_i$

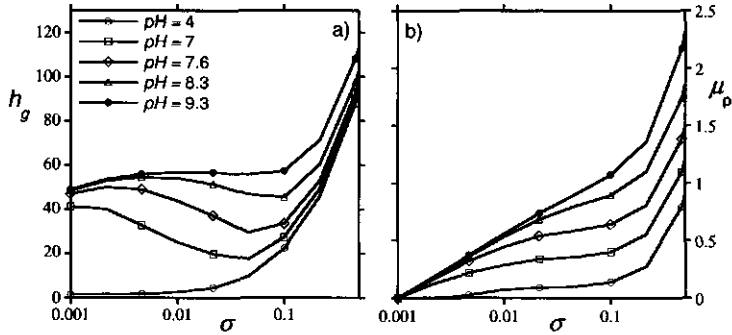


**Figure 3.11:** a) The brush height  $h_g$  evaluated as a function of the logarithm of the grafting density  $\sigma$ , b) The normalised segment chemical potential in units of  $k_B T$  of the grafted chains  $\mu_p$  as a function of the grafting density. The brush is composed of chains with annealed charges and the degree of charging of the C segments is controlled by the pH. The values of the pH are indicated. All other parameters have their default values.

with  $\mu_i$  given in Eqn 3.34.

We see that for both brushes the segment chemical potential is an increasing function of the grafting density. This implies that the system is stable and that the brush is expected to remain laterally homogeneous. For an instability against the formation of regions along the surface with lower and other regions with higher grafting density, we should have had a negative slope of the chemical potential as a function of the grafting density. The lateral segregation of the brush happens in the case of repulsive or neutral polymer-surface interactions and this effect will be discussed below in section 3.8. We recall that in the default parameter settings the interactions with the substrate are chosen such that the polymer wets the surface. The drop of the brush height upon an increase in  $\sigma$  as shown in fig. 3.11a is therefore not due to some lateral thermodynamic instability, but rather must be attributed to the collapse transition which, in the present parameter setting, occurs homogeneous along the surface.

The nature of the collapse-stretch transition becomes more clear when we consider the overall volume fraction profiles and the corresponding end point distributions on a logarithmic scale. In figure 3.12 we compare once again the quenched (view graph a) with the annealed case (view graph b). The advantage of plotting the profiles on the logarithmic scale is that the very dilute tails that are present at low grafting densities, can be investigated. Now the differences between the two brushes become more clearly visible.

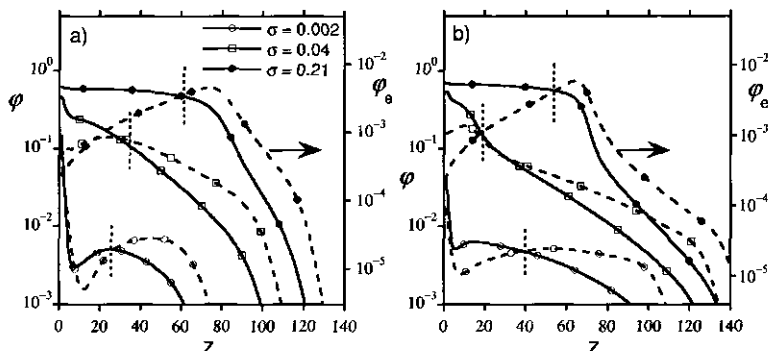


**Figure 3.12:** Overall volume fraction profiles (continuous lines and left ordinate) and end-point distributions (dashed lines and right ordinate) on the logarithmic scale. a) quenched brush with  $\alpha = 0.5$  b) annealed brush with  $\text{pH} = 7.6$ . Three values of the grafting density are indicated. The small vertical dashed lines represent the heights  $h_g$ . All other parameters have their default values.

As mentioned above, the quenched brush does not protrude as far into the solution as the annealed one and the difference is large for low grafting densities.

In these graphs (fig. 3.12) we take the opportunity to indicate where in the profile the estimate of the overall height of the brush as expressed by  $h_g$  is located. The short dashed lines are positioned at these height values. It is clear that the first moment over the end-point distribution does not give the true periphery of the brush. This point may well be a factor two further out. Nevertheless  $h_g$  may be used for comparative studies.

From polymer adsorption theory we know that the end-point distribution has a special meaning. The integral over this quantity is directly related to the chain partition function. If the position of the end point is seen as an order parameter, we can interpret  $F(z) = -k_B T \ln \phi_e(z)$  as a Landau free energy as a function of its (end-position) order parameter. Now, if the end-point distribution is not monotonic, i.e., if it has a local minimum, as is the case in fig. 3.12 for the low grafting density  $\sigma = 0.02$ , we may envision a scenario that there is a phase transition with a local energy barrier separating the two (locally) stable states. Indeed, the local minimum in the end-point distribution points to a gap in the distribution of conformations. Some types of conformations are especially unfavorable. Such a phenomenon suggests that the collapse/swelling transition has first-order features. We haste to mention that a true first-order transition can only be expected in the limit of infinitely long chains and in our case the barrier separating the local minima

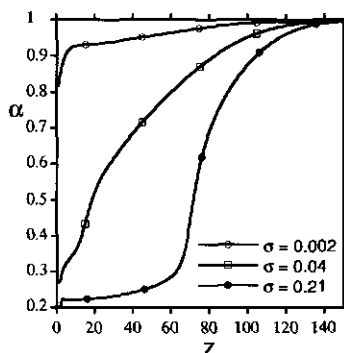


**Figure 3.13:** The degree of dissociation  $\alpha$  as a function of the distance from the surface for three values of the grafting density as indicated for the case of an annealed brush with  $\text{pH} = 7.6$ . All other parameters have their default values.

is not infinitely high and fluctuations over the barrier are possible (and do occur). Hence the transition remains smooth.

In figure 3.8 we already shown examples of how the degree of dissociation varies in an annealed polyelectrolyte brush, where the effect of the degree of polymerisation was examined. In figure 3.13 we pay once again attention to this property and consider how this profile changes when the grafting density is varied. The results of fig. 3.13 correspond to the system presented in fig. 3.12b. At low grafting density the brush is mainly in the swollen state and only very close to the surface we find that the chains tend to lower their charge somewhat. For higher grafting densities more and more of the chains are in the collapsed state and the dense region extends to significant distances away from the surface. In this region the chains have significantly fewer charges than at the brush periphery.

The next step of our investigation focuses on the response of quenched and annealed PE brushes to a change in the solvent quality. Experimentally, it may be clear that the PE chain is in a poor solvent, but it may appear difficult to estimate how poor the solvent really is. For this reason it is important to understand what changes are expected upon lowering of the solvent quality. The first point of interest is to show how the volume fraction profiles and the end-point distributions are affected.

As seen from figures 3.14a,b lowering the solvent quality results in a gradual transition of the brush from a swollen to almost fully collapsed state. The distinctive feature in the transition of the quenched and annealed PE brushes is that the annealed one retains an effectively charged, though extremely dilute tail even at higher values of the polymer - solvent interaction



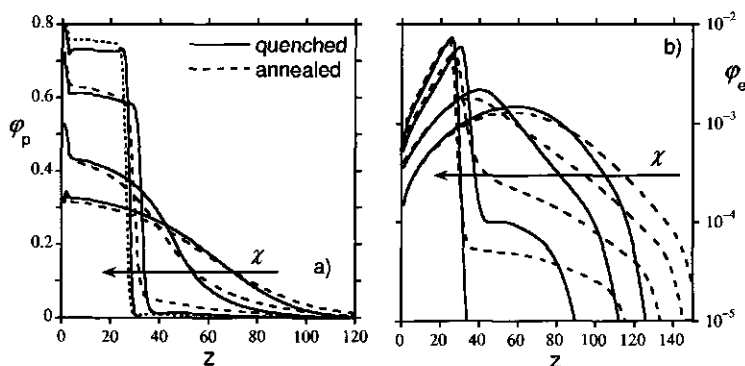


**Figure 3.14:** a) The overall polymer volume fraction profile and the end-point distribution (on logarithmic scale) for both annealed (dashed line and  $\alpha = 0.5$ ) and quenched (solid line and  $\text{pH} = 8.3$ ) PE brushes. Three values for the polymer-solvent interaction parameter are used,  $\chi_{PW} = 0.5, 1, 1.5, 2$ . All other parameters have their default values.

parameter  $\chi_{PW}$ . Indeed, at  $\chi_{PW} = 1.5$  both brushes still have an effectively charged tail, which is illustrated in fig. 3.14b. These matters change for stronger non-solvent conditions, i.e., at  $\chi_{PV} = 2$ : the annealed brush still has the tail, whereas the quenched one is fully collapsed. Apparently, at high values of  $\chi_{PW}$  the presence of a tail at the brush-water interface is favored over a full collapse; in fact the tail is highly charged (close to  $\alpha = 1$ ). The corresponding quenched brush is only partially charged,  $\alpha = 0.5$ , and this is apparently not enough to make protrusions of the tails into the water phase.

As the poor solvent conditions provide the driving force for the collapse transition, it is natural to investigate the collapse/swollen transition as a function of the solvent quality and compare this with the same transition for neutral polymers. From figure 3.15 it follows that the collapse transition is rather smooth, in any case much more smooth than in the corresponding neutral brush case,<sup>91,92</sup> and the transition is very similar for the quenched brush and the annealed brush (provided the average degree of charging is approximately the same). The collapse transition, as judged from the drop of the height of the brush upon the worsening of the solvent quality, shifts in the direction of poorer solvents when the charge density in the PE brushes is increased. This is expected because the charges provide a repulsive interaction preventing the close packing of the chains. The bare second virial coefficient  $v_{\text{bare}} = 1 - 2\chi$  is clearly negative (order  $-5$ ). To estimate the electrostatic contribution we might evaluate the electrostatic virial coefficient

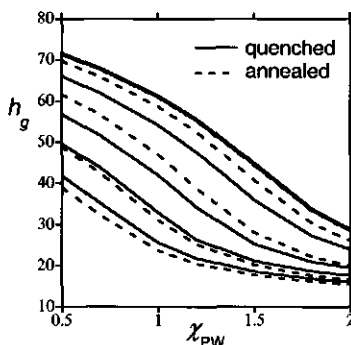


**Figure 3.15:** The height of the PE brush  $h_g$  as a function of the solvent quality given by the value of  $\chi_{PW}$  for charged brushes with quenched (solid lines) and annealed (dashed lines) charges. Corresponding sets of (pH (for annealed brush),  $\alpha$  (for quenched brush)) = (5.3, 0.1) (7.3, 0.3) (8.3, 0.5) (9.3, 0.8) (10.3, 1) for pairs of curves from bottom to top. For the highest charge densities the difference between the annealed and quenched lines is barely visible. All other parameters have their default values.

from  $v_e = (f\alpha)^2/C_s$ . In our case the fraction of segments that carry a charge  $\Phi = 0.25$  and  $C_s = 5 \times 10^{-4}$ , and thus  $v_e$  is typically of order 10 or smaller. From this we may understand that the transition strongly shifts to larger values of  $\chi_{PW}$  with increasing  $\alpha$  or increasing pH. It is hard to make this analysis more precise because the transition is so smooth.

To bring the analysis of the flat PE brush to a close, we present in the last three plots of this section the response of the PE brushes to variations in the ionic strength. We start with the quenched case. In figure 3.16a we show that the height of the brush is mostly a decreasing function of the ionic strength. Only at high ionic strength there is a small increase in the height. This is an artifact of our set of parameters. The polymer units are in a poor solvent, which is reflected in the value of  $\chi_{PW} = 1$ . However, with increasing ionic strength the solvent quality gets gradually better because the interactions of the polymer units with the ions is kept athermal. As we are not so much interested in the high ionic strength regime, we accept this feature.

The response of the brush height on the salt concentration depends on  $\alpha$ . At high charge fractions ( $\alpha > 0.5$ ) the brush is, at low salt concentration, swollen by the osmotic pressure of the counterions. When the ionic strength in the bulk becomes comparable to that in the brush, the brush height gradually relaxes to lower values. The reason is that difference in osmotic pressure of the counterions in the brush and the osmotic pressure outside the

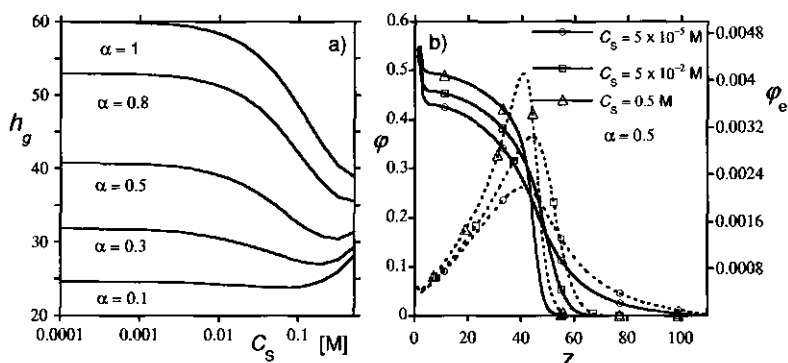


**Figure 3.16:** a) The height of the PE brush  $h_g$  as a function of the ionic strength  $C_s$  in mole per liter for the quenched PE brush. The degree of dissociation of the C segments is indicated. b) the polymer volume fraction profile (solid line and right ordinate) and the end-point distribution (dashed line and left ordinate) of quenched PE brushes with fixed  $\alpha = 0.5$  and for three values of the ionic strength as indicated. All other parameters have their default values.

brush decreases. Thus the driving force for swelling decreases. The response of the brush height can be rather large because the poor solvent conditions may drive the brush from the swollen into the collapsed state. As poorly charged brushes are already collapsed at low salt concentrations, for low  $\alpha$  the brush height remains almost constant with increase in salt concentration.

A small selection of overall volume fraction profiles as well as the end-point distribution profiles are shown in figure 3.16b. We have selected the case that  $\alpha = 0.5$  and give results for a wide range of ionic strength conditions. The profiles show that there is a gradual change in brush structure with increasing ionic strength. The dense region of the brush gets a bit more dense and the tail becomes less extended. The end-point distributions are consistent with this and become more sharp with increasing ionic strength, implying that more and more end-points are found at the interface between the dense part of the brush and the aqueous solution.

The salt concentration dependence is somewhat different for an annealed brush (see figure 3.17). Here, at very low salt concentrations the brush is hardly charged, thus retaining electroneutrality by capturing the more abundant hydrogen ion instead of a salt one. As the hydrogen ions our model are connected to water molecules, they have the same solvency effects as water. As can be seen from the polymer and dissociation profiles (fig. 3.17b and fig. 3.18) in the low salt limit the brush is essentially collapsed,

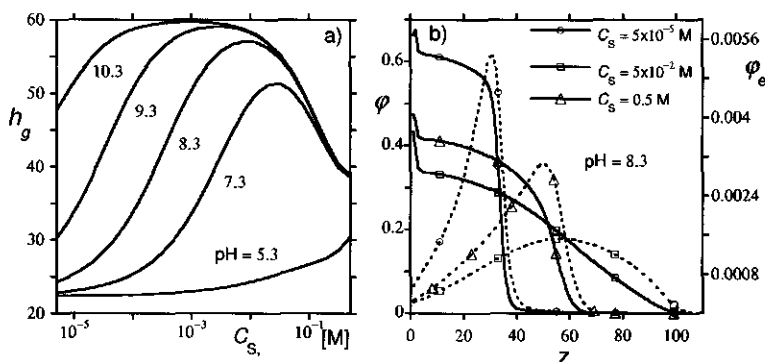


**Figure 3.17:** a) The height of the PE brush  $h_g$  as a function of the ionic strength  $C_s$  in mole per liter for the annealed PE brush. The pH of the solution is indicated. b) the polymer volume fraction profile (solid line and left ordinate) and the end-point distribution (dashed line and right ordinate) of annealed PE brushes at fixed pH = 8.3 and for three values of the ionic strength as indicated. All other parameters have their default values.

and there is only a very dilute charged tail at the exterior. Upon increasing the ionic strength the ionisation becomes possible. A pronounced maximum of the swelling occurs due to ionization of the C units at all ionic segments. The further increase in salt concentration is not accompanied by a built-up of extra charges. Instead the charges are screened and similarly as in the quenched brush a decrease in brush height will take place when the ionic strength outside the brush resembles that of the brush interior. With the decreasing osmotic pressure difference between outside and inside with increasing ionic strength the brush height decreases naturally and universally, i.e., independent of pH. The maximum of the brush height increases and also occurs at lower ionic strength with increasing pH.

For very low pH, the brush is unable to pick up many charges and the growth of the brush height only occurs at very high ionic strength. Again, we should be aware of the fact that for these high ionic strength systems the solvent quality becomes (by choice of our parameters) an increasing function with ionic strength.

Inspection of the selection of the overall volume fraction profiles as well as the corresponding end point distributions indicates that for the default parameter set the transition from collapsed to swollen state can also be induced by increasing the ionic strength. The degree of dissociation of the same system is presented in fig. 3.18 which is consistent with this picture.

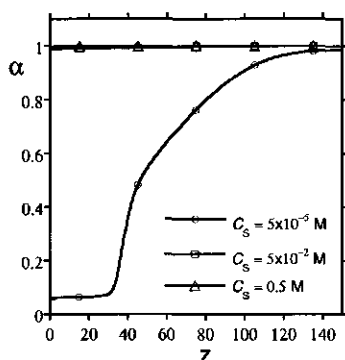


**Figure 3.18:** The degree of dissociation of C units in the polymer chains as a function of the distance from the surface for the annealed PE brush at fixed  $\text{pH} = 8.3$  and for three values of the ionic strength as indicated, i.e., for the system presented in fig. 3.17 All other parameters have their default values.

The very low ionic strength case,  $C_s = 5 \times 10^{-5} \text{M}$  reveals that the chains are extremely weakly charged up to layer  $z = 35$  and only charges up to almost unity in the periphery of the brush where a small tail exists. For the two higher ionic strength cases  $C_s = 5 \times 10^{-2}, 0.25 \text{M}$  the volume fraction profiles and end point distributions indicated a swollen layer and consistent with this we find that the degree of dissociation is high throughout the brush. The drop in the height of the brush at higher ionic strength is therefore not accompanied by a collapse of the brush. The brush relaxes from a swollen state (characteristic for a PE brush) to a parabolic brush (characteristic for a neutral brush).

In summary, we have presented detailed SCF predictions for the behavior of a single flat hydrophobic PE brush in a wide range of the parameter space. The following conclusions can be drawn which will be relevant for the further study of interacting brushes discussed below. The first conclusion is that there are noticeable differences between the weak (annealed) and strong (quenched) PE brushes, but that the overall behavior of these two systems is remarkable similar. For example both type of brushes can be in a two-phase state, when the charge in the chains is not too high. This is an important factor for the further investigations: we noticed that the study of interacting PE brushes requires significant computation times especially for cases where the polymer chains are not very short. As explained in the theoretical section of this paper, the case of PE brushes with annealed charges is met with even more computational difficulties than the quenched ones. As a result we will

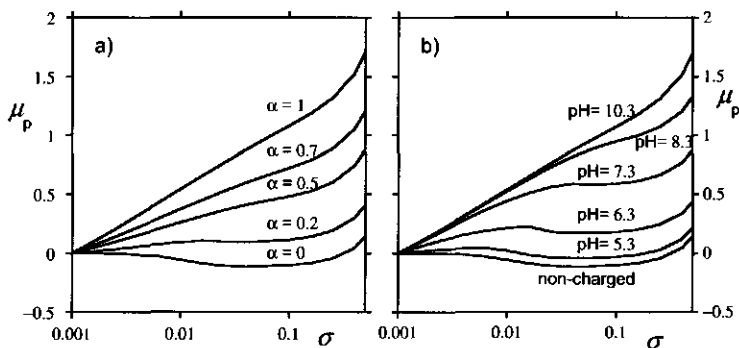


**Figure 3.19:** Normalised chemical potential per polymer segment in units of  $k_B T$  (i.e.,  $\mu_P(\sigma) - \mu_P(10^{-3})$ ) for quenched (a) and annealed (b) PE-brushes in poor solvent and in the absence of surface attraction.  $N = 200$ ,  $\Phi = 0.25$ ,  $\chi_{PW} = 1$ ,  $\chi_{SC} = \chi_{SP} = \chi_{SW} = 0$  and  $C_s = 5 \times 10^{-4}$  mol/L.

restrict ourselves to quenched systems especially when we consider the two-gradient problems.

The second relevant conclusion is that in most cases the PE brush forms a rather distinctive structure. There is a collapsed interior, where the hydrophobic interactions are dominant, and a very dilute charged tail, where the electrostatics plays a role. Guided by this structure we can anticipate the behavior of two brushes being compressed against each other: there should be an electrostatic barrier in the interaction potential which at further compression may be followed by merging of the brushes into a single structure. It is of interest to study the peculiarities of the confinement induced changes in the brush, not only for the approach of two flat PE brushes but also for other systems such as the compression of the bilateral brush and the confinement of the PE star.

Above we have assumed that the brush remains laterally homogeneous. However, for hydrophobic polyelectrolyte chains this may not always be the case. Before we commence with the colloidal stability issues, we pause to discuss the signatures of the lateral instability that can be extracted from the thermodynamic data of a one-gradient SCF approach.

## 3.5 Thermodynamic stability of the flat PE brush

### 3.5.1 Description and parameters

Above we pointed to the possibility that a hydrophobic PE brush can form some laterally inhomogeneous structure. Now we will consider this case in more detail. There are several ways to study this. The most natural way to investigate this issue is to introduce a two-gradient model and generate laterally inhomogeneous brushes. Such an analysis is possible but has many intricacies, especially when it is complemented by the proper thermodynamic underpinning. Here we choose to follow a simpler approach and consider brushes using a one-gradient model only. It turns out that the signatures for the occurrence of lateral inhomogeneities can be derived already from the analysis of the lateral homogeneous brushes. More specifically, one has to turn to the analysis of the chemical potential of the brush chains as a function of the grafting density. In analogy with adsorption isotherms, there may exist a van der Waals loop indicative for such a surface phase transition. Above in fig. 3.11b we have shown that in the default parameter set such a loop is not present. The goal of this short section is to show that such a loop can occur in our system especially when the polymers have significantly less affinity for the surface. Once again we will focus on those features that are important for the pair interactions that will be discussed below. For a detailed and rather comprehensive study we refer the reader to an excellent paper by E.B. Zhulina and coworkers<sup>31</sup> and to a recent letter.<sup>93</sup> These authors have studied the range of parameters for which the flat brushes becomes laterally inhomogeneous, paying still little attention to the brush structure for these systems. Below we do pay some attention to the volume fraction profiles.

The majority of the parameters used in this section are identical to those used in the first part of our study. Only the relevant parameters that determine the nature of the surface will be changed. More specifically, we will decrease the hydrophobicity of the surface and thus decrease the attraction of the polymer segments to the surface. We have two segments in the chains and to simplify the situation change the surface parameters for these two segments in concert and set the surface to be non selective for any segment, i.e.,  $\chi_{SC} = \chi_{SP} = \chi_{SW} = 0$ . We expect that in the absence of surface interactions the laterally homogeneous layer is no longer the ground state. The problem of marginal surface interactions is the common assumption in polymer brush theory and therefore there is much information for this case in the literature already (see references cited above). Therefore, we will only briefly discuss the main properties of such system with particular attention to the limits where inhomogeneous brushes occur.

### 3.5.2 Results and discussion

Let us first consider, by way of example, a non-charged hydrophobic brush. The brush structure that comes in mind first is that of a homogeneously collapsed one. If the surface is polymer-repelling, and hydrophilic, there also may be a layer of water at the interior. But what happens when there is not enough material to form a homogeneous collapsed high-density layer, in other words, the grafting density is not sufficiently large? The answer is to form so-called "pinned micelles",<sup>31</sup> which may be of spherical or elongated morphology depending again on the grafting density. One of the signatures for the instability of a homogeneously collapsed brush is that the polymer layer has a negative compressibility: a gradual increase of the density inside the brush layer leads to a better situation because this minimizes the unfavorable polymer-water contacts. One can observe such negative compressibility by studying the chemical potential of the grafted polymers as a function of the grafting density.

Switching attention from the stability of a brush composed of uncharged polymers to that of a charged one brings in the possibility to tune this behavior. Of course the range of the polymer-solvent interaction parameters for which the lateral inhomogeneity occurs will be subject to change. We must also anticipate that an increase in the degree of ionization of the polymer either set manually as for the quenched case or by changing the pH or salinity as for the annealed case, should promote the formation of a homogeneous brush. This trend is illustrated in figure 3.19. In this figure we plot the chemical potential of the PE chains as a function of the grafting density for the quenched (fig. 3.19a) and annealed (fig. 3.19b) cases over a range of degrees of dissociation. The bottom curves on both plots correspond to the uncharged hydrophobic brush, and the grafting density is plotted on a logarithmic scale. As expected the uncharged brush is most unstable. It has a region of negative compressibility, the chemical potential decreases with increasing grafting density, already at rather low  $\sigma$  values. In this region the laterally homogeneous structure of the brush is unfavorable. Further increase in grafting density  $\sigma > \sigma^{cr}$  results in a normal growth of the chemical potential with the grafting density. This means that at sufficiently packing density the PE-brush system is laterally homogeneous again. Note that the results of fig. 3.19 have been obtained within a one-gradient SCF calculation; when, e.g. in a two-gradient SCF analysis the non-homogeneous structure of the brush is allowed to develop, the chemical potential of the brush chains would of course not show such pronounced region of negative compressibility. The mean-field approximation in the one-gradient SCF analysis forces the negative compressibility in a similar way as van der Waals loops occur in



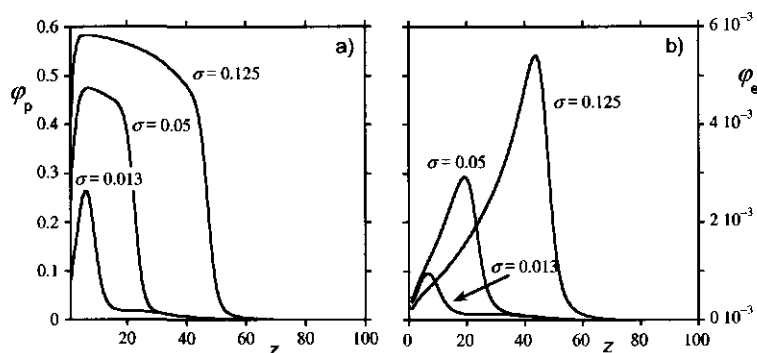


**Figure 3.20:** a) Overall volume fraction profiles for the polymer  $\phi_p(z)$ , b) corresponding volume fraction profiles for the free ends  $\phi_e(z)$  for a quenched PE brush with no polymer-surface interactions;  $\alpha = 0.2$ . Three values of the grafting density are indicated.

adsorption isotherms of molecules with strong lateral interactions.

As the brushes start to be charged, the overall picture develops as anticipated. Now, at very low grafting densities the slope of the chemical potential is in both quenched and annealed cases positive: sparsely grafted PE layers are stable against the development of a lateral inhomogeneous structure by their charges. This trend continues, provided the charge is high enough: strongly charged brushes are stable against lateral segregation for all grafting densities. In the regime of intermediate charge density, the features are slightly different for the quenched and annealed cases. The quenched brush needs just a few charges to become homogeneous throughout the grafting density range, whereas the annealed brush needs a rather high pH to remain stable. This difference in behavior is expected, as, once again, in an annealed brush the degree of dissociation along the chain can vary. The annealed chains can use this degree of freedom by making the parts of the chain that are exposed to the solvent highly ionized, whereas keeping the ones trapped inside the collapsed regions protonated. This difference may also be explained in another way: increasing the charge on the quenched brush is equivalent to a fixed reduction of the polymer-solvent interaction parameter along the chain, whereas in the annealed case the improvement of the solvent quality is not a constant along the contour of the polymer chain (in different regions of the brush).

In the following figures we will present the structural properties of the brushes at various grafting densities, in an attempt to obtain some further insight in the conformations of the PE chains. We haste to mention that

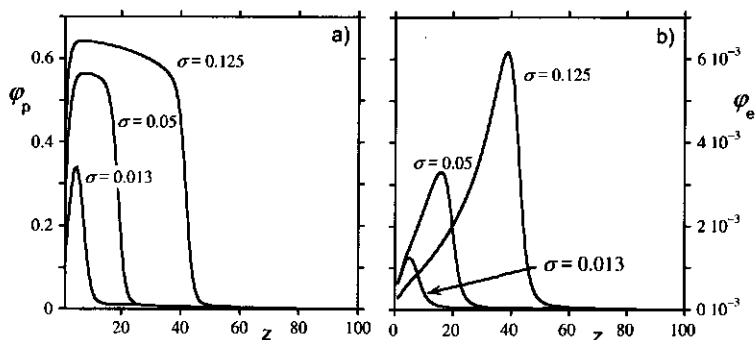


**Figure 3.21:** a) Overall volume fraction profiles for the polymer  $\phi_p(z)$ , b) corresponding volume fraction profiles for the free ends  $\phi_e(z)$  for an annealed PE brush with no polymer-surface interactions; pH = 6.3. Three values of the grafting density are indicated.

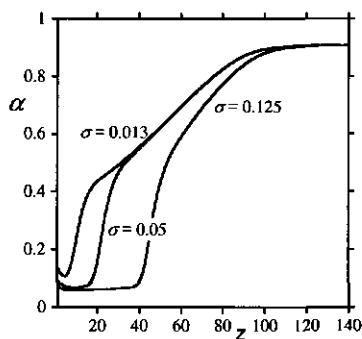


**Figure 3.22:** The profile of the degree of ionisation  $\alpha(z)$  for an annealed PE brush with no polymer-surface interactions at pH = 6.3. Three values of the grafting density are indicated.

the density profiles are realistic both at high and at low grafting densities, but at intermediate grafting densities the profiles must be interpreted as being averaged over a lateral inhomogeneous layer. In figures 3.20 and 3.21 we present the overall volume fraction profile and the distribution of the free ends in the quenched (fig. 3.20) and annealed (fig. 3.21) cases. Here we would like to point to the main differences in the two cases: while the profiles are rather similar, the annealed brush has a higher density in the collapsed part. Note that there is a depletion gap between the surface and the collapsed region which is due to the absence of polymer - surface attraction. In the annealed case the collapsed part of the brush is deionized, while both the interior (directly next to the surface) and exterior interface are charged. In fig. 3.22 we show the degree of dissociation of the segments for three values of the grafting density. The system with the highest grafting density suppresses the ionisation the most. Just near the surface the chains can dissociate slightly more than the collapsed region. We will present a more detailed discussion of the lateral inhomogeneous brush structure in the part of the paper where we study the interaction between two inhomogeneous brushes, which is done in a two-gradient SCF analysis (see section 3.8).

### 3.6 Interactions between two flat HPE brushes

Above we have extensively analysed the structural as well as the thermodynamical states of polyelectrolyte brushes with an apolar backbone. Brushes are typically administered in colloidal systems to modify the colloidal stability. The reason is that brushes dramatically influence the particles interactions. We recall that hydrophobic PE brushes may be of interest in applications, not because they are the natural choice to provide sufficient stability, but rather that these brushes can be used to provide some marginal stabilisation (e.g. in paint applications) and they provide antagonistic contributions. These involve contributions that make particles repel (charges) and those that bring them together (solvophobe). The remainder of this chapter is devoted to these interactions.

In this section we describe the forces that appear when two flat homogeneous hydrophobic polyelectrolyte brushes are pressed against each other. We will also pay attention to the internal structure that develops upon compression. The parameters of the system will be kept identical to the ones described in the first parameter section, i.e., we consider the case that the polymers are attracted to the surface such that the brush layers remain laterally homogeneous. Technically, the calculations are done as follows. One brush is placed at one side of the system and then (in steps) the system size is

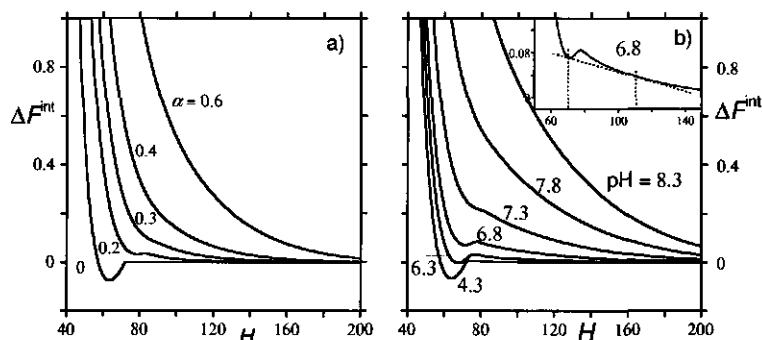


**Figure 3.23:** Free energy of interaction  $F^{\text{int}}(H)$  (in units of  $k_B T$  per unit area per brush) as a function of the distance between two flat brushes  $H$  (in units of lattice sites). a) The interaction between two quenched brushes; the degree of charging of the chargeable groups is indicated, b) the interaction between two annealed brushes. The pH is indicated. The inset is an enlargement of one of the curves of the annealed case (pH = 6.8). In this graph a common tangent line is plotted. All parameters have their default values (polymer units have affinity for the surface).

changed in such a way that the brush is confined. At the system boundary that compresses the brush, a reflecting boundary is present. Such boundary condition mimics the situation that two brushes with the double distance are pushed against each other. This approach of pushing a mirror boundary against a brush is proved to be exactly identical to the compression of a pair of brushes placed at a double distances. The method that is chosen requires significantly less computer times. This is relevant, especially in the case when the chains are long. Preventing the system to choose a different molecular structure near one surface compared to the other, may indeed be an approximation. Spontaneous symmetry breaking has been discussed by Leermakers and coworkers in the context of confined surfactant layers.<sup>94</sup>

In the following we will consider the free energy of interaction in units of  $k_B T$  per unit area per brush, as given by Eqn 3.35, versus the distance  $H$  between two brushes for chains composed of  $N = 200$  segments and a fraction  $\Phi = 0.25$  charged/chargeable groups. In figure 3.23 we present a comparison of two cases; on the left there are the results for a quenched system (fig. 3.23a) and on the right those for the annealed brushes (fig. 3.23b). The curves represent different fixed degrees of dissociation (fractional charge)  $\alpha$  (fig. 3.23a) or variable charge according to the indicated pH values (fig. 3.23b). The bottom curves represent brushes with little or no charge. In this case the two brushes fuse upon contact resulting in an energetically

favorable collapsed layer (free energy falls below zero). Indeed, prior to the compression of these brushes, they were already in a collapsed state, having an interface with the (poor) solvent. The result of the compression is that the interfaces between the brushes and the poor solvent are eliminated. Hence the interaction is strongly adhesive (attractive). In the annealed case there is still a very small barrier in the interaction curve prior to adhesion which is due to a few charges on the brush surface.

In the other extreme, i.e., the top curves in fig. 3.23, when the brushes are highly charged, the interaction force is purely repulsive: the brushes that are swollen by the osmotic pressure of the counterions are effectively in a good solvent and repel each other. The layer in this case provides excellent stabilizing properties. The repulsion already starts before the brushes physically overlap because there is an electric double layer on top of the brush. This double layer gives an exponential decaying free energy of interaction with the Debye length as the governing length scale.

The most interesting, both from a theoretical as well as a practical point of view, are the interaction curves falling in between the two extremes. The intermediate interaction curves are typically non-monotonic. Upon the approach of two brushes, first (at large  $H$ ) a repulsion between the two layers is found. This repulsion is due to the overlap of counterion clouds which gives an increase of the osmotic pressure of these ions. The repulsive force per unit area, which is the pressure needed for pushing the particles together is found by the derivative of the interaction curve, i.e.,  $f = -\partial F^{\text{int}}/\partial H$ . Upon a further compression of the brushes, the hydrophobic forces take the lead, and the free energy reduces with decreasing distance: the sign of the interaction force turns negative (attraction). A further compression leads to repulsion again. This repulsion is attributed to the finite compressibility of the brush.

It is not trivial to interpret such non-monotonic interaction curves. In fact, the exact interpretation depends on which variables are fixed in the system and which are allowed to vary. In principle one can envision two types of experiments, one type where the force is the control parameter and the other wherein the distance is imposed. In a constant force (pressure) ensemble, one can impose some force between the particles (by way of an osmotic stress experiment) and measure the resulting average inter-particle distance (particle concentration). In a controlled distance ensemble one measures the average forces for given imposed distances. In principle the latter experiments are feasible in a surface force apparatus or an atomic force microscope (AFM) experiment. In such AFM experiments, the full curves of fig. 3.23 may be found (provided that the spring allows for it). Indeed, while decreasing the distance, one first needs to push to reduce the

distance and than to pull to keep the distance to the specified value. In the fixed force ensemble it is not operational to fix the exact distance between all particles; in other words the interparticle distances can fluctuate. Indeed in such an experimental system the individual distances between the particles can fluctuate and the force that is felt by the particles (the colloid osmotic pressure) assumes some measurable value. For such a system it is not possible to have a region with a negative compressibility. Instead the osmotic pressure must be an increasing function with the decrease of the average particle separation.

The inset in fig. 3.23b presents a enlargement of the most interesting region in the free energy curves for an intermediate degree of ionization. In general, when in the fixed distance ensemble the free energy loses its monotonic character, it corresponds to the possibility of (macroscopic) phase segregation in a system of many colloids. In some region of the system the particles are still far apart and in other regions they are closer together; both phases have the same osmotic pressure. In this case a tangential line touching the free energy curve in two points can be drawn, the points where this common tangent touch will correspond to the two distances for which the osmotic pressures are the same. The two distances correspond to separated and fused brushes. As the two phases are in equilibrium with each other, the chemical potentials of all molecules in each phase are equal as well. If we now consider the free energy curve presented in the insert of fig. 3.23b, we see that the two phases correspond to brush separations of 112 and 70 layers. In this case the phase transition scenario develops as follows. If one is going to increase the osmotic pressure in a macroscopic system of interacting brushes, one will effectively reduce the (average) distance between the particles (increase the concentration), then when the distance reaches a value close to 112b, the system starts to separate into two phases: one dilute phase where the distance between the brushes remains fixed to 112b and a concentrated phase where the distance between the particles is 70b. Upon increasing the concentration the osmotic pressure in the system remains fixed and one just makes more of the concentrated phase at the expense of the dilute phase. Only after the dilute phase is gone, the osmotic pressure increases when the average particle concentration increases.

Alternatively, with some imagination one can consider two brushes grafted onto two flexible surfaces, such as some membrane. Then the segregation of the system could also occur in the lateral direction. Going along the surface one then finds regions where the distance between the two membranes is close to each other and other regions where these are far apart. Upon decreasing the average distance between the membranes the regions where the membranes are close to each other increase in frequency at the expense

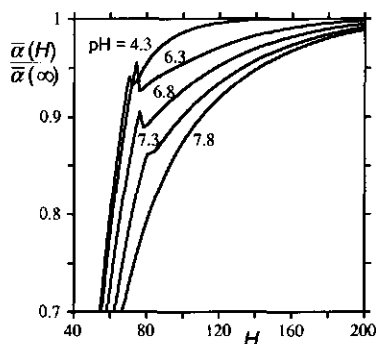


**Figure 3.24:** The overall degree of dissociation of chargeable groups  $\bar{\alpha}$  as a function of the distance between two annealed brushes ( $H$ ) normalised to the overall degree of dissociation of the chargeable groups when the brushes are far apart. The value of the pH is indicated.

of regions where the membranes are far apart. Finally, when all the distances are small, the osmotic pressure becomes an increasing function with decreasing distance between the membranes.

This type of behavior has been predicted for PE brushes that are in poor solvent conditions by Ross and Pincus<sup>33</sup> for a step - density brush model, and later Misra et al.<sup>34</sup> elaborated the overall picture with a self-consistent field model for the brushes, briefly describing the possible brush collapse as a continuous one. We would like to stress that according to our ideas the transition in the constant pressure ensemble is discontinuous, with two distinct stable phases, and a wide region of concentrations where part of the system is represented by the separated phase and the other part by the joined one. Such a discontinuous phase transition is of course only acceptable when the brushes are nearly flat (large particles) and that there are no possibilities for the brush to relocate a significant fraction of the chains in response to the interactions. For systems with small particles such possibilities may exist. We will consider such systems below and then we will argue that the transition may become smoother.

Before we continue to investigate the profiles that are typical for interacting brushes that feature a collapse transition, we like to present one more result, that is, the average degree of dissociation of groups in the annealed brushes upon compression, relative to that at infinite separations at different pH values, figure 3.24. Here  $\bar{\alpha}(H) = \sum_{z=1}^H \varphi_C(z) \alpha(z) / \sum_{z=1}^H \varphi_C(z)$ . Here  $\alpha(z)$  is the local degree of dissociation of the C-mers. The normalisation of the average degree of dissociation to the value found for brushes that are far

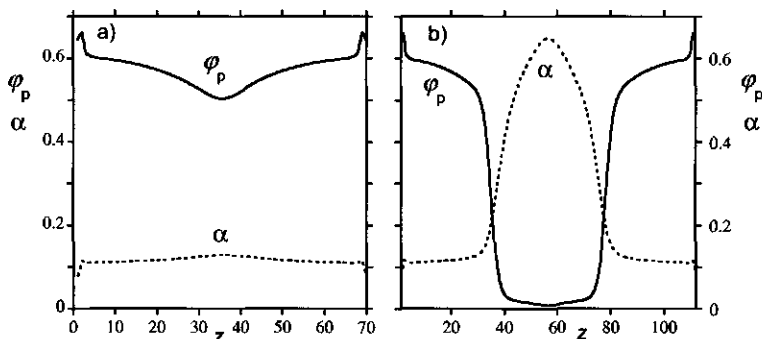


**Figure 3.25:** Two overall volume fraction profiles of two annealed brushes, and corresponding profiles for the degree of dissociation, for pH = 6.8 a) for a distance between the surfaces  $H = 71$ , b) for a distance  $H = 113$ . The two systems have the same interaction force per unit area and thus coexist with each other in a constant force ensemble.

apart, allows us to plot the results for a range of pH values in one and the same graph. We learn from this figure that upon compressing one brush by the other, the degree of ionization tends to drop. The compression brings the charged groups closer to each other and this induces the tendency to pick up a proton and go to the neutral state. In line with the results of the interaction curves, this occurs in a monotonous way for high pH values. Interestingly, for the curves with lower pH values there are regions for which the degree of dissociation increases upon compression. Indeed, this is a rather peculiar feature of the system. The brushes repel each other because of their charges, but at the moment they fuse to form a hydrophobic layer the degree of dissociation suddenly grows instead of decreases. The explanation is that when the two layers fuse the overall polymer volume fraction near the surfaces decreases slightly, so the solvent concentration within the brushes increases.

The previous discussion suggests that studying the structural features of the confined brushes may help us to understand what happens. We therefore proceed by presenting profiles of polymer chains and the distribution of charged segments in figure 3.25. In these figures we present the profiles of two coexisting brushes (in the constant force ensemble), i.e., two brushes with the same interaction force per unit area; the symmetry-planes are located at  $z = 35.5$  and  $z = 56.5$  in figs 3.25a and b, respectively. Inspecting figures 3.25a,b in detail, we see that the collapse transition is accompanied by the complete disappearance of the high ionized parts of the brush, i.e., the protonation of most acid groups, and the disappearance of the polymer-



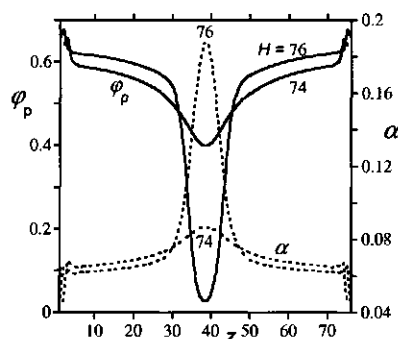


**Figure 3.26:** Two overall volume fraction profiles (left ordinate) of two annealed brushes, and corresponding profiles for the degree of dissociation (right ordinate), for  $\text{pH} = 6.8$  for a distance between the surfaces  $H = 74$ , for a distance  $H = 76$ . The two systems are close to the local maximum in of the interaction curve (see inset of fig. 3.23b).

solvent interfaces that were present at large separations. The decrease in free energy, as observed in some of the curves in fig. 3.23 at small values of  $H$ , is thus (as anticipated) due to the removal of the unfavorable interfaces. This effect disappears for higher degrees of ionization due to the repulsion generated by the large amount of charged groups at these interfaces. In the example of fig. 3.25, however, the transition is accompanied by the deionization of the brushes exterior interfaces and the formation of a rather homogeneous fused layer. Inspection of a large set of profiles shows that upon approach the layers first retract and collapse and only then fuse, thus supporting the idea that the adhesion in such a system can only be triggered if the layers are brought in close contact. This close proximity is needed to overcome the barrier in the free energy. As long as this barrier is not crossed the interaction will remain repulsive. In other words, there will be some characteristic distance (concentration) in an experimental system that must be crossed before the onset of entanglements takes place. A free energy barrier, or equivalently a non-monotonic interaction curve also implies that the interpenetration of the brushes will need some time to form. This is a common consequence of the presence of energy barriers in dynamical situations.

For comparison reasons we also show volume fraction profiles and corresponding degree of dissociation profiles for the same system as in fig. 3.25 at two other distances. We choose for this the separations  $H = 74$ ,  $76$ , where the interaction curve is just over the maximum. Here the profiles change

rapidly with distance. Referring to figure 3.26 we see that when the free energy is just over the maximum, and the attraction sets in, the water-rich region between the two brushes disappears very rapidly. The chains that are in the water-rich region are highly charged, but when this solvent-rich region disappears the chains have to drop their charges also. As a result we see that when  $H = 74$  the maximum in  $\alpha(z)$  is much lower than that at  $H = 76$ . We note that the free energy curve near this maximum remains fully continuous; there is no kink in the interaction curve. This is noteworthy because such features present themselves if, e.g. the brushes are not attracted to the surface. Then, upon bringing in the two brushes, they can jump into contact, i.e., the chains can increase the depletion zone near the surface to jump wise remove the water gap between the surfaces. A kink in the free energy of interaction is typically found when major relocations of chains are involved. To illustrate this we will consider the interaction between bilateral brushes, for which this phenomenon occurs, in the next section.

### 3.7 Interactions between flat bilateral brushes

Above we speculated that when a system has a degree of freedom to change the number of chains in the confinement region the interactions must be influenced by this. For this reason we now will consider the interactions between two bilateral brushes. A flat bilateral brush is composed of long polymer chains which are not grafted to an impenetrable surface, but rather to a single layer somewhere in the middle of the lattice system. As the chains are allowed to distribute themselves according to the surrounding media, they have the flexibility to bring in or remove chains from the confinement region. In our view this property makes the bilateral brush to be in between the case of a flat brush and a star. Above we did not devote any special attention to the bilateral brush, because at infinite dilution conditions (in isolation) this results in a symmetrical bilateral brush, which is similar to two flat brushes put together. Indeed, the differences present themselves when such brushes are compressed: the chains in this case will redistribute from one side of the grafting layer to the other. This additional degree of freedom should result in a softer interaction profile, provide us with insight of how the two approaching brushes rearrange to face each other and serve as a first approximation towards the interaction of two stars.

The parameters of the system are again fixed to be identical to the ones of the previous systems with minor adjustments due to geometry, namely the grafting density is doubled, so that  $\sigma = 0.2$  on each side of the bilateral brush. As we are mostly interested in the redistribution of chains and what

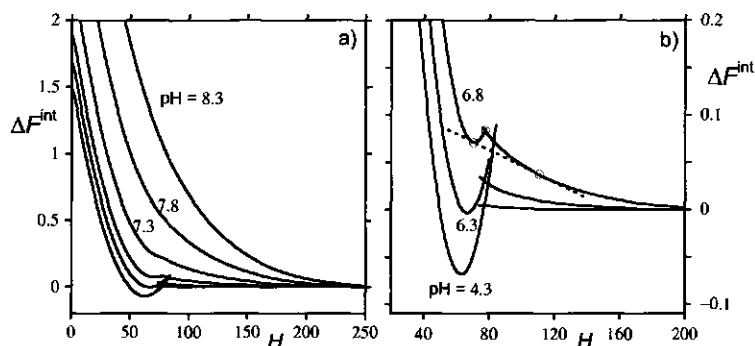


**Figure 3.27:** The free energy of interaction  $F^{\text{int}}(H)$  in units of  $k_B T$  per unit area per brush as a function of the distance  $H$  (in units of lattice sites) between two annealed bilateral brushes at various pH values as indicated. In view graph (a) the interaction curves are presented on the full scale; the three curves that are not labeled are enlarged in viewgraph (b). For the curve labeled pH = 6.8 we present the common tangent line (dotted) and have indicated three points on the curve by a circle. For these cases we present the structural information in fig. 3.28.

happens with the charges on the chains, we will only study the annealed brush case. Once again, the quenched brushes will show a very similar behavior, but it makes more sense to analyze the details for annealed ones when the calculation of this type is not extremely time-consuming.

In figure 3.27a we present the free energy  $F^{\text{int}}$  (in units of  $k_B T$  per unit area per brush) as a function of the separation distance  $H$ . These curves may be compared to the results for flat brushes given in fig. 3.23b. Here we choose to present a few enlargements of the transition regions in figure 3.27b. Similarly to the case of a surface-grafted flat brush (see figure 3.23b), at low pH the layers are attractive and at some distance the free energy of interaction falls below zero. It is of interest to mention that strong compression always leads to a rise in the free energy. Unlike in the flat brush case, for the bilateral brush we can reach the zero separation ( $H = 0$ ) as all the chains may translocate to the other, open, side of the bilateral brush. At the point of  $H = 0$  we simply produce a new bilateral brush with the double grafting density. As the parameters of the bilateral brush are chosen in such a way that the layer is saturated before the compression, i.e., the brush at any pH is homogeneous in the lateral direction, the further compression even at low pH leads to a rise in the free energy. This would not necessarily have been the case for an unsaturated collapsed bilateral layer, especially if this has a region of negative compressibility. A density increase in that case

may easily lead to a reduction of unfavorable polymer-solvent contacts in such a way that the new bilateral brush with double grafting density has an overall lower free energy. The opposite case of high pH leads again to a fully repulsive interaction curve once again. The layers are swollen due to the osmotic pressure of the counterions, which resists any compression.

At intermediate pH values we observe once again in the interaction curves a transition (cf fig. 3.27b), which is similar to the one discussed previously in fig. 3.23b in its origins, but has distinctly new features. As an example we may consider the upper curve of figure 3.27b, that is the interaction at  $pH = 6.8$ . If we follow this interaction curve, we see that upon approach the free energy first rises monotonously, but then there is a region where more than one solution is possible in the system. The stable and (parts of) the metastable branches are shown. The instable branch is not presented. While doing the calculations we use the solution for the brush at one distance as the initial guess for a new distance. In such a procedure it is possible to generate the stable and metastable states: one branch is found upon approach the brushes, and the other one is generated when the brushes retract. In a situation that there is more than one possible solution, the idea is that the one with the lowest free energy is always the stable one; the one with a higher free energy is metastable. At the transition (binodal) point the curves for the free energy of interaction cross. We will see that at this crossing point there are major adjustments of the brush structure in the system. As before the physical interpretation of these curves depends on the experiment at hand. In a constant force ensemble there is again a macroscopic phase transition and the coexisting phases can be found by the common tangent construction as explained above. In a surface force apparatus where the distance of between brushes can be controlled the full curves may be probed and then the crossing of two branches of the force curves may give rise to hysteresis phenomena.

A selection of polymer volume fraction profiles and corresponding degrees of ionization are presented in the next set of figures (Figs 3.28, 3.29). At the onset of the macroscopic phase separation, the brushes have a relative large spacing with highly charged chains between them (fig. 3.28b) at  $H = 112$ . At the other side of the transition the brushes are near each other and the two layers are fused together; the hydrophobic regions are protected from water only on the outer sides (fig. 3.28a)  $H = 70$ . Again, in between these two points a structural transition occurs (figure 3.28c,d): at the same separation distance ( $H = 78$ ) the layers can be in two different states with the same free energy. A separated state, where there is a water-rich layer between the brushes (fig. 3.28d) and a fused one where this water-rich region disappeared (fig. 3.28c). Many of the details that can be discussed in fig. 3.28 are very similar to those discussed in fig. 3.25 and 3.26. We therefore

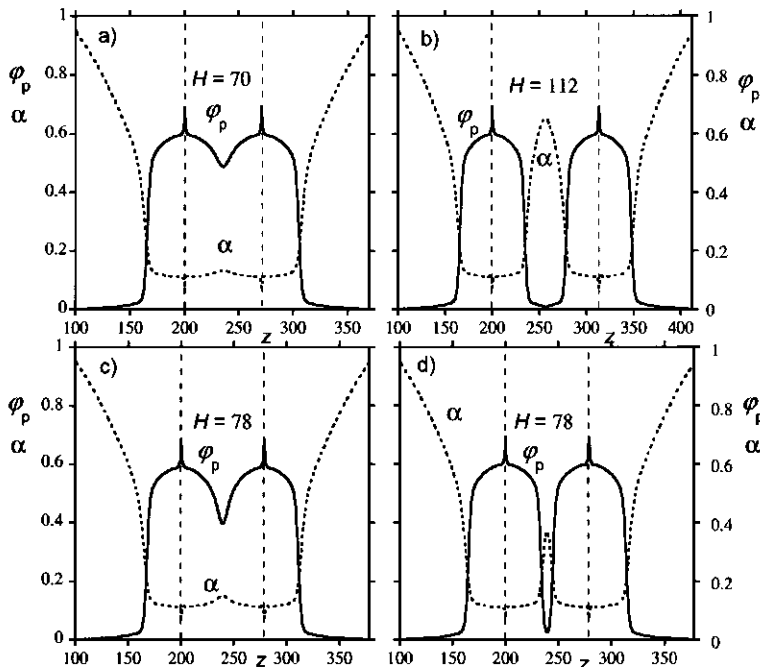


**Figure 3.28:** The overall polymer volume fraction profile for two interacting annealed bilateral brushes at pH = 6.8 and the corresponding profiles for the degree of dissociation. The vertical dashed lines represent the grafting coordinates. The distance  $H$  between the grafting planes is indicated. a) for fused brushes at  $H = 70$ , b) for two bilayer brushes that are far apart  $H = 112$ . The two brush systems of view graph a) and b) are in equilibrium with each other in a constant force ensemble. c) and d) two brushes that both exist at the same distance  $H = 78$  (binodal). The brushes in (c) are fused and have no water film in between them, in (d) there remains a water film in between the brushes.

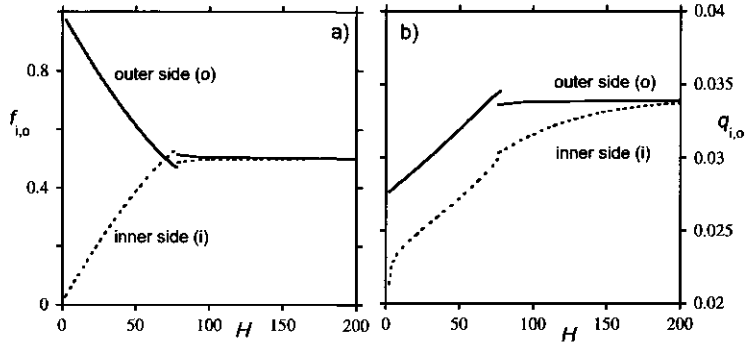


**Figure 3.29:** The fraction of chains on the outside  $f_o$  and on the inside  $f_i$  and the corresponding overall degree of dissociation  $q_i$  and  $q_o$  (for definitions see text), for an annealed polymer brush at  $pH = 6.8$  as a function of the distance between two bilateral brushes.

do not discuss these here. Instead we focus on the novel issue that the two sides of the bilateral brushes, which may be called the inside (the one that interacts with the other brush) and the outside (the one that is free from interactions), become different upon interaction. It is of interest to analyse how this asymmetry develops. Indeed the transition from the separated to the fused state is accompanied by a redistribution of chains and a significant change in the number of charges.

To illustrate this we computed the fraction of chains in the compressed region and the fraction of uncompressed chains. Here  $f_o = \sum'_z \varphi_p(z) / \sum_z \varphi_p(z)$  is the fraction of polymer segments on the outside of the bilateral brushes (uncompressed). The prime on the summation indicates that only those  $z$  values are used outside the grafting layers. Similarly  $f_i = \sum''_z \varphi_p(z) / \sum_z \varphi_p(z)$  is the fraction of polymer segments on the inside, where the double prime indicates that only the layers in between the two grafting layers are used. We plot these fractions in fig. 3.29a as a function of the distance between the brushes  $H$ . The corresponding overall degree of ionization is also computed. Here  $q_o = \sum'_z \varphi_{A^-}(z) / \sum_z \varphi_p(z)$  and  $q_i = \sum''_z \varphi_{A^-}(z) / \sum_z \varphi_p(z)$ , where  $A^-$  points to the dissociated polymer segments and the prime and double prime indicate that the summation is outside or inside the grafting layers, respectively.

The overall degrees of ionization are given in figure 3.29b). When the brushes are far apart the brushes are symmetrical and the fraction of chains on each side is  $f_o = f_i = 0.5$ , and the overall degree of dissociation amounts to  $q_o = q_i \approx 0.034$ . Upon compression the polymers first start to switch to the

exterior (uncompressed) part of the bilateral brush, and this is accompanied by a deionization of the inner part. Then, at the point of the structural transition, a number of chains choose to be in the interior region between the two grafting planes such that the initial loss of the chains upon compression is overcompensated. At this point the chains on the outside increase their charge a little bit, while the chains inside the gap lose a significant part of their charges. The increase in the charge on the outside is contributed to the decrease of number of chains on the outside: the remaining chains are less dense packed and can increase their charges somewhat. The hydrophobic nature of the polymer segments is responsible for the pulling-in of chains: it is favorable to form a dense collapsed layer at the interior. Note that for bilateral brushes with a lower grafting density this effect of pulling-in chains into a confined region will be more pronounced: there is an optimal density of the collapsed interior and to reach it at lower grafting density more chains must relocate. Finally, upon further strong compression, one gradually pushes the chains to the outside. Upon an increase of the grafting density on the outside the charged chains are pushed closer to each other and this causes a reduction of the charge density.

If we now imagine a macroscopic system of bilateral brushes, the existence of this structural transition will not change much in the overall behavior of the system. This statement needs some elaboration. At a certain concentration when the brushes start overlapping and the average distance between them falls in the region between 70 and 120 lattice layers, there will be a phase separation in this imaginary system: part of the brushes will still be separated and the other part has fused together. Then upon further compression one ends up with bilateral brushes with double density. Such brush with a higher grafting density occurs at a somewhat closer overall distance. Hence the transition becomes more smooth. Alternatively, if we consider the interaction on a microscopic scale, i.e., when we consider two approaching brushes in the controlled distance ensemble, then we can follow the interaction curve. We then typically see a difference in the case of two approaching and two retracting layers. Hence we find a first order structural transition. This has corresponding experimental consequences. AFM force measurements are in fact always dynamical in nature. This means that the thermodynamic equilibrium is not necessarily obtained during the measurements. The most likely outcome will be that during approach we will stay on the repulsive branch of the interaction, and the retraction will become attractive only if one has a sufficiently long contact time. The time scales involved for such effects will depend strongly on the chain length. In other words, we expect stronger hysteresis effects especially when the chains that must translocate are long.

### 3.8 Interacting laterally inhomogeneous brushes

We now focus on laterally inhomogeneous brushes of hydrophobic PE chains. From a theoretical point of view there are several challenges, not only because it is hard to solve the SCF equations properly for these cases, but also because these systems feature a large number of unique peculiar phenomena upon confinement.

As mentioned above, when the hydrophobic polyelectrolyte brush is attached to a repulsive substrate at relatively low grafting densities, it becomes laterally unstable and tends to form so-called pinned micelles instead of a laterally homogeneous layer.<sup>31</sup> One relatively unexplored aspect is what happens when two substrates covered with pinned micelles approach each other.

For such a system a two-gradient flat lattice is mandatory, wherein the mean-field approximation is applied along a line of lattice sites parallel to the substrate ( $y$ -direction), one of the gradient directions is perpendicular to the grafting plane ( $z$ -direction) and the other is parallel to this plane ( $x$ -direction) (cf. fig. 3.2). Using this two-gradient lattice allows the system to develop laterally inhomogeneous structures when this is favorable from a free energy perspective. As the system has only two gradients and not three, the surface micelles that form will have the cylindrical shape, even when the system would rather prefer smaller spherical ones. We argue that nevertheless the present Ansatz provides first-order insight into phenomena taking place upon interaction of such lateral inhomogeneous brushes.

Such two-gradient SCF calculations are performed in a 'calculation box' of which the dimension in the gradient direction parallel to the surface is limited in size. As we anticipate that there is some periodic feature along the surface we must choose the size of the "box" to be compatible with the wavelength of these lateral features. In other words, the number of lattice sites in the  $x$ -direction that is accounted for must be optimized. For example, the "aggregation number", that is the number of chains per unit length along the micelles, is a function of the lateral size of the system. When the box is either too small we will force a relatively large aggregation number or when the box is too large we will force the micelles to be relatively small. Obviously, both cases do not correspond to equilibrium. In the results discussed below the system size is optimised to find the optimum aggregation number for brushes that are far apart. The system size in the  $x$ -direction is fixed during subsequent confinement steps (where the number of layers in the  $z$  direction is reduced). In practice this means that we do not allow for a readjustment of the "wavelength" of the inhomogeneities along the surface upon the interaction of the brush with an opposite one. In passing we note that the polymer chains are pinned locally to the substrate (so-called



quenched pinning). This means that they can not move with their grafting segments in the  $x$ -direction. For systems where the chains are free to move along the surface, it is possible that the chains redistribute their grafting points to facilitate the formation of the micelles. Such systems thus behave differently.

As mentioned already above, for the two-gradient SCF results we will restrict ourselves to the quenched systems. As in the quenched brush the charges are evenly distributed along the chains it makes it harder to distinguish where the polymer chains (including the local counterions) are effectively charged. Some local mismatch between the charge distribution of the polymer and that of its counterions is used below to get some idea of the effective charge distribution (as these would occur in annealed brushes).

The idea is to focus on systems that are laterally inhomogeneous. As explained in section 3.5, the chances to catch this phenomenon is larger when the collapsed brush does not wet the substrate. Thus the substrate should be relatively hydrophilic. The parameters are thus chosen to exemplify the relatively rich behavior of such systems.

The following parameters were selected. The grafting density,  $\sigma = 0.023$ , is chosen to be slightly lower than the critical grafting density  $\sigma^{\text{cr}} = 0.025$  which signals the transition from the inhomogeneous to homogeneous layers for this case, so that the isolated brushes are in the "pinned micelle" state. When two of such brushes come together, the chains will interpenetrate somewhat and when doing so they effectively increase their grafting density. Because the grafting density is close to the critical value, we can anticipate that eventually there is a tendency to transform into a homogeneous brush structure. Indeed this is what is found as will be discussed below. The brush chains are  $N = 100$  segments long, a fraction  $\Phi = 0.25$  of the C-segments is negatively charged (equivalent to a fractional charge per C-segment  $\alpha = 0.25$ ). In line with the systems discussed above, the non-charged segments are hydrophobic,  $\chi = 1$ . The surface is (as mentioned) hydrophilic. More specifically the substrate does not discriminate between the interactions of solvent or polymer segments with the surface, that is  $\chi_S = 0$  and  $\chi_{SP} = 0$ , respectively. In such a setting there exists an effective repulsion of the polymer chains for the substrate which is attributed to the conformation entropy loss of the chains. This relatively small effect causes a depletion layer of polymer near the substrate.

The free energy of interaction when two of these laterally inhomogeneous layers are pressed against each other is presented in figure 3.30. It is easily seen that the curves differ significantly from the case shown in fig. 3.23. Parameter wise, the important difference between the systems of figs 3.30 and fig. 3.23 is the way the polymer interacts with the surfaces being hydrophilic

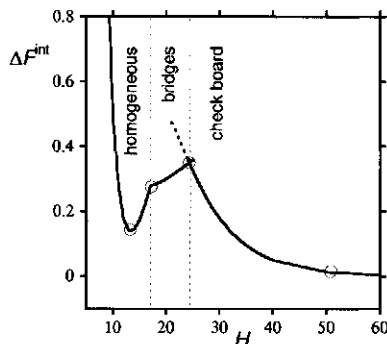


**Figure 3.30:** Free energy of interaction (in units of  $k_B T$  per unit area per brush) as a function of the distance between the surfaces. At large separations  $H$  the surface structures are heterogeneous (labeled as 'check board'), at intermediate distance bridges form and the layer becomes laterally homogeneous at small  $H$ . Around the transition point  $H = 25$  it is possible to have meta-stable branches to the interaction curves. One of these metastable branches is plotted by a dashed line. The parameters are discussed in the text. The open spheres point to profiles shown in figs. 3.31 and 3.32.

(polymer-repellent) in fig. 3.30 and polymer attractive in fig. 3.23. Of special interest is the peculiar shape of the interaction energy curve for the present system: it clearly shows two distinct deflections (breaks) - one at a distance  $H = 25$  and another one at  $H = 17$ . Apart from the poor solvent conditions for this system that are responsible for the microphase segregated state of the brush, there are two microscopic structural transitions within the layers that are triggered by the confinement. We found that around one of the deflections (at  $H = 25$ ), it was possible to register metastable branches of the interaction curves pointing to the first-order character of the transition. We have presented such a branch by a dashed line in fig. 3.30. The presence of metastable branches suggest that there are important changes in the structure of the layers that occur upon the confinement. When there are metastable branches there should also be an unstable branch connecting the endpoints of the metastable branches (spinodals). We were however unable to compute the spinodal points.

The description of each regime of interaction in the interaction curve is facilitated by inspection of the structure of the layer as a function of the separation distance  $H$ . For the open circles in Fig. 3.30 we present relevant contour plots of the overall polymer concentration and charge distribution for the  $x$ - $z$  plane in fig. 3.31 and fig. 3.32, respectively. We will discuss the

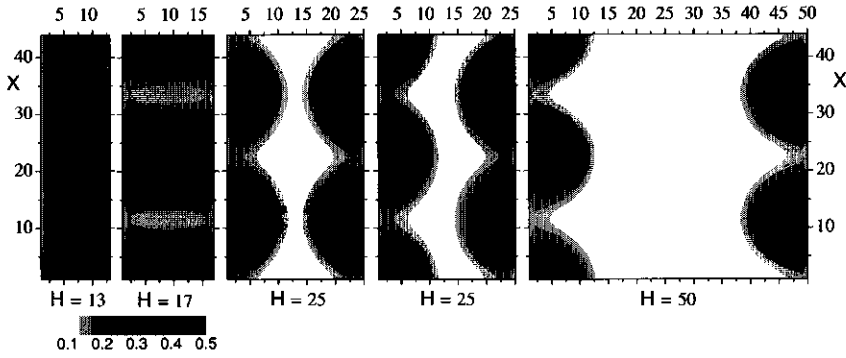


**Figure 3.31:** Two-gradient volume fraction profiles  $\phi(x, z)$  where  $z$  is the direction perpendicular to the surfaces and  $x$  parallel to the surfaces (the mean field averaging is applied in the  $y$ -direction), for various distances  $H$  between the surfaces as indicated. Parameters as in fig. 3.30 and the distances correspond to the open circles in the interaction curve.

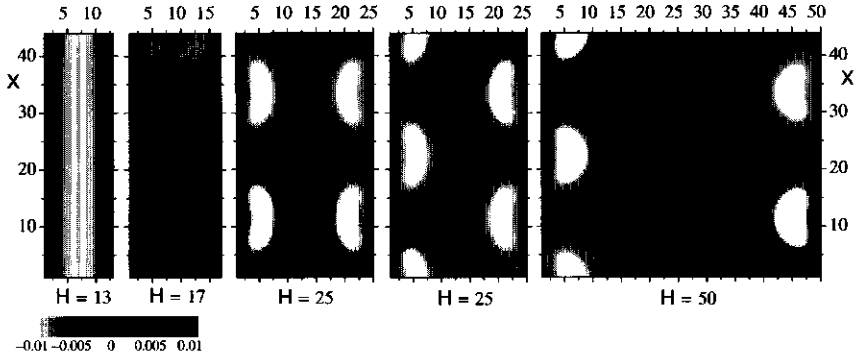


**Figure 3.32:** Two-gradient overall charge density profiles  $q(x, z)$  where  $z$  is the direction perpendicular to the surfaces and  $x$  parallel to the surfaces (the mean field averaging is applied in the  $y$ -direction), for various distances  $H$  between the surfaces as indicated. Parameters as in fig. 3.30 and the distances correspond to the open circles in the interaction curve.

results using all three graphs in concert.

At very large distances between the surfaces (contour plots are not presented) the two brushes do not feel each others presence. The micelles on each surface are uncorrelated, that is, the  $x$ -positions of the pinned (cylindrical) micelles are arbitrary. The pinned micelles are composed of a dense inner part (with a very small negative charge) which are stabilized by a corona layer of chains that are more charged. The "legs", which connect the micelles to the surface, are also charged. The counterions have almost completely compensated the charge, but there is an excess of counterions outside the layer.

Upon approach the electrostatic repulsion makes the micelles occupy the most distant locations, resulting in a checker board ordering. This configuration is presented for  $H = 50$ . The positions of the micelles of opposite surfaces are now correlated, which is clearly shown in the volume fraction contour plot of fig. 3.31 (right hand side). In the corresponding contour plot for the charge distribution, it is seen that where the polymer density is high the net negative charge of the micelles prevails. These regions with a negative charge are separated in the lateral direction by a layer of positive counterions. In between the layers there is still a region where the net charge is close to zero.

For larger confinements, i.e., upon a shorter distance between the surfaces, we find an increase in free energy of interaction (cf. fig. 3.30) and at  $H = 25$  there are two states with equal free energy: one is computationally found upon the approach of the two surfaces, and the other one upon the retraction of the surfaces. Contour plots for both coexisting layers are shown in figs. 3.31 and 3.32. Upon reducing the distance between the surfaces the micelles are still in check board order, whereas upon increasing the distance the micelles face each other. The transition at  $H = 25$  thus is a major structural transition, for which the relocation of many polymer chains must take place. The faced micelles apparently are stable at short separation, but to understand this we must know to what structure these evolve when the surfaces are brought even closer.

The structures that are present for distances around  $H = 17$  are bridges of high polymer density that are laterally separated from dilute regions of polymer. Apparently, at such high confinement it is favorable to fuse micelles of opposite layers rather than to smear the polymer concentration in the lateral direction. It is also easy to see that the fused micelles for  $H = 17$  represent a more favorable configuration of the system than the faced micelles in  $H = 25$ . This explains the attraction which is seen in the interaction curve for distances below  $H = 25$  and the subsequent transition to the checker board configuration. Clearly in the region  $17 < H < 25$  there are too many

polymers between the walls to retain separate micelles, but still not enough to form a homogeneous layer. Inspection of the contour plot for the overall charges, we find again that the bridges are negatively charged and that the space in between the bridges is enriched with positive counterions.

Further compression  $H < 17$  makes the laterally inhomogeneous conformation unfavorable and again the layer undergoes a sudden change. From inspection of the volume fraction contour plot as well as the charge density contours we find that the layers have become laterally homogeneous with the maximal density in the central layers and the lowest density very close to the surfaces. We were unable to find metastable branches for the interaction curves for this transition, but we believe that these should be there because the layer changes its structure so suddenly (first-order transition). Compressing the homogeneous layer even further first decreases the free energy (attraction), since the system trends to form a more compact state. Then this attraction is replaced by repulsion due to steric effect of pushing the chains into a smaller and smaller volumes.

We recall that for the present case the polymer chains have a small unfavorable effective polymer-surface interaction, and that for apolar surfaces the system suffers less dramatic changes upon confinement. This implies that the nature of the grafting plane affects the overall behavior of polymer brushes in a dramatic way. We believe that this result is not a rare and isolated case. Very often polymer brushes are administered to modify the surface properties. Typically, the substrate and the polymer brush chains may thus be rather incompatible. For such systems the pair interaction can show the peculiarities just described. The observation that the properties of the substrate matter is very interesting because most frequently these are ignored in polymer brush studies. The typical argument for doing so, is that the polymer brush is much thicker than the range of the interactions of the polymer segments with the substrate, and that therefore these interactions are irrelevant. The present results thus prove that this argument is in principle flawed.

One may possibly argue that with increasing chain length,  $N$ , also in the current type of systems the finite size effects will vanish. However, with increasing  $N$  the critical grafting density for the formation of pinned micelles decreases with  $N^{1/2}$ . As soon as there are surface micelles in the system, the coverage is too low to ignore the properties of the substrate, and our results are robust for systems that feature pinned micelles.

We conclude this section by a short discussion on the parameter space for which the rather complex type of interaction curves as discussed starting from section 3.6, can be expected, focusing on the solvent quality and the grafting density.

As mentioned above, phase segregation is controlled by two opposite types of interactions: the repulsive electrostatic contribution and the attractive hydrophobic one. This means, that, generally speaking, the onset of phase segregation upon approach of two brushes takes place when the solvent quality of the non-charged segments of the polyelectrolyte is sufficiently poor, that is (depending on the lengths of the chains) when  $\chi$  is above the  $\theta$ -point, i.e.,  $\chi_{NC} > 0.5$ . On the other hand, at very high values of this Flory-Huggins parameter the attractive hydrophobic interaction becomes dominant and the brushes remain fully collapsed at any value of the pH.

In the absence of attractive surface interactions, i.e., for weakly repulsive surfaces, we find non-monotonic interaction curves for a wide range of grafting densities. With increasing grafting density one will naturally find a thickening of the collapsed phase. Bringing two of such interfaces towards each other gives the system the opportunity to get rid of the unfavorable brush-solvent interfaces. The removal of these interfaces decreases the free energy and thus the observed attraction is quite generic: it occurs for collapsed or microphase segregated PE brushes for a wide range of grafting densities.

Hydrophobic PE brushes composed of polymer chains that are not attracted to the substrate generally form pinned micelles at low grafting densities. Although the shape of the interaction curves depends somewhat on the grafting density, the overall qualitative picture stays the same: we always find a repulsion at large separations (due to the overlap of dilute layers of charged chains) which is followed by attraction where the overlap of opposite brushes allows the system to find microphase segregated states where surface micelles of opposite surfaces have fused.

### 3.9 Isolated HPE stars

In the first part of this chapter the focus was on flat HPE brushes. Such brushes occur on macroscopically large flat interfaces. They are also a good approximation for colloidal systems for which the brush height  $H$  is small compared to the radius  $R$  of the particles. Indeed for such a system the brush is quasi-flat. However, in experimentally relevant cases one can easily be in the situation that  $H \gg R$ . When this is the case, we may not ignore the curvature. In the limit  $R \rightarrow 0$  we arrive at the so-called 'star' limit. In this case the curvature effects are largest. We will now commence with the discussion of hydrophobic polyelectrolyte stars and mention that in many experimental cases one typically will be in between the flat and the star limits.

Theoretical investigations of HPE stars, and in particular the mean-

field analysis of the collapse transition in these stars, are known for several years already.<sup>33,95,96</sup> More recently, experimental studies have been reported as well.<sup>97-99</sup> In these mean field theories the spherical symmetry of the (partially) collapsed stars is preassumed. Such an assumption is challenged in complementary scaling theories<sup>27</sup> that point to the possibility that there is a local collapse of the arms in a hydrophobic polyelectrolyte star with very long arms. In such scenario one envisions several arms grouping together into collapsed bundles upon the worsening of the solvent quality. The latter predictions are supported by very recent MD-simulations<sup>100</sup> wherein (partial) bundling of arms was seen. At present there is no consensus on whether these complex structures are transient intermediates towards the spherical symmetric state, or are part of the equilibrium nature of these collapsing stars.

The systems that will be discussed in the present section are chosen because of their relevance for the corresponding problem of interacting HPE stars (see sections 3.9.1 and 3.9.2) and to exemplify the differences between flat and curved hydrophobic polyelectrolyte brushes. Due to our mean-field approximation we imposed the spherical symmetry and therefore the possibility of bundle formation is omitted here.

The first target is to illustrate how various environmental parameters affect the conformations of chains that are grafted by one end to a very small particle. We keep the structure of the polymers similar to that used above, and study both quenched and annealed stars. An isolated star can be modeled within one-gradient spherical lattice; the polymer chains are grafted in the center of this system. As the central layer of this coordinate system contains only about four lattice sites, we can not graft all the chains we wish to this layer; instead we have chosen to set a small offset of 3 lattice layers to gain enough available sites for the grafting. The star is then composed by default  $f = 20$  chains of length  $N = 200$  each. Again every fourth segment is charged in the quenched case and ionizable in the annealed one. The most important difference between the star-like conformation and a flat one is that in the spherical geometry the volume available for the polymer chains grows as a second power with the distance from the center of the lattice, whereas in a flat system this remains constant. This increase in available volume is playing a key role in many observations specific for star-like polymer systems.

The chain length dependence of polyelectrolyte stars is considered first. As we will see, in contrast to the flat PE brush, the degree of polymerisation plays a crucial role in the overall conformation of the stars, as well as in scenarios of possible structural transitions. Figure 3.33 presents the changes in the size  $h_g$  of the star, which is computed as the first moment over the end-point distribution, as a function of the length of the arms  $N$  for a few

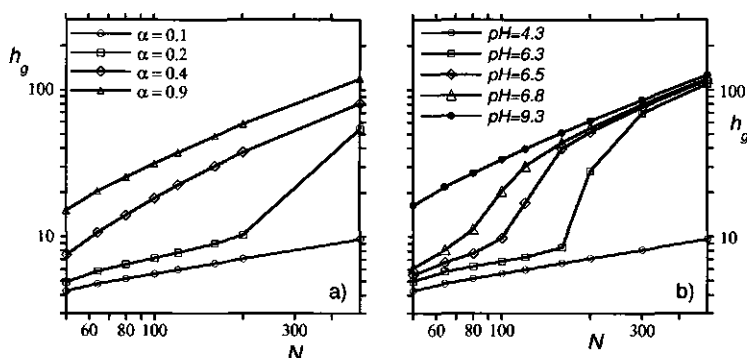


**Figure 3.33:** a) The size  $h_g$  (first moment over the end point distribution in lattice units b) of the quenched PE star as a function of the length of the arms  $N$  in log-log coordinates for a selected number of values of  $\alpha$  as indicated. The number of arms  $f = 20$ . b) The size  $h_g$  of an annealed PE star as a function of the length  $N$  of the arms in log-log coordinates for a selected number of pH values as indicated. The number of arms  $f = 20$ .

different degrees of charging of chains for both the quenched (fig. 3.33a) and annealed (fig. 3.33b) stars. Note that both graphs are in double logarithmic coordinates. From such a plot one can estimate how the size of the star scales with  $N$ . When the polymer chains are effectively uncharged (bottom curves) they form a compact globule rather than a star: in this case  $h_g \propto N^{1/3}$ . In the other extreme, when the chains are highly charged (top curves), they tend to strongly stretch and the scaling is a bit less than unity:  $h_g \propto N^{0.8}$ . Between these two extremes there are significant differences in the behavior of quenched and annealed stars, but the generic behavior is similar. In both types of stars there is a region in the parameter space (pH or  $\alpha$ ) for which it is possible to find a transition from a collapsed globule to a swollen star upon an increase in chain length. In the quenched system this happens in a much more gradual way than in the annealed case. This rather peculiar response upon the increase of the length of its arms (side chains) is worth discussing. The stars with short arms are in a compact state, close to be in a globular state. With increasing chain length the stars suddenly become swollen. Such rather abrupt transitions were not seen for flat hydrophobic polyelectrolyte brushes. Indeed, this happens due to the increase in volume available for polymer chains when they probe the outer regions of the stars. Very short chains would have to fully stretch in order to obtain more space in the exterior layers. This is entropically unfavorable and exposes its hydrophobic segments to the solvent. So the globule is the ground state. Stars with long arms can



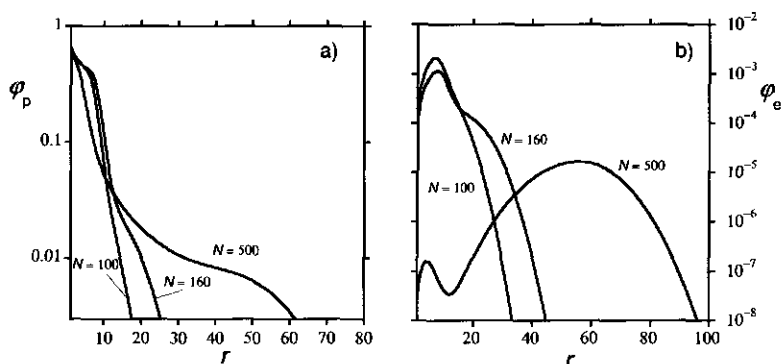


**Figure 3.34:** a) The radial volume fraction profile, b) the corresponding radial end-point distribution for three values of the length of the arms  $N = 100$ , 160 and 500, for the quenched polyelectrolyte star with  $f = 20$  and  $\alpha = 0.2$  in semi-logarithmic coordinates.

retain partially their collapsed state and allow a few arms to be swollen to reach the spacious periphery.

The next two sets of plots, figures 3.34 (quenched) and 3.35 (annealed) illustrate the internal structure of the star upon variation in  $N$ . In these plots panel a gives the overall radial volume fraction profile, and panel b the corresponding end-point distribution. Note that as we plot the true volume fraction and not the number of segments as a function of the distance from the center, the profiles drop dramatically with increase in distance from the center  $r$ . For this reason we have used a semi-logarithmic scale. We selected a system with some intermediate value of the fraction charge ( $\alpha = 0.2$ ) and pH ( $\text{pH} \approx 6.5$ ) to illustrate what happens with these stars when the changes (upon the increase in length of the arms) are most dramatic. Here we like first to draw the attention to the changes in the interior layers of the stars. Upon larger values of  $N$  the volume fraction in the central layers strongly decreases. Indeed, the stars with long arms tend to stretch their chains at the expense of a dense inner part to reach the outer space. The arms that escape from the dense core are highly swollen and strongly stretched. The local volume fraction of arms is very low indeed. This suggests that the arms extend mostly by intra-chain excluded volume interactions. The exact nature of the structure and detailed conformation of the side arms may in fact be different from what SCF-theory suggests. It may well be that the side-chains have a pearl-necklace configuration, that is that there may be more dense regions of uncharged (globule-like regions) polymers along the

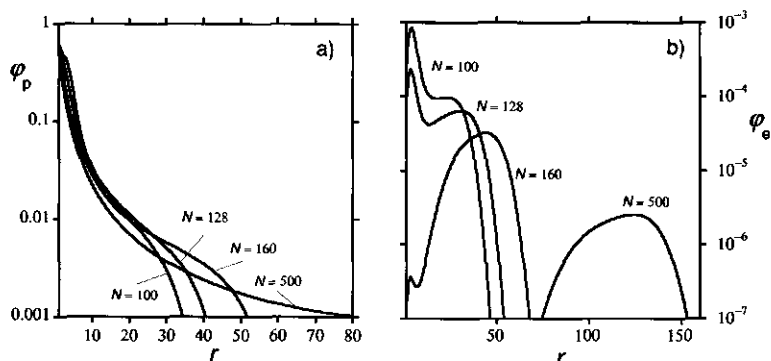


**Figure 3.35:** a) The radial volume fraction profile, b) the corresponding radial end-point distribution for four values of the length of the arms  $N = 100, 128, 160$  and  $500$ , for the annealed polyelectrolyte star with  $f = 20$  and  $pH = 6.5$  in semi-logarithmic coordinates.

otherwise charged and extended arms. Computer simulations are currently executed to search for such complex structure.

The profiles of the polymer ends (panels b) change dramatically with  $N$ . More specifically, at intermediate values of  $N$  there is a bimodal end distribution (for example for  $N = 500$  in fig. 3.34b and somewhat small chain length  $N = 128$  in fig. 3.35b). Such bimodal distributions point to the presence of two populations of polymer chains. One subset of the chains is collapsed, forming a dense core, and the other subset is stretched to make a dilute charged shell (corona) layer. And finally, we point the reader's attention to the profile for the chain ends in fig. 3.35b for the case  $N = 500$ . For these long arms all the chains are stretched, and there is a profound "dead-zone" in the polymer ends distribution: none of the chains ends show up in a large zone  $0 < r < 70$ .

For the flat PE brushes we found strong effects of the degree of ionization on the conformations of the HPE brushes. It is of interest to present complementary results for HPE stars. As with flat brushes, we anticipate that upon charging the star the system will suffer a collapse-swelling transition, but there should be in addition a strong effect of the chain length  $N$ .

In fig 5.4 we show typical results for the size of the stars as a function of the parameter that controls the charge in the stars, for both the quenched (fig 5.4a) and annealed systems (fig 5.4b). In these graphs results are given for a selected number of chain lengths ranging from  $N = 50$  to  $N = 500$  and for the quenched case up to  $N = 1000$ . The radius of the stars is measured

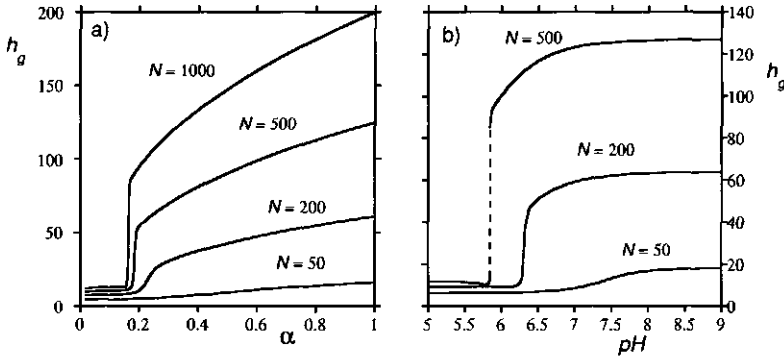


**Figure 3.36:** a) The size of the quenched star as a function of the degree of dissociation  $\alpha$  b) the size of the annealed star as a function of the pH for a selected number of chain lengths  $N$  as indicated;  $f = 20$ .

as previously by the first moment over the distribution of the polymer ends. In both cases, the charging up of the systems induces the collapse-swelling transition as expected; when the stars are barely charged the chains are collapsed and the star is effectively a globule; when the arms charge up, the star becomes much larger. For the quenched stars the transition is always continuous, though it becomes increasingly sharp at large values of  $N$ . In the annealed case, the transition is definitely more sudden and it becomes even discontinuous for large enough chains. More specifically, for  $N = 500$  the size of the star changes jump-like around  $pH = 5.8$ . From the end-point distribution discussed above we know that there is a region for which this distribution is bimodal. This implies two populations and two local minima in the Landau free energy. The maximum in between these distributions is of course not infinitely high and thus the transition (formally) can not be first order. In a mean field theory however, one may be able to observe two distinct states of the PE star. The details of this transition must therefore be rather special and for a more complete picture we will present a few other characteristics for the annealed system.

The average degree of ionization for the various chain lengths as a function of pH is shown figure 3.37. Both for  $N = 200$  as well as  $N = 500$  there appears a kink in  $\langle \alpha(pH) \rangle$ . However, close inspection reveals that there is a very small jump in average  $\alpha$ . For  $N = 50$  the degree of dissociation is still smoothly varying with pH. The Helmholtz energy  $F$ , which is presented in figure 3.38, appears in first inspection to be smoothly varying function with pH. However, close inspection disproves this. In the inset we show that also

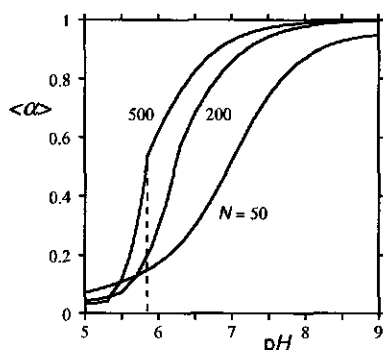


**Figure 3.37:** The average degree of dissociation  $\langle \alpha \rangle$  as a function of the pH for the annealed polymer star with  $f = 20$  and arm lengths as indicated. The vertical dashed line points to a kink in the curve.

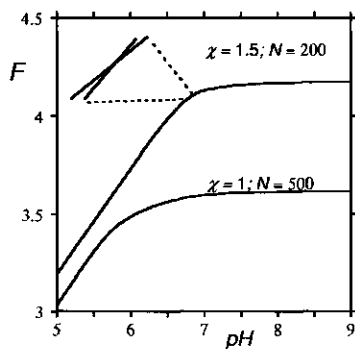


**Figure 3.38:** The Helmholtz energy  $F$  in units of  $k_B T$  as a function of the pH for two lengths  $N$  and two values of the  $\chi$  parameter as indicated;  $f = 20$ . The inset enlarges a small region for the upper graph, showing that the free energy lines cross each other, indicating that on the mean-field level the transition is first-order.

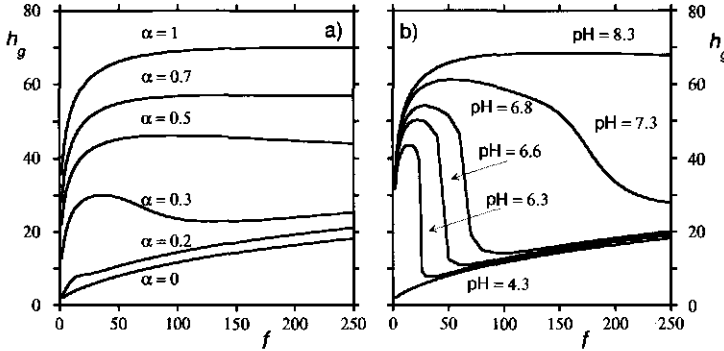


**Figure 3.39:** a) The size  $h_g$  of the quenched star as a function of the number of arms  $f$  for various values of the fractional charge  $\alpha$  as indicated. b) The size of the annealed star as a function of the number of arms for various values of the pH as indicated.  $N = 200$ .

from the free energy perspective the transition is weakly first-order. Indeed, for a system with  $\chi = 1.5$  and  $N = 200$ , the free energy lines cross each other and a similar crossing of lines occurs in the other system. We hasten to mention that this feature is extremely subtle and hardly shows up in the radial volume fraction or charge density profiles. This is consistent with the idea that for small systems the transition should (in practice) be smooth.

Let us next consider the number of arms  $f$  as the variable. This parameter corresponds to the grafting density  $\sigma$  for the flat brush. One would expect to find an increase in the size with increasing number of arms. Both for very small and for large  $f$  values this is the case but at an intermediate number of arms one can find the opposite behavior. The radius of the HPE star for the quenched case is given in fig. 3.39a and for the annealed star in fig. 3.39b. For the quenched case the normal growth of the star with number of arms  $f$  is found for a wide range of  $\alpha$  values. Only around  $\alpha = 0.3$  the size decreases in an intermediate regime of number of arms per star. The non-monotonic behavior of  $h_g(f)$  is due, once again, to the hydrophobic nature of the polymer backbone. With increasing  $f$  one increases the density of chains, which makes it favorable to collapse and form the globule. In other words, we can drive the collapsed  $\rightarrow$  swollen transition by decreasing the number of arms.

Indeed, such behavior is remarkable. Comparing this phenomenon with a simple gas, it means that when we increase the number of particles (and thus increases the pressure) we find a reduced volume. Such an effect thus corresponds to a negative compressibility. For the PE stars, this negative

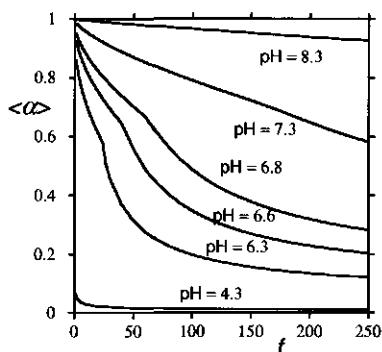


**Figure 3.40:** The average degree of dissociation as a function of the number of arms of an annealed brush with  $N = 200$  for various values of the pH as indicated.

compressibility region is much more pronounced in the case of an annealed star (fig. 3.39b). Indeed the changes in star size are much more dramatic; the negative compressibility is found for a rather wide pH range and for a large range of  $f$ -values. The reason is that the annealed brush is capable of deionization its arms upon collapse. This extra degree of freedom can make the transition more abrupt as extensively argued above.

The average degree of dissociation as a function of the number of arms is given in figure 3.40 for  $N = 200$  and for a number of pH values. As expected from the above we find that with decreasing number of arms in the star the chains can accommodate more charges along their arms. Again the system suffers a collapse transition which appears as a kink in  $\langle \alpha(f) \rangle$ . Close inspection once again reveals a very small jump, pointing out that on the mean-field level the transition is weakly first order.

The next plots give slightly more information on the transition that takes place when the number of arms is changed from  $f = 40$  to  $f = 50$  for pH = 6.3 (corresponding to the systems close to the kink in the curve of fig. 3.40). In fig. 3.41a the overall radial volume fraction profile is given. The distribution of end segments is presented in fig. 3.41b and finally in fig. 3.41c the radial distribution of the fractional charge  $\alpha$  is presented. Inspection of these profiles shows that the dilute swollen part of the stars remains almost intact during the collapse. With increasing number of arms one only changes the interior. In other words, the newly added chains contribute only to the core of the star, increasing the density of this part. This results in the shift of the maximum in the bimodal free ends distribution from the exterior of the star to its interior, and thus the "measured" radius decreases abruptly. We

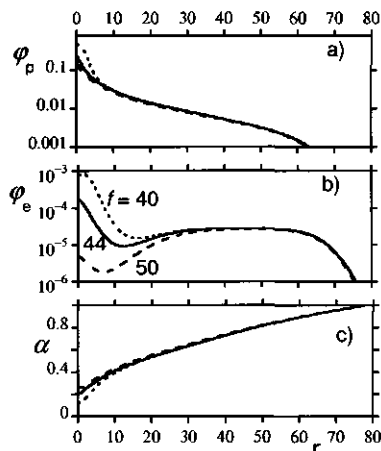


**Figure 3.41:** The radial overall volume fraction profile (a), the corresponding end point distribution (b) and the radial degree of dissociation  $\alpha$ , for an annealed brush with  $N = 200$  for three values of the number of arms:  $f = 40$  (dotted lines),  $f = 44$  (solid lines) and  $f = 50$  (dashed lines) and  $pH = 6.3$ .

would like to point out that even when there is a significant globule in the core, swollen and charged chains are still present in the exterior part of the stars. This implies that the transition remains unnoticed in e.g. a dynamic light scattering experiment. Indeed the hydrodynamic radius, which is set by the chains that extend most, is expected not to change at all.

Let us briefly discuss the possible consequences of the above for how HPE stars might interact with each other. Similar to the flat brushes, strongly charged stars should repel each other, while poorly charged ones will aggregate. At intermediate values of the ionization however, stars should, when they are pushed towards each other (e.g. by increasing the osmotic pressure) first repel each other and then at very close proximity attract each other. In a solution this may result in a two-phase state where a dilute phase of stars coexists with a much more concentrated one. The stars in the dilute phase have a strongly charged corona. The stars in the concentrated phase have very few charges. In order to check this scenario we investigate the concentration dependence of relevant HPE star systems in the next section.

### 3.9.1 Interacting PE Stars in cell-model

The average effect of interacting stars can conveniently be accounted for by adjusting the so-called Wigner-Seitz cell dimension. This is rather simply

implemented an SCF calculations. In this approach there exists a multiarm star in the centre of a spherical lattice geometry (the Wigner-Seitz cell). The number of lattice layers,  $D$ , in this geometry set the dimension of the calculation cell. At the upper boundary of the cell, at  $r = D$ , one implements reflecting (mirror-like) boundary conditions. When the cell dimension exceeds the star size by far, the system has enough volume to consider the stars being at infinite dilution. This type of lattice arrangement has been employed in section 3.9 for the study of isolated stars. When the cell dimension is reduction, that is when the number of layers is reduced, one effectively implements the interactions between a central star with surrounding ones. More specifically, as the boundaries of the lattice are mirror-like, the central star starts to interact with its images. This approach is reasonable for an ideally homogeneous concentration of stars. It implements an approximation as the discrete nature of the interaction between the stars and its neighbors is ignored. Clearly the distance between two stars  $H$  is twice the value of  $D$ . Below we will use both distance measures.

We will briefly investigate what happens to the stars when we increase their concentration, implemented by reducing the cell dimension  $D$ , for both the annealed and quenched stars. Here we will focus on the effect of the available charges in the annealed case and the pH-dependence for the annealed case. Based on the results discussed above for a single star-like HPE and the HPE brushes, our working hypothesis is that upon a rise in the star concentration, under certain conditions, we should find that the system undergoes phase-separation into a dense phase wherein the stars are collapsed and wherein the hydrophobic attractions prevail, which coexists with a dilute phase with swollen micelles wherefore the electrostatic repulsion plays a key role. This issue will be revisited in the next section 3.9.2 wherein the interactions of two stars are studied in more detail. In the current calculations there are gradients in density only in the radial direction (1-dimensional) and therefore we have few limitations as it comes to the choices of the dimension of the Wigner-Seitz cell or the chain length of the polymer. In the two-gradient calculations in the next section 3.9.2 we are much more constrained in these choices. Therefore we can present results for a relatively larger range of parameters in this section.

We start by discussing the free energy for a central star as a function of the cell size for both the quenched and annealed stars. These results are presented in figure 3.42. In these plots the free energy is normalized with respect to the value at infinite dilution  $\Delta F^{\text{int}}(D) = F(D) - F(\infty)$  and plotted per segment of the polymer chain in units  $k_B T$  for stars with  $f = 20$  arms each of length  $N = 200$ . This choice of parameters is motivated by results of isolated HPE stars in section 3.9. In line with this we see that



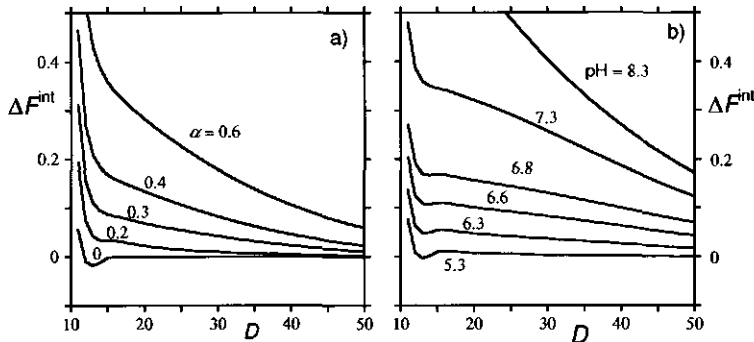


**Figure 3.42:** The free energy per segment in units of  $k_B T$  of the central star in a Wigner-Seitz cell with dimension  $D$  normalised to the value at  $D \rightarrow \infty$ . The number of arms  $f = 20$ . The length of the arms  $N = 200$ . Other parameters have the default value. a) Quenched polyelectrolyte stars and fractional charge  $\alpha$  as indicated. b) Annealed star with pH values as indicated.

for low charge density  $\alpha$  in fig. 3.42a or low pH in fig. 3.42b the system is unstable. This follows from the fact that at high concentrations (small  $D$  value), the free energy falls below the value found for isolate stars (large  $D$  values). In other words  $\Delta F^{\text{int}} < 0$  for small  $D$  values. Hence, stars with a low number of charges will precipitate due to the hydrophobic nature of the uncharged segments. For highly charged stars,  $\alpha \sim 1$  or high pH values, the stars are colloidal stable. This follows from the fact that  $\Delta F^{\text{int}}$  increases upon a decrease of  $D$ , or in other words, they progressively repel each other upon increasing concentrations. In the intermediate cases we see, similar to the flat brushes case, a non-monotonous behavior of the free energy: the electrostatic repulsion at low concentrations (relatively large  $D$ ) is followed by hydrophobic attraction at higher concentrations (smaller value of  $D$ ) and at strong confinement a steric repulsion is found again. The interpretation of these non-monotonic interaction curves depends on what type of ensemble one is in.

In the constant pressure ensemble one should anticipate phase separation into two phases, one concentrated and one dilute phase. Similar to the flat brushes case, in these coexisting phases the polymer chemical potentials will be equal and the points of phase separation are determined by equal osmotic pressures in the two phases. We may use once again a common tangent construction to find the coexisting phases, but we should realise that for such a construction we should plot  $\Delta F(D^3)$  where the  $D^3$  is proportional to the volume of the Wigner-Seitz cell. For example, the coexistence cell

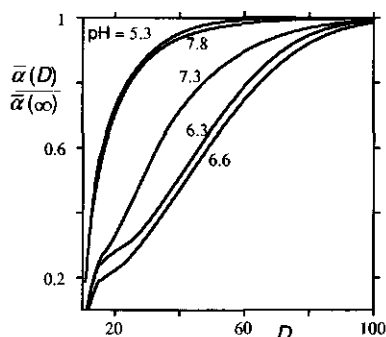


**Figure 3.43:** The average degree of dissociation in the annealed polyelectrolyte star as a function of the cell size  $D$  normalised to the value at  $D \rightarrow \infty$ , for several values of the pH as indicated. The star has  $f = 20$  arms each of length  $N = 200$  segments.

dimensions are  $D_{\text{low}} = 14$  and  $D_{\text{high}} = 20$  in the quenched system for  $\alpha = 0.2$  and  $D_{\text{low}} = 12$  and  $D_{\text{high}} = 26$  in the annealed star system with  $\text{pH} = 6.3$ .

There is a large number of measurable quantities that depend on the size of the Wigner-Seitz cell. As an example we show in figure 3.43 how the overall charge of the annealed star changes under isotropic compression. In this figure the overall charge in the star is normalized to that at infinite dilution for various values of the pH as indicated. The stars discharge upon compression. The degree of dissociation has almost the same dependence on the compression in acidic and basic solutions even though these systems are vastly different. In acidic conditions the chains are collapsed. Therefore the onset of discharge appears at rather high compression. In basic solutions the chains are highly stretched and fully charged. Obviously they do not easily give up their charged groups and only reduce their charge under high compression. At intermediate pH values the discharging already takes place upon weak compression. At these values of the pH the chains are swollen, compared to the low-pH case, and catch protons more easily compared to the high-pH case. This explains why the discharging starts already at relatively high separation distances. The kink at  $D = 13$  for curves at  $\text{pH} = 6.3, 6.6$ , and  $7.3$  corresponds to transitions from an electrostatic repulsive state to an hydrophobic attractive state in the constant distance ensemble.

In figure 3.43 the overall charge of the star is given. It is of considerable interest to see how confinement influences the local characteristics inside the stars. For this reason we show in figure 3.44 how the radial polymer profiles and the corresponding degree of dissociation change upon confinement.

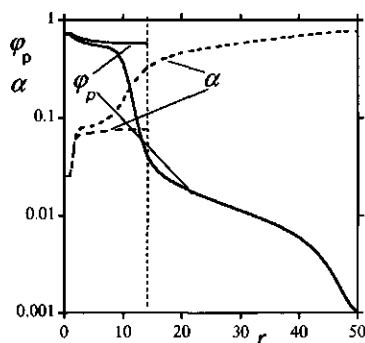


**Figure 3.44:** The radial polymer volume fraction  $\varphi(r)$  and radial degree of dissociation  $\alpha(r)$  profiles in semi-logarithmic coordinates for two values of the cell size  $D = 14$  (dashed lines). The cell dimension is indicated by the vertical dotted line, and  $D = 50$  (solid lines) for annealed PE stars with  $f = 20$  arms and arm length  $N = 200$  at  $\text{pH} = 6.6$ .

Here we selected  $\text{pH} = 6.6$  which, in the constant force ensemble, has a metastable distances in the range  $14 < D < 21$ . In figure 3.44 we present the profile for  $D_{\text{low}}$  and a profile for  $D = 50$  (representing a weakly interacting system). In these graphs the profiles are presented in semi-logarithmic scale so that also the dilute tail can be seen. In the dilute phase ( $D = 50$ ) the star is in a microphase segregated state: there is a poorly charged high-density core and highly-charged dilute tail. The structural features dramatically simplify in the compressed case (for  $D = 14$ ). Now the chains are homogeneously collapsed and barely charged throughout the entire star volume. The homogeneous state is consistent with a system of stars that is precipitated. The segment density and the degree of charging found in the collapsed part of the micro-phase segregated stars, tend to have the same values as the collapsed chains in strong confinement. This indicates that the transition found upon compression of the system is driven by the tendency to remove dilute tail as well as the interface between collapsed and swollen regions in the microphase segregated state.

### 3.9.2 Interacting PE stars in two-gradient model

The isotropic confinement as studied by means a systematic reduction of the dimension of a Wigner-Seitz cell is relevant for the interaction of a star with many neighbours, but had the intrinsic problem that the discrete nature of the interaction of the micelles was compromised. Therefore it is appropriate

to briefly pay attention to the interaction between two quenched HPE stars. This is possible using a two-gradient cylindrical coordinate system wherein two stars are positioned at the axis of the cylinder a distance  $H = 2D$  apart (cf fig. 3.2d). These calculations are targeted to deliver the interaction free energy between two similar stars. This type of information is often the input for more coarse grained (simulation) approaches, or are relevant for, e.g., AFM experiments wherein the interaction forces is measured between two particles: one adsorbed on the AFM tip and one sitting at a flat substrate. Moreover, the two-gradient modeling allows for a better microscopic picture of the changes in star morphology upon approach to another similar star, and provides additional insight in how a solution of hydrophobic polyelectrolyte stars behave in solution.

Here we study interacting stars for which cylindrical symmetry is imposed. Interestingly, this allows for a local bundling along the central axis analogous to the scaling predictions<sup>27</sup> and MD simulations<sup>100</sup> mentioned above. Yet in the radial direction the stars have a homogeneous distribution. By imposing the cylindrical symmetry on the pair of stars one will of course affect the mode of interaction between them: as compared to 'real' systems for which the lateral symmetry is not imposed, we will slightly overestimate the repulsive forces and/or underestimate attractive ones, albeit less severe than in the spherical symmetric case discussed above in section 3.9.1.

We here discuss just a single example of interacting stars with fixed amount of charge, that is, the quenched case. Unlike in one-gradient calculations, we are more restricted in the choice of parameters in two-gradient calculations. In this section we focus on quenched stars with  $f = 20$  arms, each arm is  $N = 50$  segments long. We select a relatively low salt concentration of  $C_s = 0.5\text{mM}$  to make sure that the charges are relevant compared to the otherwise poor solvent conditions. In more detail, we place a single star in the middle of a cylindrical lattice which is  $z_M = 60$  lattice sites high and has a radius of  $r_M = 30$  sites. Both at  $z = 1$  and  $z = z_M$  we implement reflecting boundary conditions. Also in the radial direction we impose reflecting boundary conditions at  $r = r_M$ . These dimensions are sufficient to consider this relatively small star to be in an isolated (non-interacting) state. While the star remains pinned with its center to the pinning coordinates  $(z, r) = (30, r \leq 2)$ , we reduce the system size in the  $z$ -direction by placing the upper boundary  $z_M$  to lower values of  $z$ . Hence the upper boundary comes towards the central star. Because of the mirror-like boundary conditions, the central star will start to interact with its image as soon as the distance between the grafting point and the upper boundary, which we will denote again by  $D$ , is close to the unperturbed star size. The interaction free energy of the system for given value of  $D$   $\Delta F^{\text{int}}(D)$

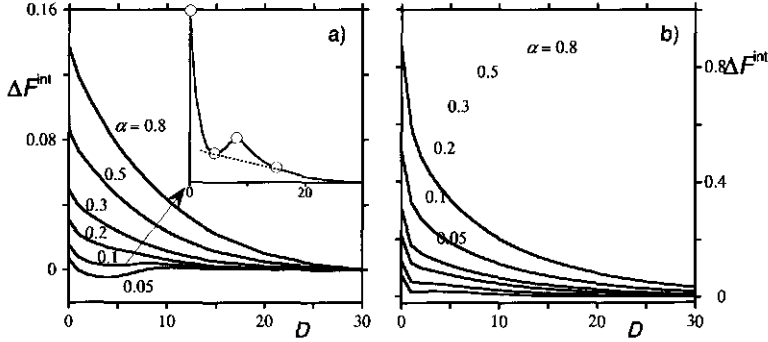


**Figure 3.45:** Free energy of interaction  $\Delta F^{\text{int}}(D)$  of quenched stars in different confinement geometries: a) interaction between two stars in a cylindrical coordinate system, b) in a Wigner-Seitz cell. Parameters: length of the arms  $N = 50$  and number of arms  $f = 20$ . The degree of charging  $\alpha$  is indicated. Recall that the distance between two stars is  $H = 2D$ . In the inset of panel a, an enlarged view is given for  $\alpha = 0.1$ . The circles indicate the positions for which in fig. 3.46 we present the profile and charge density contour plots. The dotted common-tangent line indicates the two distances that coexist in a constant force ensemble.

is computed from the free energy (partial open) for the distance  $D$  minus this value when the stars are far apart. As above we give this quantity in units of  $k_B T$  and normalise this per segment.

The interaction free energies depends on the fractional charge  $\alpha$  imposed on the charged segment as is shown in figure 3.45a. In line with results discussed above, we once again recover that when the brush is highly charged, e.g.  $\alpha = 0.8$ , the system is in the repulsive state, that is the stars repel each other monotonically. When the stars are weakly charged, on the other hand, there is a local minimum in the interaction curves, signaling attraction. At intermediate charge densities the force ( $-\partial \Delta F^{\text{int}} / \partial D$ ) is non-monotonic, pointing to a force-induced phase transition. For comparison we also present results for the same stars that are isotropically compressed in a Wigner-Seitz cell (cf fig. 3.42) in fig. 3.45b. From general considerations we should expect that a system which has the least number of constraints has the lowest free energy and of course the results of fig. 3.45 follow this trend. Clearly, significant values for the pair interactions of two stars set in at lower values of  $D$  (or  $H = 2D$ ) than for isotropically confined stars. Indeed, the pair interaction is much softer in the pair interaction than in the isotropic compression scenario. In the latter case stars are restricted

from all directions, while in the pair interaction the stars can change their morphology to adopt a more favorable conformation.

In a 3d configuration of closely packed stars, one typically expects that one star is surrounded by six neighbours (bcc lattice). From this we may anticipate that the  $\Delta F^{\text{int}}$  for very small values of  $D$  becomes 6 times higher in fig. 3.45b than in fig 3.45a. One should recall that the shortest separation in the two-star problem is  $D = 1$ , because the segments can be pushed out of the confinement region. In the isotropic confinement problem it is impossible to decrease  $D$  to such low values. Taking the free energy of interaction at the shortest possible compression distances in fig. 3.45a,b shows that the free energy is indeed approximately 6 times higher in fig 3.45b than in fig 3.45a.

Close inspection of results of figs 3.45a,b we notice that at very low charge density along the chain ( $\alpha = 0.08$ ) the two cases are significantly different: the pair interaction curve falls below zero in a rather wide range of distances  $D < 15$ , while in the isotropic compression case there is a strong repulsion  $5 < D < 20$  and a weak attraction when  $D \approx 3$ . We may explain this result from the overall notion that the isotropic confinement should be more repulsive, and thus less attractive, than the binary interaction case. More mechanistically we may mention that when two stars interact the chains can move out of the confinement region. This gives less electrostatic repulsion and also less changes in average conformations of the arms. Particularly in the contact region there is a change in the star density. When counterions match up with the polymer density the overall charge density can remain very low. In such case the hydrophobic forces can cause attraction between the polymer layers. This can happen when the charge density in the polymer is not very high. Quite obviously when the polymer charge is sufficiently high, there are also many hydrophilic counterions. These counterions mask the hydrophobic interactions and the stars can not attract each other.

We can only rationalize the more soft interaction potential found for the pair interactions as compared to the isotropic confinement with a relocation of the segments, it is appropriate to show this in corresponding polymer and charge distributions within the stars for various  $D$  values. For this, we focus on the system with a relatively low charge density  $\alpha = 0.1$  which has a non-trivial pair interaction curve, as in this system there is a two-phase state in the constant force ensemble. In the inset of fig. 3.45a, we present the interaction curve for  $\alpha = 0.1$  in an expanded scale. In this graph we have indicated by circles the distances  $D$  for which in figure 3.46 detailed profiles are presented. For  $H > 30$  the stars are far from each other and we may still consider these stars to be non-interacting and therefore we do not show these cases. At  $H = 30$  ( $D = 15$ ) and  $H = 8$  ( $D = 4$ ) the two stars feel approximately the same force. These two systems can coexist in the

constant force ensemble. This is seen from the common tangent line drawn in the inset of fig. 3.45a. At  $H = 32$  ( $D = 16$ ) we are in the meta-stable region of the interaction curve (only possible to observe in a fixed distance ensemble) the system switches from repulsion to attraction, and finally at  $H = D = 0$  the two stars have merged together to form one larger star with  $f = 40$  arms. The equal density contour plots for the polymer volume fraction  $\varphi_p(z, r)$  are given in the logarithmic units in the left panels of fig. 3.46. The corresponding overall charge density  $q(z, r)/e$  are given in the right panels. Cross sections of  $\varphi_p$  and the charge  $q/e$  through the common centers of the stars (that is in the  $z$  directions) are given for  $H = 16$  and  $H = 8$ .

On the top profiles, at  $H = 30$  the stars are still rather far apart and the stars remain close to the centrally-symmetric state and the profiles resemble the ones found in one-gradient calculations. The dense interior of the stars is surrounded by a very dilute corona composed of extended arms. The charge density has its highest absolute value at the center of the star, where the polymer density is the highest. The charge density gradually goes down towards the exterior. The white region outside the star has a positive charge density. This diffuse layer of counterions compensates the negative charge that is accumulated inside the stars. In the very center of the star the charge density oscillates which some artifact from the grafting condition of the charged chains at the core. More specifically, as we need to graft  $f = 20$  chains to the center we need a very small region. Also the grafting segment is neutral. This explains why in the very center the charge is relatively low. Due to the grafting the local polymer and thus the local charge density is high. This strongly attracts counterions and therefore we see just next to the center a region with lower charge density. Further away from the center the charge density behaves much more regular.

On the bottom profiles, at  $H = 0$ , the two stars have merged into a single one with double number of arms. As the overall polymer density is higher, the arms stretch more and the star has a larger dimension than in the top graphs. As the number of arms increased to  $f = 40$  we technically need also a slightly larger space to graft the arms onto. This is clearly seen in the charge contour plot where the black region is now somewhat wider than in the top graphs.

Recalling that in the constant force ensemble the star-system presented on the top of fig. 3.46 ( $H = 30$ ) coexist with the third set of graphs for  $H = 8$ . We therefore proceed to discuss the profiles for this distance. At this distance the system also switches from having an attractive force  $H > 8$  to a repulsive force  $H < 8$ . From the volume fraction contour plots we see that the two stars have now a central region with almost constant density (apart from the increased density at the grafting spots). The dimer star has

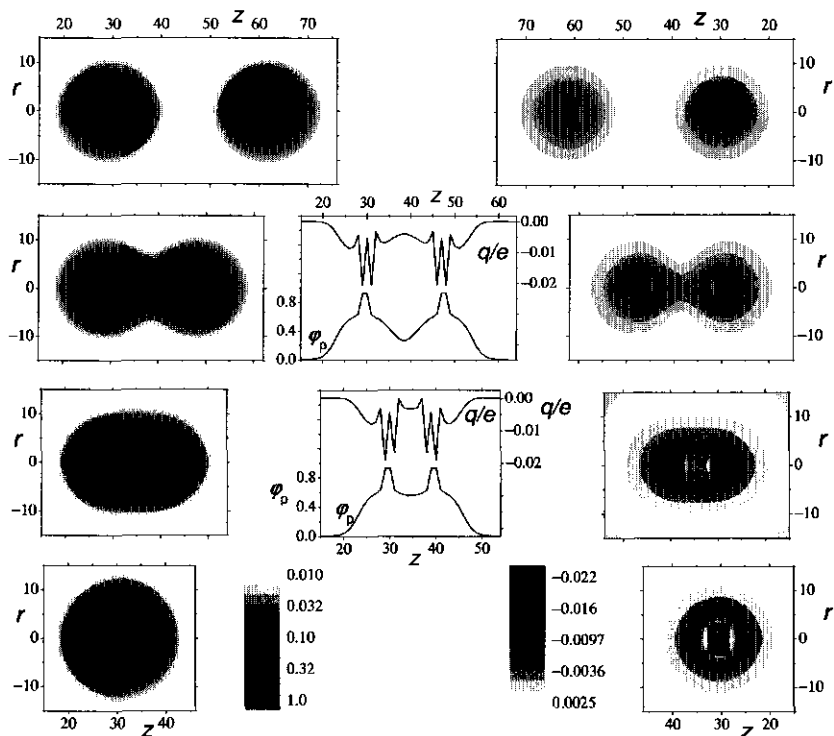


**Figure 3.46:** Equal polymer density (volume fraction) contour plots in logarithmic units  $\log(\phi_p(z, r))$  (left panels), equal overall dimensionless charge density contour plots  $q(z, r)/e$  (right panels) for four distances between the stars. From top to bottom:  $H = 30$  ( $D = 15$ ),  $H = 16$  ( $D = 18$ ),  $H = 8$  ( $D = 4$ ),  $H = 0$  ( $D = 0$ ) (see also the inset of fig. 3.45a). The color code for both types of contour plots are given at the bottom. For  $H = 16$  and  $H = 8$  we further present cross-section profiles at  $r = 0$  of the polymer volume fraction  $\phi_p(z, 0)$  as well as the dimensionless charge density  $q(z, 0)/e$ . Parameters  $N = 50$ ,  $f = 20$ .



an ellipsoidal form where the long axis of the core region is twice as long as the short axis. The peripheral part of the dimer star has a similar polymer decay as a single polymer star. The corresponding charge density has the remarkable feature that the overall charge in the region between the two grafting points is relatively low. As the polymer density and therefore the charge due to the polymer is not low, this must imply that the counterions have entered this region. We argued above that such a process is expected when the stars attract each other. The charge compensation due to the counterions allow the hydrophobic interactions to come into play and this causes the homogeneous polymer density between the cores.

For the intermediate distance  $H = 16$  ( $D = 8$ ), which corresponds to the local maximum in  $\Delta F^{\text{int}}$  we see that the merging of the stars has not yet taken place, albeit that a neck is being formed. From the volume fraction distribution we notice that between the two centers there is still a dilute region of tails sitting in the way. Also the charge density inbetween the two cores is relatively high. All this is consistent with the repulsive branch of the interaction curve.

More detailed information on the volume fraction profile and the charge density profile can be seen from the cross-section profiles that goes through both centers of the stars, that is at  $r = 0$ . In these graphs we notice the escape of polymer chains from the gap region to the regions away from the contact zone. This is seen because the polymer concentrations  $\varphi_p(z, 0)$  increase going from  $H = 16$  to  $H = 8$  case. This asymmetry is noticed better in the overall charge density profiles. As the polymer chains are quenched the difference between the polymer density and the charge density must be attributed to the counterion distributions. As already mentioned for  $H = 8$ , there are more counterions in the confined region than for  $H = 16$ . The asymmetry in the polymer density is particularly interesting in the  $H = 16$  system, where the polymer in the confinement region is relatively low compared to the unconfined region. For the  $H = 8$  system the asymmetric distribution of the counterions is most pronounced.

As expected there are interesting similarities for the interaction between two stars and that of the bilateral brush discussed in section 3.7. This is an interesting observation as the latter calculations are computationally inexpensive. The much more expensive calculations necessary for the interactions between two stars can therefore be replaced to a large extent by calculations of the bilateral brush. For example, similar calculations for the interaction between two annealed apolar polyelectrolyte stars will be of interest. We do not do this here and refer to the qualitative effects that are expected to the calculations of the corresponding bilateral brush.

Another very interesting next step would be to investigate how a third

polymer star merges with the dimeric polymer star. Basically one can envision two scenarios. 1. one will form a linear string of stars, 2. one will form a compact tri-angular object. The system will select the scenario with the lowest interaction energy. To solve this problem we have to go to a three dimensional SCF model.

It is appropriate to point to the similarities in behavior of the flat brushes and stars upon compression. Apparently there is a high degree of generality of the observed phenomena. Indeed, both for the flat brush (fig. 3.27) and for the star (fig 3.42) the free energy of confinement is non-monotonic: there is a long-distance repulsive interaction, which turns to a modest attraction at shorter distances for those cases that the chains are not extremely highly charged. This is followed by a strong steric repulsion at high compressions. These results indicate that such a repulsive-attractive-repulsive behavior is not specific for a particular geometry of the model, but rather depends on the molecular composition of chains themselves. This is an important finding for our potential generalizations of to practical applications where the detailed molecular structure may not be as ideal as assumed in our model. For example, in core shell particles, where the corona layer may be distinctly different from the ideal brush, or for which the core size does not differ much from the corona size, one may easily find cases that charged groups in the corona induce a repulsive contribution to the pair interactions at lower concentrations and hydrophobic attraction may lead to discharging of the corona at higher concentrations. This may have consequences of how suspensions of these core-shell particles turn into a film upon drying. Our results may also have important consequences for the rheology of concentrated solutions of core-shell particles.

### 3.10 Discussion and conclusions

We have studied polymer brushes and polymer stars composed of hydrophobic polyelectrolyte chains. The molecular features were chosen to mimic properties of acrylic core shell particles that are used in waterborne paints. The flat blush is appropriate for the case that the core is large compared to the shell whereas the star is relevant for the opposite case. We extensively studied both weak and strong polyelectrolyte systems. We limit ourselves to ideal homodisperse brushes and stars with homogeneously distributed charged groups.

We used the self-consistent field method. For many polymer brush problems there are analytical predictions. However for the hydrophobic polyelectrolyte (HPE) systems there are so many complications that we have resorted to a

numerical analysis using the method of Scheutjens and Fleer. It is believed that for polymer brushes and many-armed stars the theory gives a good description both in terms of the structural as well as thermodynamic properties. We used one-gradient calculations to study the conformations of brushes and stars under various conditions and found that the HPE brush and stars can be in a microphase segregated state. This complex internal structure has consequences, e.g. for the colloidal stability. The study of two interacting brushes is still possible in a one-gradient theory. However, for the interaction between two stars we used a computationally more expensive two-gradient version. Interestingly the interaction of stars with many neighbours can still be mimicked using a one-gradient approach, confining the star effectively in a cell with decreasing size. In passing we have studied how a sparsely grafted brush can form surface micelles on a hydrophilic surface when the grafting density is sufficiently low. The interaction between two of such layers also required a two-gradient analysis. A novel aspect of our work is the study of the interaction between a bilateral flat brush. In this case the chains are grafted onto a penetrable surface so that upon confinement the chains can escape from the compression region. A similar chain rearrangement is possible when two polyelectrolyte stars are interacting.

Our most important results are:

- 1 In a broad range of parameters both brushes and stars can segregate in dense (weakly charged) hydrophobic 'core' phase and dilute (highly charged) shell phase. The distribution of end-points tends to be bimodal proving that for very long chains this two phase state develops abruptly upon an increase in grafting density, decrease in solvent quality and increase in ionic strength. The intermediate polymer density case is highly unfavourable as the intermediate density suffers from many unfavourable polymer-solvent contacts and strong electrostatic repulsion.
- 2 In concentrated solutions of microphase segregated stars, or upon compression of two microphase segregated brushes, we observed non-monotonous interaction forces. At large distance the layers repel each other. This repulsion originates from the overlap of the dilute charged regions. This repulsion turns into attraction at some intermediate distance. In this attractive regime the dilute shell disappears and the interface between core and shell disappears. Obviously further compression increases the free energy again wherein the core layer becomes more dense. There are various consequences of this type of interactions. One of these is that macroscopically a system of HPE stars may phase separate into a two phases, one rich and one more dilute phase above a given osmotic

pressure. The nonmonotonic interaction curves point to non-trivial rheological behaviour of concentrated HPE star solutions.

- 3 Many results found for the flat HPE brushes have a close resemblance with results for HPE stars. This indicates that the curvature effects are minor. Realising that a microphase segregated star, the size of the core is not extremely much smaller than the shell and therefore the outer region of the composite star is not so much different from its flat counterpart.
- 4 The bilateral brush allows for chain repartitioning when broad in asymmetric compression. Qualitatively this mimics the degree of freedom that chains have in interacting stars. Hence, the bilateral brush may be effectively used for a fast qualitative analysis of pair interactions in polymeric colloidal solutions. Upon confinement of annealed (pH dependent charge) brushes, it was found that in the attractive range of interactions part of the chains may enter the confined zone while discharging themselves. Upon further compression the chains are pushed away again.

Our results are not only relevant for acrylic core shell particles and their colloid chemical stability. There are many polyelectrolyte brushes of various geometry in nature which consist of relatively poorly soluble chains decorated both with positively and negatively charged units. The interesting interplay between the hydrophobic attraction and the electrostatic repulsion makes these systems responsive for external stimuli.

## Chapter 4

# Interactions Between Acrylic Core-Shell Particles Measured with Colloidal Probe AFM <sup>a</sup>

### 4.1 abstract

Colloidal probe AFM force measurements were performed between randomly closely packed monolayers of acrylic core-shell particles (CSP) irreversibly adsorbed onto silanized SiO<sub>2</sub>. Interaction forces were measured at room temperature both in water and in a 30wt% butyl glycol - water solution. The cores contain many methacrylates and are glassy in the absence of butyl glycol. The chains that form the shells of the particles are composed of a mixture of hydrophobic acrylic and methacrylic acid monomers and are solvated by water at sufficiently high pH. The measurements were performed at several pH values and for ionic strengths of 0.1 M and 0.01 M. In line with theoretical predictions for corresponding hydrophobic polyelectrolyte brushes, the results show a clear pH-dependence of the interaction forces. The AFM results correlate well with dynamic light scattering and proton titration measurements of these CSP dispersions. Our data point to the possibility of a microphase segregated state of the shell chains, which upon compression form a neutral, dense, homogeneous film. In a window  $6 < \text{pH} < 8$  the forces differ between approach and retraction, which is consistent with the formation of bridges. Retraction curves were measured for several surface waiting times  $t_s$ . The probability of occurrence of bridges increases with increasing  $t_s$  and/or lower measurement speeds. Bridges form with a characteristic time of about 10 s. The formation of bridges was confirmed by

---

<sup>a</sup>To be submitted P.A. Iakovlev, J.M. Kleijn, F.A.M. Leermakers

fitting the retraction curves by self-consistent field predictions for stretching of hydrophobic polyelectrolyte chains in the brush configuration. The co-solvent butyl glycol is a plasticizer for the core and facilitates the irreversible detachment of shell chains from the core at high pH values. The dramatic influence of butyl glycol on the force curves is attributed to the de-looping of shell chains. The combination of AFM force measurements and modeling thus presents a detailed picture of the conformation of and interaction between these core-shell particles.

## 4.2 Introduction

The colloidal probe AFM (CP AFM) method was developed by Ducker and coworkers<sup>101</sup> and by Butt et al.<sup>102</sup> In this technique one glues a rigid spherical particle of a few  $\mu\text{m}$  in size to an AFM cantilever. The shape of the probe is well defined, which eliminates uncertainties regarding the cantilever tip size and geometry and makes a comparison between theory and experiment possible. First experiments with CP AFM considered interactions between bare surfaces.<sup>101,103–109</sup> Later this technique expanded to studies of interactions between polymer-covered surfaces.<sup>110–113</sup> In general, colloidal probe force measurements are used to consider interactions between homogeneously covered surfaces, but measurements of interactions between surfaces covered with separate polymeric micelles,<sup>114</sup> or dendrimers<sup>115</sup> are reported as well. Here we study interactions between large core-shell particles (CSP), adsorbed on the surface of a silica colloidal probe and a flat silica surface. As we show below, the number of particles that contribute to the interaction is rather low (order 50). Hence we needed to measure the interactions enough times to obtain statistically significant results.

Polyelectrolytes are often used in colloidal systems to provide their stability.<sup>4</sup> In some cases polyelectrolytes are chemically attached to the surfaces of colloids, in other they may be physically adsorbed onto them. The theory for adsorbed or grafted polyelectrolyte layers is well-developed in a large number of theoretical publications. Surface force measurements have been used to investigate interactions between surfaces in the presence of polyelectrolytes in solution, and more recently between polyelectrolyte brushes as well. For an overview of theory and force measurements on surfaces in the presence of polyelectrolytes we refer to the work of Claesson et al.<sup>62</sup> and references therein. In general, the presence of even a small amount of ionic groups in the interacting polymer layers, provides for their strong electrostatic repulsion.

Our core-shell particles have acrylic chemistry and are an analogue of the basic colloidal component in commercial waterborne automobile paint

dispersions. The methacrylic cores are in a glassy state in aqueous environment at room temperature, and the shells may be described as hydrophobic polyelectrolytes (HPE): the monomeric composition of the polymer chains is 56%wt butyl acrylate, 25%wt hydroxyethyl acrylate and 18%wt methacrylic acid (for a detailed description of the CSPs see chapter 2 of this thesis). The CSPs are extremely responsive to pH changes in the region around pH 7, and our main interest lies in the changes in particle interaction forces with change in pH. The influence of the ionic strength of the solution on the interaction of polyelectrolytes is much investigated and well understood (see references above), and will be studied as well for our specific system, but in less detail. Concentrated dispersions of the particles are non-Newtonian, showing shear-thinning behaviour with roughly a four orders of magnitude drop in viscosity with an increase in shear rate. This behaviour is relevant for industrial applications and has been modelled with coarse-grained MD simulations.<sup>116</sup> These coarse-grained simulations need interaction potentials between the particles as an input. Such interaction curves can, at least in principle, be extracted from CP AFM measurements. Inversely, with the help of MD simulations CP AFM results can be related to the macroscopic properties of a CSP dispersion. To rationalize the CP AFM results we here make use of the Scheutjens-Fleer self-consistent field (SF-SCF) method.<sup>85,86</sup> In chapter 3 we have built a general theory for HPE brushes and stars using this approach. Below we will use the same method with a tuned molecular model for the corona chains to rationalise the CP AFM findings.

In waterborne paint systems used in applications where durability is necessary, there is typically some co-solvent present.<sup>117</sup> The most widely used co-solvent is 2-butoxyethanol (butyl glycol; BG). BG is miscible with water in all proportions and has proven to be the most effective of large number of organic solvents tested in a wide range of aqueous coating systems. It serves as a coalescing aid, lowering the film-forming temperature and improving evaporation behavior of water during hot drying. There are many detailed questions on the effect of a co-solvent on CSPs. For this reason we report here on the effects of BG as seen by CP AFM measurement and compare the results with those in the absence of co-solvent. Contrary to water, butyl glycol is a good solvent for all non-ionic monomers composing the CSP. This means that these monomers are solvated by BG<sup>118</sup> and that density of polymer, at least when deionized at low pH, will be lower than in pure water. The interplay of solvents, one of which is a good solvent for non-ionics and the other one for ionized groups, is interesting in itself and needs a separate theoretical consideration.

This chapter is organized in the following manner: we first describe the method used to immobilize the CSPs at a silica surface without loosing their

solution properties. Then we present the results of interaction measurements in aqueous solutions for several pH and ionic strength values obtained during fast and continuous approach-retract cycles. Results are interpreted by comparison with complementary SCF predictions. After this we focus on the origins and dynamics of polymer bridge/entanglement formation. This is done by studying the stretching of bridges that form after compressing the particles for a fixed time  $t_s$ . Again our interpretation is assisted by SCF modeling of stretching chains. We finalize our study with a short overview of the effect of co-solvent on the force curves and finish by presenting our conclusions.

## 4.3 Materials and Methods

### Core-Shell Particles

The core-shell particles (CSP) were synthesized via emulsion droplet polymerization by Nuplex Resins BV. The monomeric composition of the particles is described in chapter 2 of this thesis (and table 2.1). The particle dispersion was dialyzed in-house against demi-water through an MWCO = 50000 spectrapor membrane for two weeks. The dialysis step is necessary to eliminate low molecular weight residues of the synthesis: the surfactant, unreacted monomers, short soluble polymer chains and salt ions.

An extensive characterization of the particles is given in chapter 2. Relevant parameters for the AFM force measurements can be found in table 2.2 of the same chapter. When the CSPs are, at room temperature, dispersed in water, the cores of the particles are in a glassy state, because they are formed by apolar methacrylic polymers with a high  $T_g$  ( $T_g > 40$  °C). Butyl glycol is expected to penetrate into the cores and act as a plasticizer for them.

The shell polymers bear pH-dependent chargeable groups (methacrylic acid). In the absence of charges the HPE precipitate due to the remaining hydrophobic nature of the chains. Hence the colloidal stability is lost at low pH values (pH < 4.5 at an ionic strength of 0.01 M; pH < 4.8 at 0.1 M and pH < 5.5 at 1 M).

### Adsorption

To perform reliable AFM interaction measurements between two layers of adsorbed CSPs the density (surface coverage) of these layers should be reproducibly as high as possible. The adsorption of such large particles is described by the random sequential adsorption (RSA) model.<sup>44-46</sup> According to this model, the maximal surface loading, also called the jamming limit, occurs



when 54.7% of the surface is covered by particles (for spherical particles adsorbing on an infinite surface). To reach this value, the particle-particle repulsion should be screened to the maximal possible level, yet preventing direct precipitation of the particles (critical solution) and the particle-surface attraction should be switched on. We adsorbed the particles from 1 M NaCl solution at pH = 5.5 and particle concentration  $c_p = 2$  g/l. This solution is indeed near critical: particles slowly precipitate within a day. Additionally, the silica surfaces had to be hydrophobized before adsorption of CSPs occurred.

The colloidal probes are silica spheres ( $R_{cp} = 3 \mu\text{m}$ ) from Philips Research Laboratories (Eindhoven, The Netherlands). The probes are glued to standard silicon nitride contact mode cantilevers (Veeco, CA) with a spring constant of  $k = 0.07 \pm 0.02$  N/m, determined by the thermal noise method.<sup>119</sup> The flat silica surfaces are silicon wafers (WaferNet, Germany) with a silicon oxide layer of 100 nm on top of them. Both the silica probe and the flat substrate were extensively cleaned and immersed in a "piranha solution", i.e., a hot mixture of 30%  $\text{H}_2\text{O}_2$  and concentrated  $\text{H}_2\text{SO}_4$ , for 15 minutes. The latter is needed to obtain a high density of Si-OH groups on the surfaces. Immediately after the activation, the cantilevers and wafers were placed in a dessicator with a few ml hexamethyldisilazane (Sigma-Aldrich) on the bottom. After overnight stay in a dessicator, the surfaces are hydrophobic and ready for use during the next 12 hours.<sup>120</sup> The particles were adsorbed from solution during 5 minutes, and then the excess was thoroughly rinsed with water. A schematic picture of the adsorbed layers (both on the flat- and on the probe surfaces) is presented in figure 4.1a.

For each series of measurements we adsorbed the particles on two identical wafers. One of them is used for the CP AFM measurements and the other one for AFM imaging. The latter experiment is to check the success of the adsorption procedure. A typical image of a layer of CSPs on the flat surface is presented in fig. 4.1b. This image was obtained in a fluid cell using tapping mode in a Nanoscope IIIa scanning probe microscope (Veeco). Graphical analysis of this image reveals that the coverage is indeed close to the maximal possible packing value, namely  $52 \pm 2\%$ .

The immobilization of the particles was checked both by scratching the layer in contact mode AFM and attempts to remove them with a strong flow of water, air or concentrated NaOH and HCl solutions. Every attempt failed.

However, the layer degrades with time, as seen by force curves reported below. Typically, after some 12 hours at ionic strength  $I = 0.01$  M, the measurements become less reproducible. We attribute this effect to the desilanization of the surfaces. Especially the hydrophobicity of the colloidal probe is at risk. Contrary to the flat wafer, a single spot on the colloidal

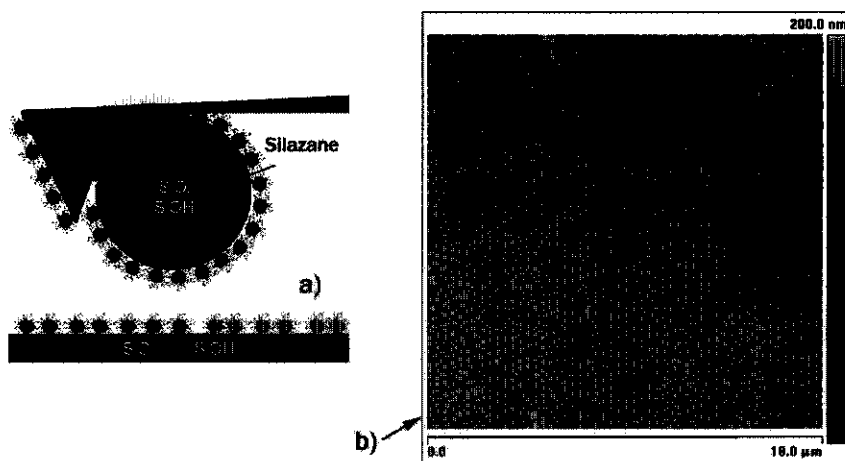


**Figure 4.1:** a) Schematic illustration of the adsorbed CSP layers on the flat substrate and the colloidal probe (CP). Both the CP and the flat surface were first covered with a layer of hexamethyldisilazane onto which the CSPs readily adsorbed from a 1 M NaCl solution. b) Tapping-mode AFM image of the CSP layer on the flat substrate in aqueous solution. pH = 5.5,  $I = 0.1$  M.

probe is used continuously during the measurements. The degradation of the layer is faster at high ionic strengths of the solution (and in the presence of butyl glycol).

### Force Measurements

CP AFM force measurements were performed using a Nanoscope III AFM (Veeco), equipped with a fluid cell and PicoForce extension. Electrolyte solutions with different pH values were prepared with a phosphate buffer, and protected against bacterial growth with 0.02 % NaN<sub>3</sub>. Solutions were degassed, filtered and the pH was measured before each series of force measurements. After each change in solution conditions the system was allowed to equilibrate for 30 minutes. The solution in the cell was kept under a slight external pressure to avoid bubble formation.

As estimated from AFM images, the size of the core of the CSP  $R_d$ , is  $60 \pm 5$  nm (in a dry layer when the size of the shell is negligible). As the colloidal probe is curved, there will be a limited number of CSPs that can possibly come into *direct* contact with the opposite flat monolayer of CSPs. We make an estimate of this number via simple geometrical construction (see

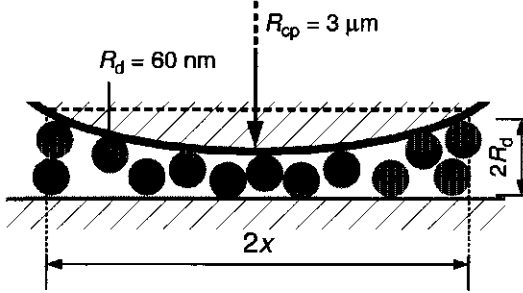


**Figure 4.2:** Calculation of the number of particles in the contact area between CP and flat surface  $n_{\max}$ . Here  $2x$  is the diameter linked to the maximal possible area in close contact. This value is found via a simple geometrical consideration and a parametric equation for the points on a circle with center at  $(0,0)$  (center of CP), i.e.,  $x = \sin(t)$ ;  $R_{cp} - R_d = y = \cos t$  where  $t$  is the angle between two lines: one from the center to a point  $(x,y)$  on the circle, the other is the vertical line through the center.

figure 4.2), i.e.,

$$n_{\max} = \Gamma_{\text{surf}} \times R_{\text{cp}}^2 \times \frac{1 - \left( \frac{R_{\text{cp}} - R_d}{R_{\text{cp}}} \right)^2}{R_d^2} \quad (4.1)$$

where  $\Gamma_{\text{surf}}$  is surface coverage of the CSP layer ( $\Gamma_{\text{surf}} = 0.52 \pm 0.02$ ) and  $R_{\text{cp}} = 3 \mu\text{m}$  is the radius of the colloidal probe. From this the estimate of  $n_{\max} = 50 \pm 2$  particle cores that come in direct contact is found. This is a rather small number, and due to the random position of the particles the pairs of head-on contacts is likely less. As a result, our measurements are intrinsically discrete. Hence we need some statistical averaging. This is done by performing similar measurements on different spots of the flat substrate. Typically, five spots were used, namely four spots that are located at the corners of a square with 300 nm sides and one at the center of this square. Several measurements are taken at each of these spots. Typically, at least 30 approach-retract cycles were taken at constant measurement conditions such as speed, applied force and surface delay time  $t_s$ . Unless mentioned otherwise the speed of approach and retraction was 300 nm/s. Sometimes a lower speed of 60 nm/s was used as well.

The approach curves were treated as measurements on homogeneous layers. The motivation for this is that the shell polymers extend far enough to cover the empty spaces on the surfaces. In this case it is possible to use

the Derjaguin approximation and divide the measured force  $f(H)$  for given distance  $H$  by the radius  $R$  of the colloidal probe:<sup>121</sup>

$$f(H)/R = 2\pi\Delta F(H) \quad (4.2)$$

to obtain the interaction energy  $\Delta F(H) = F(H) - F(\infty)$  per unit area. The latter can directly be compared to the interaction energy as predicted by numerical SF-SCF modeling.

### Measurements in 30% butyl glycol solutions

Dynamic light scattering (DLS) combined with pH titration is used to measure the hydrodynamic size of the particles as a function of pH. Viscosities of butyl glycol - water mixtures were measured using a Vilastic-3 (Vilastic Scientific Inc., Austin, Texas, USA) apparatus. The viscosities were used to convert the diffusion coefficient of the particles to the size of the particles.

The DLS-titration measurements are performed at a scattering angle  $\theta_s = 90^\circ$  on an ALV light scattering instrument, equipped with an ALV-5000 digital correlator, a 1 W argon ion laser operating at a wavelength  $\lambda = 514.5$  nm, and a custom-built measuring cell to which acid or base can be automatically titrated with a Schott-Geräte titration setup. After each addition the solution is stirred and allowed to equilibrate for 10 minutes. The ionic strength of titrant was matched to that of solutions and the temperature was controlled using a Haake F3-K thermostat.

The adsorption of CSPs onto wafers and colloidal probes was performed in a similar manner as for the aqueous solutions, though the particles were adsorbed from a solution of  $I = 0.5$  M ionic strength because at an ionic strength of  $I = 1$  M the 30wt% butyl glycol solution phase separates into a water rich and butyl glycol rich phase. Note that the ionic strengths are given in moles per liter of butyl glycol - water mixture.

### Theoretical fitting of the data

The structural properties of hydrophobic polyelectrolyte brushes can, on the mean field level, be simulated using the SF-SCF theory. In this approach a freely-jointed chain model is used to estimate the conformational degrees of freedom of the conformationally disordered shell chains, with the constraint that one of the chain ends is at the surface. The hydrophobic nature of the chains is accounted for using the Bragg-Williams approximation and parameterized by Flory-Huggins nearest-neighbour interaction parameters ( $\chi$ ). Electrostatic interactions are treated on the Poisson-Boltzmann level, wherein the ions have a finite molecular volume. The pH dependence of the

chargeable groups is accounted for locally and the system is expected to be, also locally, incompressible. For a detailed description of this theory we refer the reader to the chapter 3 of this thesis and refs.<sup>85,86</sup>

The SF-SCF theory pre-assumes equilibrium. Even though the experimental systems rarely are fully relaxed, it is still reasonable to use this approach to try to rationalize some aspects of the CP AFM interaction curves. A key step is to come up with an accurate model for the shell chains. The general theory of hydrophobic polyelectrolyte (HPE) brushes and stars, developed in chapter 3, was elaborated on using a somewhat idealized model. Here we use an adjusted set of parameters that, as we believe, is more reasonable tuned to the experimental system. Again, in the SF-SCF model equilibrium is assumed. From this we do not expect any differences between approach and retraction curves. Insufficient equilibration in a molecular system can only be mimicked by imposing additional constraints. The latter appears necessary to understand the forces found upon retraction.

The calculations are performed on a discrete lattice, and all the dimensions in the procedure are expressed in units of lattice sites, which for polyelectrolyte systems is usually taken as the Bjerrum length,  $l_b = 0.7$  nm. For the direct comparison with experimental data we convert the results of our model to nanometers, nanoNewtons, etc. The ionic strengths and the pH values of the solution closely match the experimental ones. Below we will use this approach for two distinct aspects of the CP AFM results, namely the forces found upon approach of two layers of CSPs, and for the stretching of chains that bridge between two particles. The latter is a process which is expected when the distance between the surface and the probe is increased, that is, when the cantilever is retracted.

*Modeling the forces upon approach.* We will model the approaching surfaces as if two flat surfaces are covered by two laterally homogeneous HPE brushes. Here we adopt the model of spherically symmetric core-shell particles, which was presented in chapter 2 of this thesis.

Polymers are composed of slightly hydrophobic segments,  $\chi_m = 1$  and a fraction  $\alpha$  of these segments is weakly acidic with  $pK = 5.3$ . Polymer chains consist of  $N$  segments and are grafted to a planar surface with density  $\sigma_N$ . To avoid depletion effects near the surface, it is made attractive for polymer segments,  $\chi_{sm} = -1$  and hydrophobic as well  $\chi_{sw} = 1$ . This choice effectively compensates for the entropy loss of chains near an impenetrable surface.

To fit the experimental data closely we choose to adjust the polymer chain length,  $N$ , or even take polydisperse brushes into consideration. The reason behind this is our view that the shell chains form multiple loops (the reasoning is elaborated in more detail in the results section and conclusions).

On the other hand, we wish to keep our model alike the experimental system, so we stick to the well-defined properties of the CSP system such as acid groups fraction,  $\alpha = 0.25$ , and charge density per unit of surface area,  $\Theta_c = 5.5\text{nm}^{-2}$ . Fixing these two parameters also means a fixed polymer density per unit area,  $\Theta_p = \Theta_c/f = 22\text{nm}^{-2}$ . For the monodisperse brush  $\Theta_p = N\sigma_N$ , thus adjusting  $N$  to fit the data would mean changes in polymer grafting density as well: longer polymer chains would be grafted more sparsely than short ones. For the polydisperse brush we adjust  $\Theta$  for every chain length so that the total density would stay equal  $22\text{nm}^{-2}$ .

*Modeling the forces upon retraction.* Below we will show that the retract curves depend on the delay time, that is, the time that the surfaces are forced to be in close contact. We believe that when the shell chains strongly overlap entanglements develop, or, equivalently, bridges form. When subsequently the surfaces are pulled apart with a sufficient speed, the entanglements/bridges remain present for some displacement and the forces that are measured are dominated by the stretching of chain fragments that make contact with opposite surfaces (bridges). Quite obviously we need a different model for these stretched chains. As the length of the chains is important we opt for a system of polydisperse chains with a degree of polymerization  $N = 100, \dots, 212$  with a steps of 28 segments. All these segments have two constraints: the chains are grafted by both ends, one end on each surface. Thus the chains bridge between two flat opposing surfaces. The polymer density per unit area is fixed once more, that is  $N \times \sigma_N$  is constant. As the bridging occurs when the shells of two interacting particles form a single dense phase, we choose that the overall densities of the layer ( $\theta$ ) is twice that of the ones used in previous paragraph. The motivation to have smaller values for  $N$  as in the previous paragraph is that it is unlikely that in experiments the bridging occurs by the end segments of the polymers. More realistically, a bridge forms by adsorption of chain fragments onto opposing surfaces or stick to opposite shell chains (entanglements), which involves tens of monomeric units and loops can be formed as well. So the effective stretchable length of the chains is not the full contour length. The SF-SCF theory gives the free energy as a function of the separation distance  $H$ . These results can be reduced to the force exerted to each chain. The fitting of the measured force by these theoretical results gives insight in the number of active bridges with specified length.

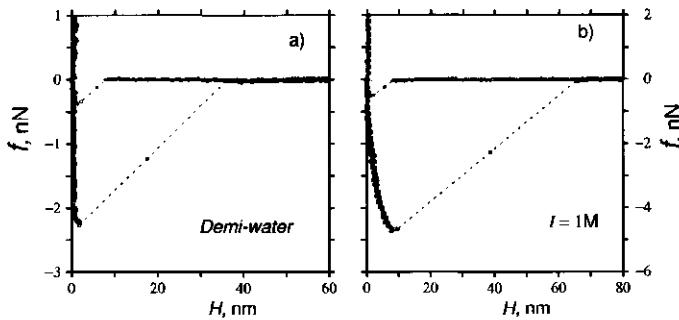


**Figure 4.3:** CP-AFM force curves upon approach (circles) and retract (squares) for bare hydrophobized silica wafer and hydrophobized colloidal probe surfaces in a) demi-water. b)  $I = 1 M$  (NaCl).

## 4.4 Results

### Bare surfaces

We start this section with AFM force plots of bare silanized silica surfaces interacting without any particles adsorbed (Fig. 4.3) for both demi-water and 1 M buffer solution. These measurements serve as a reference: if (by chance) the CSPs are removed from the interacting surfaces in the course of our measurements, we would start seeing the bare surfaces interactions. For both demi-water and 1 M salt solution there is absolutely no electrostatic repulsion between the surfaces: the surface charge is removed by the pre-treatment of the surfaces, and the OH groups have reacted with the silane molecules that turned the surfaces hydrophobic. Referring to fig. 4.3 we see adhesive forces on both approach and retraction. The surface jumps into contact upon approach at a small distance. Upon retraction the surfaces refuse to separate until a large force is applied and then a jump-like release is observed. Such hysteresis loops are consistent with the fact that the solvent does not interact favorably with the substrates, confirming the successful silanization of the silica surface and probe.

### Force measurements upon approach of CSP layers in aqueous solutions

In fig. 4.4 we present typical force curves recorded during the approach of the probe to the surface in semi-log coordinates at  $I = 0.01 M$  for several pH values indicated on the plot. Measurements for  $v = 300 \text{ nm/s}$  and  $v = 60 \text{ nm/s}$  piezo movement velocities are presented in fig. 4.4a and 4.4b, respectively.

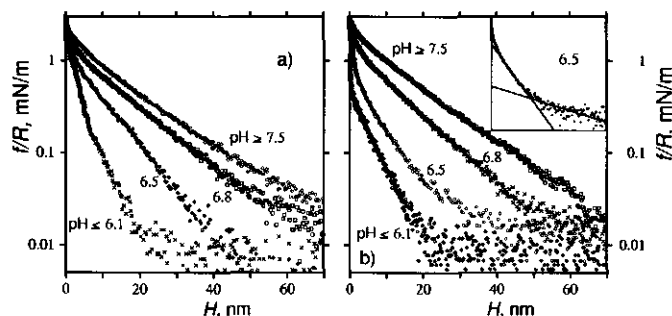


**Figure 4.4:** CP-AFM force curves upon approach of two CSP layers in semi-log scales for a number of pH values as indicated. The ionic strength is  $I = 0.01$  M. Speeds: a)  $v = 300$  nm/s and b)  $v = 60$  nm/s. Interaction curves for  $pH \geq 7.5$  were very similar to the one at  $pH = 7.5$  and are not presented here. The same applies for the curves at  $pH \leq 6.1$  which were close to the one at  $pH 6.1$ .

It was found that the interaction curves depend on the pH in a window of pH values between 6.1 and 7.5. Curves for both  $pH \leq 6.1$  and  $pH \geq 7.5$  are all similar to those at the lower and upper limit, respectively. The fact that only around pH 7 the curves are pH sensitive is consistent with the CSP characterization (see chapter 2): at a high pH ( $> 7.5$ ) the shell chains are (nearly) fully charged and swollen and at low pH ( $< 6.1$ ) they are (almost) deionized and collapsed. In these extremes the chain conformation will not change much when the pH is changed.

From comparison of figs. 4.4a and fig. 4.4b we can judge the influence of the speed at which the force curves were recorded. At a high pH, that is,  $pH \geq 7.5$  there is little influence of the measuring speed. At a lower pH, however, there is a clear trend that curves recorded at a lower approach velocities are generally less repulsive. This indicates that there is a rather slow equilibration taking place upon approach. At high speed ( $v = 300$  nm/s) there is not enough time for an equilibrium collapse to a dense phase. Hence the repulsion is stronger than when the system had sufficient time to collapse their shell chains (e.g. for  $v = 60$  nm/s). We conclude that the deionization and compactization of the shell polymers is not an extremely fast process. Considering that the brush height is on the order of 60 nm we conclude that the relevant relaxation processes apparently are on the second time scale.

The rather straight lines in the semi-log coordinates indicate that the force curves in fig. 4.4a follow a single-exponential decay. At high pH the repulsive force is characteristic for the compression of a hydrated polyelectrolyte brush. In fact, one has to work against the osmotic pressure generated by the



counterions inside the shell layer. Only at very small separation distances some extra repulsion is found, which is steric in nature (compacting a dense brush is hard). We note that for  $\text{pH} = 6.1$  and  $6.5$  a double-exponential decay was found, with a sharp change of slopes at  $H = 20$  nm. In the inset of fig. 4.4b we present the curve for  $\text{pH} = 6.5$  with the exponential fits. A break in a force curve indicates that the layer suffers a sharp structural transition.

The theory of hydrophobic polyelectrolyte brushes predicts that an isolated HPE brush can be in a micro-phase segregated state. In such two-phase state some chains are charged and fully extended, whereas other chains are uncharged and collapsed in a dense, melt-like film. Upon compression the theory shows that there is a repulsion at large distance due to the compression of the charged and swollen PE-layer. Upon confinement the set of charged chains can suddenly disappear (they cooperatively loose their charge) and then attraction is found. This attraction is characteristic for the interaction of two neutral collapsed brushes: the removal of excess water is favorable. Upon further compression one always will return to a repulsive regime again when the collapsed brush is compressed to higher and higher densities. The theory also indicates that there can be scenarios that the attractive part in the curves is small or even absent and then the force is fully repulsive. This occurs when the swollen and charged shell layer is not very large at the moment of the transition. In this case the kink in the curve separates the regime of compression of a water swollen shell from the regime of the compression of a uncharged dense brush. The theory proves that a gradual transition with part of the chains still charged and repelling each other and the other part deionized and attracting, is unfavorable. In part this is attributed to the cooperative escape of the hydrophobic monomers of the chain from the water-rich phase (for more information see chapter 3).

One interesting aspect of the force curves of fig.4.4 is that, though the ionic strength of the solution is the same for all curves, they have a pH-dependent slope (in the log-lin coordinates). One may explore the idea that the forces are of a DLVO-nature. In the DLVO theory, e.g. for colloids with a pH-dependent surface charge, one would expect a shift in the strength of repulsion with pH, but not a shift in the decay length. The latter is, in the DLVO-context, a function of the ionic strength of solution.<sup>122,123</sup> The ionic strength in our measurements is fixed to 0.01 M. So, the Debye length  $r_d \approx 3$  nm. The range of the interactions we measure is substantially larger. Hence, we conclude that the reason for the long-range repulsion in fig. 4.4 must be related to the HPE brush properties. Indeed, we notice that only when the shells physically start interacting ("touch") the repulsion sets in.

In our system the number of charges in the shell chains depend on the pH. To a reasonable approximation we may expect that there is a local

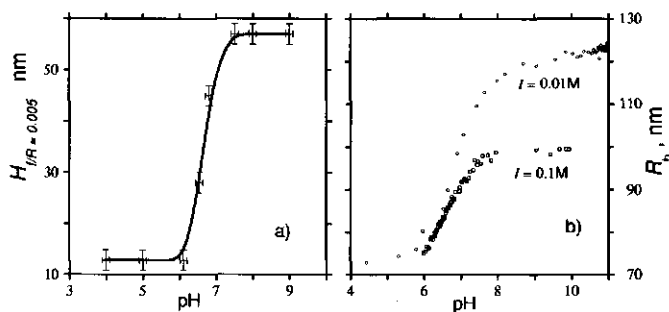


**Figure 4.5:** a) The distance between colloidal probe and silica wafer measured during CP-AFM force measurements at  $f/R = 0.005$  mN/m vs pH of solution.  $I = 0.01$  M b) DLS-titration measurements of particle hydrodynamic radius  $R_h$  as function of pH of the solution. The ionic strength is indicated.

electroneutrality. This implies that the number of counterions is locally equal to the local number of dissociated acid groups. When the shell is compressed, we also limit the space for the counterions. Indeed, the force we measure when the shells are compressed is related to the work against the osmotic pressure of the counterions. As our chains have annealed charges, the compression leads to some deionizing of the chains. If the chains completely loose their charge, that is at low pH, the hydrophobic attraction becomes the dominant one.

Above it was mentioned that the onset of the repulsion of the brush appears to correlate with the size of the particles in the swollen state. Interestingly, this opens a route to determine the CSP shell thickness as function of pH. To make this idea operational we need to decide from the force-curves where the interaction starts. One may use the Ansatz that the free energy of interaction should be around  $k_B T$  per particle. Unfortunately, the value of interaction energy ( $f(H) \sim 1 k_B T$ ) is way below the sensitivity of our CP AFM measurements. This is why a more pragmatic choice is implemented. To see a qualitative trend for the size of the particles with pH we draw a line at arbitrary low value of the force, namely at  $f/R = 0.005$  nN, and determine the intersections of this line with the curves as a measure of shell thickness. We present the results of this approach in fig.4.5a alongside with results from DLS - titration experiments in fig.4.5b (which give the hydrodynamic radius as a function of pH). From the qualitative agreement of these two graphs we conclude that our assumption that the onset of the interaction is due to the physical contact between the particles is a good one. In both graphs it is noticed that the main changes in particle size occurs between pH 6 and 8.

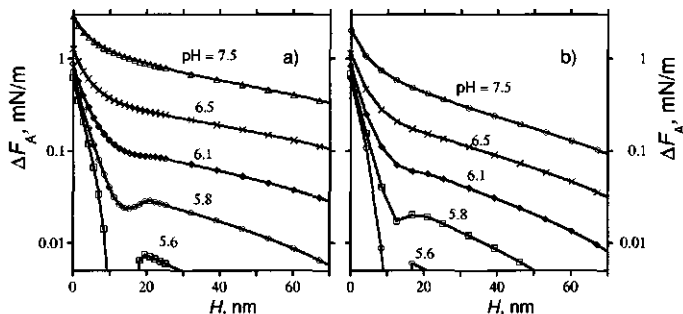


**Figure 4.6:** Two examples of theoretical SF-SCF interaction curves for approaching flat brushes for various pH values as indicated: a) monodisperse brush with  $N = 350$  and b) polydisperse brush with  $N = 100, 120, \dots, 300$ . Other parameters are the same for both models:  $f = 0.25$ ,  $pK = 5.3$ ,  $I = 0.01$  M.

It was mentioned already that it is possible to use the SF-SCF model for HPE brushes and predict the free energy of interaction. The model that approximates our system has been presented above and the corresponding predictions for the interaction curves for two homodisperse brushes are presented in fig.4.6. These results should be compared to the experimental data presented in fig.4.4, where it is understood that in the latter case the Derjaguin approximation has been implemented to convert the force to a free energy.

From the comparison of fig.4.6a and fig.4.4 we see that, in general, the trends in both graphs are similar. More specifically, in fig.4.6a we notice that there is a large long-range repulsion at high pH, which weakens with a decrease in pH. Importantly, the curves become non-monotonous around pH = 6.5, clearly showing the existence of a phase transition between long-range weak electrostatic repulsion and short-range hydrophobic attraction which has been already discussed above. Indeed, the transition occurs at rather high compression, so it is not too surprising that in the experimental system the attraction is somehow masked by the repulsion needed to compress the collapsed polymer layer.

We note that the increase in repulsion upon the approach of the surfaces is steeper in the experiment than in the theoretical model. We attribute this difference to the idealized model that is used for the HPE brush. In particular, the chains were taken to be monodisperse and the acid groups are distributed evenly throughout the chain, making it a regular copolymer. In reality the chains are more random than regular and perhaps blocky, and certainly polydisperse in length. The polydispersity of the chains could be responsible for a more sharp increase of the repulsion. The argument for

this is that in the case of different lengths of chains, upon compression more and more shorter chains come into play to resist further compression. In such a scenario the longest chains determine the hydrodynamic radius  $R_h$ , as measured with DLS, and the shorter ones, who reside much closer to the core, dominate the repulsive interactions, which, due to their shorter lengths, is shorter ranged. A polydisperse brush has a steeper segment density profile than a monodisperse one, so it is quite expected that also the steric repulsion as a function of distance is steeper in the overlap region.

The randomness and/or blockiness of the monomer distribution within each chain may be responsible for the formation of sequence specific loops, where the charged groups may preferentially be in the dangling outer parts of the shell. Such inhomogeneously charged chains may still stretch strongly at high pH, but may develop more loops at a lower pH, making the chain length effectively shorter and the grafting density higher<sup>b</sup>.

In fig.4.6b we present a selection of results intended to show that a polydisperse HPE has a steeper interaction curve. As explained above, the brush is now composed of regular HPE chains of different lengths. To keep the comparison fair we fixed the amount of polymer on the surfaces to the same value as in fig.4.6a. The polydisperse system has indeed the expected features: the repulsion is somewhat steeper than in fig.4.6a.

In fig.4.7 we present force curves for two opposing CSP layers at different ionic strengths, i.e. in 0.01M 0.1M buffer solutions. Unfortunately, at 0.1M the hydrophobic coating of the surfaces degrades rather quickly and we only obtained results at pH > 7.5. One of these curves for pH = 7.5 (which was similar to the curves at higher pH) is presented in fig.4.7 together with a curve for the same pH at an ionic strength of 0.01 M NaCl. The repulsion between the CSP layers at 0.1M starts at a closer distance between the surfaces than at 0.01M. This is fully in line with the theory of HPE brushes. The height of these brushes increases with decreasing ionic strength in this range of ionic strengths (the so-called salted brush regime). With increasing salt concentration the repulsion between the chains is better screened and the stretching of the chains is diminished. Alternatively, one can argue from an osmotic pressure point of view. As long as the osmotic pressure of the counterions is higher inside the brush than outside the brush, it is favorable

---

<sup>b</sup>We note that the suggestion that a HPE brush with irregular segment distributions which is in a two-phase state is characterized by inhomogeneous conformations, is in strong contrast to the known behavior of homogeneous (regular) HPE chains. For such a brush in a two phase state it is known that there are two populations of conformations. In one population the chains are uncharged and fully collapsed in the melt-like phase on the surface. The other population is charged (at least outside the collapsed region), is highly swollen and extends far away from the surface.

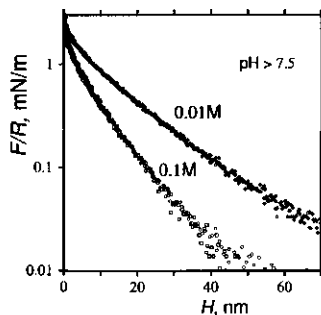


**Figure 4.7:** CP-AFM approach curves for interacting CSP layers at  $I = 0.01\text{ M}$  and  $I = 0.1\text{ M}$ .  $pH = 7.5$ .

for the chains to stretch; this gives more space for the ions in the brush. With increasing salt concentration the osmotic pressure difference between the brush interior and the outer solution goes down, so that the reason for swelling of the shell is reduced. The smaller size of the particles at higher ionic strength is also found from DLS-titration data for as shown in fig.4.5b. Upon strong compression the free energy of interaction is almost independent of the ionic strength.

#### Forces upon retraction of CSP layers in continuous measurements; Aqueous solutions

The force curves found upon approach of two layers of CSP are relatively well understood. When the pH is well above 7 the force curves upon retraction closely follow the approach ones. Around neutral pH there are indications that the layer undergoes a structural phase transition. In such case hysteresis is expected. When the measuring speed is sufficiently high and no delay times at close contact are implemented, the retraction curves still resemble the approach ones and therefore we present these results first.

In fig.4.8 we show the force divided by the probe radius as a function of the distance  $H$ , that is,  $f(H)/R$  which is comparable to a free energy per unit area, in linear coordinates. We have chosen for these coordinates simply because adhesion caused negative force values. Again, the top curve for  $pH \geq 7.5$  is identical to the approach one (cf. fig. 4.4). The remainder of the curves are pH dependent and differ from the approach traces. A decrease of the pH of the solution leads to a slight adhesive contribution just below pH 7, and to a stronger net adhesion around pH 6. This is fully consistent with our theoretical results and is attributed to the free energy

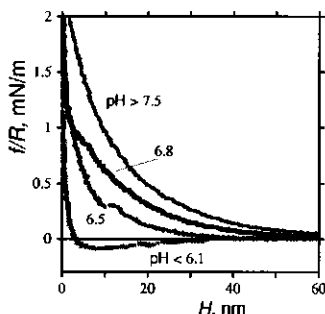


**Figure 4.8:** CP-AFM force measurements upon retraction of two CSP layers for a number of pH values as indicated,  $I = 0.01M$ , and speed  $v = 300nm/s$ . The curves for  $pH \geq 7.5$  are similar to the one at  $pH = 7.5$  and are not presented.

losses while exposing the hydrophobic boundary of the collapsed shell chains to the aqueous solution. On approach, the particles from opposite layers form a (more or less) continuous collapsed phase which upon retraction has to be broken into two. Especially when the retraction curve is recorded relatively fast, metastable branches of the structural phase transition will be sampled and attraction is found over a range of separation distances.

Indeed, the retraction curves at intermediate pH are double-exponential decays. As soon as the layers separate, their boundaries become hydrated and the shell chains recharge. At the same time the shell chains start swelling again. The volume, available for these shell chains is initially not large and this confinement can result in a repulsive force (e.g., seen for  $pH = 6.5$ ).

#### CP-AFM force measurements with surface delay time.

Above we argued that the HPE brush undergoes a confinement-induced structural transition. Upon strong confinement (small separation distances) the neutral collapsed layers of two opposing brushes form a single compact, that is melt-like, film of polymers. In time, this film will try to become as homogeneous as possible. This means that entanglements will form by chains of opposite particles. One can study this phenomenon systematically by recording the approach-retract curves sufficiently slowly -this gives the system effectively time to generate entanglements-, or implement a surface delay time  $t_s > 0$ , sometimes called 'surface waiting time'. As there are only a limited number of particles in the contact zone, it is possible that the number of bridges is small. In such case the results are discrete: one retraction curve may look very different from another one. Hence, we mostly

consider a statistical set of measurements, though we will sometimes pick a particular curve to point to some effect of interest.

To illustrate this discrete nature of our experimental system, we present in fig.4.9 12 (almost) consecutive measurements, in which the waiting time was set to  $t_s = 10$  s. In this case the pH and ionic strength were fixed to pH 6.5 and  $I = 0.01$  M, respectively. In this example, in measurement number 105 there is only a short-range adhesion, whereas in the remainder of the curves there is a short-range adhesion as well as some long-range negative force. Importantly, there are large differences between the curves. These negative forces have some type of saw-tooth form which resemble the ones first seen when the AFM was used to unfold large, multi-block titin proteins<sup>124,125</sup> (by pulling on the chain end). In the protein case, the interpretation is that the protein is elastically stretched first to a threshold value and then multiple H-bonds between peptides break all at once and the globule falls apart into sub-globules or just single peptide chains. The same type of curves are seen in case of single polymer chains,<sup>126-128</sup> polymer melts<sup>129</sup> and adsorbed polymer layers<sup>130,131</sup> as well. The measurements on single chains can be used for estimation of chain elasticity,<sup>126-128,132</sup> and the measurements on adsorbed polymer brushes as well as "grafted from" ones even prove to be an elaborate way of determining the molecular weight and polydispersity of polymers (from estimation of their contour length).<sup>133</sup>

It is of interest to elaborate on the possible origin of the zigzag type disjoining force curves in our case. For this reason we present four characteristic retraction curves with long-range nature for pH 6.5 and  $t_s = 0, 2$ , and 5s as indicated in figure 4.10, which are representative for the complete set. The trace shown in fig.4.10a, which is often found in the absence of a delay time, barely indicates a negative force. In our view this poorly visible adhesive force is coming from the separation of two collapsed shell layers as discussed above. In figs.4.10b, c and d there are additional attractive forces which become more pronounced with increasing separation and then abruptly disappear. We attribute this type of forces to bridges, formed by polymer chain fragments that go from one CSP to the opposing one. These bridges are semi-permanently secured on both sides by a strong attractive interaction which presumably is hydrophobic in nature, likely assisted by entanglements, i.e., topological knot-like constraints. Such chain fragments can be stretched until the bridges break cooperatively. Here a breaking event should be understood as the disentanglement of a chain end, so that a tail is formed which can retract to its parent particle. In case of hydrophobic attraction, a breaking event is related to the pulling of a hydrophobic sequence of segments out of a melt-like environment. It is known that this occurs when a threshold force is applied (essentially the force is necessary to compensate for the

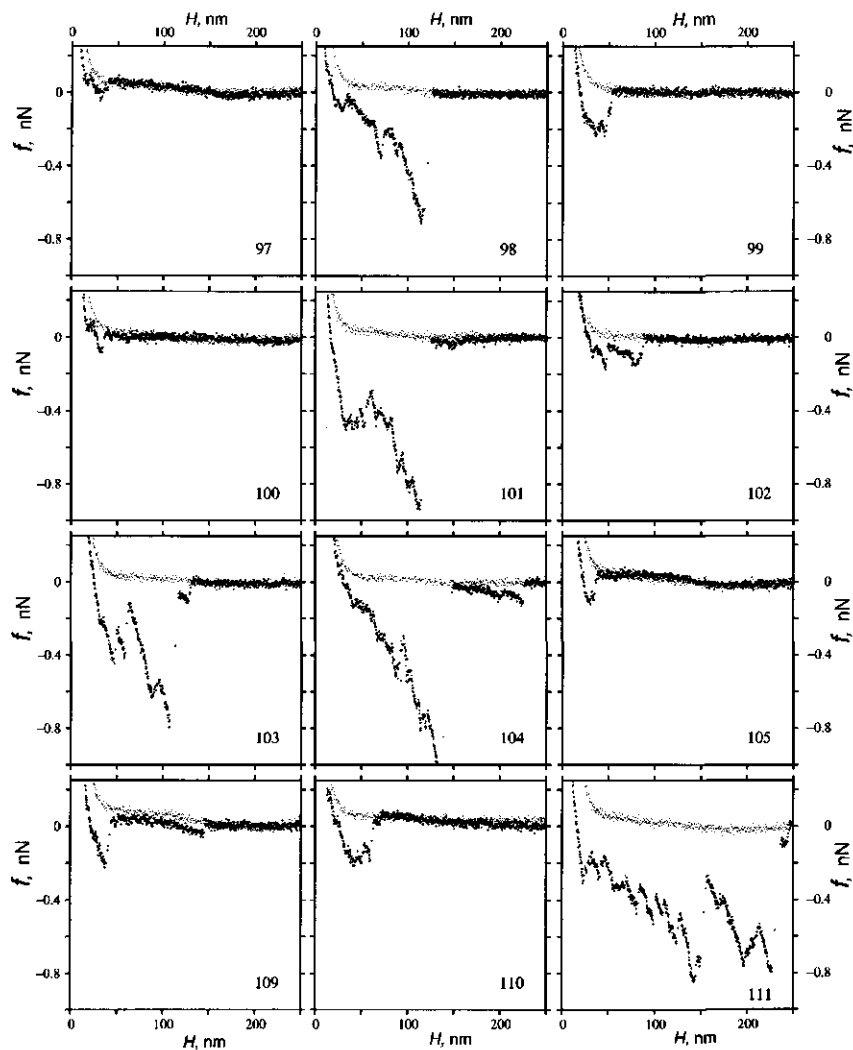


**Figure 4.9:** Set of 12 continuous CP-AFM measurements of retraction traces between CSP layers at pH 6.5,  $I = 0.01$  M and  $t_s = 10$  s,  $v = 60$  nm/s. Here we plot the force in nN as a function of the separation distance  $H$  in nm. Measurements 106 – 108 are not shown as these ones were rejected due to some unidentified noise. The approach curves are presented in light gray for reference purpose.



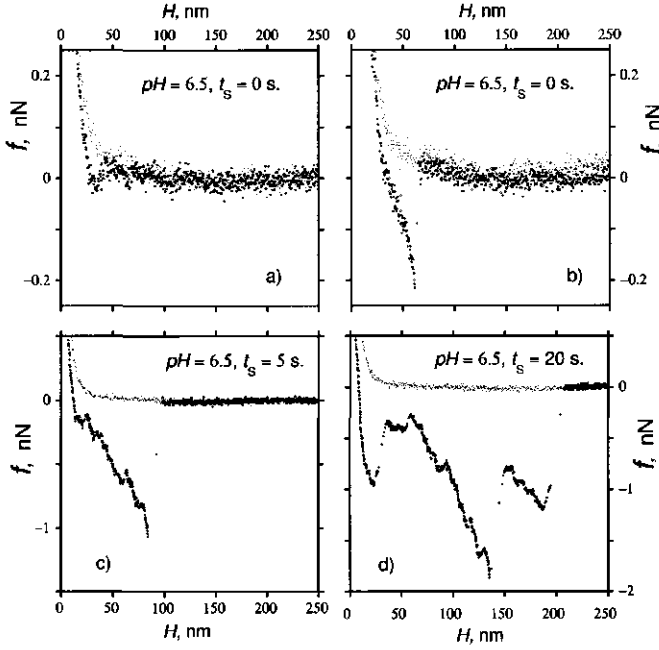


**Figure 4.10:** Four examples of possible approach-retract scenarios in CP-AFM measurements of interaction between CSP layers. Speed  $v = 60 \text{ nm/s}$ ,  $\text{pH} = 6.5$ ,  $I = 0.01 \text{ M}$  and surface waiting times  $t_s$  are indicated on the plots. a) no bridging b) one bridge breaking event c) a few consecutive breaking events d) multiple breaking events.

solvation of hydrophobic segments).

Apparently, the bridging or formation of entanglements is a slow process that happens only at strong confinement. We have tried to keep the layers for a long time at a separation distance close to the onset of the repulsion, and never found the formation of bridges. Indeed, bridges only form when the two CSP layers are strongly compressed against each other. Bridges may be found in the absence of delay times  $t_s = 0$ s only when the measurement speed is low ( $v \leq 60$ nm/s). To our opinion we can see bridges that are formed between individual pairs of core-shell particles. In fig.4.10b there is a single bridge-breaking event. This is a very rare case that most frequently is observed when  $t_s$  is low (in this example  $t_s = 0$ s). In fig.4.10c, where the delay time  $t_s = 5$ s several consecutive breaking events occur, adding on top of each other to produce a force curve with several minor teeth. In fig.4.10d, a force curve for which the waiting time was increased to  $t_s = 20$ s is presented. In this case there are many breaking events. At some distances a more cooperative breaking event occurs than at other distances; for example the negative force almost disappears at  $H \approx 60$ nm, but then starts growing again, and this is repeated at  $H \approx 150$ nm. Most of the times the force vanished at large separations  $H > 200$ nm. The fact that bridges break at different separation distances  $H$ , is, at least in part, due to the curvature of the colloidal probe. Particles at different points on the colloidal probe will be at different separation distances at a given moment. This means that the interaction curves from separate particles (or groups of particles) each with its own separation distance are superimposed. The major breaking events, as seen in fig.4.10c and even more pronounced in fig.4.10d, are due to these subpopulations of particles that cooperatively decouple. More on the molecular scale, we expect that a given bridge breaks when it is extended on the order of its contour length. This opens up, at least in principle, the possibility to measure the length distribution of bridges and thus the length distribution of the hydrophilic fragments that form the shell layer.

To prove that the force traces shown in figs 4.10 correspond to the stretching of bridges, we perform SCF calculations to evaluate the force needed to stretch polymer chains in a dense HPE brush. In these calculations we force the chains to have both their ends grafted at opposing surfaces. Details of these calculations were mentioned above and a selection of the results is presented in fig.4.11a. In this graphs we give the force (in pN) per chain needed to stretch it to a distance  $H$  in nm. It is necessary to mention that we tried to mimic the pulling of bridges that are formed when two opposing brushes have merged. This is why the amount of polymer per unit area was taken rather high ( $\Theta_p = 22$ nm<sup>-2</sup>, which is double the value for a single brush). Upon compression it is found that the repulsive force diverges. This

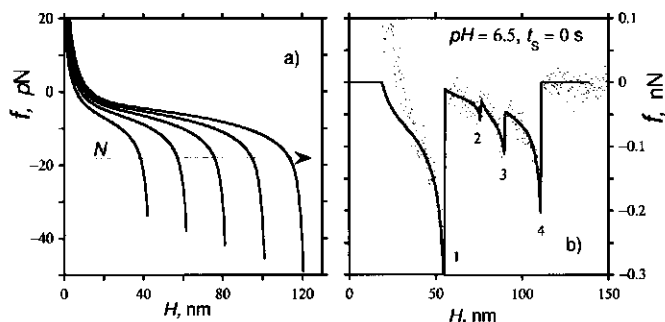


**Figure 4.11:** a) Numerical SF-SCF results for stretching of chains in homodisperse HPE brushes. Here all chains are grafted with their ends to opposite surfaces. The forces are computed from taking the derivative of the free energy of interaction with respect to the separation distance. This result was converted to pN and normalized per chain. The degrees of polymerization are (from left to right)  $N = 100, 128, 156, 182$  and  $212$ . Other parameters are  $pH = 6.5$ ,  $I = 0.01M$ ,  $f = 0.25$ ,  $\Theta_p = 22nm^{-2}$  b) A typical force curve as measured by CP AFM ( $t_s = 0s$ ) with relatively few bridge-breaking events (points), was fitted using the SF-SCF result by superposition of force curves as found in panel a for  $N = 100$ . The fitted number of bridging chains that break at distances indicated at points 1, 2, 3, 4 are  $n = 10, 1, 2$  and  $6$ , respectively.

is due to the fact that the chains take up volume and one cannot bring the two chain ends closer than  $D_{min} = \Theta * a^3nm$  where  $a = 1nm$  is a unitary length. We here define the distance  $H$  as the true distance between the grafting points minus the minimum distance  $D_{min}$  (in nm). In the calculation the HPE brush is homodisperse. As a freely-jointed chain model is implemented one cannot extend the chains further than their contour length ( $Na$  in nm). Hence, we find that for given length of the chain the (negative) force diverges. This divergence shift to larger  $H$  value with increasing  $N$ .

In fig.4.11b we show that it is possible to fit an experimental force-curve by shifting a theoretical force extension curve (here we used the one for chain length  $N = 100$ ) along the  $H$ -axis and adjusting the number of the bridges that break at a given distance (the fitting numbers are provided in the legend). The slopes of the curves, especially near the breaking point of the bridges are well reproduced by the extension of freely-jointed chains. This implies that in the CP AFM force measurements we truly observe the stretching of (relatively short) chains / chain fragments that bridge between the particles. What the origin is of the bridging (entanglements and/or hydrophobic interactions) cannot be judged from these calculations.

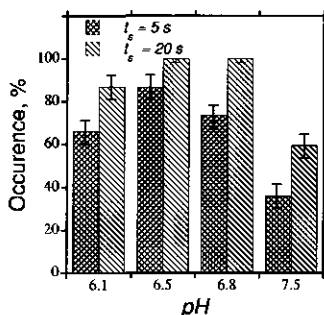


**Figure 4.12:** The statistical occurrence (in % of retraction curves with clear bridging features) of bridges as found in fast measurement cycles ( $v = 300\text{nm/s}$ ) with delay times  $t_s = 5\text{ s}$  (double hatch) and  $20\text{ s}$  (single hatch) for  $\text{pH} = 6.1, 6.5, 6.8$  and  $7.5$ .  $I = 0.01\text{ M}$ . For each point at least 30 force curves were used.

Bridge formation between CSP particles is a slow process. As mentioned already, we never see entanglements at  $t_s = 0\text{ s}$  when approach-retract cycles were recorded at high speed ( $v = 300\text{nm/s}$ ). Moreover, when the shell goes through its structural transition, the shell layers *should* first come into close contact, collapse and loose their surface charges before bridges can form. Shortly after the merging of the collapsed layers the chains of opposite brushes start to overlap and go towards an entangled state.

It is possible to quantitatively analyze the CP AFM measurements to learn more about the statistics of bridging. It is expected that the probability that a bridge can form depends both on the pH of the solution and the delay time  $t_s$ . In two series of at least 30 measurements for a fixed waiting time (here we used  $t_s = 5\text{ s}$  and  $20\text{ s}$ ), we evaluated the percentage of the retraction force curves that show bridging and present the result in fig.4.12 for a few selected values of the pH. We extract two trends from this histogram. The first one is that the occurrence of entanglements grows, as expected, with waiting time. Indeed, the longer the particles are kept in contact, the higher the chance is that the shells entangle (overlap) forming a bridge. The other trend is that the occurrence of entanglements has an optimal value around  $\text{pH} = 6.5$  both for  $t_s = 5$  and  $20\text{ s}$ , where the probability that a bridge forms is near unity: bridges are formed at every measurement. Below and above this pH value the probability to form bridges is less. The drop of the bridging probability at high pH is expected: when the chain is highly charged there is a barrier to form a bridge which makes bridging less likely. A similar drop of bridging efficiency at low pH is less obvious. We attribute this fact to the high density of a fully collapsed shell layer. Especially at low pH the collapsed

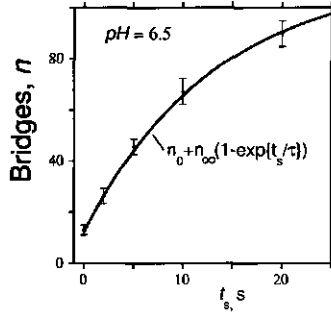


**Figure 4.13:** The average amount of bridges that break during retraction vs surface waiting time  $t_s$  for  $pH = 6.5$  (points). Each bridge breaking event is expected to give a 20pN change in the force. The line is a fit to equation 4.3.

film is very dense and likely less mobile (near a glassy state). Apparently, it takes more time for the shell polymers to interpenetrate in this case.

Eventually the interest is in the characteristic time that is needed to form bridges. For this we analyzed many retraction force curves and counted the number of bridges  $n_{bridge}$  as a function of the surface delay time. To facilitate the counting we used the approximation that each bridge can carry a load of  $f = 20$  pN. This approximation comes from the theoretical fit of the retraction curve presented in fig.4.11b. In this way we can estimate the number of bridging polymers, breaking loose at each abrupt step in the recorded force curve, and then sum them up to get the total amount of bridges formed during the measurement.

In fig. 4.13 we present the number of bridges found at  $pH = 6.5$ , speed  $v = 60$  nm/s and various surface delay times  $t_s = 0, 2, 5, 10$  and 20 seconds. It is clear that the number of bridges increases as a function of the delay time. The results could be fitted by

$$n_{bridges}(t) = n_{bridges}(0) + n_{bridges}(inf) \times \left[ 1 - \exp\left(-\frac{t_s}{\tau}\right) \right] \quad (4.3)$$

From this fit we found that the characteristic time for bridge formation  $\tau \approx 13$  s and that for long surface waiting times one can get upto approximately 100 bridges.

#### Measurements on CSP in 30% butyl glycol in water solutions

In all results discussed so far we paid little attention to the properties of the core of the particles. It is believed that in aqueous solutions the cores are in

the glassy state (at room temperature). Of course a strong proof of this was not yet extracted from the CP AFM measurements. In the remainder of this results section we will report on our findings for the interactions between the CSPs in aqueous solutions in which 30wt% butyl glycol was added.

Butyl glycol is expected to penetrate into the core of the acrylate CSP and to make the core more liquid like. As a result one might expect significant changes in the force measurements. In passing we further mention that the use of BG in these systems is motivated by the fact that in waterborne coatings, where the CSP find an important application, the BG is often used as a cosolvent. From this perspective there is an intrinsic interest in knowing how the CSPs behave in the BG-water mixture.

The hydrodynamic radius  $R_h$  of the CSP in the BG-water mixture, as a function of pH of the solution, again measured with DLS titrations, is presented in fig.4.14. In this experiment the ionic strength was fixed to  $I = 0.01M$  NaCl. In the same graph we present the (normalized) scattering intensity  $I/c_p$  (where  $c_p$  is the concentration of particles) of the sample. The particle sizes in BG-water mixtures typically are larger than in pure water (under otherwise similar physical chemical conditions). The uptake of BG into the hydrophobic part of the particle is not likely fully responsible for this increase. Qualitatively, the particle size increases with pH similarly as in the absence of BG (cf. fig. 4.5)). Again, the shell polymers are collapsed at low pH and the shells swell as soon as the MMA groups become charged. A dramatic difference however shows up at high pH values: the hydrodynamic radius  $R_h$  goes through a maximum and above  $pH \approx 11$  decreases with pH. The intensity of the scattered light also drops significantly for  $pH > 11$ . The latter indicates that in the BG-water system, at this high pH, the particles gradually disappear from solution.

To understand this it is important to know how the particles are formed. Information about this is given in chapter 2. Importantly, the formation of the CSP occurs in such a way that the core forming chains (which are hydrophobic) are not chemically linked to the corona forming chains. The latter ones appear to be trapped with parts of their segments in the core domain. In fact it is believed that the shell forming layers are trapped in the core on several places along the contour (order 10 places per chain), and as a result they form some type of fence-like brush layer (large loops). In water the core is glassy and the corona chains cannot detach themselves from the core. When BG is added, we expect that BG is absorbed preferentially into the hydrophobic parts of CSP, that is, BG partitions mainly inside the core. This increases the mobility of the chains in the cores. At the same time it reduces the forces that keep the chain fragments of the shell chains inside the cores. We may say that butyl glycol acts as a lubricant for the shell chains to

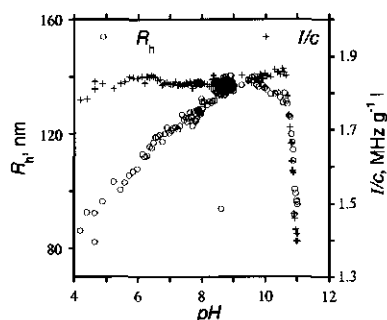


**Figure 4.14:** The hydrodynamic radius (left ordinate),  $R_h$ , of the CSPs and the normalized scattering intensity  $I/c_p$  (right ordinate) as a function of the pH, measured with DLS in a 30wt% butyl glycol - water mixture at an ionic strength of  $I = 0.01$  M NaCl.

free themselves from the cores. At moderate pH, the hydrophobic segments of the shell chains remain associated with the core. However at high pH values, where the MAA segment are fully charged, the electrostatic forces peel the shells away from the cores. This is seen as a reduction of the hydrodynamic size of the particles. Without the colloidal stabilization provided by the shell layer, one should expect that the hydrophobic cores precipitate. When time proceeds, we end-up with a phase separated solution: one phase is formed by hydrophobic chains from the cores which is rich in co-solvent, and the other phase is a rather dilute solution of shell polymers which does not scatter much light. This explains the drop in scattering intensity at high pH. Apparently, at  $\text{pH} > 11$  the system is on its way to this two-phase state.

The CP AFM force measurements in the presence of the BG co-solvent (always 30wt%) give additional information on the structure and dynamic stability of the particle shells. The force curves were measured for several pH values. Again the approach and retraction curves are recorded and the latter ones are, not unexpectedly, a function of the surface delay times as for the system without BG. As shown in fig. 4.15a on the approach of a flat hydrophobized silica surface loaded which the CSPs and a hydrophobized colloid probe also covered by a layer of CSP, the forces are, similarly to the pure water case, repulsive. In line with the increase in  $R_h$  with respect to the pure water case, the onset of the repulsion found in CP AFM is at larger separation distances, albeit that the increase in this distance appears somewhat more pronounced. Consistent with this the slopes of the force curves in log-lin coordinates are smaller in the BG-water mixture than in pure water systems. From numerical SF-SCF calculations we see that these

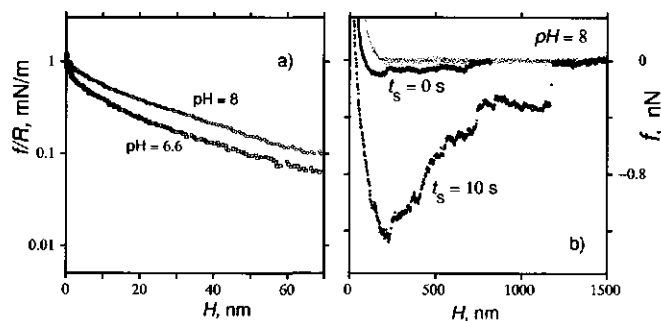


**Figure 4.15:** CP-AFM approach (a) and approach-retract (b) measurements for CSP layers immersed in a 30wt% butyl glycol - water mixture at  $I = 0.01M$  ionic strength. pH values and surface waiting times  $t_s$  are indicated.

results are consistent with shells that are composed of very long chains that are relatively sparsely grafted (cf. fig.4.6a). We see this as evidence that the addition of butyl glycol reduces the number of loops in the shell chains, effectively increasing the length of the chains in the brush at the expense of the grafting density. The strength of adsorption of hydrophobic groups onto the core decreases with increasing concentration of BG co-solvent. This is consistent with the desorption of loop-forming parts of chains and the escape of these chains to the solution at high pH. This explanation also points indirectly to some "blockiness" of different types of monomers in the shell chains: in order to form large loops in aqueous solution large blocks of hydrophobic segments must be alternated with blocks containing a sufficient number of chargeable groups. In principle it is possible to elaborate an SF-SCF model for such a shell layer composed of large loops and grafting blocks. Detailed information on the blockiness is a prerequisite for this.

The retraction curves in the BG-water mixtures are often dramatically different from those in pure water. As can be seen from fig. 4.15b an extremely long-range adhesion is observed, reaching sometimes upto  $1\mu\text{m}$ . In some cases a regime with a constant negative force is found, which is characteristic for pulling tethers out of a condensed phase (the curve labeled  $t_s = 0$  s). In other retraction curves one may find attractive forces that grow with extension which subsequently suddenly disappear (the example for  $t_s = 10$  s). The latter force curves point to the breaking of bridges similarly as discussed above in the absence of BG. The main difference concerns the distances upto which bridges can exist and at which separation distance the bridges fail; these are much larger than in the pure water systems.

Another important point is that bridges appear in every retraction measurement.



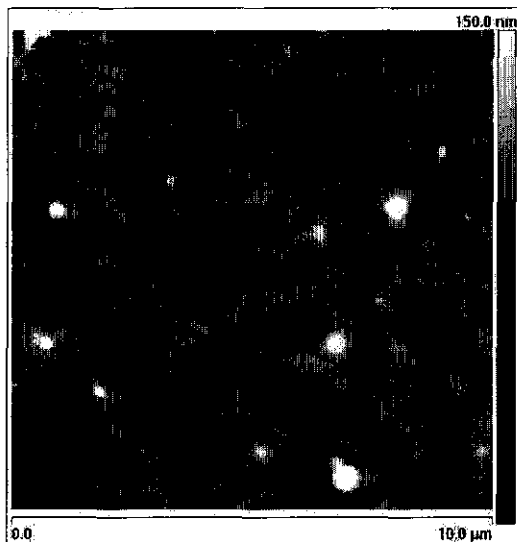


**Figure 4.16:** *Tapping mode AFM image of a CSP layer deposited from a 30wt% butyl glycol water mixture and subsequently dried.*

Bridges are seen even when the surface delay time is zero or when the measuring speed is high. In our view, this adds to our proposition of de-looping of shell polymers. From size exclusion chromatography we know (cf. chapter 2) that the peak in the molecular weight of the shell polymers is around  $M_w = 10^6$  gram/mol, which corresponds to  $N \approx 5000$  monomers. The contour length of such chains is on the order of 500 nm. Hence a de-looped shell chain can form bridges that break at large separation distances consistent with those found in fig. 4.15b. Additionally, as the cores appear to be fluid-like, some (parts of the) chains can probably travel from one CSP to another during a measurement cycle and thus we do not need long surface delay times to find bridges. As the shell is less dense and the shell layer is composed of longer chains we believe that the shell chains can more easily reach the opposite cores, adsorbed or entangled, and form a bridge. The other possible explanation is that the BG-water mixture is a much less poor solvent for the hydrophobic monomers. Hence in the presence of BG the hydrophobic segments are solvated by BG so that the shell polymer density remains lower. All this adds up to a much more dynamic system. We estimate that the characteristic time to form bridges is now sub second ( $\tau < 1s$ ).

We finish the result section by presenting in fig.4.16 an AFM tapping

mode image of a layer of core-shell particles adsorbed on hydrophobized silica from a butyl glycol - water mixture (as used in the force measurements) and subsequently dried. The same procedure for CSPs adsorbed from pure water gives random packing of the CSP layer (cf fig.4.1b). Obviously, the distribution shown in fig.4.16 is not a random one. Many particles are fused together, forming patches. We believe that during the preparation of this sample, the adsorption was still a random process, and that the coalescence occurred upon drying. If coalescence would occur already in the wet stage, we should have noticed strong adhesion in our force measurements when bare hydrophobic surfaces are in close proximity. We did not find such behavior: all approach measurements suggested that there is more or less homogeneous distribution of particles. The overall surface coverage in fig.4.16 was determined to be  $\rho = 54 \pm 2\%$ . This corresponds to randomly packed layer of particles, which also supports our view that the coalescence takes place upon drying.

The fusion of the particles, as shown in fig.4.16, supports our conclusions from the DLS-titration data. The co-solvent does not only reduce the strength of adsorption of shell polymers onto cores, but facilitates the lateral mobility of the shell chains as well. The lateral mobility may have assisted the process by which the random closed packed layer of CSP aggregated into a spinodal decomposition-like coalesced pattern.

## 4.5 Conclusions

Using the colloid probe atomic force microscope (CP AFM) technique we have measured interaction forces between layers of densely packed (close to random sequential adsorption theory jamming limit) core-shell acrylic particles (CSPs) in aqueous solutions as well as in butyl glycol (BG) - water mixtures at several pH values and ionic strengths. Even though the force measurements between such layers proved to be intrinsically discrete, we showed that it is possible to obtain valuable data through statistical averaging. The results, supported by experimental evidence from DLS-titrations, SLS and potentiometric titrations and theoretical mean-field modeling, leads to a detailed and consistent picture of structure and dynamic properties of the particles. Our main conclusions are split in the results for the CSP system in pure water and in those found for butyl glycol - water mixtures.

### 1 CSPs in aqueous solutions

- Forces measured upon approach are typical for hydrophobic polyelectrolyte (HPE) brushes for which the charge density is pH dependent. For

a sufficiently high pH, when the HPE brush is highly charged, the forces increase exponentially with decreasing distance. The decay length is slightly pH dependent.

- In line with theoretical SF-SCF predictions the shell layer can undergo a non-trivial confinement induced conformational transition, revealed by a change in the slope of the logarithm of the force as a function of the distance. At large separations there is a swollen shell layer. At a critical confinement the chains fully discharge and collapse. All this is driven by hydrophobic attraction.
- The results can only be rationalized by acknowledging that the shell consists of polydisperse chains. Unlike in the SF-SCF calculations, presented here, the chains are expected to have an irregular distribution of polar and apolar segments. It was argued that an irregular distribution of the charges along the chain may lead to inhomogeneous conformations characterized by loopings to the hydrophobic dense sublayer. The number of such loops decreases upon charging of MAA groups, that is when the pH is increased.
- Force measurements upon approach and upon retraction of the cantilever prove the existence of a phase transition between a collapsed and decharged state of the shell polymers and a charged and swollen state near neutral pH values. This transition is due to the hydrophobic nature of the monomers composing the shell. The SF-SCF theory supports this confinement-induced transition and links this behavior to the micro-phase segregated state of the HPE brush when such brush is in the isolated (non-interacting) state.
- Force measurements upon retraction, especially those that are recorded at low speeds and wherein surface waiting times in the order of seconds are implemented, show bridging of single and multiple polymer chains. This bridging is a slow process in aqueous solution with characteristic times of about 10 s. The bridging efficiency goes through a maximum around  $\text{pH} \approx 6.5$ .

## 2 CSPs in 30wt% butyl glycol - water solutions

- Dynamic light scattering measurements, in combination with acid-base titration, indicate that the addition of butyl glycol co-solvent makes the shell polymers effectively adsorbed on the cores and CSPs become less stable. This is in contrast to the case in aqueous solutions where the shell polymers are effectively grafted

on the core and the shell remains attached even in highly alkaline environment.

- AFM force measurements in BG-water mixtures support the proposition that long shell chains form multiple (mostly permanent) loops in pure water. In the presence of butyl glycol, the hydrophobic attraction of shell polymers to the cores is screened. This increases the mobility of the shell chains and possible de-looping upon extension. This explains the long range of the forces found upon retraction.
- Upon retraction, bridging always occurs, independently of the measurement speed and the surface waiting time. Again this points to faster dynamics of the interpenetration of shell layers. The faster dynamics is attributed to screening of hydrophobic interactions to some extent by the presence of the co-solvent.
- The layer of CSPs coalesces upon drying in the presence of butyl glycol. This coalescence is possibly facilitated by an increased lateral mobility of the shell chains which again results from partitioning of the co-solvent into the core with concomitant plasticizer action.

## Chapter 5

# On the curvature energy of a thin membrane decorated by polymer brushes <sup>a</sup>

### 5.1 abstract

In this chapter we present approximate analytical predictions for the contribution to the free energy of curvature of a thin (flexible) membrane rising from a polymer brush, grafted to both sides of this membrane. The influence of the approximations is revealed by a detailed comparison with numerically exact self-consistent field (SCF) calculations. We consider both the quenched, that is the grafting density is the same on both sides and the annealed case, when the polymer chains can upon bending translocate from one side of the membrane to the other. It is found that the analytical predictions give the correct sign for the brush contribution to the free energy of curvature. Moreover, for spherically curved membranes a reasonably accurate scaling with the grafting density  $\sigma$  and the chain length  $N$  is obtained. However, in the case of a cylindrical curvature the analytical models overestimate the dependence on the polymer chain length. It is shown that the mean bending modulus is positive which implies that the grafting of polymers onto membranes makes these stiffer. The Gaussian bending modulus is negative and scales with the chain length in the power three, whereas the mean bending modulus scales with the chain length with a power two. This is in contrast with the analytical predictions which point to the same power-law dependence of three. Our results imply that for sufficiently long polymers

---

<sup>a</sup>Published by T.M. Birshtein, P.A. Iakovlev, V.M. Amoskov, F.A.M. Leermakers, E.B. Zhulina, O.V. Borisov in *Macromolecules* 41 (2008) 478-488.

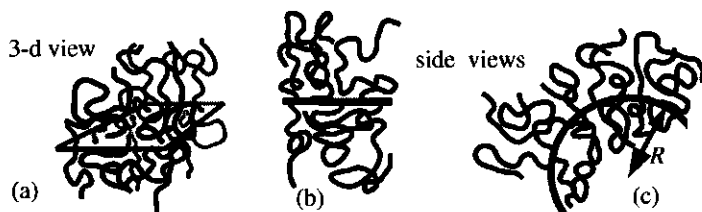


**Figure 5.1:** *a) A '3d' schematic illustrations of a flat bilateral brush. On both sides of the bilayer the grafting density is the same (i.e. the number of chains per unit area). b) A side view of a cross-section of the bilateral brush. Again on both sides one sees the same number of chains. c) A section of the cross-section of a curved membrane with radius  $R$ . In this case the number of chains on the concave side is less than the number of chains on the convex side, that is some chains have flipped, or translocated. View graph (b) can also be seen as a line onto which side chains are grafted (in 2d). Then (c) is the curved line. This illustrates that the curved bilateral brush is also a model for a curved molecular bottle-brush. In this work we will take the supporting fluid membrane to be so flexible that its contribution to the overall rigidity can be ignored, or better, that the intrinsic flexibility of the supporting membrane should be added on top of the predictions elaborated on below. Also, in this work we focus on laterally brushes with a laterally homogeneous grafting density.*

the flat conformation becomes unstable in favor of bending.

## 5.2 Introduction

The investigation of the influence of a grafted polymer layer on the bending elasticity of a membrane has a long history. There are few issues that are commonly recognized. For example, it is clear that grafting of polymer chains on one side of a membrane would lead to a spontaneously curved conformation.<sup>134,135</sup> One may further argue that permanent grafting of an equal number of chains onto both sides of a membrane would both stabilize a flat conformation and increase the resistance against bending, i.e., such chains stiffen the bilayer. In this last example it was taken that upon bending the chains can not relocate from one side of a membrane to another. Such systems are referred to as quenched (with respect to chain redistribution through flop-flop).

At the same time, there are ample issues that are currently actively discussed in the literature. For example, the subtle question is what will happen with the stability and stiffness of a flat membrane when upon bending

the grafted chains can redistribute from one side of the membrane to the other (see figure 5.1). We refer to such a system as an annealed bilateral brush, or, for simplicity - a bilateral brush. While the quenched state may be relevant in a fluctuating membrane at short time scales, the annealed one is of interest for equilibrated systems. Most experimental studies<sup>136,137</sup> as well as some theoretical papers on polymer - decorated membranes<sup>138,139</sup> deal with self-organizing lipids, partially coupled to polymer chains.<sup>140,141</sup> In this case of self-assembly, polymers are found on both sides of a membrane and ideally their distribution is governed by the minimal free energy condition. Thus, the polymers can attain an asymmetric distribution in curved regions of membranes.<sup>26</sup> However, the extraction of the polymer contribution from the total free energy of the system is less straightforward here due to the polymer-lipid and lipid-lipid interactions.

The behavior of a bilateral brush system immersed in an athermal solvent was first studied by Birshtein and Zhulina.<sup>142</sup> The analysis was based on the Daoud-Cotton blob model for curved brushes<sup>143</sup> (see also<sup>77,144</sup>). Two bending modes, spherical and cylindrical, were considered. These two different membrane geometries allowed for the calculation of the polymer contributions to the mean and Gaussian bending rigidities. It was demonstrated that the bending of a membrane indeed leads to a redistribution of the chains from the concave side of the membrane to the convex one. At a large membrane curvature, the difference in chain redistribution for spherical and cylindrical types of bending is of solely quantitative character. In both spherical and cylindrical modes, the chains are accumulated on a convex side of a bending membrane thus leading to the decrease in overall free energy per chain. At a weak curvature, the situation is more delicate. According to the blob model<sup>142</sup> and subsequent studies, the spherical bending always leads to a decrease in the total free energy per chain in a bilateral brush. At the same time, the cylindrical bending leads to an initial increase in the free energy per chain.<sup>142</sup> Therefore in the framework of the blob model, at small curvatures of a membrane, a spherical type of bending is favorable, whereas cylindrical bending is unfavorable. In terms of the membrane elasticity this means that the polymer, grafted to both sides of a membrane and being allowed to redistribute upon bending makes a membrane stiffer, but less stable.

The observation that the sign of the effect depends on the type of bending, demonstrates the delicacy of the problem, and this explains why so many issues in the field are still heavily debated. The small change in the free energy upon an imposed curvature results from subtracting two large numbers (the free energies of the curved and the flat membrane conformations). Meanwhile, the analytical theory contains invariably a number of approximations. In particular, the results in ref<sup>142</sup> were based on the assumption that all the free

polymer ends are fixed at the external boundary of a brush. At first sight this assumption seems reasonable as it is similar to the approximation made in, e.g., the classical Alexander-de Gennes box model for flat brushes<sup>145,146</sup>). Another approximation inherent for the Daoud-Cotton blob model,<sup>142</sup> is the so-called quasi-planar approximation (QP).<sup>147</sup> In this framework, the local structure in a curved brush at distance  $r$  from the membrane coincides with that in a planar brush with  $r$ -dependent grafting area per chain. As a result, the polymer density profile in a curved brush is unaffected by the peripheral parts of the brush. It is described by a power law which is independent of molecular weight of the grafted chains.

For almost two decades the Daoud-Cotton blob model<sup>143</sup> served as the main tool to rationalize the experimental data on curved brushes and related systems (polymer-decorated colloids, solutions of star-like polymers, block copolymer aggregates of various morphologies, etc.). A recent revision of this model<sup>147</sup> indicated that although the quasi-planar approximation has the adequate asymptotic power laws for the average brush thickness and the free energy, it fails to predict correctly the polymer density and lateral tension distribution profiles in curved brushes. A more accurate calculation of these characteristics is possible by direct minimization of the free energy, which indicates that the local brush structure is affected by the brush peripheral parts, and therefore the distributions of the polymer density and the lateral tension depend on the molecular weight of the chains (see ref<sup>147</sup> for details). Therefore, the local features in the brush are determined by the overall spatial distribution of the polymer. This model is therefore referred to as having the non-local (NL) approximation. In this framework, the polymer density profile does not obey a power law, the chains are more stretched, and more polymer material is expelled to the periphery of a convex brush. The difference between the two frameworks (QP and NL) becomes quite noticeable for charged grafted chains. For a neutral polymer brush, which is the focus of this paper, the difference between outputs of the two models is relatively small. However, due to the delicacy of the bilateral brush behavior at small curvatures, the non-local effects can contribute to the overall behavior of the bilayer. We therefore believe that it is timely to try to understand the thermodynamics of bending of a bilateral brush using up-to-date considerations for the structural organization of curved brushes.

An important class of polymers directly relevant to the topic of this study comprises the so-called molecular brushes or comb-like macromolecules.<sup>148-154</sup> When such macromolecules adsorb onto a strongly attractive substrate, they become effectively two-dimensional. Locally, the conformations of an adsorbed molecular brush can be envisioned as a cross-section of a cylindrically curved three-dimensional bilateral brush (see fig. 5.1). The interactions between



the side chains stiffen the macromolecule and this determined its adsorption-induced persistence length. For a quenched system with prohibited redistribution of side arms from one side of the molecular backbone to the other, the straight configuration of the macromolecule is thermodynamically stable and the optimal one; in this case the persistence length is large. For an annealed system (two-dimensional bilateral brush), the flip-flop of side chains leads to a smaller persistence length and this can even cause a spontaneous curvature in adsorbed comb-like macromolecules.<sup>155,156</sup> The latter theoretical prediction turned out to be model-dependent and is challenged by results in ref.<sup>154</sup> Overall, the current understanding of a molecular brush behavior is far from being complete.

The aim of this work is therefore to present the most accurate analytical predictions available up-to-date for the free energy change due to the bending of a planar bilateral brush. Both limits of weak and strong membrane curvature in spherical and cylindrical modes will be considered, and the bending and the Gaussian modules will be analyzed. The results will be critically compared to the predictions of the numerically exact Scheutjens - Fler self-consistent field (SF-SCF) method. From this comparison we will derive the conclusions regarding the accuracy of the analytical models as well as what must be expected in experimental systems.

The remainder of the paper is organized as follows. In the next part we present an outline of the Scheutjens-Fler self-consistent-field (SF-SCF) approach. It is followed by the presentation of the analytical theory which includes two sub-parts: the analysis of weakly curved brushes with emphasis on the quasi-planar and the non-local approximations, followed by the predictions for a curved bilateral brush. In the results section we will present and discuss our numerical data. The summary of our conclusions is presented at the end of the paper.

## 5.3 Numerical SCF method

For the most accurate evaluation of the free energy of bending we use the Scheutjens-Fler self-consistent-field (SF-SCF) approach.<sup>81,85,86,90</sup> The target of these calculations is to find the structural and thermodynamic properties of the system that optimised its free energy. As a result of the calculations both the end-grafted chains and their free ends occupy the most favorable positions. Therefore this model does not suffer from the assumptions that the free ends are constrained to the edge of the brush. All possible and allowed conformations of the chains are included and therefore it also automatically included the non-local contributions discussed below. Due to the model,

which will be discussed below, the calculations also account rigorously for the redistribution of chains from one side of a membrane to another, and thus the calculations are ideally suited to the annealed brush system, i.e. the bilateral brush.

The SF-SCF approach is based on mean-field and lattice approximations. In this method the space is taken to be composed of lattice sites with characteristic length  $l$  and the volume per cell is fixed to  $v \propto l^3$ . The lattice sites are arranged in layers numbered  $r = 1, \dots, M$ . The number of lattice sites in each layer,  $L(r)$ , depend on the geometry. For a flat lattice this number does not depend on  $r$  and  $L(r) = L = L_x \times L_y$ . In a cylindrical coordinate system the number of sites in the radial direction is  $L(r) \propto rL_x$  when the long axis of the cylinder is in the  $x$ -direction. In the spherical coordinate system  $L(r) \propto r^2$ , where in the last two cases  $r = 1$ , is the central layer. Typically we will impose reflecting (mirror-like) boundary conditions in the lattice, although for the spherical and cylindrical geometries the natural boundary condition at  $z = 0$  is that at this coordinate there are no lattice sites (no place for any molecules).

We consider polymer chains in a good or  $\theta$ -solvent ( $\chi = 0.5$ ) monomeric solvent. The solvent molecules are assumed to occupy one lattice site each. A chain is divided into  $N$  segments and numbered  $s = 1, \dots, N$ . A polymer segment is also assumed to fit exactly on one lattice site. All dimensions are thus represented in units  $l \approx 0.5\text{nm}$  of the lattice site length. As usual all energies are expressed in units of  $k_B T$ .

In the bilateral brush model we graft the polymers with their first segment  $s = 1$  to a given coordinate  $R \equiv r_g$ . In this case all polymers are free to take all possible  $r$ -positions, i.e.  $r \leq R$  as well as  $r \geq R$ . Typically, we choose  $M \gg R \gg 1$  and the chains are grafted far from the system boundary. However, when the brushes are highly curved, it may be the case that  $R$  is not far from  $r = 1$  and then the 'inner' space becomes limited. This spatial confinement is in such cases accurately accounted for in the calculations. The mean curvature of the grafted layers in the cylindrical and spherical coordinates systems is given by  $J = 1/R$  and  $J = 2/R$ , respectively. We can also study the characteristics of quenched convex or concave brush layers separately. In this case the grafting surface  $R$  is taken to be impermeable. In the concave system only the space  $r < R$  is available for the chains, whereas in the convex problem the other half-space  $r > R$  is used. In this quenched system it is possible to mimic the redistribution of the chains from one side of the membrane to another only by vary the grafting densities (number of grafted chains per unit area)  $\sigma$  at both sides of the grafting plane, calculate the free energy as a function of  $\Delta\sigma$  ( $\sigma_{\text{convex}} \equiv \sigma_+ = \sigma + \Delta\sigma$ ;  $\sigma_{\text{concave}} \equiv \sigma_- = \sigma - \Delta\sigma$ ) and then minimize it with respect to  $\Delta\sigma$ .

Again, the SCF calculations are optimizing the polymer conformations so that the free energy is minimal. The allowed conformations are generated using a Markov approximation. This means that only correlations between the neighbor segments are included. This results automatically in a freely-jointed chain model. The optimization is done by solving the Edwards diffusion equation:

$$\frac{\partial G(z, N)}{\partial N} = \frac{1}{6} \nabla G(z, N) - u(z) G(z, N) \quad (5.1)$$

where the  $\nabla$ -operator is different for the various geometries. Eqn 5.1 must be complemented with appropriate boundary and starting conditions. Here  $G(r, N)$  is a chain weighting factor which is related to the single chain partition function  $G(N) = \sum_r L(r) G(r, N)$  and thus to the volume fraction distributions. The self-consistent segment potential  $u(r)$  is given by

$$u(r) = -\ln(1 - \varphi(r)) - 2\chi \langle \varphi(r) \rangle \quad (5.2)$$

where  $\varphi$  is the polymer volume fraction. Here  $\chi$  is the well-known Flory-Huggins interaction parameter. The angular brackets represent a three-layer average similarly as used below. The volume fraction profile of the solvent  $\varphi_S(r)$  is found from the incompressibility constraint:  $\varphi_S(r) = 1 - \varphi(r)$ .

On the lattice the equation 5.1 transforms into a set of propagator equations, which provides a very efficient way to evaluate the volume fractions. We will illustrate the equations with the bilateral brush in mind. In this formalism the polymer volume fractions are found by the so-called composition law:

$$\varphi(r) = \sum_{s=1}^N \varphi(r, s) = \frac{\sigma L(R)}{G(N)} \sum_{s=1}^N \frac{G(r, s|R, 1) G(r, s|N)}{G(r)} \quad (5.3)$$

where we have introduced a slight modification of the notation of the chain weighting factor to clarify that the grafting condition has broken the inversion symmetry in the chain statistics. The segment weighting factor is given by the Boltzmann weight  $G(r) = \exp -u(r)/k_B T$ . The chain weighting factor  $G(r, s|R, 1)$  is found by the forward propagator, whereas the complementary one  $G(r, s|N)$  is found by the backward propagator. The forward propagator starts with  $G(R, 1|R, 1) = G(R)$  and  $G(r, 1|r, 1) = 0$  for  $r \neq R$ . Then,

$$G(r, s|R, 1) = G(r) \sum_{r'=r-1, r, r+1} G(r', s-1|R, 1) \lambda(r', r) \equiv G(r) \langle G(r, s-1|R, 1) \rangle \quad (5.4)$$

wherein the *a priori* step probabilities obey to the internal balance equation  $L(r) \lambda(r, r') = L(r') \lambda(r', r)$  and give the (lattice type and geometry dependent)

probability to step from layer  $r$  to  $r'$ . They further obey to the constraint  $\sum_{r'} \lambda(r', r) = 1$ . The rhs of Eqn 5.4 defines the angular bracket notation already used in Eqn 5.2 for the weighting of the volume fractions. The backward propagator is started by the unconstrained end of the chain and therefore  $G(r, N|N) = G(r)$  for all  $r$  and reads

$$G(r, s|N) = G(r) \sum_{r'=r-1, r, r+1} G(r', s+1|N) \lambda(r', r) \quad (5.5)$$

where it is understood that the single chain partition function in this case is connected to the forward propagator  $G(N) = \sum_r L(r) G(r, N|R, 1)$ .

As told the potentials ( $u$ ) depend on the volume fractions and the latter in turn are a function of the potentials. A self-consistent solution is routinely found numerically up to high numerical precision. For such solution it is possible to evaluate the free energy accurately. Of interest is the free energy in units of  $k_B T$  per unit area measured at the grafting plane at which there are  $L(R)$  site:

$$F \equiv \frac{F}{L(R)} = \sigma \ln \frac{\sigma L(R)}{G(N)} + \sum_r L(r) \ln(1 - \varphi(r)) + \sum_r L(r) \varphi(r) \chi(\varphi(r)) \quad (5.6)$$

Below we compare the results of these calculations with the those of the analytical theories.

## 5.4 Analytical theory

### 5.4.1 Theory for curved brushes

The overall characteristics of a polymer brush, its thickness  $H_d$  and free energy  $F_d$ , are related to the segment density  $\varphi(r)$  and free energy density  $f[\varphi(r)]$ . Here we introduce the subindex  $d$  as the geometry-index ( $d = 1$  for a flat plane,  $d = 2$  for the cylindrically curved layer and  $d = 3$  for the spherical geometry). We can write for the free energy

$$F_d^\pm = \pm \frac{1}{R^{d-1}} \int_R^{R \pm H_d} f[\varphi(r)] r^{d-1} dr \quad (5.7)$$

It is clear that the integration over the volume fraction profile should conserve the number of segments in the chain, and thus should obey the constraint

$$N = \pm \frac{1}{\sigma_{\pm} R^{d-1}} \int_R^{R \pm H_d} \varphi(r) r^{d-1} dr \quad (5.8)$$

Again, we used  $R$  as the curvature radius of a grafting surface and the indexes  $+$  and  $-$  represent the outer and inner sides of a curved surface, and  $\sigma_+$  and  $\sigma_-$  are the grafting densities for polymers at the corresponding sides. In Eqn 5.7 the free energy is calculated for a unit of surface area and we will refer to it as the specific free energy of the brush. This free energy must be directly compared to the SF-SCF result given in Eqn. 5.6.

The task is to find a minimum in  $F_d^{\pm}$  taking the constraint of Eqn 5.8 into account. Unfortunately, the rigorous analytical solution for the distribution of the free ends of the polymer (which is related to the single chain partition function) is not possible for curved convex brushes; it is only available numerically (SF-SCF) as mentioned above. The common Ansatz for analytical considerations is to assume that all the free ends are located at a certain distance from the grafting plane, that is exactly at the brush thickness  $H_d$ . This approximation implies that all the chains in the brush are equally stretched. We note, that for polymer chains in curved geometries the local stretching along the chain is known to be different in different parts of the brush. The area per chain, or equivalently, the effective grafting density in each thin cylindrical or spherical layer depends on the coordinate  $r$ :

$$\sigma(r) = \sigma_{\pm} \left( \frac{R}{r} \right)^{\pm(d-1)} \quad (5.9)$$

The minimization of the free energy of Eqn 5.7 with respect to  $\varphi(r)$  and taking into account the constrain 5.8 leads to the following equation:

$$\frac{\partial f(\varphi(r))}{\partial \varphi(r)} = \lambda \quad (5.10)$$

where  $-\lambda$  is an indefinite Lagrange multiplier. As could be seen from Eqn 5.10), we can interpret  $\lambda$  as an exchange chemical potential "polymer - solvent", which must remain constant throughout the brush.  $\lambda$  should also provide the equilibrium between the brush boundary and the solvent, which is equivalent to the minimum of the free energy per polymer segment at the boundary (or equal to zero chemical potential of solvent):

$$\left. \frac{\partial \left( \frac{f(\varphi(r))}{\varphi(r)} \right)}{\partial \varphi(r)} \right|_{r=R \pm H_d} = 0 \quad (5.11)$$

The Eqns 5.2-5.11 can be used to solve for the brush characteristics for a given imposed radius  $R$ , a chain length  $N$  and a grafting densities  $\sigma$ . For curved brushes Eqns. 5.10 and 5.11 provide the polymer concentration distribution  $\varphi(r)$  depending on the conditions at brush boundary. Following the recent work,<sup>145</sup> where a similar theory was presented for curved brushes, we call this approach the non-local (NL) theory. For flat brushes these equations lead to the well-known box-model with constant polymer density  $\varphi$  in the brush and the free energy density represented as:

$$f(\varphi) = \frac{3}{2} \frac{\sigma^2}{\varphi} + f_{\text{int}}(\varphi) \quad (5.12)$$

with  $\varphi = N\sigma/H_1$ .

The first term in Eqn 5.12 accounts for the free energy of stretching of a Gaussian chain, and the second is responsible for the free energy of chain interactions. In this work we restrict ourselves to the case of uncharged layers in a good or  $\theta$ -solvent. In this case

$$f_{\text{int}} = \begin{cases} v\varphi^2 & \text{good solvent} \\ \omega\varphi^3 & \theta\text{-solvent} \end{cases} \quad (5.13)$$

Here  $v$  and  $\omega$  are the dimensionless second and third virial coefficients for the segment interactions, which we set equal to unity. In Eqns 5.12-5.13, we follow Flory<sup>7</sup> by using the mean-field Ansatz that the probability of pair interactions is proportional to  $\varphi^2$ .

Minimizing Eqn 5.12 with respect to  $\varphi$  we obtain well-known scaling expressions:

$$\varphi = \begin{cases} \sigma^{2/3} & \text{good solvent} \\ \sigma^{1/2} & \theta\text{-solvent} \end{cases} \quad (5.14)$$

$$H_1 = \begin{cases} N\sigma^{1/3} & \text{good solvent} \\ N\sigma^{1/2} & \theta\text{-solvent} \end{cases} \quad (5.15)$$

$$F_1 = \begin{cases} N\sigma^{5/3} & \text{good solvent} \\ N\sigma^2 & \theta\text{-solvent} \end{cases} \quad (5.16)$$

We will use these characteristics of the flat brush,  $H_1$  and  $F_1$ , (instead of  $N$  and  $\sigma$ ) as a starting (reference) point and note that a useful measure for curvature for a non-planar brush is given by  $H_1/R$ .

**Table 5.1:** Coefficients in the expansion of the free energy of the curved brush, Eqn 5.19 for the non-local (NL), quasi-planar (QP) and quasi-planar with correlations (QP') analytical models.

Regime	Approach	$a_1$	$a_2$	$a_2$ ( $d = 2$ )	$a_2$ ( $d = 3$ )
Good solvent	NL	$\frac{d-1}{3}$	$\frac{(d-1)(2d+1)}{27}$	0.18	0.52
	Qp	$\frac{d-1}{3}$	$\frac{d(d-1)}{9}$	0.22	0.67
	QP'	$\frac{5}{12}(d-1)$	$\frac{5}{216}(d-1)(7d-1)$	0.30	0.93
$\theta$ solvent	NL	$\frac{d-1}{3}$	$\frac{(d-1)(5d-1)}{24}$	0.37	1.17
	QP	$\frac{d-1}{2}$	$\frac{(d-1)(3d-1)}{12}$	0.42	1.33

It will be obvious that it should be possible to see the weakly curved brushes to be slightly perturbed with respect the flat brush, and that corrections can be written in series expansion in this small parameter  $H_1/R$ . The NL theory for convex brushes as developed in,<sup>145</sup> gives the result of the free energy for a weakly curved convex brush as

$$F_d^+ = F_1 \left[ 1 - a_{1d} \left( \frac{H_1}{R} \right) + a_{2d} \left( \frac{H_1}{R} \right)^2 + \dots \right] \quad (5.17)$$

The coefficients  $a_{1d}$  and  $a_{2d}$ , that were found in<sup>145</sup> are presented in table 5.1 (the values of  $a_{1d}$  and  $a_{2d}$  that were derived using the quasi-planar (QP) approximation, are presented in this table as well). In the QP approximation each layer of a brush is taken to be in equilibrium with the solvent, i.e. Eqn 5.11 is obeyed for each  $r$  and the density of the brush in layer  $r$  is defined by Eqn 5.14 with  $\sigma$  substituted by  $\sigma(r)$  as given in Eqn 5.9:

$$\varphi(r) = \begin{cases} (\sigma(r))^{2/3} & \text{good solvent} \\ (\sigma(r))^{1/2} & \theta\text{-solvent} \end{cases} \quad (5.18)$$

As a result, according to the QP approximation the free energy expansion for weakly curved brushes can be presented in a general form for both the concave ( $F_d^+$ ) and convex ( $F_d^-$ ) brushes with the same coefficients:

$$F_d^\pm = F_1 \left[ 1 \mp a_{1d} \left( \frac{H_1}{R} \right) + a_{2d} \left( \frac{H_1}{R} \right)^2 \mp \dots \right] \quad (5.19)$$

It follows from table 5.1 that both approximations lead to similar coefficients for the linear term. The coefficients  $a_{2d}$  however have different forms for the two approximations, but the numerical difference is small.

In table 5.1 we have also included the coefficients  $a_{1d}$  and  $a_{2d}$  that were calculated in the early work of Birshtein et al.<sup>139</sup> for the good solvent case using the QP approximation, but taking into account the correlation corrections. Such correlation corrections are possible with the scaling approximation where it is taken that the probability of pair interactions is proportional to  $\varphi^{9/4}$  or equivalently, the free energy per blob is equal to  $k_B T$ .<sup>12</sup> These results are denoted in table 5.1 by QP'.

For the general case of an arbitrarily curved brush, we will present equations only in the QP approximation. According to Eqns 5.7 and 5.8 and taking into account Eqns 5.9, 5.14 and 5.18 we obtain for the conservation of segments in the chain

$$N = \begin{cases} \pm \frac{3}{d+2} \frac{R}{\sigma_{\pm}^{1/3}} \left( \left( \frac{R \pm H_d}{R} \right)^{\frac{d+2}{3}} - 1 \right) & \text{good solvent} \\ \pm \frac{2}{d+1} \frac{R}{\sigma_{\pm}^{1/2}} \left( \left( \frac{R \pm H_d}{R} \right)^{\frac{d+1}{3}} - 1 \right) & \theta\text{-solvent} \end{cases} \quad (5.20)$$

and for the free energy of the curved brush

$$F_d^{\pm} = \begin{cases} \pm \frac{3}{4-d} R \sigma_{\pm}^{4/3} \left( \left( \frac{R \pm H_d}{R} \right)^{\frac{4-d}{3}} - 1 \right) & \text{good solvent} \\ \pm \frac{2}{3-d} R \sigma_{\pm}^{3/2} \left( \left( \frac{R \pm H_d}{R} \right)^{\frac{3-d}{3}} - 1 \right) & \theta\text{-solvent, } d \neq 3 \\ \pm R \sigma_{\pm}^{3/2} \ln \left( \frac{R \pm H_d}{R} \right) & \theta\text{-solvent, } d = 3 \end{cases} \quad (5.21)$$

In Eqn 5.21 (and below) there are two different equations for the  $\theta$ -solvent case, one for the  $d \neq 3$  and one for  $d = 3$ . Using  $H_1$  and  $F_1$  of Eqns 5.15 and 5.16 as parameters we then get from Eqns 5.20 and 5.21

$$F_d^{\pm} = \begin{cases} \pm \frac{3}{4-d} \frac{R}{H_1} F_1 \left( \left( 1 \pm \frac{d+2}{3} \frac{H_1}{R} \right)^{\frac{4-d}{2+d}} - 1 \right) & \text{good solvent} \\ \pm \frac{2}{3-d} \frac{R}{H_1} F_1 \left( \left( 1 \pm \frac{d+1}{2} \frac{H_1}{R} \right)^{\frac{3-d}{1+d}} - 1 \right) & \theta\text{-solvent, } d \neq 3 \\ \pm \frac{1}{2} \frac{R}{H_1} F_1 \ln \left( 1 \pm 2 \frac{H_1}{R} \right) & \theta\text{-solvent, } d = 3 \end{cases} \quad (5.22)$$

$H_1$  and  $F_1$  in these formulas are functions of  $\sigma_{\pm}$ . Series expansion of Eqn 5.22 with respect to  $H_1/R$  can be casted in the form of Eqn 5.19 with coefficients presented in the QP lane of table 5.1.

#### 5.4.2 The curvature free energy of a bilateral brush.

We now consider the change in the specific free energy when a flat bilateral brush is curved in such a way that the chains can translocate, i.e., the



free energy of bending of the bilateral brush. When the flat membrane is homogeneously bent, the outcome is a cylindrical or spherical object with radius  $R$ . In this process the area is conserved, i.e., we assume that the flat membrane splits up into various parts and that each part is subsequently bent into the specified object.

As long as the bilayer is flat, we assume that both sides of the membrane are covered by the same number of grafted chains. Upon bending the overall grafting density is fixed, however the grafting density on either side of the bilayer is allowed to change. The translocation of chains that is necessary for this is sometimes referred to by the flip or flip/flop of chains. It is clear that when this relaxation mechanism is available for a system, it will be used to lower its free energy. The number of flips that is chosen in a particular case will be controlled by the minimum of the free energy. In this way

$$\sigma_{\pm} = (1 \pm x)\sigma \quad (5.23)$$

introducing  $x = \Delta\sigma/\sigma$ . The relative change in the specific free energy upon bending can be written as

$$\delta F = \frac{\Delta F}{F_1} = \frac{F_d^+ + F_d^- - 2F_1}{F_1} = \frac{F_d}{A_d} - 2 \quad (5.24)$$

where, according to Eqns 5.16, 5.22-5.24

$$F_d = \begin{cases} \frac{2+d}{4-d} \left\{ (1+x)^{4/3} \left( B_{d+}^{\frac{4-d}{2+d}} - 1 \right) + (1-x)^{4/3} \left( 1 - B_{d-}^{\frac{4-d}{2+d}} \right) \right\} & \text{good solvent} \\ \frac{1+d}{2-d} \left\{ (1+x)^{3/2} \left( B_{d+}^{\frac{3-d}{1+d}} - 1 \right) + (1-x)^{3/2} \left( 1 - B_{d-}^{\frac{3-d}{1+d}} \right) \right\} & \theta\text{-solvent, } d \neq 3 \\ (1+x)^{3/2} \ln B_{d+} - (1-x)^{3/2} \ln B_{d-} & \theta\text{-solvent, } d = 3 \end{cases} \quad (5.25)$$

Quantities  $A_d$  and  $B_d$  for different solvent strengths are given by

$$A_d = \begin{cases} \frac{d+2}{3} \frac{H_1}{R} = \frac{d+2}{3} \frac{N\sigma_{\pm}^{1/3}}{R} & \text{good solvent} \\ \frac{d+2}{3} \frac{H_1}{R} = \frac{d+2}{3} \frac{N\sigma_{\pm}^{1/2}}{R} & \theta\text{-solvent} \end{cases} \quad (5.26)$$

$$B_{d\pm} = \begin{cases} 1 \pm A_d (1 \pm x)^{1/3} & \text{good solvent} \\ 1 \pm A_d (1 \pm x)^{1/2} & \theta\text{-solvent} \end{cases} \quad (5.27)$$

In this problem we need to minimize the free energy 5.25 with respect to the  $x$  variable

**Table 5.2:** Coefficients in the expansions of key characteristics of the bilateral brush, Eqns 5.29 and 5.30, for the non-local (NL), quasi-planar (QP) and quasi-planar with correlations (QP') analytical models.

Regime	Approach	$b_1$	$b_2$	$b_2 (d = 2)$	$b_2 (d = 3)$
Good solvent	NL	$\frac{3}{2}(d-1)$	$0.25(d-1)(1.88-d)$	-0.030	-0.56
	QP	$\frac{13}{22}(d-1)$	$0.18(d-1)(2.25-d)$	0.045	-0.27
	QP'	$\frac{13}{22}(d-1)$		0.068	-0.28
$\theta$ solvent	NL	$\frac{3}{2}(d-1)$	$0.36(d-1)(1.91-d)$	-0.032	-0.78
	QP	$\frac{13}{22}(d-1)$	$0.28(d-1)(2.18-d)$	0.050	-0.45

$$\frac{dF_d}{dx} = 0 \quad (5.28)$$

which gives the equilibrium values for  $x$  and  $\delta F$  at given values of  $d$  and  $A_d$ .

Using Eqn 5.19 we obtain the first terms of the expansion in the weak curvature limit

$$x = b_1 \left( \frac{H_1}{R} \right) \quad (5.29)$$

and

$$\delta F = b_2 \left( \frac{H_1}{R} \right)^2 \quad (5.30)$$

Here  $b_1$  and  $b_2$  are numerical coefficients,  $b_1$  is proportional to the coefficient  $a_{1d}$  of the free energy expansion given in Eqn 5.19, and  $b_2$  depends on two coefficients  $a_{1d}$  and  $a_{2d}$  of this expansion. The  $b_1$  and  $b_2$  coefficients for all cases in Eqns 5.29 and 5.30 are presented in table 5.2. The calculation of coefficients in the NL model, similar to calculation in QP models, were based on Eqn 5.19. Note that from paper<sup>145</sup> we know the theoretical coefficients  $a_1$  and  $a_2$  only for the convex brush (cf. Eqn 5.17).

From table 5.2 one can see that the values of the  $b_1$  coefficient are the same for both QP and NL approximations. The value of the  $b_2$  coefficient as used in Eqn 5.30 is more delicate. As follows from the expansion 5.19, and Eqns 5.24 and 5.28, the  $b_2$  coefficient is found by the difference between  $a_2$  and a term that depends on  $a_1$  (or  $b_1$ ). As a result, we find that for spherical bending ( $d = 3$ ) this difference ( $b_2$ ) is always negative, whereas for cylindrical bending the sign of the  $b_2$ -value is model dependent. Indeed, according to the QP and QP' models  $b_2$  for cylindrical bending is positive, which is in line with the early predictions.<sup>139</sup> The positive value indicates that the curvature

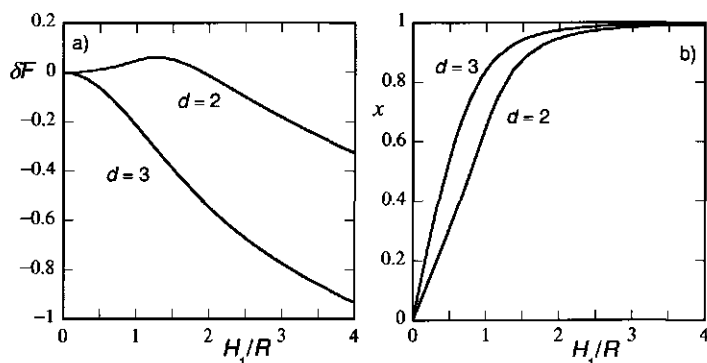


**Figure 5.2:** a) The relative change in the specific free energy upon bending  $\delta F$  using the QP approximation, see Eqns. 5.24-5.28 and b) the fraction of translocated chains  $x$  as functions of relative curvature  $H_1/R$  for spherical ( $d = 3$ ) and cylindrical ( $d = 2$ ) curvatures. The initial grafting density per side is  $\sigma = 0.1$  and the solvent quality is good ( $\chi = 0$ ).

free energy for weakly cylindrical bending, is unfavorable. This is contrasted with the prediction of the NL model which predicts that  $b_2 < 0$  for both the spherical and cylindrical bending cases (table 5.2).

Up to this point we have limited ourselves to the weakly curved regime. The dependence of  $x$  and  $\delta F$  on  $H_1/R$  for a large range of  $R$ -values is presented in fig. 5.2 for the QP model. In this graph it is seen that  $\delta F$  changes sign upon curvature in the cylindrical geometry. For weak curvature it is positive and becomes negative at large curvatures. For the spherical curvature we find  $\delta F$  to be negative for all values of the imposed radius  $R$ . Interestingly, the physically more correct NL model predicts a monotonically decreasing values for  $\delta F$  in both geometries. These results are in accordance with a signs of  $b_2$  presented in table 5.2. In all cases  $\delta F$  turns negative when  $H_1/R$  becomes large, i.e. when  $R$  becomes small. Thus the extreme curvatures are always favorable. It is relatively easy to understand this effect. In the limit of very high  $H_1/R$  most of the polymers will be on the exterior side of the membrane as  $x$  tends to unity. Taking the spherical bending as an example, one is left with a very small sphere of radius  $R$  decorated with end-grafted chains with a grafting density of  $2\sigma$ . That means that the number of chains at the surface  $n = 8\pi R^2\sigma$  is also small. These chains become so dilute that they do not interact, i.e., do not stretch each other.

The results of analytical considerations presented in this part of the article serve as a guide for the numerical SF-SCF analysis presented in the next

section. Equations 5.29 and 5.30 and fig. 5.2 show that there are two scaling parameters. The free energy of a curved brush is proportional to the free energy of the planar brush, which is proportional to  $N$ , (cf. Eqn 5.16), while the natural measure of the curvature is  $H_1/R$ , which is also proportional to  $N$  (cf. Eqn 5.15). The scaling as obtained in the QP model also applies to the NL approximation because, according to Zhulina and Birshtein,<sup>145</sup> a shift from the QP to the NL approximation does not affect the scaling relationships for convex brushes; it changes only the numerical coefficients (see table 5.1).

As follows from equations 5.15, 5.16, 5.24 and 5.30, the predicted scaling dependences for the initial part of free energy curves are

$$|\Delta F| \sim \begin{cases} \frac{N^3 \sigma^{7/3}}{R^2} & \text{good solvent} \\ \frac{N^3 \sigma^3}{R^2} & \theta\text{-solvent} \end{cases} \quad (5.31)$$

and because  $\delta F = \Delta F/F_1$  we can alternatively write

$$|\delta F| \sim \begin{cases} \frac{N^2 \sigma^{2/3}}{R^2} & \text{good solvent} \\ \frac{N^2 \sigma}{R^2} & \theta\text{-solvent} \end{cases} \quad (5.32)$$

Note, that the redistribution of the chains from the inner to outer layer does give an additional entropy loss upon bending. This increase of the free energy due to this entropy loss is per unit area given by

$$\Delta F_S = -\sigma [(1+x) \ln(1+x) + (1-x) \ln(1-x)] \quad (5.33)$$

For fixed  $x$  this value will not depend on  $N$ . Taking Eqns 5.23 and 5.29 into account, we get a scaling dependence for the low curvature case

$$|\Delta F_S| \sim \begin{cases} \frac{N^2 \sigma^{5/3}}{R^2} & \text{good solvent} \\ \frac{N^2 \sigma^2}{R^2} & \theta\text{-solvent} \end{cases} \quad (5.34)$$

so for the large  $N$  it becomes negligible as compared to the contributions given in Eqn 5.31.

## 5.5 Numerical Results and Discussion

In this section we will present results from the numerical SF-SCF calculations. We split this section into two. In the first part we will consider the structural and thermodynamic effects of curving a quenched brush. In the second part we will consider the annealed, bilateral brush.

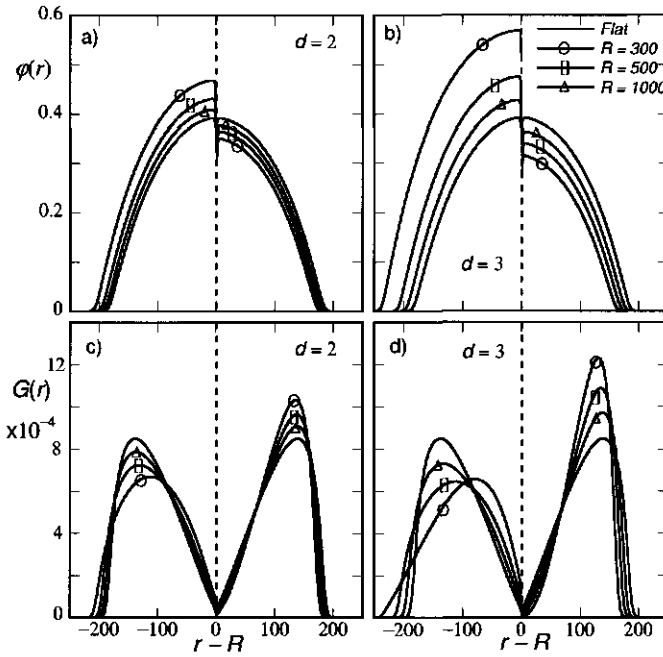


**Figure 5.3:** The polymer density profiles  $\phi(r)$  (a,b) and the distribution of free ends  $G(r)$  (Eqn 5.35). (c,d) for cylindrically curved brushes (a,c) and for spherically curved brushes (b,d) in cases when the redistribution of the polymers is not possible, i.e. the geometrically quenched brush. Besides the flat case, the radii of curvature  $R=300, 500$  and  $1000$  as presented as indicated. The chain length  $N=500$  and the grafting density is  $\sigma=0.1$ , solvent quality is good ( $\chi=0$ ).  $G(r)$  is normalised to  $\sigma$ , but note that the polymer profile obeys to  $N\sigma = \sum_r L(r)\phi(r)$ .

### 5.5.1 Curved quenched polymer brush

The polymer profiles for the concave and convex brushes at weak curvatures are presented on fig. 5.3. The discontinuity in profiles is due to the fact that there is no translocation of the chains allowed (the grafting densities on both sides of the plane are fixed  $\sigma_+ = \sigma_- = \sigma$  for each brush) and thus the profiles that are computed for two independent cases of concave and convex geometries, are put together for comparison with the annealed case.

From fig. 5.3 one can see that there are strong non-local effects present (fig. 5.3a,b). According to the QP model, the polymer volume fraction in the each layer  $r$ , irrespective whether one considers a point on the convex or concave side, is fully determined by the effective grafting density in that layer (cf. Eqns 5.9 and 5.18). In this case, the grafting densities for the convex and the concave brushes are fixed and is the same for both sides. However, as evident from the SF-SCF predictions, the polymer volume fractions at the first lattice layers just next to the grafting surface are noticeably asymmetric. The polymer segments of the chains grafted to a convex surface trend to position themselves far from the grafting plane in the exterior of the brush, where they can sample more space. On the concave side, however, there is progressively less space when the segments move away from the grafting plane and as a result the segments are pushed toward the grafting plane. This increases the volume fraction next to the grafting plane. The smaller  $R$ , the larger are these effect.

In figure 5.5 below a similar set of graphs is shown for the bilateral (annealed) brush, where profiles are given for higher curvature (smaller  $R$  values). Even though the redistribution was allowed for in this case, we still can refer to the volume fraction profiles to discuss how the profiles in general respond to the imposed curvatures.

For both brushes with strong and weak curvature, and both on the convex and concave sides, the polymer volume fraction profile decreases with distance from surface. For low curvatures as in fig. 5.3 these profiles are approximately parabolic. In the convex brush with a large curvature (very small values of  $R$  as, e.g., in fig. 5.5a,b) the radial volume fraction distribution can be divided into two regions. There is a power-law dependence of  $\varphi(r)$  for the layers near the grafting surface, and a parabolic-like dependence for the region further from the grafting surface (i.e. the exterior). The analytical theory of convex brushes (both in the QP and NL approximations) describe only the power-law dependence, due to the constraints on the free ends. For weakly curved layers (fig. 5.3a,b) this power-law dependence is absent, and this illustrates a potential problem for the analytical models.

On the concave side the profiles are fundamentally different. Again the

**Table 5.3:** Coefficients in the free energy expansion found from Eqn 5.23, fitted from the numerical SF-SCF results for the curved convex and concave brush (no redistributions of chains)  $N = 500$ ,  $\sigma = 0.1$ .

$d$	Solvent side	good		$\theta$ -solvent	
		$a_1$	$a_2$	$a_1$	$a_2$
2	+	0.377	0.251	0.52	0.44
	-	0.376	0.254	0.52	0.45
3	+	0.754	0.669	1.03	1.39
	-	0.752	0.731	1.03	1.39

characteristics are best seen for high curvatures as given in figs. 5.5a,b. Basically the decrease of polymer volume fraction with increasing distance from the grating surface weakens with the increase in the curvature  $H_1/R$ . In a limit  $H_{in} = R$  the volume fraction profile for the concave layer becomes nearly constant. However, the increase in volume fraction toward the center of curvature as predicted by QP and even NL theories is not observed. The noted difference between the SF-SCF results and the analytical predictions, as well as the existence of a parabolic part of density distribution in the convex brush, is largely due to the distribution of free polymer ends. Recall again that in the analytical models these distributions are delta functions.

Figures 5.3c,d (and correspondingly figs. 5.5c,d) present the distribution of ends  $G(r)$  as a function of the distance  $r$  from the grafting surface both for spherically as well as cylindrically curved brushes. The end-point distribution gives the number of end-points per unit grafting area. Therefore  $G(r)$  is connected with corresponding volume fraction distribution  $\varphi(r, N)$  (in the literature often the notation  $g(r) \equiv \varphi(r, N)$  is found) by

$$G(r) = \frac{L(r)}{L(R)}\varphi(r, N) \equiv \frac{r^d - (r-1)^d}{R^d - (R-1)^d}\varphi(r, N) \quad (5.35)$$

Note that this distribution is normalized to  $\sigma$ , i.e. there are exactly  $\sigma$  end-points. As can be seen from figs. 5.3c,d and 5.5c,d, with the increase of the curvature (decrease in  $R$ ) the distribution of free ends tends to shift to the periphery of the brush in the convex layer (toward the parabolic part of density profile), and toward the grafting surface in concave layer. The relative absence of end-points near the grafting surface in the strongly curved convex brush is known as the dead zone.<sup>26,157-159</sup> This dead zone is easily observed (near the surface on the convex side) in the figs. 5.5c,d. In the weak curvature case (fig 5.3) the dead zone is absent.

Let us next compare the free energy of curved brushes as predicted by the SF-SCF method with those given by the analytical models for the good

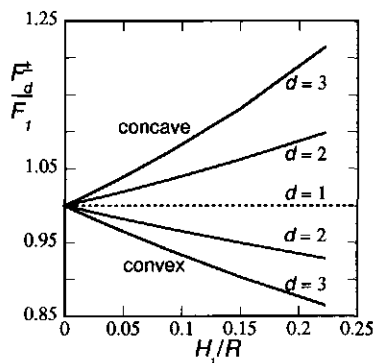


**Figure 5.4:** The relative change in free energy  $F_d^\pm/F_1$ , as a function of the relative curvature  $H_1/R$  in the weak curvature limit for the quenched (no flip-flop) case. The chain length  $N = 500$ ,  $\sigma = 0.1$  and  $\chi = 0$ . The cylindrical curvature ( $d = 2$ ) and spherical curvature ( $d = 3$ ) cases are indicated. The horizontal dotted line (labeled ( $d = 1$ )) is for the flat geometry (plotted for illustrative purpose only even though there is no  $R$ -dependence in this case).

solvent case. The initial part of the free energy curve for the low curvatures is presented in fig. 5.4 showing that the change in the free energy is a relative simple function of the curvature parameter. The expansion coefficients  $a_1$  and  $a_2$  for a fit similar to Eqn 5.19 are presented in the table 5.3. Note that for this expansion it is necessary to determine the height of the brush  $H_1$ . In the analytical models the free ends of the polymer are fixed at the brush exterior, exactly at the distance  $H_1$  from the grafting surface, so that the height is uniquely determined. In the SF-SCF model, however, the free ends are distributed throughout the layer. As a result there are several options of how to determine the brush height  $H_{1(\text{SF})}$  and correspondingly, the  $a_1$  and  $a_2$  coefficients. We will use the first moment of the free ends distribution,  $G(r) = \varphi(r, N)$ , given by

$$H_{1(\text{SF})} = \frac{\sum_r r G(r)}{\sum_r G(r)} \quad (5.36)$$

as a measure for the brush height. Comparing the calculated coefficients (table 5.3) with the analytical ones (table 5.1), we see a reasonable agreement between the analytical methods and the numerical results. To further summarize this part of the study, we present the scaling for the free energy difference  $\Delta F$  upon bending:



$$\Delta F \sim \begin{cases} \frac{N^3 \sigma^{2.7}}{R^2} & \text{good solvent} \\ \frac{N^3 \sigma^{3.3}}{R^2} & \theta\text{-solvent} \end{cases} \quad (5.37)$$

which is in good agreement with early scaling predictions<sup>160</sup> and more recent computer simulation studies.<sup>161</sup> The power exponent for the grafting density in good-solvent conditions (2.7) is somewhat larger than that of the scaling prediction (7/3). This is probably due to the relatively high grafting densities ( $0.05 \leq \sigma \leq 0.25$ ) used in our calculations. We would also like to mention that there is no difference in scaling for bending into spherical or cylindrical geometries. The only differences are in numerical coefficients.

### 5.5.2 Bending of a bilateral polymer layer

A selection of polymer volume fraction profiles and corresponding distributions of free ends for the cylindrically and spherically curved bilateral polymer layers is presented in figure 5.5. Again we present results of the SF-SCF method for a set of curvatures, implemented by a set of  $R$ -values somewhat smaller than used in fig. 5.3. We recall that in this case the polymer chains are allowed to pass through the layer thereby effectively changing the grafting density of the convex and concave sides. Of course in this redistribution process the overall grafting density remains constant. In the limit of very high curvatures, it is found that the volume fractions in the inner (concave) part tends to become independent of coordinate  $r$ ; the chains that probe the concave region become highly confined and fill the inner region almost homogeneously. The dependence of the chains redistribution parameter ( $x = \Delta\sigma/\sigma$ ) (cf. Eqn 5.23) on the curvature parameter ( $H_{1(\text{SF})}/R$ ) is presented in fig. 5.6b, which may be compared to fig. 5.2b. For small values of the curvature parameter the level of redistribution of the chains depends linearly on the curvature parameter (see Eqn. 5.29), which is similar to the analytical predictions, but with a difference in the slopes (for the cylindrical case  $b_1 = 0.6$  (analytical),  $= 0.3$  (SCF) and for spherical case  $b_1 = 1.1$  (analytical)  $= 0.56$  (SCF)).

We are now in the position to discuss the main result of this paper. In fig. 5.6a we present the numerical result for the change in free energy upon the bending for a bilateral brush, i.e., for the annealed case. This result should be compared to the corresponding figure 5.2a where the predictions for the QP models was presented. The first impression is that the curves of fig. 5.6a are similar to those of fig. 5.2a. For the spherically curved membrane we find a monotonic decreasing free energy change upon bending, whereas for

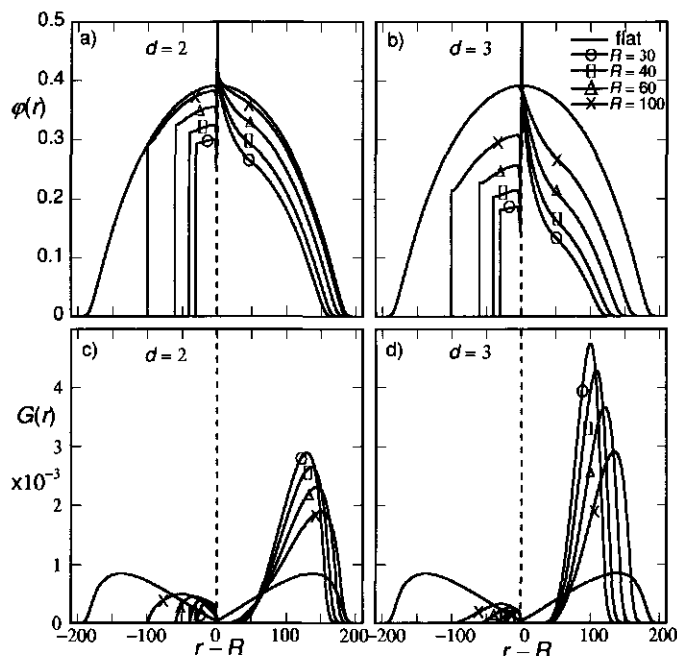


**Figure 5.5:** The polymer density profiles  $\phi(r)$  (a,b) and the distribution of free ends  $G(r)$  (Eqn 5.35) (c,d) for cylindrically curved brushes (a,c) and for spherically curved brushes (b,d) for the annealed bilateral brush. Besides the flat case, the radii of curvature  $R = 30, 40, 60$  and  $100$  as presented as indicated. The chain length  $N = 500$  and the grafting density is  $\sigma = 0.1$  and solvent quality is good ( $\chi = 0$ ). Note that the volume fraction profile trivially becomes zero when  $r - R < -R$ , i.e. when the  $r$  coordinate becomes zero.  $G(r)$  is normalised to  $\sigma$ , but note that the polymer profile obeys to  $N\sigma = \sum_r L(r)\phi(r)$ .

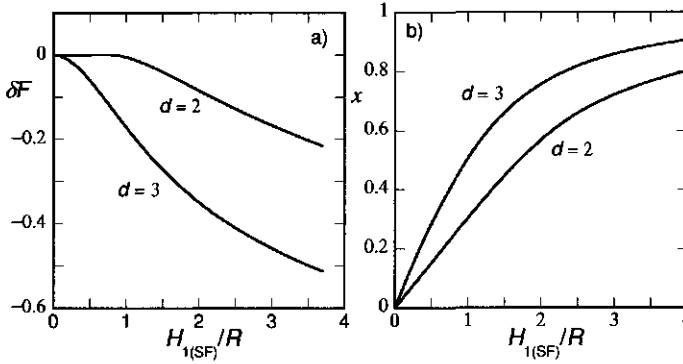


**Figure 5.6:** a) The relative change in the specific free energy upon bending  $\delta F$  as obtained from the SF-SCF model and b) the fraction of translocated chains  $x$  as functions of relative curvature  $H_1/R$  for spherical ( $d = 3$ ) and cylindrical ( $d = 2$ ) curvatures. The polymer length ( $N = 500$ ) and grafting density on each side of the grafting plane ( $\sigma = 0.1$ ), the solvent quality is good ( $\chi = 0.$ )

the cylindrical bending case there is an initial rise of free energy, similarly as in fig. 5.2a, followed by a decrease of the free energy at larger curvatures. For spherical bending this result appears natural and matches the theory independent of the model used. For cylindrical bending the dependence is indeed non-monotonous. It is surprising, because the NL model predicted a monotonic behavior also for the cylindrical case, which now appears to be qualitatively in conflict with the numerical results. It is necessary to point out that the variation of the free energy in the SF-SCF calculations, at low curvatures, is much weaker than predicted in fig. 5.2a for both NL and QP models.

A more essential disagreement between results of figs. 5.6a and 5.2a appear when the dependences of the free energy increase for the cylindrical bending on the governing parameters  $N$  and  $\sigma$  are considered. According to the analytical theory the free energy increments for different  $N$  and  $\sigma$  values should follow a universal curve in the reduced coordinates of fig. 5.2a. In figs 5.7 and 5.8 we present these dependencies for the cylindrical and spherical cases as computed from the numerical theory. For the spherically curved bilateral brush we indeed find a universal dependence; all curves collapse onto one single master curve. In the cylindrical case however, shown in figs 5.7a and 5.8a, this is not the case. Close inspection shows that there are pronounced deviations at low curvatures. In the initial positive parts of  $\delta F$  the relative deviations are important showing that the dependences for the

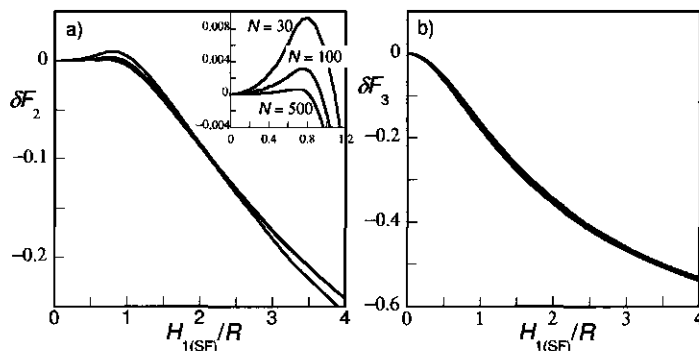


**Figure 5.7:** The free energies of curvature for a) cylindrical and b) spherical cases calculated with SF-SCF model for one grafting density  $\sigma = 0.25$  and three different chain lengths  $N = 30, 100$  and  $500$ . The inset in viewgraph (a) demonstrates the initial (low curvature) growth of free energy for the cylindrical bending. Solvent quality is good  $\chi = 0$ .

various  $N$  and  $\sigma$  values definitely do not follow a single master curve as expected in these reduced coordinates.

The scaling dependencies for the increase of  $\Delta F$  for small curvatures were numerically fitted and found to be given by

$$\Delta F_3 \sim \begin{cases} -\frac{N^3 \sigma^{2.7}}{R^2} & \text{good solvent} \\ -\frac{N^3 \sigma^{3.2}}{R^2} & \theta\text{-solvent} \end{cases} \quad (5.38)$$

for the spherical geometry and for the cylindrical geometry

$$\Delta F_2 \sim \begin{cases} \frac{N^{2.1} \sigma^{1.9}}{R^2} & \text{good solvent} \\ \frac{N^{2.3} \sigma^{2.3}}{R^2} & \theta\text{-solvent} \end{cases} \quad (5.39)$$

These result should be compared to similar predictions presented in Eqns 5.31 and 5.34. In the spherical case we get a rather satisfactory agreement with the analytical theory. Apparently, the analytical theory correctly accounts the influence the convex and concave curvature on interactions and deformation of chains. The positive entropic term (Eqn. 5.34), due to the redistribution of chains between the layers, is small compared to this relatively large negative term and is not important.

The opposite situation present itself for weakly curved layers in the cylindrical geometry. The numerically found  $\Delta F_2$  value (Eqn 5.39) is much weaker than

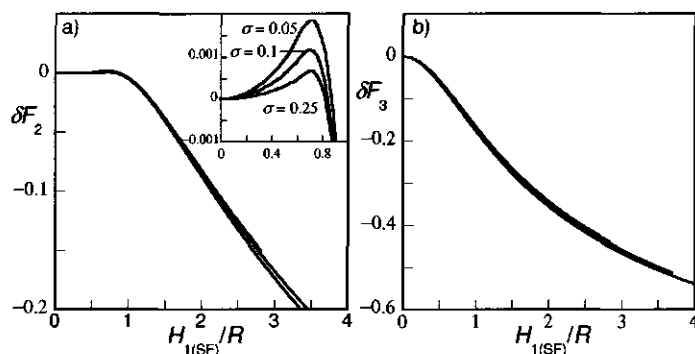


**Figure 5.8:** The free energies of curvature for a) cylindrical and b) spherical cases calculated with SF-SCF model for one chain length  $N = 500$  and three different grafting densities  $\sigma = 0.05, 0.1$  and  $0.25$ . The inset in viewgraph (a) demonstrates the initial (low curvature) growth of free energy for the cylindrical bending. Solvent quality is good  $\chi = 0$ .

the theoretical  $\Delta F$  given in Eqn 5.31; rather it has the magnitude of the entropic term  $\Delta F_S$  given in Eqn 5.34.

Finally, in fig. 5.9 an additional demonstration of these results is presented. In this figure we give the curvature free energy in the cylindrical geometry in the limit of low curvatures, this case normalised per chain, i.e.,  $F_1 \delta F_2 / \sigma$ . It follows from fig. 5.9 that the free energy change per chain upon a weak cylindrical bending appears to be a universal function of the relative curvature  $H_{1(SF)}^2/R$ . Hence for weak cylindrical curvature one can see only the entropic term  $\Delta F_S$  which has masked the  $\Delta F$  even for  $N = 500$ . This means that the numerical calculations by the SF-SCF method, which take all the specificity of the bilateral polymer brush into account, give very low values for the  $b_2$  coefficient in Eqn 5.30. The question about the sign of this coefficient, which is practically equal to zero, loses sense especially for not too large values of the chain length of the grafted chains. In our calculations we have restricted ourselves to  $N \leq 500$ .

### 5.5.3 Bending moduli of a bilateral polymer brush

The physics of curved interface is very often put in the perspective of the Helfrich free energy expansion.<sup>162</sup> In this approach the bending free energy is presented as

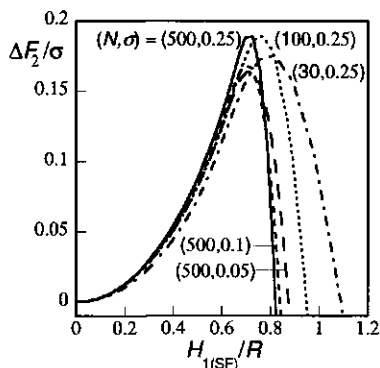


**Figure 5.9:** The initial part of the free energy of curvature in the cylindrical geometry normalise per polymer chain,  $\Delta F_2/\sigma$  (defined in the text) plotted as a function of the natural measure of the curvature  $H_{1(\text{SF})}/R$  as found by the SF-SCF method. The different lines present several chain lengths and grafting densities as indicated. Solvent quality is good  $\chi = 0$ .

$$\Delta F = \int \left( \frac{1}{2} k_c (c_1 + c_2 - 2c_0)^2 + \bar{k} c_1 c_2 \right) ds \quad (5.40)$$

Here the integral is over the whole area of the membrane,  $c_1 = 1/R_1$  and  $c_2 = 1/R_2$  are the local curvatures in each point and  $c_0$  is the spontaneous curvature, which is absent in our case due to the symmetry reasons. The bending modulus  $k_c$  and the Gaussian modulus  $\bar{k}$  can be obtained from considering the homogeneously spherical and homogeneously cylindrical bending cases, separately. The free energies per unit area are then expressed as  $\Delta F_2 = k_c/2R^2$  and  $\Delta F_3 = (2k_c + \bar{k})/R^2$ . Thus we directly translate our scaling predictions to those expected for the mechanical bending rigidities. From the previous expressions 5.38 and 5.39 we directly arrive at

$$k_c \sim \begin{cases} N^{2.1} \sigma^{1.9} & \text{good solvent} \\ N^{2.3} \sigma^{2.3} & \theta\text{-solvent} \end{cases} \quad (5.41)$$

$$\bar{k} \sim \begin{cases} -N^3 \sigma^{2.7} & \text{good solvent} \\ -N^3 \sigma^{3.2} & \theta\text{-solvent} \end{cases} \quad (5.42)$$

Note that as  $\bar{k}$  is much larger in numerical value than  $k_c$ , its scaling remains similar to the one for  $\Delta F_3$  as given in Eqn 5.38. We would like to

note here as well that although the  $k_c$  is positive, which means that grafted polymer makes the membrane stiffer, it scales almost  $N$  times smaller than  $\bar{k}$ . Therefore, when polymers are long enough the flat conformation becomes increasingly unstable in favor of bending. From the Helfrich analysis it is known that the flat conformation remain stable as long as  $2k_c + \bar{k} > 0$ . When this is no longer the case, i.e. when the chain length is sufficiently large, one should expect non-lamellar geometries such as worm-like or micellar-like objects. Of course to model these transitions it becomes necessary to also consider what happens with the rigidity of the surface (membrane) onto which the chains were grafted. Such an analysis is possible in the SF-SCF approach<sup>163–165</sup> but requires a more elaborate model.

## 5.6 Conclusions

The bending of a bilateral symmetrical polymer brush leads to the formation of two inequivalent curved brushes (convex and concave). We have evaluated the free energy of bending of such membrane when the redistribution of chains from the concave to the convex layer is allowed for. Bending of bilateral brushes in the limit of large curvatures is well understood. According to the analytical theory such brushes stabilize highly curved vesicles from becoming planar. These results are totally confirmed by numerical SF-SCF calculations both for the spherical as well as the cylindrical type of bending.

For spherical bending the same situation persist up to the weak curvature regime. The bending free energy in the spherical bending case is negative and monotonically decreases with the imposed curvature. The numerical results obey a universal scaling for the chain length and grafting density dependencies.

The weak cylindrical curvature regime for a bilateral brush differs from the strong curvature limit. As mentioned in the introduction, the analytical theory shows contradictory results for a few different approaches. When the free ends are fixed at the external brush boundary, the change  $\Delta F$  in the conformational free energy of a bilateral brush in the cylindrical mode is positive in the Daoud-Cotton model (QP framework, Birshtein and Zhulina<sup>142</sup>). On the other hand, in the NL framework  $\Delta F < 0$  ( see Table 5.2 and also Potemkin<sup>155,156</sup>). The relaxation of free ends (Subbotin et al.<sup>152</sup>) leads to inversion in sign of  $\Delta F$ , making the cylindrical mode of curvature unfavorable.

At weak curvatures and for relatively short chains, the conformational contribution  $\Delta F \sim F_1 H_1^2 / R^2 \sim N^3$  could be comparable to the entropic contribution,  $-\Delta F_s \sim H_1^2 / R^2 \sim N^2 > 0$ , which opposes chain flip-flop from

one side of a membrane to the other. The sum of the two terms governs the stability of the flat bilayer at weak cylindrical bending. Clearly, the result is sensitive to both, the sign and the value of numerical coefficient in  $\Delta F$ . The numeric SF-SCF results, that are expected to be the most realistic, lead to the peculiar conclusion that in the range of molecular weights investigated ( $N \leq 500$ ), the free energy contribution  $\Delta F$  is in fact close to be non-existent (the above mentioned coefficient is very small). The modest penalty for the weak cylindrical curvature turned out to be determined by a mere entropic loss due to the redistribution of the chains from one side of a membrane to the other.

Thus, the increase of the free energy caused by the weak cylindrical bending poses just a low and surmountable barrier for the formation of relatively strong and thermodynamically favorable cylindrical curvatures. The other important aspect is that the change in sign of the curvature free energy takes place at  $H_1(SF)/R \leq 1$ . The bilayer thus retains its ability to bend long before the interactions between oncoming layers at the concave side occurs.

In the introduction we have discussed the connection between the results for the cylindrical bending of an initially flat bilayer and the bending of an adsorbed molecular brush (a comb-like polymer). Our numerical results explain the nature of the tendency for such macromolecules to form highly curved structures. Similar situation was found in the solution.<sup>151</sup> Note that at least qualitatively, the redistribution of side chains in a cross-section of a bent molecular brush in the solution resembles that in a two-dimensional comb-like polymer (adsorbed molecular brush). It occurs predominantly from the concave to the convex part of a locally bent macromolecule.



## Summary and General Discussion

In this thesis we discuss polymeric nanoparticles with a core-shell topology (CSP), which are the main component in waterborne automotive base-coat dispersions. These particles are composed of various acrylic monomers, linked together via a two-step emulsion droplet polymerization procedure. During the first step the compact cores of the particles are formed. The main component of the cores is methacrylate, which makes them glassy and hydrophobic at room temperature. During the second step of the particle synthesis, the shells are formed. The shells give these particles not only an excellent colloidal stability, but interestingly, they also contribute, in concentrated solutions, to a pronounced pseudoplasticity. This unique combination of properties must be related to the chemical composition of the shell polymers: a relatively small fraction of methacrylic acid (MMA) groups is intermixed with hydrophobic monomers (butyl-acrylate). On top of these major moieties, both the shells and the cores are functionalized with acrylic polymers that have an OH-group. In the coating application, these segments are used to cross-link the resulting film. In this thesis we did not study the cross-linking aspects and focused primarily on the nanoparticles, their interactions and the resulting dispersion properties.

It appears that the current waterborne automotive coating dispersions still need a significant amount of butyl-glycol as a co-solvent. This addition proved necessary to obtain a high quality coating. There are good reasons to minimize the use of this co-solvent in the future. However, one should not lose the quality of the final film when doing so. It therefore turned out that there is a need for a better understanding on the properties of the nanoparticles, how these particles interact with each other and how this results in the dispersion properties. The goal of this thesis is to contribute towards this insight. The more general aim is to determine the interaction between the CSPs in order to be able to formulate suggestions for improvement of the properties of the waterborne coating systems. This is an insight that is not only vital for the industry, but also provides an interesting challenge from scientific point of view.

It is known that butyl glycol acts as a plasticizer for the otherwise glassy cores. In this context it is relevant to mention that the shell polymers are not chemically linked to the cores. During the synthesis the temperature is about 85 °C. At this elevated temperature the core is in a molten state and the shell chains are physically adsorbed onto the core. Upon cooling to room temperature the cores become glassy and the shell polymers become trapped with some of their (hydrophobic) segments in the outer parts of the core. In this way the shell is 'irreversibly grafted' to the core. However, in the presence of butyl-glycol the shell may return to the freely adsorbed state. The use of butyl-glycol may therefore be rather fundamental and that is why in our work we have also considered the role of butyl-glycol.

Detailed information about the structure and the structural changes in the particles with a change in solvent quality, the pH and ionic strength, is collected in chapter 2. The main conclusions are:

- i The particles have a spherical shape, with a minimal radius  $R$  of about 70 nm when the MAA groups in the shells are completely deionized (low pH).
- ii Upon an increase of the pH ( $\text{pH} > 6$ ), the shells become negatively charged and swell (they take up water) so that the hydrodynamic radius changes from  $R \approx 70$  nm to about 150 nm ( $\text{pH} \approx 9$ ). This change in size is attributed to the osmotic pressure generated by the counterions that partition inside the shell layer to compensate for the charge of the dissociated MAA segments.
- iii The shell polymers are (in the absence of butyl-glycol) effectively grafted onto cores: even at a rather high pH ( $> 9$ ), the shells remain associated to the core and apparently cope with the increasing electrostatic/osmotic forces.
- iv Each particle carries roughly  $2.5 \times 10^5$  acid groups.
- v The core-shell particles are rather monodisperse.

The data obtained from the characterization experiments resulted in a model for the core-shell particles. In this model the cores are represented as inert, solid, non-interacting spherical particles and the shell polymers are seen as end-grafted chains, that is, they are mimicked by a homodisperse brush of hydrophobic polyelectrolyte chains. The model can be used in a self-consistent field (SCF) analysis. It is found that this theoretical approach can mimic the (size) behavior of real particles as a function of the acidity and salinity of the solution.

At this point it is important to stress that the model is deliberately kept as simple as possible: the shell polymers are considered to be monodisperse and composed of only two types of monomers - ionizable weak acids and hydrophobic monomers between them. Nevertheless, as this model fits, in first order, the experimental data, it shows that the main features of the system are represented. It is possible to refine the model, e.g., (i) by considering particles with a polydisperse brush, that is by chains with different lengths, (ii) by a polymer brush with a tapered segment distribution, that is, chains that have more MAA segments at the free end of the shell chains than near their grafting point, or (iii) by representing the shell layer as a brush of loops, that is by chain fragments that are grafted by both ends to the core. Undoubtedly such a more complex model is closer to reality. However, it will also have more unknown variables and this hampers a systematic analysis. For this reason we decided to focus on the simple model.

In chapter 3, we elaborated on the SCF analysis of the model system. Within the SCF framework, originally developed by Scheutjens and Fleer (SF-SCF), one evaluates numerically the equilibrium properties of rather sophisticated polymeric systems, and one can extract detailed predictions both with respect to structural as well as to thermodynamical aspects. In more detail, we focused on homodisperse hydrophobic polyelectrolyte brushes (HPB) in various geometries, both in isolated as well as in interaction mode. Typically we assumed that the brush is laterally homogeneous, so that we could simplify the problem doing an one-gradient analysis. In this way we could study the limiting cases of star-like hydrophobic polyelectrolyte (HPE) brushes (small particle limit) and flat HPE brushes (mimicking large particles). In this chapter we have systematically analyzed the importance of the relevant physical chemical parameters for such HPE brushes.

The modeling work reported in chapter 3 is performed in such a way that it is not only relevant for our particular CSP system, but rather for a wide class of end-tethered moderately hydrophobic polymers (Flory-Huggins interaction parameter is  $\chi = 1$ ) that also contain ionic segments. Such systems frequently occur in applications and there are also examples in natural systems: unstructured protein tails with a sufficiently number of charged amino acids intermixed with hydrophobic ones qualify for this and occur, e.g. in neurofilaments.<sup>166</sup> We have studied both the weak acid cases, when the number of charges on the polymer chains depend on the surroundings, as well as the strong acid cases, for which the charge density along the chain is independent of solvent conditions (pH, ionic strength, co-solvent).

In this type of polymer systems there is an interesting interplay between

hydrophobic attraction and electrostatic repulsion. In a relevant part of the parameter space, this results in two populations of conformations of the chains, giving rise to non-trivial polymer density profiles in the direction perpendicular to the grafting surface: part of the chains are charged and stretched due to the electrostatics and the other part is uncharged and collapsed due to hydrophobic interactions. This implies that intermediate chain conformations, that is conformations which are partly collapsed and with few charges, are avoided. In our view, such a micro-phase segregated brush may occur in the CSP system and is at the basis of its intriguing properties. Our main interest was drawn to the consequences with respect to the colloidal interaction forces.

Colloidal interactions are studied by considering two interacting objects (HPE-brushes) at large separation and then reduce the distance between them in several steps. For each value of the distance we recomputed the equilibrium conformations of polymers within the gap. As in the SCF approach the mean-field free energy is available, one can compute the interaction free energy and interaction forces as a function of the imposed distance. Typically when the HPE brush is in a micro-phase segregated state, or is very close to such a transition, one may induce abrupt changes upon the confinement of the opposing brushes. In the case of such a sharp change in the conformation upon approach (phase transition on a microscopic level), meta-stable states of the system, that is states of the system with a higher free energy than the ground state, may be probed as well. Typically, upon approach of the two HPE brushes (or corresponding stars) they first repel at large distances, due to the electrostatic contributions, and then, close to contact, attract due to hydrophobic forces. The transition between the repulsion and attraction may become rather sharp as the intermediate situation with partially charged chains is unfavourable as mentioned already.

In general, information on the free energy of interaction between two particles is only the first step to understand the macroscopic behaviour of a large set of such particles in a suspension. As explained in the introduction of this thesis, we have collaborated within this project with the group of prof. Briels in Twente University who set out to model the rheology of CSP suspensions. In their responsive particle dynamics (RaPiD) simulations<sup>116,167</sup> they need the pair interactions of their coarse-grained particles, e.g., such as those computed using the SCF approach, as an input. To date, the RAPID simulations have been executed by using ad-hoc pair potentials. We now argue that introducing the SCF predictions in these simulations is of more than average interest. A possible outcome of this is that we can relate the non-linear rheology, which is the outcome of the RAPID simulations, to the features of the interaction potentials and thus to the physico-chemical

properties of the CSPs. Work in this direction is strongly recommended.

In chapter 3 we have studied various end-tethered HPE systems. More specifically we considered the 'flat polymer brush', the 'bilateral brush' and the 'star-like brush'. In this order there is a growing degree of freedom for the grafted chains to reposition themselves when such brushes are confined. In the flat brush case there is no possibility for polymers to escape from the contact zone. In the bilateral brush, by construction of this brush, the chains may flip from the interior to the exterior of two interacting layers (reorganization in one dimension). In star-like configurations the chains may leave the field of contact in any direction (reorganization in two dimensions) (see figure 1.3 in chapter 1). Intuitively, one would expect that upon confinement the chains make use of this degree of freedom and escape from the contact zone to lessen the confinement force. For HPE the opposite happens. In this case, upon confinement, the polymers rather decharge and come into the contact zone, leaving more space to the remainder of the chains so that these can stay charged more easily. This illustration shows that a suspension of core-shell particles can show rather complex behaviour when the concentration increases, e.g., upon drying.

In a coating formulation the concentration of the CSPs is rather high and the pH is such that the shells are swollen. Typically, the CSPs interact strongly under these conditions and they have a high zero-shear viscosity. From a polymer physics point of view the system is in the overlap regime. The response of the particles upon confinement is therefore also relevant for these application conditions. When the HPE brush is in the microphase segregated state, the application of shear may induce local/temporary deionization of the chain and a redistribution of the chains in the collapsed or swollen state. This may contribute to an explanation of the shear thinning found for concentrated CSP systems.

We mainly focused on laterally homogeneous one-gradient cases, but two-gradient ones have been studied as well. In a flat lattice this allowed for an inhomogeneous structure in the lateral direction. In the case of low grafting densities this resulted in the possibility to form "droplets" of polymers on the surface. In the interaction-mode, two surfaces with droplets behave in a rather peculiar, but understandable, manner: the droplets arrange themselves in a check-board order on opposite surfaces in order to minimize their contact area. Then upon closer contact the droplets order face-to-face so that compact bridges can form. Further confinement results in a homogeneous polymer layer (in the lateral direction). These findings are in line with results found for two interacting stars: upon approach the polymer chains fill the area between the stars rather than escaping from contact. This provides for a compact collapsed bridge-contact between stars, as well as for

more space for the remainder of the chains, so that these can be charged more easily. We can now speculate, that this scenario results in elongated clusters of core-shell particles in concentrated solutions: from a geometrical point of view such a structure optimizes the surface area of the cluster, and this helps to keep the less-confined chains in a charged state. This may be contrasted to the formation of spherical clusters of particles which minimize the surface area and which suppresses the presence of charged chains. It would be interesting to check this scenario experimentally, e.g., by doing scattering studies or osmotic pressure experiments.

The complex behaviour of HPE brushes, as discussed in chapter 3, is expected to be relevant for the CSP system. For this reason we decided to perform atomic force microscopy (AFM) force measurements on the CSP system. As the particles are rather small, we have chosen to measure forces between layers of particles rather than to measure single-particle interactions. We report on our results in chapter 4. The making of densely packed layers of CSPs on top of a flat silica surface proved to be a rather tricky task. It took some time and experience to realize that in order to adsorb these particles on a surface, the particle-particle repulsion should be screened and the surface should be hydrophobised. Under such conditions, reproducible layers of CSP have been obtained. These layers were found to be stable under all relevant solution conditions. Forces between two such layers were routinely measured using the colloidal probe AFM technique in varying solvent conditions (acidity and ionic strength), as well as in the presence of co-solvent.

The results of these experiments proved to give further insights in the behaviour of the core-shell particles. We consider the forces upon approach and those upon retraction of the surfaces separately. The approach forces are in good agreement with the theoretical predictions. Predominantly repulsive and long-ranged forces are attributed to the presence of the electrostatically swollen polymer shell that exist on the particles. Both the pH and ionic strength dependences qualitatively follow the predictions. However, from a detailed fitting of the experimental data we concluded that a more elaborate model, that is a model wherein the shell brush is composed of chain with different lengths, is necessary. As discussed above, due to the number of unknown variables, that makes a systematic analysis difficult, we did not pursue this further.

The measured forces upon retraction of the surfaces, depend on the time the surfaces are kept in a close contact. At zero waiting time the retraction forces often exactly reproduce the approach ones. Differences only appear at low pH values when some adhesion is observed. Longer waiting times (several seconds) resulted in the formation of bridges between individual core-shell

particles. These bridges are well-explained and fitted rather precisely with a theoretical model for the stretching of bridging polymers (that is, chains that are grafted by both ends to opposite surfaces). Systematic experiments with variation in surface waiting times, gave us information on the characteristic time of bridge formation. This characteristic time is in good agreement with the time-scales used for the "memory function" in the simulations to predict the onset shear rate after which shear-thinning behavior of the CSP dispersion occurs, performed in the group of prof. Briels of Twente University.

The addition of a co-solvent, butyl glycol, has been studied with AFM as well as with dynamic light scattering (DLS) measurements. The addition of butyl glycol facilitates the transition of cores from a glassy to a molten state. As a result, the shell particles become physically adsorbed to the cores rather than effectively grafted (as in pure water). Under highly charged conditions (very high pH), in the presence of butyl glycol (30wt% solution in water), the shells can detach from the particles and this results in a precipitation of the naked cores. Under mild pH conditions ( $\text{pH} < 9$ ), the particle interaction changes (with respect of the ones measured in pure water) only slightly upon approach. Again, unless the pH is very low the forces are repulsive.

The retraction forces, however, were noticeably different. In the presence of butyl-glycol very long bridges were found, which persist on a 10 times longer length-scale than in pure water. We argued that the shell polymers bridge when the particles are in close contact and then upon retraction, these bridges are stretched upto their full extension before they snap loose. Apparently, the loops can become very large in the case of butyl-glycol. This effect points to the direction that the shell polymers exists as multiple loops. In the case of pure water, both ends of these loops are fixed in the glassy cores and thus form a brush of loops. In the presence of the co-solvent a similar brush of loops is present (the forces upon approach are similar) but, as the cores are liquid-like, upon retraction, the small loops can fuse into longer ones when some of the anchor points detach from the core. In this way the bridges can become very long, explaining the experimental results. In passing we note that this interpretation is consistent with the finding from size-exclusion chromatography that the shell polymers have a very high degree of polymerisation.

The fifth chapter of this thesis is somewhat different from the remainder, as it deals with a theoretical analysis of a separate system. In this work the focus was on the mechanical properties of a polymer bottle-brush. The work was triggered by the observation that a dispute existed in the literature on how the bending rigidity of bottle-brushes scales with the length of the brush chains. Analytical approaches to this problem, typically are based on the

mean-field approximation and, on top of this, implement assumption/approximations to come to scaling predictions. Such additional approximations are not necessary in the SF-SCF theory. Hence, the SF-SCF theory can be used to check the validity of the assumptions/approximations made in the analytical approaches. In this work, we invented a rather interesting way to mimic a bottle-brush in a one-gradient model and called this the bilateral brush. More specifically we end-grafted polymers to some layer on the lattice (which mimics the main chain of the bottle-brush), and allowed the chains to travel freely through this grafting layer. The geometry of such lattice can still be spherical or cylindrical, and thus we can impose a curvature on this grafting layer. This allowed for the evaluation of the bending moduli for bottle-brush like configurations. We compared this to the bending rigidity of brushes that lack the possibility to relocate their chains. In line with expectations we show that the bending rigidity of a polymer brush decreases when the chains can relocate upon the imposed curvature from the 'inner' to the 'outer' side of the curved brush. We included this chapter in the thesis, because the new method of polymer grafting to a permeable layer (that is, the bilateral brush) is also used in chapter 3 as one of the ways to mimic the ability of grafted HPE brushes to translocate their chains upon an imposed (local) confinement.

The combination of systematic experiments and corresponding molecularly realistic computer modeling is used successfully to generate information on the properties of hydrophobic polyelectrolyte brushes as these occur in core-shell particles that are relevant for waterborne automotive coatings. On the one hand we have confirmed various properties that were anticipated already for this system and provided molecular interpretation for them. On the other hand we have generated novel information on its physical chemical properties. Additionally, our work provided a physically coherent explanation for the MD results obtained in the group of prof. Briels. Typical for the research situation, we suggest answers to only a few of the initial questions, and posed many more new questions related to the behaviour of this system. Nevertheless we hope that our efforts contributed positively to the task to reduce the use of butyl-glycol as a co-solvent in waterborne automotive coating applications.



# Samenvatting

In dit proefschrift worden fysisch-chemische onderzoekstechnieken en zelf-consistent-veld berekeningen besproken welke uitgevoerd zijn aan core-shell deeltjes, de actieve component van watergedragen verfsuspensies, die gebruikt worden in de autoindustrie. De term 'watergedragen' suggereert dat er geen gebruik gemaakt wordt van organische oplosmiddelen. Echter, in de praktijk wordt er een significante hoeveelheid butylglycol toegevoegd aan de verfsuspensie om uiteindelijk een acceptable coating te krijgen.

Om de eigenschappen van de coatings te verbeteren en de butylglycol toevoeging te reduceren is het nodig om meer te weten over de eigenschappen van de core-shell deeltjes in de verfoplossing. In het eerste technische hoofdstuk (hoofdstuk 2) bespreken we resultaten van allerlei experimenten die we uitgevoerd hebben om deze deeltjes fysisch-chemisch te karakteriseren. Met behulp van statische lichtverstrooiing is informatie verkregen over het moleculaire gewicht van deze deeltjes. De hydrodynamische afmeting van de deeltjes als functie van de pH en zoutsterkte zijn onderzocht met dynamische lichtverstrooiing. Potentiometrische titraties zijn gebruikt om te achterhalen hoeveel geladen groepen er in de shell (corona) aanwezig zijn. Met behulp van deze parameters is een ruw model opgesteld voor deze deeltjes. Dit model was geschikt als invoer voor een zelf-consistent-veld (ZCV) analyse. In dit model worden de deeltjes voorgesteld als een vaste kern waarop een geladen hydrofobe borstel is verankerd.

In hoofdstuk 3 hebben we allerlei aspecten van hydrofoob geladen borstels (HGB) bestudeerd gebruikmakend van een zelf-consistent-veld theorie. Uit deze modelberekeningen kwam naar voren dat in deze borstels een interessant samenspel tussen hydrofobe en electrostatische wisselwerkingen plaatsvindt. Dit maakt dat met name de wisselwerking tussen zulke HGB lagen complex verloopt. Zonder in teveel detail te treden, wordt voorspeld dat de lagen elkaar op grote afstand afstoten, maar dat er attractie ontstaat als ze sterk op elkaar gedrukt worden. In andere woorden, er vindt een overgang plaats van hydrofiel gedrag naar hydrofoob gedrag wanneer de deeltjes elkaar naderen. Dit gebeurt ook tijdens het droogproces nadat de verfsuspensie op een oppervlak

is aangebracht. De niet-triviale paarpotentiaal tussen de deeltjes wordt ook verantwoordelijk geacht voor het pseudoplastisch gedrag van de geconcentreerde verfsuspensie onder applicatiecondities.

Gebruik makend van de atomaire kracht microscoop (AFM), en met name de colloïdale probe methode, zijn de krachten gemeten tussen twee lagen van core-shell deeltjes op een vast oppervlak. We rapporteren hierover in hoofdstuk 4. In deze experimenten kwam een complex gedrag naar voren dat in detail is bestudeerd. Samen met de inzichten van het theoretisch hoofdstuk en het karakteriseringshoofdstuk zijn we in staat gebleken om veel van de gemeten verschijnselen te duiden. Zo hebben we gezien dat bij nadering van de deeltjes, elektrostatistische repulsie domineert. Wanneer na een bepaalde contacttijd de oppervlakken uit elkaar worden getrokken, zien we dat er bruggen zijn gevormd die weerstand bieden tegen het uiteen laten gaan van de oppervlakken. De relaxatietijd die met het maken van bruggen is geassocieerd is in de orde van 10 seconde.

Onze metingen en berekeningen aan de paarpotentiaal (en de genoemde relaxatietijd) tussen de core-shell deeltjes kunnen gebruikt worden in RaPiD simulaties die ontwikkeld zijn in de groep van prof. Briels aan de universiteit van Twente, om het rheologisch gedrag van geconcentreerde suspensies te voorspellen. Simulaties welke expliciet de interactiepotentialen die wij gemeten en berekend hebben gebruiken, moeten nog worden uitgevoerd, maar als deze tot een goed resultaat wordt gebracht is het mogelijk om het macroscopische rheologisch gedrag van deze suspensies terug te voeren op de moleculaire eigenschappen van de deeltjes. Hiermee moet het mogelijk worden om de eigenschappen van een watergedragen coating te verbeteren en om het gebruik van butylglycol in de verfsuspensies terug te dringen.

## References

- [1] D.C. Webster, B.J. Chisholm, and S.J. Stafslien. *Biofouling*, 23:179, 2007.
- [2] B.J. Chisholm and D.C. Webster. *J. Coat. Technol. Res.*, 4:1, 2007.
- [3] K.D. Weiss. *Prog. Polym. Sci*, 22:203, 1997.
- [4] P. Pincus. *Macromolecules*, 24:2912, 1991.
- [5] R.R. Netz and D. Andelman. *Physics Reports - Review Sec. Phys. Lett.*, 380:1, 2003.
- [6] M. Ballauff and O.V. Borisov. *Current Opinion in Colloid and Interfacial Science*, 11:316, 2006.
- [7] P. Flory. *Principles of Polymer Chemistry*. Cornell University Press, Ithaca N.Y., 1953.
- [8] M.V. Volkenstein. *Configurational Statistics of Polymer Chains*. Interscience Publishes, New York, London, 1963.
- [9] T.M. Birshtein and O.B. Ptitsyn. *Conformations of Macromolecules*. Interscience, 1966.
- [10] S.F. Edwards. *Proc. Phys. Soc*, 85:613, 1965.
- [11] S.F. Edwards. *Proc. Phys. Soc.*, 88:265, 1966.
- [12] P.-G. de Gennes. *Scaling Concepts in Polymer Physics*. Cornell University Press, 1979.
- [13] W.F. Maier, K. Stöwe, and S. Sieg. *Angew. Chem. Int. Ed.*, 46:6016, 2007.
- [14] A.M. Winnik. *Curr. Opinion Coll. Int. Sci.*, 2:192, 1997.
- [15] H. Wang and A.R. Denton. *Phys. Rev. E*, 70:041404, 2004.
- [16] X. Guo, A. Weiss, and M. Ballauff. *Macromolecules*, 32:6043, 1999.

- [17] X. Guo and M. Ballauff. *Phys. Rev. E*, 64:015406, 2001.
- [18] A. Jusufi, C.N. Likos, and M. Ballauff. *J. Colloid Polym. Sci.*, 282:910, 2004.
- [19] M. Ballauff and Y. Lu. *Polymer*, 48:1815, 2007.
- [20] L. Zhang and A. Eiaenberg. *Science*, 268:1728, 1995.
- [21] L. Zhang, K. Yu, and A. Eiaenberg. *Science*, 272:1777, 1996.
- [22] M. Moffitt, K. Khougaz, and A. Eisenberg. *Acc. Chem. Res.*, 29:95, 1996.
- [23] W. Groenewegen, S.U. Egelhaaf, A. Lapp, and J.R.C. van der Maarel. *Macromolecules*, 33:3283, 2000.
- [24] A.S. Lee, V. Bütün, M. Vamvakaki, S.P. Armes, J.A. Pople, and A.P. Gast. *Macromolecules*, 35:8540, 2002.
- [25] P. Matejicek, K. Podhajecka, J. Humpolickova, F. Uhlik, K. Jelinek, Z. Limpouchova, K. Prochazka, and M. Spirkova. *Macromolecules*, 37:10141, 2004.
- [26] M. Daoud and C.P. Cotton. *J. Phys.*, 43:531, 1982.
- [27] O.V. Borisov. *J. Phys. II*, 6:1, 1996.
- [28] O.V. Borisov and E.B. Zhulina. *Eur. Phys. J. B.*, 4:205, 1998.
- [29] J. Klein Wolterink, J. van Male, M.A. Cohen Stuart, L.K. Koopal, E.B. Zhulina, and O.V. Borisov. *Macromolecules*, 35:9176, 2002.
- [30] A.R. Denton. *Phys. Rev. E*, 67:011804, 2003.
- [31] E.B. Zhulina, C. Singh, and A.C. Balazs. *J. Chem. Phys.*, 108:1175, 1998.
- [32] F.S. Csajka, R.R. Netz, C. Siedel, and J.-F. Joanny. *Eur. Phys. J. E*, 4:503, 2001.
- [33] R.S. Ross and P. Pincus. *Macromolecules*, 25:2177, 1992.
- [34] S. S. Misra and M. Tirrell. *Macromolecules*, 29:6056, 1996.
- [35] O.V. Borisov, T.M. Birshtein, and E.B. Zhulina. *J. Phys. II*, 1:521, 1991.
- [36] T. Ikawa, K. Abe, K. Honda, and Tsuchida. *E. J. Polym. Sci., Polym. Chem. Ed.*, 13:1505, 1975.

- [37] V. Crescenzi, F. Quadrifiglio, and F. Delben. *J. Polym. Sci.*, 10:357, 1972.
- [38] G. Conio, E. Patrone, S. Russo, and V. Trefiletti. *Die Macromolekulare Chemie*, 177:49, 1976.
- [39] W.D. Harkins. *J. Am. Chem. Soc.*, 69:1428, 1947.
- [40] W.V. Smith and H.E. Roswell. *J. Chem. Phys.*, 16:592, 1948.
- [41] M. Antonietti and K. Tauer. *Macromol. Chem. Phys.*, 204:207, 2003.
- [42] G. Markert. *Houben Weyl: Methoden der Organischen Chemie*, volume E20(2). Georg Thieme, Stuttgart, 1987.
- [43] W. Wunderlich. *Houben Weyl: Methoden der Organischen Chemie*, volume E20(2). Georg Thieme, Stuttgart, 1987.
- [44] J Feder. *J. Colloid Interface Sci.*, 78(1):144, 1980.
- [45] P. Schaaf and J. Talbot. *J. Chem. Phys.*, 91:4401, 1989.
- [46] B. Senger, J.C. Voegel, and P. Schaaf. *Colloids Surf. A*, 165:255, 2000.
- [47] B.L. Rivas, E.D. Pereira, A. Horta, and C.S. Renamayor. *Eur. Phys. J.*, 40:203, 2004.
- [48] G.A. Sorci and W.F. Reed. *Macromolecules*, 35:5218, 2002.
- [49] S.C. Lin, W.I. Li, and J.M. Schurr. *Biopolymers*, 17:1041, 1978.
- [50] W.M. de Vos, F.A.M. Leermakers, A. de Keizer, M.A. Cohen Stuart, and J.M. Kleijn. *Langmuir*, 26:249, 2009.
- [51] F.A. Plamper, H. Becker, M. Lanzendörfer, M. Patel, A. Wittemann, M. Ballauff, and A.H.E. Müller. *Macromol. Chem. Phys.*, 206:1813, 2005.
- [52] L.K. Klushin, T.M. Birshtein, and V.M. Amoskov. *Macromolecules*, 34:9156, 2001.
- [53] H. Huang and E. Ruckenstein. *Langmuir*, 22:3174, 2006.
- [54] J.L. Barrat and J.F. Johanny. *Advances in Chemical Physics*. John Wiley & sons, New York, 1996.
- [55] A.V. Dobrynin and M. Rubinstein. *Progr. Polym. Sci.*, 30:1049, 2005.
- [56] S.S. Patel and M. Tirrell. *Annu. Rev. Phys. Chem.*, 40:597, 1989.

- [57] N.A. Peppas. *Current Opinion in Colloid and Interfacial Science*, 2:531, 2006.
- [58] H. Mori and A.H.E. Müller. *Prog. Polym. Sci.*, 28:1403, 2003.
- [59] M. Zhang and A.H.E. Müller. *J. Polym. Sci. Part A: Polym. Chem.*, 43:3461, 2005.
- [60] Y. Xu, F. Plamper, M. Ballauff, and A.H.E. Müller. *Adv. Polym. Sci.*, 2010.
- [61] S. Forster, V. Abetz, and A.H.E. Müller. *Adv. Polym. Sci.*, 166:173, 2004.
- [62] P.M. Claesson, E. Poptoshev, E. Blomberg, and A. Dedinaite. *Adv. Coll. Interf. Sci.*, 173:114, 2005.
- [63] H.G. Pedersen and L. Bergstrom. *J. Am. Ceram. Soc.*, 82:1137, 1999.
- [64] T. Abraham, S. Giasson, J.F. Gohy, and R. Jerome. *Langmuir*, 16:4286, 2000.
- [65] J. Klein Wolterink, F.A.M. Leermakers, G.J. Fleer, L.K. Koopal, E.B. Zhulina, and O.V. Borisov. *Macromolecules*, 32:2365, 1999.
- [66] M. Roger, P. Guenoun, F. Müller, and et al. *European Phys. Journal E*, 9:313, 2002.
- [67] Y. Mei, M. Ballauff, and A. Jusufi. *Phys. Rev. E*, 77:031805, 2008.
- [68] D.J. Sandberg, J.Y. Carillo, and A.V. Dobrynin. *Langmuir*, 23:12716, 2007.
- [69] R. Israëls, F.A.M. Leermakers, and G.J. Fleer. *Macromolecules*, 27:3087, 1994.
- [70] R.M. Davis and W.B. Russel. *J. Polym. Sci.*, B24:511, 1986.
- [71] J.-F. Joanny and L. Leibler. *J. Phys. (Paris)*, 151:545, 1990.
- [72] V.A. Pryamitsyn, F.A.M. Leermakers, G.J. Fleer, and E.B. Zhulina. *Macromolecules*, 29:8260, 1996.
- [73] S.W. An, P.N. Thirtle, R.K. Thomas, F.L. Baines, N.C. Billingham, S.P. Armes, and J. Penfold. *Macromolecules*, 32:2731, 1999.
- [74] M. Biesalski, D. Johannsmann, and J. Rune. *J. Chem. Phys.*, 117:4988, 2002.

- [75] M. Biesalski, D. Johannsmann, and J. Rune. *J. Chem. Phys.*, 120:8807, 2004.
- [76] E. Mouri, P. Kaewsaiha, K. Matsumoto, H. Matsuoka, and N. Torikai. *Langmuir*, 20:10604, 2004.
- [77] S. Alexander. *J. Phys.*, 38:977, 1977.
- [78] P.-G. de Gennes. *Macromolecules*, 13:1069, 1980.
- [79] T.M. Birshtein, E.B. Zhulina, and O.V. Boriov. *Polymer Sci., Ser.A.*, 38:400, 1996.
- [80] A. Jusufi, C.N. Likos, and H. Lowen. *J. Chem. Phys.*, 116:11011, 2002.
- [81] G.J. Fleer, J.M.H.M. Scheutjens, M.A. Cohen-Stuart, T. Cosgrove, and B/ Vincent. *Polymers at Interfaces*. Chapman & Hall, London, 1993.
- [82] R. Israëls, F.A.M. Leermakers, G.J. Fleer, and E.g. Zhulina. *Macromolecules*, 27:3249, 1994.
- [83] G.H. Fredrickson. *Soft Matter*, 3:1329, 2007.
- [84] M. Müller, K. Katsov, and M. Schick. *Physical Reports*, 434:113, 2006.
- [85] J.M.H.M. Scheutjens and G.J. Fleer. *J. Phys. Chem.*, 83:1619, 1979.
- [86] J.M.H.M. Scheutjens and G.J. Fleer. *J. Phys. Chem.*, 84:178, 1980.
- [87] F. A. M. Leermakers, J. M. H. M. Scheutjens, and J. Lyklema. *Biochim. Biophys. Acta*, 1024:139, 1990.
- [88] C.M. Wijmans, F. A. M. Leermakers, and G.J. Fleer. *Langmuir*, 10:4514, 1994.
- [89] J.M.P. van den Oever, F.A.M. Leermakers, G.J. Fleer, V.A. Ivanov, N.P. Shusharina, A.R. Khokhlov, and P.G. Khalatur. *Phys. Rev. E*, 65:041708, 2002.
- [90] O.A. Evers, J.M.H.M. Scheutjens, and G.J. Fleer. *Macromolecules*, 23:5221, 1990.
- [91] E.B. Zhulina, V.A. Priamitsyn, and O.V. Borisov. *Polymer Science USSR*, 31:205, 1989.
- [92] C.W. Wijmans, J.M.H.M. Scheutjens, and E.B. Zhulina. *Macromolecules*, 25:2657, 1992.
- [93] P. Gong, J. Genzer, and I. Szleifer. *Phys. Rev. Lett.*, 98:018302, 2007.

- [94] F.A.M. Leermakers, L.K. Koopal, T.P. Goloub, A.W.P. Vermeer, and J. Kijlstra. *J. Phys. Chem. B*, 110:8756, 2006.
- [95] O.V. Borisov, T.M. Birshtein, and E.B. Zhulina. *Progress in Colloid and Polymer Science*, 90:177, 1992.
- [96] S. Misra, W.L. Mattice, and D.H. Napper. *Macromolecules*, 27:7090, 1994.
- [97] F.A. Plamper, M. Ruppel, A. Schmalz, O.V. Borisov, M. Ballauff, and A.H.E. Müller. *Macromolecules*, 40:5689, 2007.
- [98] J.W. Mays. *Polym. Commun.*, 31:170, 1990.
- [99] M. Heinrich, M. Rawiso, J.G. Zilliox, P. Lesieur, and J.P. Simon. *Europ. Phys. Journ. E*, 4:131, 2001.
- [100] P. Kosovan, J. Kuldova, Z. Limpouchova, K. Prochazka, E.B. Zhulina, and O.V. Borisov. *Soft Matter*, page in press, 2010.
- [101] W.A. Ducker, T.J. Senden, and R.M. Pashley. *Nature*, 353:239, 1991.
- [102] H.J. Butt, M. Jaschke, and W. Ducker. *Bioelectrochemistry and Bioenergetics*, 38(1):191, 1995.
- [103] W.A. Ducker, T.J. Senden, and R.M. Pashley. *Langmuir*, 8:1831, 1992.
- [104] L. Meagher. *J. Colloid Interface Sci.*, 152:293, 1992.
- [105] S. Biggs, P. Mulvaney, C.F. Zukoski, and F. Greiser. *J. Am. Chem. Soc.*, 116:9150, 1994.
- [106] S. Biggs, P.J. Scales, Y.K. Leong, and T.W. Healy. *J. Chem. Soc. Faraday Trans.*, 91:2921, 1995.
- [107] G. Toikka, R.A. Hayes, and J. Ralston. *J. Colloid Interface Sci.*, 180:329, 1996.
- [108] G. Toikka, R.A. Hayes, and J. Ralston. *Langmuir*, 12:3783, 1996.
- [109] D.T. Atkins and R.M. Pashley. *Langmuir*, 9:2232, 1993.
- [110] S. Biggs. *Ber. Bunsen-Ges. Phys. Chem.*, 98:636, 1994.
- [111] G.J.C. Braithwaite, A. Howe, and P.F. Luckham. *Langmuir*, 12:4224, 1996.
- [112] G.J.C. Braithwaite and P.F. Luckham. *J. Chem. Soc. Faraday Trans.*, 93:1409, 1997.



- [113] M. Giesbers, J.M. Kleijn, G.J. Fleer, and M.A. Cohen Stuart. *Colloids Surf. A*, 142:343, 1998.
- [114] J. Sprakel, E. Bartscherer, G. Hoffman, M.A. Cohen Stuart, and J. van der Gucht. *Phys. Rev. E*, 78:040802, 2008.
- [115] R. Pericet-Camara, G. Papastavrou, and M. Borkovec. *Langmuir*, 20:3264, 2004.
- [116] A. van den Noort and W.J. Briels. *Macromol. Theor. Simul.*, 16:742, 2007.
- [117] J.L. Keddie. *Materials Sci. Eng. R*, 21:101, 1997.
- [118] T.M. Birshtein and Yu.V. Lyatskaya. *Macromolecules*, 27:1256, 1994.
- [119] J.L. Hutter and J. Bechhoefer. *Rev. Sci. Instrum.*, 64:1868, 1993.
- [120] K.G. Marinova, D. Christova, S. Tcholakova, E. Efremov, and N.D. Denkov. *Langmuir*, 21:11729, 2005.
- [121] B.V. Derjaguin. *Colloid Z.*, 69:155, 1934.
- [122] B.V. Derjaguin and L.D. Landau. *Acta Physicochim*, 14:633, 1941.
- [123] E.J.W. Verwey and J.T.G. Overbeek. *Theory of the Stability of Lyophobic Colloids*. Elsevier, 1948.
- [124] L. Tskhovrebova, J. Trinick, J.A. Sleep, and R.M. Simmons. *Nature*, 387:308, 1997.
- [125] M. Rief, M. Gautel, F. Oesterhelt, J.M. Fernandez, and H.E. Gaub. *Science*, 276:1109, 1997.
- [126] C. Ortiz and G. Hadziioannou. *Macromolecules*, 32:780, 1999.
- [127] T. Hugel, M. Grosholz, H Clausen-Schaumann, A. Pfau, H. Gaub, and M. Seitz. *Macromolecules*, 34:1039, 2001.
- [128] K. Nakajima, H. Watabe, and T. Nishi. *Polymer*, 47:2505, 2006.
- [129] G. Sun and H.J. Butt. *Macromolecules*, 37:6086, 2004.
- [130] T.J. Senden, J.M. di Meglio, and P. Auroy. *Eur. Phys. J. B*, 3:211, 1998.
- [131] D. Goodman, J.N. Kizhakkedathu, and D.E. Brooks. *Langmuir*, 20:2333, 2004.

- [132] C. Bouchiat, M.D. Wang, J.F. Allemand, T. Strick, S.M. Block, and V. Croquette. *Biophys. J.*, 76:409, 1999.
- [133] D. Goodman, J.N. Kizhakkedathu, and D.E. Brooks. *Langmuir*, 20:3297, 2004.
- [134] C. Hiergeist and R. Lipowsky. *J. Phys II*, 6:1465, 1996.
- [135] R. Joannic, L. Auvray, and D.D. Lasic. *Phys. Rev. Lett.*, 78:3402, 1997.
- [136] D. Needham, T.J. McIntosh, and D.D. Lasic. *Biochim. Biophys. Acta*, 1108:40, 1992.
- [137] D. Marsh, R. Bartucci, and L. Sportelli. *Biochim. Biophys. Acta B*, 1615:33, 2003.
- [138] H.E. Warriner, S.H.J. Idziak, N.L. Slack, P. Davidson, and C.R. Safinya. *Science*, 271:969, 1996.
- [139] T.M. Birshtein and E.B. Zhulina. *Macromol. Theory Simul.*, 6:1169, 1997.
- [140] I. Szleifer, O.V. Gerasimov, and D.H. Thompson. *Proc. Natl. Acad. Sci. USA*, 95:1032, 1998.
- [141] M. Rovira-Bru, D.H. Thompson, and I. Szleifer. *Biophys J.*, 83:2419, 2002.
- [142] E.B. Zhulina. *Pol. Sci. (USSR)*, 26:794, 1984.
- [143] T.M. T.M. Birshtein and E.B. E.B. Zhulina. *Polymer*, 25:1453, 1984.
- [144] P.-G. de Gennes. *Macromolecules*, 13:1069, 1980.
- [145] E.B. Zhulina, T.M. Birshtein, and O.V. Borisov. *Eur. Phys. J. E*, 20:243, 2006.
- [146] T.M. Birshtein, O.V. Borisov, E.B. Zhulina, A.R. Khokhlov, and T.A. Yurasova. *Vysokomolekulyarnye Soedineniya Seriya, A*, 29:1169, 1987.
- [147] G.H. Fredrickson. *Macromolecules*, 26:2825, 1993.
- [148] M. Saariaho, O. Ikkala, I. Szleifer, I. Erukhimovich, and G. ten Brinke. *J. Chem. Phys.*, 107:3267, 1997.
- [149] M. Saariaho, I. Szleifer, O. Ikkala, and G. ten Brinke. *Macromol. Theory Simul.*, 7:211, 1998.
- [150] A. Subbotin, M. Saariaho, O. Ikkala, and G. ten Brinke. *Macromolecules*, 33:3447, 2000.

- [151] L. Feuz, F.A.M. Leermakers, M. Textor, and O.V. Borisov. *Macromolecules*, 38:8891, 2005.
- [152] A. Subbotin, J. de Jong, and G. ten Brinke. *Eur. Phys. J. E*, 20:99, 2006.
- [153] P.G. Khalatur, D.G. Shirvanyanz, N.Y. Starovoitova, and A.R. Khokhlov. *Macromol. Theory Simul.*, 9:141, 2000.
- [154] P.G. Khalatur, A.R. Khokhlov, S.A. Prokhorova, S.S. Sheiko, M. Müller, P. Reineker, D.G. Shirvanyanz, and N. Starovoitova. *Eur. Phys. J. E*, 1:99, 2000.
- [155] I.I. Potemkin. *Eur. Phys. J. E*, 12:207, 2003.
- [156] I.I. Potemkin, A.R. Khokhlov, S.A. Prokhorova, S.S. Sheiko, M. Müller, K.L. Beers, and K. Matyjaszewski. *Macromolecules*, 37:3987, 2004.
- [157] C.W. Wijmans and E.B. Zhulina. *Macromolecules*, 26:7214, 1993.
- [158] A.N. Semenov. *Sov. JETP*, 61:733, 1985.
- [159] G.S. Grest, K. Kremer, and N.A. Witten. *Macromolecules*, 20:1376, 1987.
- [160] S.T. Milner and T.A. Witten. *J. Phys. (Paris)*, 49:1951, 1988.
- [161] M. Laradji. *Europhys. Lett.*, 60:594, 2002.
- [162] W. Helfrich. *Z. Naturforsch.*, 28c:693, 1973.
- [163] S.M. Oversteegen and F.A.M. Leermakers. *Phys. Rev. E*, 62:8453, 2000.
- [164] M.M.A.E. Claessens, B.F. van Oort, F.A.M. Leermakers, F.A. Hoekstra, and Cohen Stuart M.A. *Biophys. J.*, 87:3882, 2004.
- [165] R.A. Kik, F.A.M. Leermakers, and J.M. Kleijn. *Phys. Chem. Chem. Phys.*, 7:1996, 2005.
- [166] E.B. Zhulina and F.A.M. Leermakers. *Soft Matter*, 5:2386, 2009.
- [167] J. Sprakel, E. Spruit, J. van der Gucht, J.T. Padding, and W.J. Briels. *Phys. Rev. E*, 78:040802, 2008.

# Acknowledgements

This book is finally finished. I thank all the people who were helping all their best, offering not only the top scientific advice, but also a friendly atmosphere. First of all, my direct supervisors, Fans Leermakers, Mieke Kleijn, and Martien Cohen Stuart, thank you for this interesting project with its multitude of opportunities. Frans, apart from all the hottest scientific discussions and the never-ending avalanche of great ideas, I wish to thank you for not showing even a slight disbelief in the positive outcome. Mieke, thank you for your very accurate eye on the correct physical interpretations in this book, and even more for your personal support. Martien, thanks for putting several degrees of order to our plans and your advice which proved to be 100 percent correct.

Hans and Gerard, it was a great inspiration to see you working at the lab, and taking an active part in the discussions. Luuk, it was a pleasure to work with you teaching students.

Great thanks to the supporting staff for providing excellent working conditions at the lab. Anita and Mara, it is always lovely to see your smiles and hear your giggles. Remco, thank you for all the help and explanations with scattering and other set-ups, you really an outstanding pro. Anton, thanks for all the chats at your room. Yep, and all the borrowed cigarettes as well.

Josie, apart from your support on daily basis, I wish to thank you for one phrase which made this book to see the press in particular, namely "I've never gave up on you".

I want to thank all the fellow PhD students at the lab, any time spent with you, guys and girls, was perfect. Wouter, it was fun to work the long-hours at Langmuir and ISIS with you, and I'm really happy to see you finishing as well! Richard, that Han-sur-Lesse school we attended together is still briskly imprinted in my mind. As well as many other occasions. Bas, I think I might be moving closer to the understanding of all the benefits of hiking with foreigners. Thanks for the mystery! Joris, thanks for sharing all your know-how on AFM, the 4th chapter of this thesis would not occur without

that. Ilja, simply seeing you is a pleasure; seeing you at work is a truly unique experience.

I greatly acknowledge all my colleagues from Nuplex, it was a priceless experience to see your applied research in its best. Fred, Hans, Martin, it was great to see your eagerness to share your outstanding experience in coating systems.

The members of the lab 25 (now lab 7) at the Institute of Macromolecular Compounds in St.Petersburg, I thank you for opening up opportunities and all your support. Special thanks to my first scientific teacher, Tatiana Maximovna Birshtein, for the deep insight into the world of polymers. I honor and praise your way of teaching.

Друзья, спасибо вам, мне с вами хорошо, лучше вас не бывает!

Марина, без тебя эта книжка не увидела бы свет. Спасибо, и прости за то что не смог.

Дети, Софья, Тимофей, папа дописал первую книжку. Обещаю, остальные подарки намного интересней!

Ксюша, спасибо тебе за веру в мои силы, и за отличную обложку.

Папа, спасибо за помощь и совет в нужные моменты.

Мама, спасибо за то что мир вокруг интересен.

*Petya  
Wageningen, 2011*

## Curriculum Vitae

Petr Alexandrovitch Iakovlev was born on 22 September 1979 in Leningrad, Soviet Union. After finishing the gymnasium 11 in 1996 at the same place, now called St.Petersburg, Russia, he started studying general physics at the Physical Faculty of St.Petersburg State University. In 1999 he has chosen Molecular Biophysics as specialization. At the same time he started research for his Masters diploma under supervision of prof. T.M.Birshtein at the Institute of Macromolecular Compounds of Russian Academy of Sciences. During this period he has collaborated closely with the Physical Chemistry and Colloid Science group at Wageningen University, which resulted in an internship of three months during the spring of 2002. In September 2003 he started the PhD-study at the same group. The result of the study is presented in this book.

# List of publications

## This dissertation

- T.M. Birshtein, P.A. Iakovlev, V.M. Arnoskov, F.A.M. Leermakers, E.B. Zhulina, O.V. Borisov, "On the curvature energy of a thin membrane decorated by polymer brushes." *Macromolecules*, 41, (2008) 478-488 (Chapter 5).
- P.A. Iakovlev, J.M. Kleijn, F.A.M. Leermakers, M. A. Cohen Stuart, "Hydrophobic Polyelectrolyte Brushes and Stars: a Numerical Self-Consistent Field Study" (Chapter 3), to be submitted to: *Advances in Polymer Science*.
- P.A. Iakovlev, F.A.M. Leermakers, J.M. Kleijn, "Interactions Between Polyelectrolyte Core-Shell Particles: AFM force measurements" (Chapter 4), to be submitted.
- P.A. Iakovlev, F.A.M. Leermakers, J.M. Kleijn, "Time-dependence of bundles formation in interacting acrylic Core-Shell particles as studied with AFM force measurements" (Chapter 4), to be submitted.

## Other work

- A.A. Mercurieva, T.M. Birshtein, E.B. Zhulina, P.A. Iakovlev, J. van Male, F.A.M. Leermakers, "An annealed polyelectrolyte brush in a polar-nonpolar binary solvent: Effect of pH and ionic strength", *Macromolecules*, 35, (2002), 4739-4752.
- T.M. Birshtein, V.M. Amoskov, L.I. Klushin, A.A. Mercurieva, A.A. Polotsky, P.A. Iakovlev "Microphase coexistence in polymeric brushes", *Macromolecular Symposia*, 191, (2003), 51-58.
- T.M. Birshtein, V.M. Arnoskov, A.A. Mercurieva, D.K. Belyaev, P.A. Yakovlev, "Polymer brushes in a multicomponent solvent", *Polymer Sci. Ser. A*, 47 (5), (2005), 476-498.

- W.T.E. Bosker, P.A. Iakovlev, W. Norde, M.A. Cohen Stuart, "BSA adsorption on bimodal PEO brushes", J. Colloid Interface Sci. 286 (2005) 496-503.
- A.A. Mercurieva, P.A. Iakovlev, E.B. Zhulina, T.M. Birshtein, F.A.M. Leermakers "Wetting phase diagrams of a polyacid brush with a triple point", Physical Review E, 74 (3) (2006) 031803.



## Overview of completed training activities

### Discipline specific activities

Winterschool	Han-Sur-Lesse, Belgium	2004
Julich Soft Matter Days	Julich, Germany	2004
Student conference	St.Petersburg, Russia	2004
International Symposium	St.Petersburg, Russia	2005
European Polymer Congress	Moscow, Russia	2005
Dutch Polymer Days	Lunteren, The Netherlands	2005
Student conference	Biezenmortel, The Netherlands	2005
Schiermonnikoog meeting	Schiermonnikoog, The Netherlands	2005
RPK B Polymeer Physics	Utrecht, The Netherlands	2005
Dutch Polymer Days	Lunteren, The Netherlands	2007

### General courses

Philosophy of Science	St.Petersburg, Russia	2004
Scientific writing in english	St.Petersburg, Russia	2004

### Optionals

Capita Selecta	Wageningen, The Netherlands	2003-2007
Colloquia PCC	Wageningen, The Netherlands	2003-2007
Preparing PhD research proposal	Wageningen, The Netherlands	2003-2004
BASF PhD excursion	BASF, Germany	2004